

# UC San Diego

## UC San Diego Electronic Theses and Dissertations

### Title

Molecular Dynamics Simulations of Shock in Silicon and Diamond

### Permalink

<https://escholarship.org/uc/item/5sg3c7dp>

### Author

Li, Alex Ceng

### Publication Date

2024

Peer reviewed|Thesis/dissertation

UNIVERSITY OF CALIFORNIA SAN DIEGO

# **Molecular Dynamics Simulations of Shock in Silicon and Diamond**

A Dissertation submitted in partial satisfaction of the requirements  
for the degree Doctor of Philosophy

in

Materials Science and Engineering

by

Alex Ceng Li

Committee in charge:

Marc A. Meyers, Chair  
Farhat Beg  
Nicholas Boechler  
Vlado Lubarda  
Robert E. Rudd

2024

Copyright

Alex Ceng Li, 2024

All rights reserved.

The Dissertation of Alex Ceng Li is approved, and it is acceptable in quality and form for publication on microfilm and electronically.

University of California San Diego

2024

## DEDICATION

To my parents,  
Morris Li and Zhaohua Ceng  
For their support throughout my life and education

## TABLE OF CONTENTS

DISSERTATION APPROVAL PAGE .....	iii
DEDICATION .....	iv
TABLE OF CONTENTS.....	v
LIST OF FIGURES .....	viii
LIST OF TABLES .....	xii
ACKNOWLEDGEMENTS .....	xiii
VITA.....	xv
ABSTRACT OF THE DISSERTATION .....	xvi
<b>Chapter 1 Introduction</b> .....	1
1.1 Research Objectives .....	4
<b>Chapter 2 Background</b> .....	6
2.1 Shock.....	6
2.2 Laser Shock Compression.....	10
2.3 Laser Shock Sample Preparation and Recovery .....	12
2.4 Dislocations.....	13
2.5 Voids .....	14
2.6 Molecular Dynamics Simulations .....	17
2.7 Interatomic Potentials.....	20
2.8 Other Computational Simulation Types.....	24
2.9 Simulation Codes .....	29
2.10 Simulation Process .....	30
2.11 Data Processing.....	35
<b>Chapter 3 Silicon Under Extremes</b> .....	42
3.1 Introduction .....	42

3.2 Computational Methods .....	46
3.3 Elastic moduli, Melt temperature vs. pressure, and Hugoniot calculations .....	49
3.4 Plasticity .....	54
3.5 Alternative Structure Identification Method .....	60
3.6 Amorphization.....	65
3.7 Summary .....	69
3.8 Acknowledgments.....	70
<b>Chapter 4 Diamond under Extremes .....</b>	<b>71</b>
4.1 Diamond Synthesis .....	73
4.2 Static Compression of Diamond .....	79
4.3 Diamond Phase Diagram.....	83
4.4 Molecular Dynamics for Diamond Under Extremes .....	85
4.5 Preliminary Simulations of Diamond Shock to High Pressures .....	89
4.6 Diamond Experimental Laser Shock .....	93
4.7 Diamond Capsules at the NIF .....	97
4.8 Acknowledgments.....	100
<b>Chapter 5 Diamond Dislocations and Effects of Voids on Shocked Diamond .....</b>	<b>101</b>
5.1 Introduction .....	101
5.2 Simulation Results .....	104
5.3 Conclusions .....	126
5.4 Acknowledgments.....	128
<b>Chapter 6 Effects of Void Size on Diamond Plasticity Thresholds .....</b>	<b>129</b>
6.1 Introduction .....	129
6.2 Void Size Effects in [111] Oriented Diamond Shock Compression.....	131
6.3 Prediction of threshold stress from dislocation mechanics .....	134

6.4 Effect of Void Size on threshold stress .....	137
6.5 Acknowledgements .....	140
<b>Chapter 7 Conclusions</b> .....	141
REFERENCES .....	144
APPENDICES .....	174
Appendix A – LAMMPS Input Files.....	174
Appendix B – Calculation of the Lu Factor.....	183



## LIST OF FIGURES

Figure 1-1 Sketch of a Two-stage light gas gun. Often used for shock experiments, capable of accelerating projectiles up to 10km/s. Taken from (6). .....	2
Figure 1-2 a) Sketch of a typical anode-cathode flier plate setup in the Z accelerator at Sandia. The current flowing through the magnetic field provides the Lorentz force which accelerates the flier plates. b) The stripline configuration, with currents of 20 MA and a magnetic field of 1200T, accelerated aluminum plates up to 45 km/s. Taken from (7). .....	3
Figure 2-1 A shock wave traveling from left to right. Ahead of the shock front, the ambient crystal is undisturbed. As the elastic wave passes, a state of uniaxial strain is imposed. Finally, a plastic wave follows where the material may attempt to undergo plasticity to relieve strain in the system. Taken from (11). .....	6
Figure 2-2 Illustration of how material piles up in front of a piston and a shock wave is created. The boundary between the compressed area in front of the piston and the uncompressed fluid is the shock wave discontinuity. Taken from (14).....	8
Figure 2-3 Characteristic Hugoniot (P-V) curve showing Rayleigh Line. Taken from (14).....	9
Figure 2-4 Left: schematic of the target and laser configuration including the hohlraum. Bottom right: the HDC capsule and DT fuel configuration. Top right: total laser power vs time and radiation temperature $Tr$ as a function of time. Taken from (10).....	11
Figure 2-5 a) Sample Recovery setup for a laser shock experiment b) Example of a silicon sample encased in impedance matched aluminum. The CH ablator provides the pressure shock pressure after being heated by the pulsed laser. Taken from (24). .....	13
Figure 2-6 Shock moving through 3% porous copper, producing shear dislocation loops from voids. Taken from (41). .....	15
Figure 2-7 Normalized von Mises stress for dislocation nucleation from a void surface as a function of normalized void radius $R/b$ . Taken from (44).....	16
Figure 2-8 A single step in the molecular dynamics simulation loop for updating atomic positions. Taken from (46).....	18
Figure 2-9 A potential profile for the Lennard-Jones pair potential. From (57).....	22
Figure 2-10 System size and simulation periods of various computer simulation types. Taken from (64). .....	24
Figure 2-11 The assumption made to simplify the solution of electronic structure calculation for Density Functional Theory. Taken from (73).....	26
Figure 2-12 Training database for the carbon SNAP machine learning potential. (a) Pressure-temperature map of QMD and static DFT simulations included in the database, each represented by a $P$ - $T$ point on carbon phase diagram sampling diamond (FC8), body-centered cubic (BC8), and simple cubic (SC) solid and liquid phases (total number of .....	29
Figure 2-13 Silicon Polycrystal with diamond-cubic grains created with atomsk. Grains are colored by orientation, with periodic boundary conditions. ....	32

Figure 2-14 Two methods of simulating shock in non-equilibrium molecular dynamics simulations. a) Piston moving at a speed $U_p$ produces shock of speed $U_s$ . b) Compression of the material as a function of time. c) Moving a sample at speed $-U_p$ into a momentum mirror produces a reflecting shock wave. Taken from (92).	34
Figure 2-15 Post-processing pipeline in OVITO. Taken from (96).	36
Figure 2-16 Differences between RDF for crystalline, paracrystalline, and amorphous cellulose. Taken from (103).	40
Figure 2-17 DXA analysis of a diamond nanoparticle a) after loading to 0.42 strain and b) After relaxation and annealing at 2000K over 1ns. Taken from (106).	41
Figure 3-1 - Elastic moduli (a) $C_{11}$ , (b) $C_{12}$ , (c) $C_{44}$ and (d) $G$ (shear modulus) calculated as a function of increasing hydrostatic pressure; compared against density functional theory results of Karki et al. (162) (e) Pressure dependent melting temperature plotted alongside shock-induced temperature rise. The experiment	52
Figure 3-2 - a) Hugoniot (as calculated for each potential) compared to experimental measurements (95, 137, 138, 165–168). b) Pressure-volume diagram for the same potentials and experiments. c) Pressure-volume diagram focused on the elastic and early plastic transition.	53
Figure 3-3 Figure 3-4 Snapshots from NEMD shock simulation performed at $U_p = 2$ km/s (12 GPa) using the MOD potential displaying simultaneous $\{111\}$ and $\{110\}$ stacking faults. (a) depth perspective showing interaction between the mutual stacking fault planes. (b) thin section illustrating the resultant angles of the $\{111\}$ and $\{110\}$ stacking fault planes with the	56
Figure 4-1 A large 155 carat single crystal diamond wafer, heteroepitaxially grown via ion bombardment on a Ir/YSZ/Si 001 substrate. (taken from Ref. (214))	74
Figure 4-2 Phase diagram of carbon showing the various temperature and pressure conditions that the various methods of creating diamond are located in. (taken from Ref. (223).)	75
Figure 4-3 375x zoom on a diamond fragment embedded within the Canyon Diablo meteorite. Taken from (225).	76
Figure 4-4 Pressure vs. temperature diagram for carbon; points 1 to 7 represent different Chapman-Jouguet states for different explosives. It can be seen that, except for Explosive 1, the points are in the liquid region. Taken from Volkov (233).	78
Figure 4-5 Schematic and images of a diamond anvil cell.(a) Diagram of the DAC (b) Zoom in on the high pressure chamber (c) Real image of the sample chamber within the DAC. Taken from (247).	80
Figure 4-6 A phase diagram for diamond up to 3.5 TPa and 15000K has been consolidated from several sources, including early first principles estimates of the phase boundaries, up to the most recent machine learned calculations for the phase transitions of diamond. Aside from the earliest calculations	83
Figure 4-7 A possible metastable pathway towards experimentally forming BC8 diamond. A) Shows the extended diamond melting line, where if the diamond is taken above this line will form a metastable supercooled liquid. If the temperature can then be lowered into the green BC8 zone, the BC8 crystal structure should	85

Figure 4-8 6 km/s piston velocity driving shock compression of cubic [001] diamond. Only elastic compression is observed, even as the structure identification algorithm fails to identify the compressed portion. ....	90
Figure 4-9 8 km/s piston velocity driving shock compression of cubic [001] diamond. Still, only elastic compression is observed. However, much more disorder within the crystalline phase can be seen.....	91
Figure 4-10 Comparison of the (top) diamond cubic recrystallized grains within an amorphous melt and the (bottom) potential energies of atoms within the simulation. The recrystallized grains are of a much lower potential energy, indicating a more stable form.....	92
Figure 4-11 A closeup of the transition region between the elastically compressed portion at the right of the image and the amorphous melt and recrystallization that follows in a second plastic wave. The recrystallized grains look to exhibit twinning-like features, due to the patterns of the atomic order present within the simulation.....	92
Figure 4-12 Target design for the laser shock of [001] oriented diamond. The diamond was wrapped in a shell of gold and molybdenum, both impedance matched materials to aid in the recovery of the diamond sample for post-shock characterization. ....	93
Figure 4-13 Diamond shocked to 60 GPa, below the Hugoniot elastic limit. As expected, the crystalline structure is perfectly preserved. ....	94
Figure 4-14 The second shot (300J) had too jagged of a surface to allow for TEM characterization.....	95
Figure 4-15 400J Diamond 3 sample shot. Crater in the middle, with an amorphous film on the top surface. ....	96
Figure 4-16 Sample of Amorphous surface and diffuse ring pattern from the diffraction. ....	97
Figure 4-17 A polycrystalline diamond sample. Alternating grains of [001] and [111] oriented diamond are present in the center, bounded by [011] grains at the tops and bottoms. A void placed in the center of the [111] grain would be affected by the presence of the grain boundaries surrounding it.....	99
Figure 5-1 Anisotropy of the dislocation response to compression of a diamond nanopillar. Taken from (262).....	103
Figure 5-2 137 GPa simulation (3.5 km/s piston velocity) for [001] shock loading direction. Blue color indicates perfectly matched diamond structure, green indicates first or second nearest neighbor diamond cubic, and white indicates a non-diamond structure.a) In the absence of a void, no dislocations or non-diamond regions.....	107
Figure 5-3 Simulation of [111] compressed diamond at 91.4 GPa (2.5 km/s piston velocity) 5 picoseconds into the simulation. Two distinct defects can be seen emanating from the piston surface. The orientations of these faults are in the {100} family of planes in the <110> directions.....	108
Figure 5-4 Initiation of Defects from the void. Image captured using DXA analysis at 1.5ps in the [111] loading orientation, just as the shock wave has finished passing over the void and the defects have initiated. Several defects can be seen to initiate opposite to the direction of shock. Blue dislocation lines indicate dislocations.....	110

Figure 5-5 Evolution of the defects emanating from the void for [111] loading orientation. The three-fold symmetric straight bands are the same as the bands seen in the case without a void present, $\langle 110 \rangle$ direction in the $\{100\}$ plane. In addition, loops with Burgers vector $1/2\langle 112 \rangle$ appear on the $\{111\}$ planes between these 3 straight bands. ....	111
Figure 5-6 Resolved Shear Stresses along different slip systems. A sphere was formed around the void with a 6nm radius, and per atom stress values were taken after the shock wave had passed through the void and dislocations just began to form. The different resolved shear stresses show the directional differences in the stress concentrations.....	112
Figure 5-7 Dislocations around a void. a) DXA dislocation and defect analysis of the [111] shocked diamond system at 3.25 ps. b) A graphical representation of the planes and orientations of the system. The rectangular bands propagate within the $\{100\}$ planes, while the half-loops connecting them are present along the $\{111\}$ planes.....	113
Figure 5-8 54 GPa (2 km/s piston velocity) simulation for [111] diamond shock at 10 ps. a) A view of all atoms within the system with coordination number other than 4, the usual value for diamond. No atoms beyond the piston surface are detected, i.e., all are diamond. b) The beginnings of dislocations can be seen to form when a void is present. ....	115
Figure 5-9 Defect propagation velocity at varying simulation pressures and piston velocities (72.6 GPa = 2.5 km/s, 91.4 GPa = 3 km/s, and 123 GPa = 3.5 km/s). An additional measurement was made at 120 GPa (3.5 km/s) corresponding to the green line, measuring the propagation velocity of a dislocation. Shear wave velocity calculated .....	116
Figure 5-10 Non-diamond atoms and DXA analysis for [011] shocked diamond at 2.5 ps. The defect bands emanating from the void are oriented in the $1/2\langle 112 \rangle$ directions, and are semicircular in shape as they expand away from the void surface. ....	117
Figure 5-11 Orientation Relationships for Shock Loading and Slip Planes .....	122
Figure 6-1 – Schematic illustration of the hohlraum and capsule used in NIF experiments. The NIF lasers enter from the top and the bottom, impinging on the gold shell of the hohlraum and heating it up, producing X-rays. These X-rays couple to the surface of the diamond capsule, causing it to ablate away, compressing the remaining capsule.....	130
Figure 6-2 - MD simulations showing the threshold for dislocation generation for different void sizes (diameters) and the shock pressure at which they first form dislocations from the void. a) 2 nm, 232 GPa b) 4 nm, 177 GPa c) 12 nm, 146 GPa d) 18 nm, 135 GPa e) and f) Differences in dislocation configurations between e) 2-nm and f) 18-nm voids .....	133
Figure 6-3 12 nm diameter void. Slice, 0.2 nm thick, with different color scales. (a) Structure type: diamond (blue), unknown (white). (b) Atomic potential energy (PE). (c) Atomic rotation, X component of the quaternion from PTM, with rmsd=0.1. The shock moves along z, causing an increase of PE in the equator, where dislocations nucleate. ....	134
Figure 6-4 - Shock stresses for the emission of dislocations as a function of void diameter; comparison of MD results with analytical predictions (1) and (5). ....	138

## LIST OF TABLES

Table 2-1 Parameters for calculation of grain size simulation capabilities .....	19
Table 3-1 Predominant ambient and high pressure ( $P < 25$ GPa) polymorphs of silicon. Data from multiple sources ( <i>142, 154–156</i> ).....	45
Table 3-2 Table of common semi-empirical silicon potentials, parameterizations, and their abbreviations. ....	46
Table 5-1 - Loading Orientations, Piston velocities, global pressure, and shock/transverse/shear stresses (GPa) for the simulations presented in this paper.....	104
Table 5-2 - Stress concentration factors for slip systems comparing the stress at the void surface vs the bulk.....	110
Table 5-3 Transformed Stress Tensors at ~140 GPa with change of basis loading direction. Original values from Orlikowski et al.( <i>324</i> ), Güler et al ( <i>320</i> ), González-Cataldo et al ( <i>325</i> )..	121
Table 5-4 Schmid and Lu Factors (resolved shear stress with transformed tensor) for relevant slip systems.....	123
Table A-1 Table of generalized Schmid factors for uniaxial [001] strain. The 3 left-most columns show the longitudinal direction, the direction of the Burgers vector and the direction of the glide plane normal. The other columns contain the data values at the pressures shown at the top. The spacing between the rows help guide the eye to cases with equal generalized Schmid factors.	188
Table A-2 Table of generalized Schmid factors for uniaxial [011] strain. The 3 left-most columns show the longitudinal direction, the direction of the Burgers vector and the direction of the glide plane normal. The other columns contain the data values at the pressures shown at the top. The spacing between the rows help guide the eye to cases with equal generalized Schmid factors.	189
Table A-3 Table of generalized Schmid factors for uniaxial [111] strain. The 3 left-most columns show the longitudinal direction, the direction of the Burgers vector and the direction of the glide plane normal. The other columns contain the data values at the pressures shown at the top. The spacing between the rows help guide the eye to cases with equal generalized Schmid factors.	190

## ACKNOWLEDGEMENTS

Molecular dynamics simulations utilized resources that were provided by the Lawrence Livermore National Labs under the Computational Chemistry and Materials Science Program, and as a collaborator to the labs. The support provided to Alex Ceng Li and Marc Meyers by the Center for Matter under Extreme Conditions (award number DE-NA0004147) is gratefully acknowledged. This work was supported by the LDRD program at Lawrence Livermore National Laboratory (21-ERD-032). This work was performed in part under the auspices of the US Department of Energy by LLNL under contract DE-AC52-07NA27344.

I would like to thank Dr. Robert E. Rudd for mentoring me through my work at Livermore, teaching me everything I needed to know to run these shock simulations and analyze the results; Dr. Eduardo Bringa for his experience and insights into diamond simulations and voids; Drs. Rachel Flanagan and Eric Hahn for their collaboration in the work on silicon and guidance on molecular dynamic simulations; Dr. Aomin Huang for insightful conversations covering materials science and more; Ms. Boya Li as my partner in the experimental sections of this work on shock; and Dr. Marc Meyers for the opportunity to study shock and computer simulations, connecting with so many talented scientists and researchers, and present research under his guidance.

Chapter 3, in part, is in preparation for publication authored by E. N. Hahn, R.M Flanagan, A. Li, and M.A. Meyers, Computational Evaluation of Silicon under Shock Compression, (2024). The dissertation author was the third author of this article.

Chapter 4, in part, is in preparation for submission for publication: A.C. Li, B. Li, R.E. Rudd, E.M. Bringa, F. Gonzalez, and M.A. Meyers, Diamond Under Extremes, (2024). The dissertation author was the first and corresponding author of this article.

Chapter 4, in part, is in preparation for submission for publication: B. Li, A.C. Li, M.A. Meyers, Shock Compression of [100] diamond using pulsed lasers. The dissertation author was the second author of this article.

Chapter 5, in part, is a reprint of material that has been published: A.C. Li, B. Li, R.E. Rudd, and M.A. Meyers, Dislocation Generation in Diamond Under Extreme Loading, *Matter* 6, 1-17 (2023).

Chapter 6, in part, is in preparation for submission for publication: A.C. Li, M.A. Meyers, E.M. Bringa, R.E. Rudd, Diamond Response to Extreme Deformation, (2024). The dissertation author was the first and corresponding author of this article.

## VITA

- 2015 Bachelor of Science in Materials Science and Engineering, Mechanical Engineering, UC Berkeley
- 2018 Master of Science in Materials Science and Engineering, Columbia University
- 2024 Doctor of Philosophy in Materials Science and Engineering, University of California San Diego

## PUBLICATIONS

Alex C. Li, Boya Li, Robert E. Rudd, Marc A. Meyers (2023) *Dislocation generation in diamond under extreme loading*, Matter, 2023, <https://doi.org/10.1016/j.matt.2023.06.044>

B.Y. Li, A.C. Li, S. Zhao, M.A. Meyers, (2022) *Amorphization by mechanical deformation*, Materials Science and Engineering: R: Reports, Volume 149, 100673, <https://doi.org/10.1016/j.mser.2022.100673>



ABSTRACT OF THE DISSERTATION

Molecular Dynamics Simulations of Shock in Silicon and Diamond

by

Alex Ceng Li

Doctor of Philosophy in Materials Science and Engineering

University of California San Diego, 2024

Professor Marc A. Meyers, Chair

The dynamic behavior of materials under shock has been a deeply studied topic due to the different ways materials respond to high strain rate situations compared to static compression or tension conditions. The methods to study shock behavior of materials have advanced greatly since World War II, with the development of better and more controllable methods of producing shock

such as gas guns, flier plate systems, or at the highest range of experiment and application, high-power pulsed lasers. The ability to simulate materials using atomic forces to recreate physical properties has also been developed and continues to grow with the rise in computational power at supercomputing centers like those available at the national laboratories. These simulations can now allow for reproduction or simulation of experiments containing billions of atoms that are on the micrometer scale and can occur on timescales up to microseconds, placing them squarely in the territory of high strain rate shock experiments.

This work focuses on the study of shock behavior in the covalently bonded materials silicon and diamond carbon. The behavior of these materials compared to others such as metals varies greatly due to the bonding, especially the strength of the  $sp^3$  bonds present in these diamond cubic materials. Under shock conditions the differences of the way in which these materials behave is of great interest due to the uses that these materials may have under high strain rate conditions. Diamond in particular is important as an ablative material for use in high energy density physics experiments, such as in the capsule material for holding deuterium and tritium fuel in the inertial confinement fusion effort at the National Ignition Facility. This diamond is produced via chemical vapor deposition, and defects such as voids may be introduced both through the growth process and the preparation methods for filling the capsules.

For silicon, a study is performed between different interatomic potentials that compare and contrast their efficacy in recreating experimental phenomena such as elastic constant, melting points, phase transformations, and amorphization. A method for easily identifying structure is applied using the angular distribution function of bonds within unidentified phase changed regions in shear bands caused by the shock and compared with pristine crystalline units of known possible phases.

For diamond, laser shock experiments were performed on [001] oriented diamond above and below its Hugoniot elastic limit and confirmed that no dislocations were present even above the expected plasticity threshold. In simulations, the effect of orientation and the presence of voids was investigated. At a piston velocity of 3.5 km/s resulting in pressures of over 130 GPa, the [001] orientation still produced no dislocations, while the [011] and [111] orientations produce considerable dislocation activity, with the [111] orientation with a 4nm diameter void present producing  $\frac{1}{2} \langle 110 \rangle \{001\}$  and  $\frac{1}{2} \langle 112 \rangle \{111\}$  dislocations in a three-fold symmetric fashion from the void. A resolved shear stress analysis was performed to explain why certain slip planes were active, dependent upon the loading conditions and the orientations diamond. This analysis is termed the Lu Factor.

Additional simulations were performed in the [111] orientation, investigating plasticity thresholds and their dependence on void size, with 2 nm diameter voids requiring 232 GPa shock pressures to produce dislocations, down to only 135 GPa for 18 nm voids. An analytical model previously used for determining critical stress thresholds against void size in metals is modified for diamond by including an important Peierls-Nabarro term, and also extending its applicability to covalently-bonded materials and a wide range of void sizes.

The results of this dissertation shed light on some of the behaviors of plasticity in silicon and diamond carbon, as well as developing and refining analytical methods for the defects generated in these materials under shock compression.

## Chapter 1 Introduction

The study of how materials deform is fundamental to our understanding of strength and how they may undergo permanent change and eventual failure. There exists a myriad of mechanisms for plastic behavior. In crystal lattices, the nucleation and flow of dislocations occurs in response to shear stresses and are governed by available slip systems, local dislocation densities, and the applied strain rate. Twinning can occur to relieve large shear stresses and in cases where mobile dislocations are unfavored. Local instabilities can cause materials to deform via shear localization, resulting in amorphous bands of disordered atoms within the material. Phase transformations can change the crystal structure of the material itself to a more favorable energetic configuration. All of these can be considered defects within the material, changes in the local structure in response to applied stresses, strains, temperature conditions that govern the stability of the composition.

Defect generation under shock deformation is an even more complex phenomenon; point defects, dislocations, stacking faults, and phase transformations are produced by the extreme stresses generated. It is essential to recognize that many of these defects are the result of deviatoric stresses, and not of hydrostatic pressure. The study of these defects stems from WW2 and the Manhattan project. Smith (*1*) was one of the first to address the problem; dislocations were proposed to accommodate the change in the lattice parameter at the shock front. There has been a cornucopia of activity in this field in the past 70 years, exploring in detail the formation of the various defects in many materials (*2, 3*).

The experimental study of shock deformation has evolved greatly over the years. The two-stage light gas gun, first invented in 1948, presented the ability to controllably and reproducibly accelerate targets to supersonic velocities through the compression of a column of gas and then

the quick release of built-up pressure by a quick-release valve (4-6). For the acceleration of flier plates for planar shock impacts, modern gas gun designs (Fig.1-1) can accelerate light targets in excess of 10 km/s. A range of other techniques can achieve these hypervelocity impacts as well, from older implementations of explosive lenses or electromagnetic railguns with velocities similar to gas guns, to modern facilities like the Z magnetic pulsed power facility at Sandia National Labs that can reach speeds of 45 km/s (7, 8) (Fig. 1-2). At the pinnacle of our abilities to create extreme shock pressures is laser shock, where facilities like the National Ignition Facility at Lawrence Livermore National Laboratories have achieved implosion speeds of near 400 km/s (9) and have reached the requisite conditions for nuclear fusion (10).

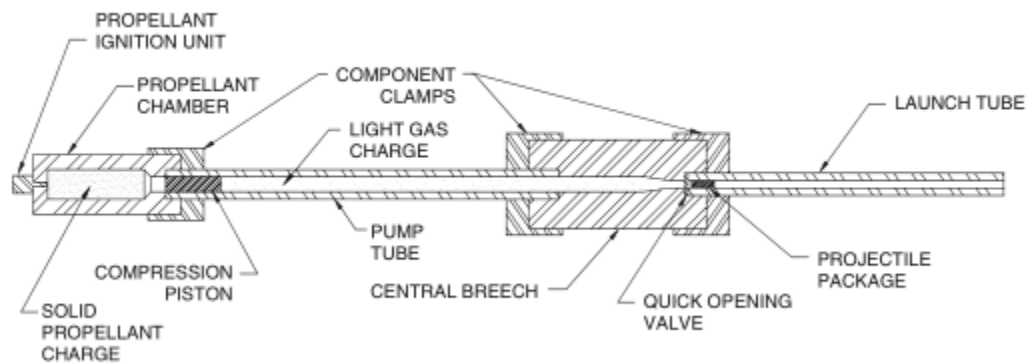


Figure 1-1 Sketch of a Two-stage light gas gun. Often used for shock experiments, capable of accelerating projectiles up to 10km/s. Taken from (6).

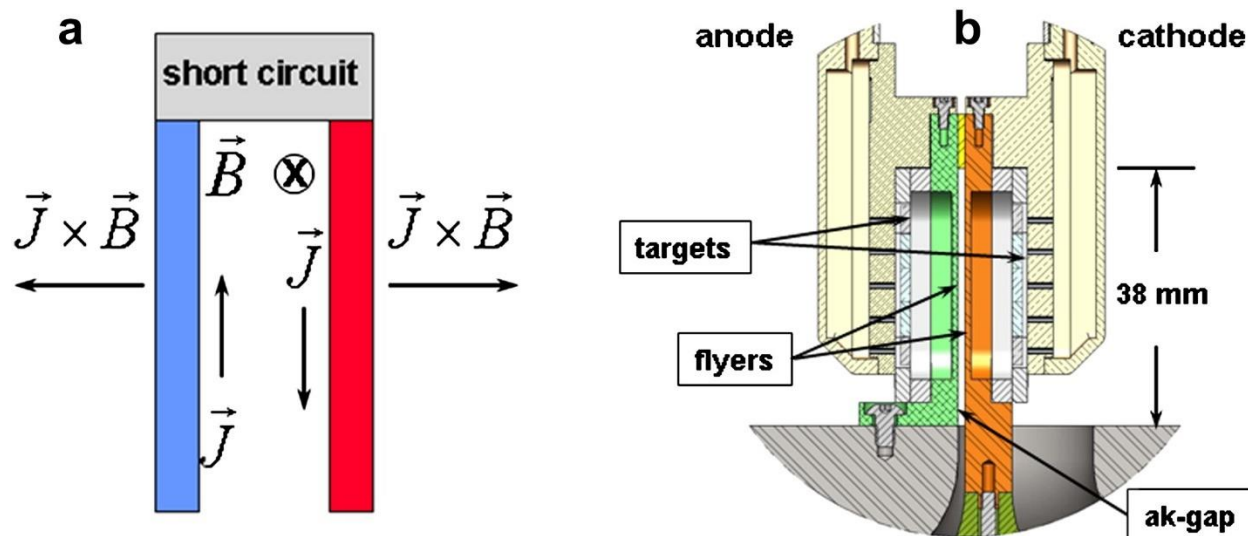


Figure 1-2 a) Sketch of a typical anode-cathode flier plate setup in the Z accelerator at Sandia. The current flowing through the magnetic field provides the Lorentz force which accelerates the flier plates. b) The stripline configuration, with currents of 20 MA and a magnetic field of 1200T, accelerated aluminum plates up to 45 km/s. Taken from (7).

At the same time as experiments were developing better and higher velocity shock impacts, the growth of computational tools and the computational power needed to simulate materials at an atomic level was also increasing exponentially. With the supercomputing clusters available today, billions of atoms can be simulated over microseconds, approaching the sizes and timescales of these real-world shock experiments. With these resources in hand, we can use simulations to model the development of materials under shock conditions, with atomic scale size resolution and femtosecond time resolution, to model from pure atomic interactions how materials deform under shock conditions.

The use of computer simulations to perform *in silico* evaluations of high energy density physics experiments can dramatically benefit their design and increase our understanding of the principles behind material behavior. Laser shock experiments can be expensive and time consuming to set up, while computational modeling in comparison can have higher throughput, providing guidance on what should be investigated. Current experimental diagnostic tools are also

unable to reach the spatial and temporal resolutions required for analysis of nanometer and nanosecond events simultaneously as they are occurring. A combination of experiments and simulations can provide the basis for constitutive models that reflect the fundamental physics of the deformation processes that may lead to plasticity and failure.

## **1.1 Research Objectives**

The crystallinity of solids makes it so that the response of solids to shock is completely different from that of better-behaved shock in gases or liquids. The presence of material strength, plastic flow, phase transitions, and other consequences of atomic bonding result in a viscoplastic heterogeneous response that is not in an equilibrium state. Even between materials, the differences in atomic bonding types and strengths heavily affect shock response. Under static loading conditions, metals deform far more easily than brittle covalently bonded solids. Under the high strain rate conditions however, even covalently bonded solids can exhibit plasticity.

The objective of the present investigation was to advance our understanding of model covalently bonded crystal structures under shock by performing computational simulations of the materials under shock conditions, focusing primarily on silicon and diamond carbon. The overall investigation had three components; the initial investigation involved simulation of phase transformations and possible amorphization in silicon. Silicon undergoes deformation processes at much lower pressures than carbon, and its multiple phase changes are better experimentally documented and understood. The second component involved transferring our understanding of shock in silicon to the similarly structured but much stronger diamond carbon. Different microstructural morphologies or shock orientation directions can be tested to see how the strength of diamond may vary depending on shock conditions, and if dislocations or other defects would form before the diamond would fail catastrophically. The third component involves an extension

of the study of voids from the initial diamond investigation, to find how their sizes affect plasticity thresholds and the strength of diamond before it would deform plastically.

When possible, theoretical models are applied or adjusted to help explain or justify our results. The mixing of theory and simulation can help provide deeper understanding of the fundamental physics behind the phenomena that are being observed in both materials.



## Chapter 2 Background

### 2.1 Shock

Before we discuss how materials and deformation modes are affected by shock compression, we must first understand shock itself. Shock compression is a dynamic mechanical process, defined as a large-amplitude wave across which there is a discontinuity in the pressure, density, particle velocity, temperature and other properties before and after the shock wave front. It occurs when material is subjected to rapid impulsive loading, on a timescale where body as a whole cannot respond inertially. In solids, this one-dimensional loading and inertial confinement result in a state of uniaxial strain, as seen in Figure 2-1.

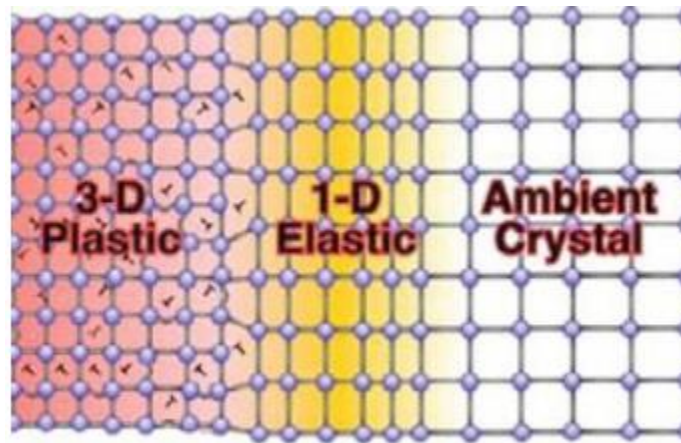


Figure 2-1 A shock wave traveling from left to right. Ahead of the shock front, the ambient crystal is undisturbed. As the elastic wave passes, a state of uniaxial strain is imposed. Finally, a plastic wave follows where the material may attempt to undergo plasticity to relieve strain in the system. Taken from (11).

Shock waves travel faster than the sound speed of the material, with a velocity that is dependent on the amplitude of the wave. Shock-wave behavior in a material can be compared to how a snowplow operates, as illustrated in Figure 2-2. The snowplow is moving at a velocity of  $U_p$ , pushing the snow and snowpack directly in front of it at that same velocity. However, snow is continuously piling up ahead of the snowplow, and this region separating the fresh snow from

the packed snow is moving at a velocity  $U_s$ . Empirically, a linear relationship called the shock wave equation of state is observed for most materials between the piston or particle velocity and the resulting shock velocity.

$$U_s = C_0 + SU_p \quad (1)$$

$C_0$  is the longitudinal sound speed of the material, and  $S$  is empirically derived. If the material undergoes phase transformation or is porous, this equation of state needs to be modified with additional terms.

The Rankine-Hugoniot equations are derived by applying the conservation of mass, momentum, and energy across the discontinuity; they describe the states of matter before and after the discontinuity of the shock wave (12, 13).

$$\rho_0 U_s = \rho(U_s - U_p) \quad (2)$$

$$P - P_0 = \rho_0 U_s u_p \quad (3)$$

$$E - E_0 = \frac{1}{2}(P + P_0)(V - V_0) \quad (4)$$

where  $\rho$  is the density,  $U_s$  is the shockwave velocity,  $U_p$  is the particle or piston velocity,  $P$  is the pressure,  $V$  is the specific volume, and  $E$  is the energy. Through combination with the equation of state, these equations may be expressed as functions of each other.

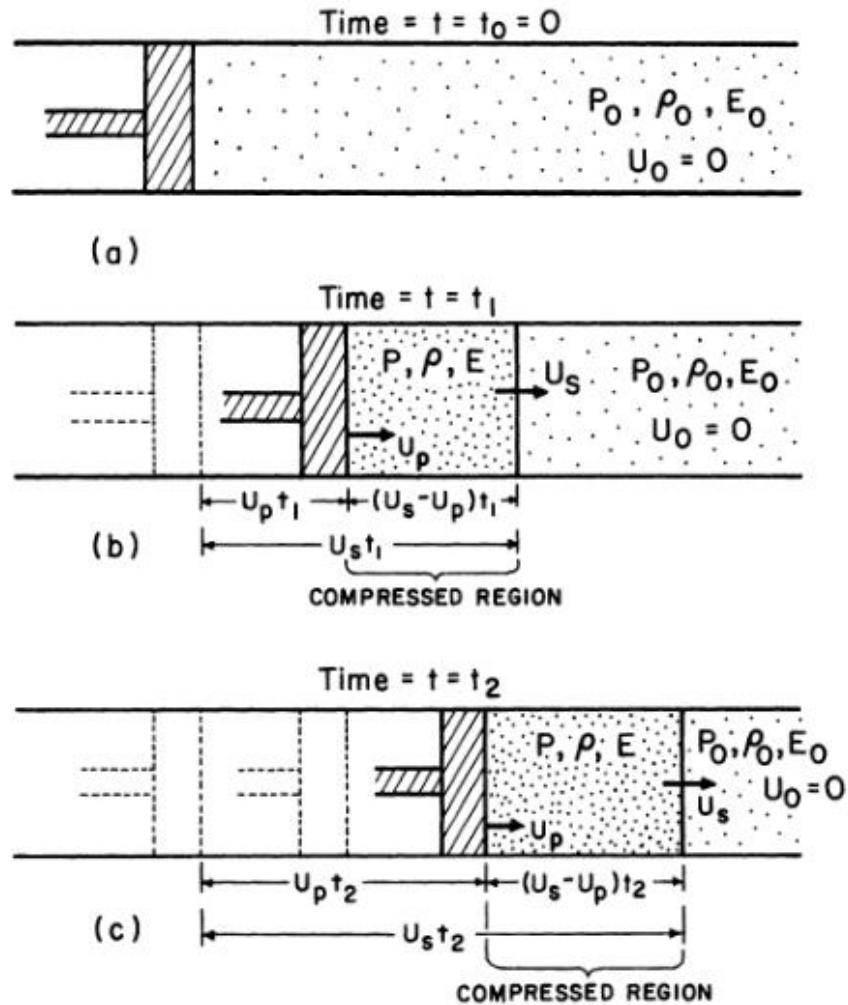


Figure 2-2 Illustration of how material piles up in front of a piston and a shock wave is created. The boundary between the compressed area in front of the piston and the uncompressed fluid is the shock wave discontinuity. Taken from (14).

The pressure-density relationship of the material before and after the shock front can be visualized as the “Hugoniot” curve seen in Figure 2-3. It is the locus of all shock states for a material. When a material is shocked, it follows the Rayleigh Line, going directly from the state  $P_0, V_0$  to state  $P_1, V_1$ . The slope of this line is proportional to the square of the velocity  $U_s$  of the shock wave. A steeper slope, meaning a larger change in pressure, results in a higher shock wave velocity, and vice versa.

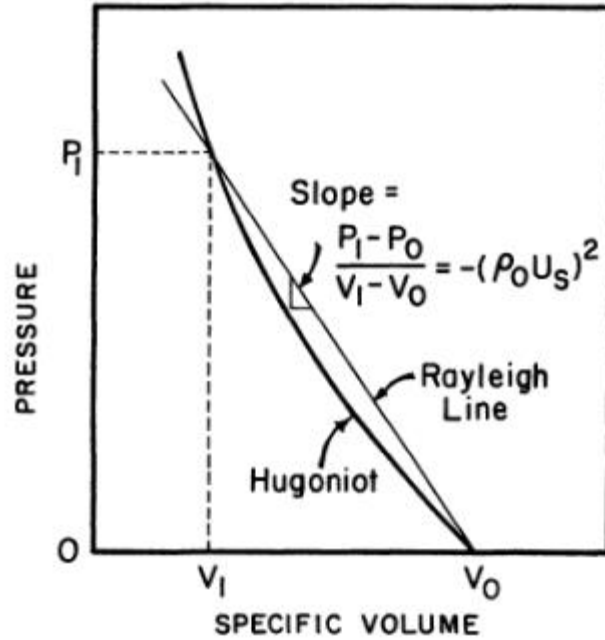


Figure 2-3 Characteristic Hugoniot (P-V) curve showing Rayleigh Line. Taken from (14)

Shock waves in experiments can generate extremely high strain rates of  $10^8 \text{ s}^{-1}$  to  $10^9 \text{ s}^{-1}$ . The large strain rates may suppress other more conventional deformation modes such as fracture. Under shock, high deviatoric stresses may exist which can lead to unexpected results, such as dislocations or phase changes that are not predicted from static compression at equilibrium conditions.

Shock in a material is also accompanied by extreme increases in the internal energy of the material. This can result in rapid temperature rises, sometimes beyond the melting points of the material. Even below the melting point, temperature changes may affect the deformation processes during plasticity or failure. This temperature rise is exceedingly difficult to measure experimentally and must usually be calculated. Temperatures are often calculated directly along the Hugoniot line, by integrating the two coupled differential equations (15)

$$\frac{dT}{T} = -\gamma \frac{dV}{V} + \frac{dS}{C_v} \quad (5)$$

$$2TdS = (V_0 - V)dP + (P - P_0)dV \quad (6)$$

where  $\gamma$  is the Gruneisen parameter and  $C_v$  is the specific heat at constant volume.

## 2.2 Laser Shock Compression

Laser ablation is the current method used to generate the highest strain rates and pressures that are experimentally possible. It is the primary method that the inertial confinement fusion effort at the National Ignition Facility has been using to achieve controlled nuclear fusion for energy purposes (10).

The core concept of producing a shock wave lies in the exchange of momentum. In flyer plate setups, the flyer plate impacts the target and two shock waves are created, one in the target and an opposite wave in the flyer plate. Momentum is exchanged for the duration of the contact between the flyer plate and the target, typically 0.1-1  $\mu$ s for gas guns.

Pulsed lasers for generating shock waves have become commonly used in high energy density physics experiments (16–18). In shock compression via direct bombardment laser ablation, laser energy is delivered directly to an ablator, generally made of low Z materials such as CH plastics, beryllium, or most recently diamond (19–22). The laser interacts with the electrons in the ablator, causing it to heat up to millions of degrees and hundreds of millions of atmospheres of pressure. The heated material rapidly expands and is propelled away at a high velocity, causing the remaining material to accelerate in the opposite direction. This method is the same as how rocket propulsion works:

$$\dot{x} = v \ln \frac{m_0}{m_1} \quad (7)$$

The shock velocity is then governed by the lost mass  $m$  and velocity of the plasma  $v$ .

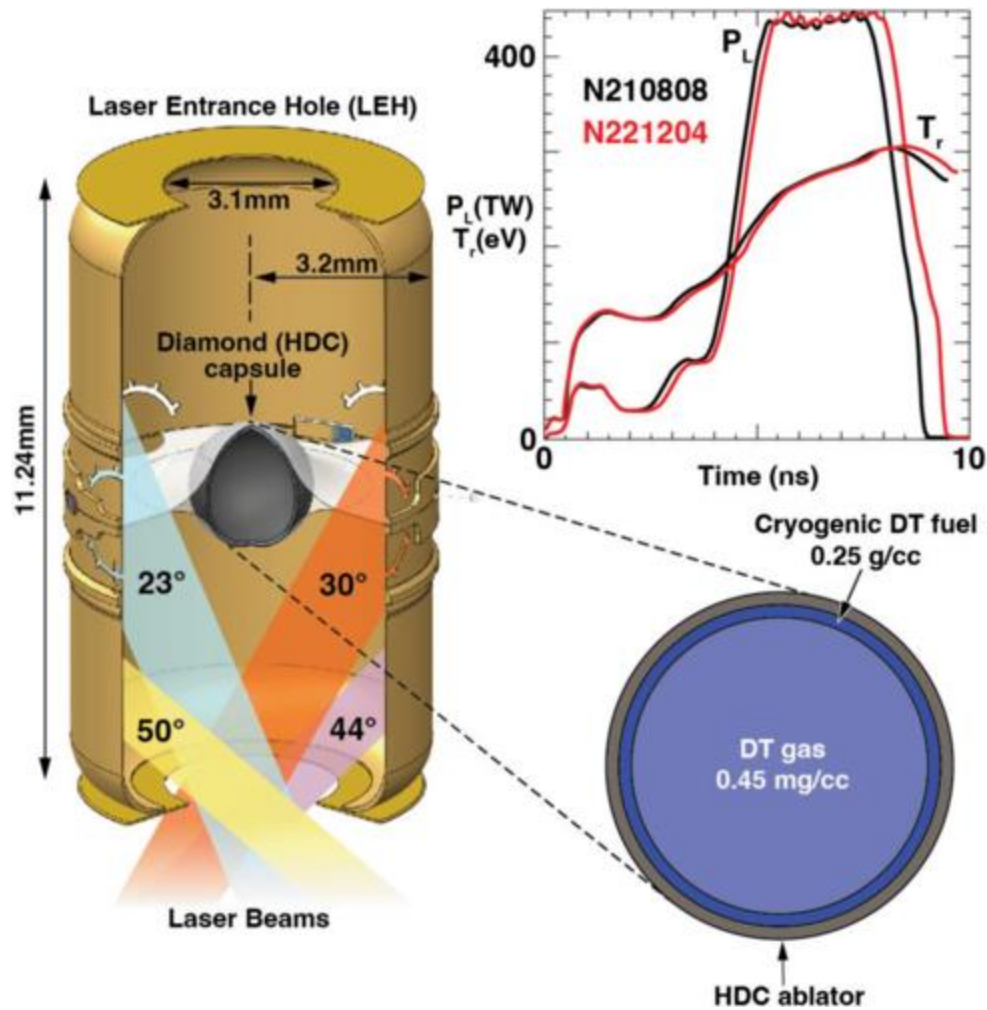


Figure 2-4 Left: schematic of the target and laser configuration including the hohlraum. Bottom right: the HDC capsule and DT fuel configuration. Top right: total laser power vs time and radiation temperature  $T_r$  as a function of time. Taken from (10).

Figure 2-4 shows the current setup used at the NIF that reached ignition, with a spherical high density carbon diamond shell surrounding the DT fuel. Instead of direct drive, lasers instead shine onto the inside of a gold capsule called a hohlraum, which produces x-rays. These x-rays then couple to the ablator surface and the rocket effect takes place.

The Lindl equation empirically relates the laser parameters and the shock pressure achieved (23):

$$P = C_A \left( \frac{I_{12}}{\lambda_{\mu m}} \right)^{\frac{2}{3}} \quad (8)$$

Where  $P$  is the shock pressure in GPa,  $I_{12}$  is the laser intensity in TW/cm<sup>2</sup>,  $\lambda$  is the wavelength in micrometers, and  $C_A$  is the adsorption coefficient, typically 40 for low Z ablation material. For diamond ablaters tested at the OMEGA laser facility at the University of Rochester Laboratory for Laser Energetics, it has been found that an exponent of 0.71 is more appropriate (24). The laser intensity in this equation can be calculated from the laser energy  $E$ , pulse duration  $t$ , and spot size  $A$  as:

$$I_{12} = \frac{E}{At} \quad (9)$$

For an example pulse on OMEGA, a 532 nm wavelength laser with 300 J energy and a 3 ns duration with a spot size of 1 mm<sup>2</sup> results in a peak pressure of around 100 GPa.

### 2.3 Laser Shock Sample Preparation and Recovery

In laser shock experiments, the targets involved are often subjected to such extreme conditions that they may undergo unrecoverable transformations, such as fragmentation by spall. If the sample is intended to undergo post-shock characterization, some soft recovery technique must be employed to prevent destruction of the sample (24, 25). One method is the use of low-density aerogels to slowly catch the sample, along with the encapsulation of the target in impedance matched material. Shock impedance is calculated as the product of the initial density of the material by its longitudinal wave velocity. For silicon, aluminum is a good match to its shock impedance. Matching the impedance allows for the shock wave energy to transfer over the material barrier more efficiently, preventing rebounding waves from reflecting back into the material and creating the tensile state that could initiate spalling. The samples can thus be

recovered after the shock, and sent for characterization such as transmission electron microscopy (TEM).

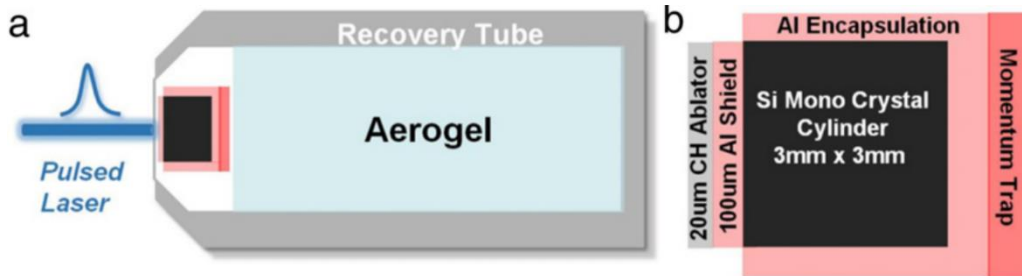


Figure 2-5 a) Sample Recovery setup for a laser shock experiment b) Example of a silicon sample encapsulated in impedance matched aluminum. The CH ablator provides the pressure shock pressure after being heated by the pulsed laser. Taken from (24).

## 2.4 Dislocations

The first theories for describing the necessary shear stress required for atomic planes to slip in a perfect crystal predicted a minimum stress of  $\frac{G}{2\pi}$ . This predicted value was far higher than experimentally recorded values for any material by multiple orders of magnitude. The description of the elastic fields created by defects was first developed by Volterra (26) in 1907. The theory of dislocations used this analytical framework and was first proposed in 1934 simultaneously by Orowan (27), Taylor (28, 29), and Polanyi (30). Dislocations explained the lower barrier to plasticity by positing that a half plane of atoms could advance by only breaking one line of bonds at a time, instead of breaking all of the bonds within the half plane at the same time. Burgers (31, 32), Cottrell (33), Nabarro (34), and Eshelby (35) followed up on this work, proposing other types of imperfections and interactions between defects which have helped to explain the mechanical properties of crystalline material. Many books exist on the topic of dislocations including the work of Hull and Bacon (36). Bulatov and Cai (37) focuses on the simulation of dislocations. Meyers (3) covers how shock can affect and be affected by dislocation slip, density, and mobility.



## 2.5 Voids

Voids play an important role in shock wave studies, either through their nucleation and growth during the ductile failure, or when they are pre-existing defects in material that undergo collapse during the compression of the sample. When shock waves reach the free surface of a material, they reflect and form a rarefaction wave which can result in large tensile stress in the material. This can lead to spalling, planar separation of the material parallel to the wave front; the growth and coalescence of voids is crucial to this behavior (38). While there were continuum level studies of void growth, they did not have specific explanations for the atomic level mechanisms that enabled voids to grow. Reisman (39) performed shock compression of irradiated steel filled with nanosized voids resulting in their collapse above 40 kbar and noted that only the emission of vacancy-type dislocation loops could result in both void shrinkage and overall volume reduction of the steel. Rudd and Belak's (40) atomistic simulations of copper with voids undergoing triaxial expansion also saw dislocations transporting platelets of material away from the void, allowing it to grow. Erhart et al. (41) performed molecular dynamics simulations of void collapse in nanoporous metals and also found that voids served as dislocation sources and enabled massive plastic deformation, as seen in Figure 2-5. Lubarda et al. (42) proposed a specific mass transport mechanism for void growth based on the emission of dislocations from the surface of the void. Through laser shock experiments and measurements of voids in the material, they determined that vacancy diffusion alone was insufficient for explaining the sizes of the voids in the material at the strain rates present. Instead, a non-homogeneous plastic deformation process was involved where the maximum shear stress at  $45^\circ$  to the void surface produces prismatic shear loops, which for a loop of radius  $R/2$  would carry away material and increase the void volume by  $\pi R^2 b/2$ .

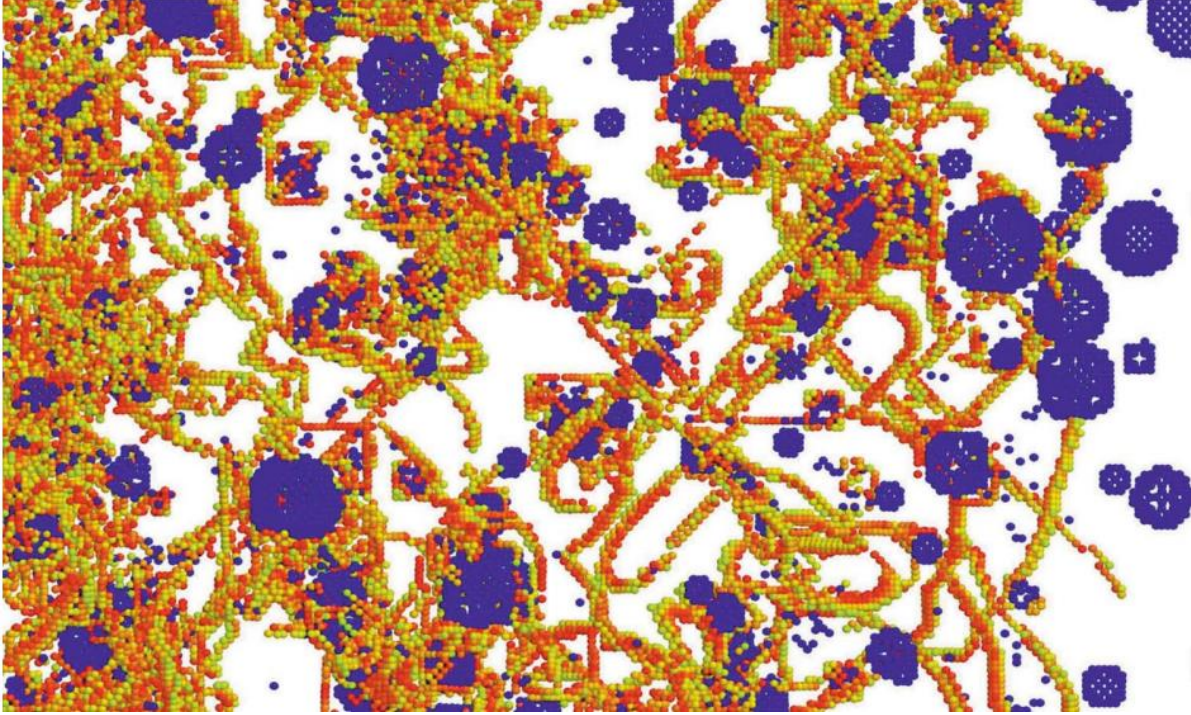


Figure 2-6 Shock moving through 3% porous copper, producing shear dislocation loops from voids. Taken from (41).

Lubarda et al. (42) also observed that the critical stress for dislocation emission decreased with increasing void size and with wider dislocation cores. Hatano (43) performed shock on an fcc Lennard-Jones solid and also found the emission of dislocations and a decrease in the Hugoniot elastic limit with increasing void size. Tang et al. (44, 45) proposed a new model for the nucleation and emission of dislocation loops from a void based on its size. The required shearing stress was based on two components: the creation of a new surface step during emission, and the stress required to generate and bow a dislocation loop to a radius  $R_1$  a certain fraction of the void's radius. The total shear stress required is given as:

$$\tau = \frac{2\gamma}{\pi\rho b} + \frac{Gb(2-\nu)}{4\pi(1-\nu)R_1} \ln \frac{8mR_1}{e^2\rho b} \quad (10)$$

where  $\gamma$  is the surface energy,  $\rho b$  is the size of the dislocation core,  $b$  is the Burgers' vector,  $\nu$  is the Poisson ratio, and  $m$  is a geometric factor for the shape of the dislocation (2.2 for a semi-

circular loop). After conversion to a global von Mises stress by solving the elastic field around the void, when plotted against their molecular dynamics simulations of shock in tantalum for critical stresses vs void size they saw good agreement, as seen in Figure 2-6.

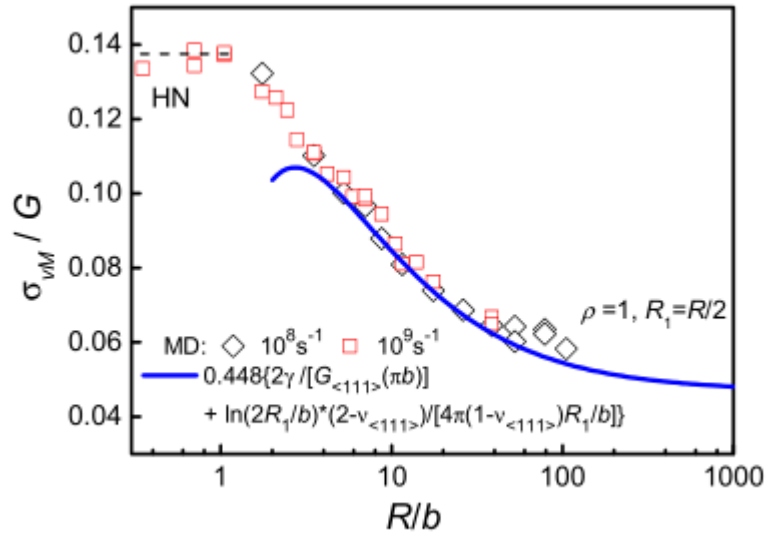


Figure 2-7 Normalized von Mises stress for dislocation nucleation from a void surface as a function of normalized void radius  $R/b$ . Taken from (44).

## 2.6 Molecular Dynamics Simulations

Molecular Dynamics is a simulation method to analyze the physical behavior of atomistic systems. At its core, individual atoms are modeled using Newton's equations of motion to see how the system evolves. The forces on each atom in the simulation are calculated to determine their trajectory, then all the atoms are advanced in time, the forces are recalculated, so on and so forth, in a loop illustrated in Figure 2-5. This method records the complete information for each atom at each time step, allowing for direct observation of atomic mechanisms through the position, velocity, and even energies of individual participating atoms. Every timestep in the simulation must capture thermal vibrations of the atoms, known as the Debye period (around  $10^{-13}$  seconds), so individual timesteps are typically set as 1 femtosecond. For simulations where atoms are moving fast enough that even 1 femtosecond may cause unintentional and unphysical overlapping of atoms, even shorter timesteps may be required. While there are even more ground level calculations that can be made (quantum mechanics), molecular dynamics simulations can provide a near ground-up recreation of macroscale characteristics like material strength, melting points, and other parameters, without making any assumption beyond the force or energy interactions between individual atoms. Laser shock experiments in particular are well-suited to be simulated via molecular dynamics, as the high strain rates and short timescales currently involved lie in the domain of modern molecular dynamics simulation capabilities.

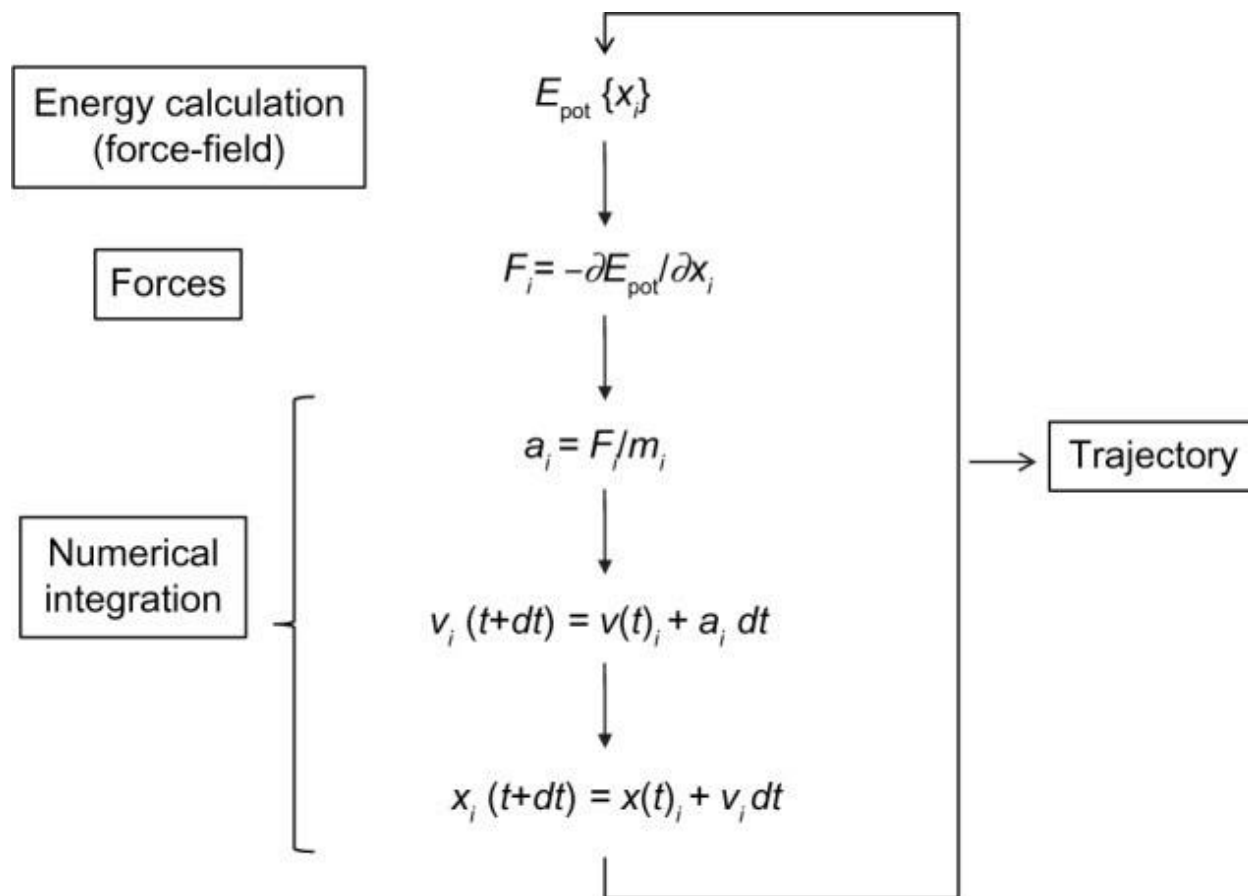


Figure 2-8 A single step in the molecular dynamics simulation loop for updating atomic positions. Taken from (46).

### 2.6.1 Computational Capabilities

The computational power available in computers has grown exponentially since their invention. At the forefront of computational power are the supercomputing clusters that are available at national laboratories around the world. Advances in both raw computational speed as well as the rise of parallel processing using GPU architectures has enabled simulations to reach unprecedented size and time scales. Molecular dynamics in particular is well-suited to the parallel processing method as each individual atom can be calculated concurrently with every other atom in the system. Current trends expect that computational power should be able to increase 1000-fold every 13-17 years (47). The top computing resources recently achieved the performance milestone of 1 Flop, or  $10^{18}$  floating point operations per second (48). If this were to be converted

to the possible size of a simulation utilizing the full resources available, then over a 24 hour period the maximum grain size  $D$  of a polycrystalline simulation can be (11):

$$D = \frac{2.494 \times 10^{-6} a_0}{x r_c} \sqrt[3]{\frac{AW \Delta t}{\rho_m t_s} (AP \times PSP \times PM^{-1}) \times \sqrt[3]{FLOPPS}} \quad (11)$$

Table 2-1 Parameters for calculation of grain size simulation capabilities

Parameter	Meaning	Example Value
$a_0$	Lattice Parameter	4.090 Angstroms
$AW$	Atomic Weight	107.8682 AU
$\rho_m$	Mass Density	10.501 g/mol
$x$	Grains	1
$r_c$	Cutoff Radius (Neighbors)	7.2 Angstroms
$\Delta t$	Timestep	1fs
$t_s$	Simulated Time	1ns
$AP$	Allocation Percentage	100%
$PSP$	Parallel Scaling Performance	0.8
$PM$	Potential Multiplier	2.3
$FLOPPS$	Floating Operations per Second	$10^{18}$

An example of possible parameter values is given in Table 2.1. With these values, it would be possible to compute a fully atomic simulation of a  $1\mu m$  sized single grained sample with femtosecond time resolution over a period of 1 nanosecond, all within 24 hours of maximum computation utilization. The ability to simulate real world experiment size samples has come to fruition, even if still on shorter time scales.

Previous work has already shown the capabilities of simulations with micrometer dimensions along at least one axis, and much smaller periodic boundaries in the others (49). Advances in possible computational methods and programs utilizing different methods of storing and calculating atomic data have led to the ability to perform calculations on up to twenty trillion atoms at a time (50). More advanced and computationally expensive machine learning potentials that can approach quantum accuracy without associated quantum computing costs have also reached the billion-atom simulation range (51).

## **2.7 Interatomic Potentials**

At the heart of classical molecular dynamics simulations lies the interatomic potential. These potentials describe the forces between an atom and its neighbors based on a range of factors such as distance, bond order, embedding energy, quantum mechanical calculations, and others. The accuracy of a potential determines its ability to reproduce the physically correct behavior of a material, and to predict real phenomena and material properties without having to be directly fitted to those situations. The parameters of a potential are often fit to data outside the regime of shock physics. As such, determining the transferability of those potentials into the higher pressure and temperature ranges can be a key component of producing accurate simulations of shock. There exist a large variety of different potentials with different formulations, parameters, and physical models. This can affect their accuracy when applied in different scenarios; for example, a ReaxFF potential is designed with chemical reactions and multi-component interactions in mind, but may not perform as well when subjected to hundreds of gigapascal pressure situations because the parameters are not parameterized in detail.

These potentials can be derived in many ways with a range of complexity, from the simplest Lennard-Jones pair descriptor to the recent advancements in machine learning. The classical potentials are semi-empirical, with the parameters being fitted to experimental results or to

quantum mechanical modeling results from *ab initio* studies such as Density Functional Theory (DFT) simulations. The properties that are being fit to include the cohesive energy, vacancy energy, elastic tensor values, surface energies, melting points, and many other measurable quantities. Due to their simplified empirical nature, they are less expensive than direct quantum mechanical calculations of atomic interactions and therefore can be applied to much larger systems for the same computational cost.

The basis of these empirical potentials is still deeply rooted in how electrons operate in solids and how those bonds between atoms operate (52). One of the simplest interatomic potentials that still finds use in calculating the behavior of some gases and fluids is based on the Lennard-Jones pair potential (53, 54)

$$\phi(r) = \frac{6m\epsilon}{m-6} \left( \frac{1}{m} \left( \frac{\sigma}{r} \right)^m - \frac{1}{6} \left( \frac{\sigma}{r} \right)^6 \right) \quad (12)$$

where  $\sigma$  is the separation distance and  $\epsilon$  is the well-depth. A classic plot of this potential can be seen in Figure 2-6, for  $m=12$ . With the distances between atoms calculated during the simulation, the potential energies between them can be extracted and used to update forces and positions, advancing the simulation in time. Other simple two-body potentials have also been proposed and see use in molecular dynamics simulations as well such as the Morse potential (55) and Buckingham potential (56). These two-body potentials are also often used as the bases for describing two-body interactions in more complex potentials.



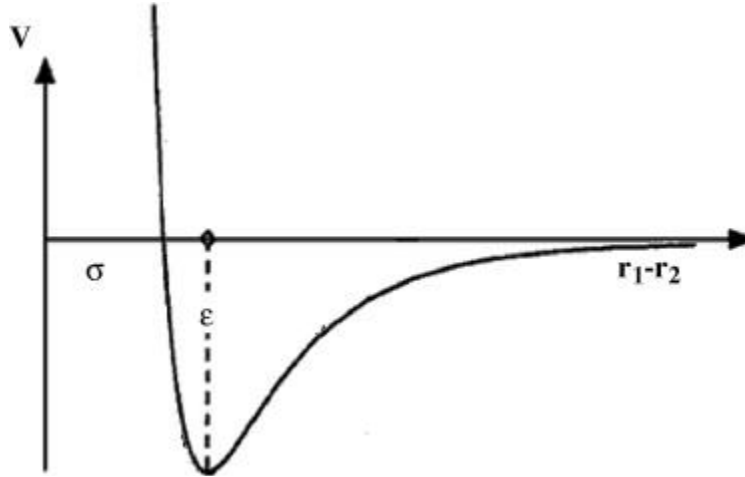


Figure 2-9 A potential profile for the Lennard-Jones pair potential. From (57).

More complex potentials were not devised until after the rise of computers and molecular dynamics simulations became possible. One early potential that was a significant advancement in describing metal properties was the Embedded Atom Model (EAM) created by Daw and Baskes (58). This potential included delocalized interactions along with nearest neighbor contributions and had the form

$$E_{tot} = \sum_i F_i(\rho_i(R_i)) + \frac{1}{2} \sum_{i,j} \varphi(R_{ij}) \quad (13)$$

where  $\rho_i$  is the electron density for each site  $R_i$ , through an embedding function  $F$ . This embedding function represents the energy required to place an atom into the electron cloud. The second term is the short-range pair potential for each pair of atoms  $R_{ij}$  with the  $\frac{1}{2}$  added to avoid double counting. Because the electron cloud density is a summation over all atoms, limited by some cutoff radius for mathematical purposes, this potential acts as a many-body potential. All of the many-body interactions are contained within the first embedding function term.

The Tersoff (59–62) potential was another early potential whose formulation enabled it to describe 2-body and 3-body interactions through bond angles and environmental functions. It was

initially developed for describing the covalently bonded crystal structure of Si and was extended to SiC and C as well. It is considered a bond order potential that incorporates structural chemistry into its formula.

$$E_{ij} = \sum_i E_i = \frac{1}{2} \sum_{i,j \neq i} V_{ij} \quad (14)$$

$$V_{ij} = f_c(r_{ij}) [A \exp(-\lambda_1 r_{ij}) - B_{ij} \exp(\lambda_2 r_{ij})] \quad (15)$$

$$B_{ij} = B_0 \exp\left(-\frac{z_{ij}}{b}\right) \quad (16)$$

$$z_{ij} = \sum_{k \neq i,j} [w(r_{ik})/w(r_{ij})]^n \times [c + \exp(-d \cos \theta_{ijk})]^{-1} \quad (18)$$

$$w(r) = f_c(r) \exp(-\lambda_2 r) \quad (19)$$

The A term describes repulsive forces, as seen in other two body potentials. The B term describes bonding forces, including bond order and local environment. Any considerations for bond angles, competing bonds, and bond strengths are folded into this variable. This equation is further expanded upon by Tersoff's parameterization seen in the trial potential  $B_{ij}$ .  $z_{ij}$  measures number of bonds competing,  $b$  measures how bond strength falls with increasing coordination,  $w$  is the ratio of bond strengths,  $n$  determines how much closer bonds are favored, and is arbitrarily chosen.  $\theta_{ijk}$  is the angle between bonds  $ij$  and  $ik$ , and  $f_c$  is the cutoff function, which limits the range at which atoms will interact with each other, substantially reducing the computational load. For certain choices of the parameters in the Tersoff and EAM potentials, it can be seen that the equations describe the same things (63). The main difference between the two is how the bond angles are incorporated into the equations.

These potentials and other candidates for use in the simulation of silicon and carbon will be discussed in the overview of potentials for each element in chapters 3 and 4.

## 2.8 Other Computational Simulation Types

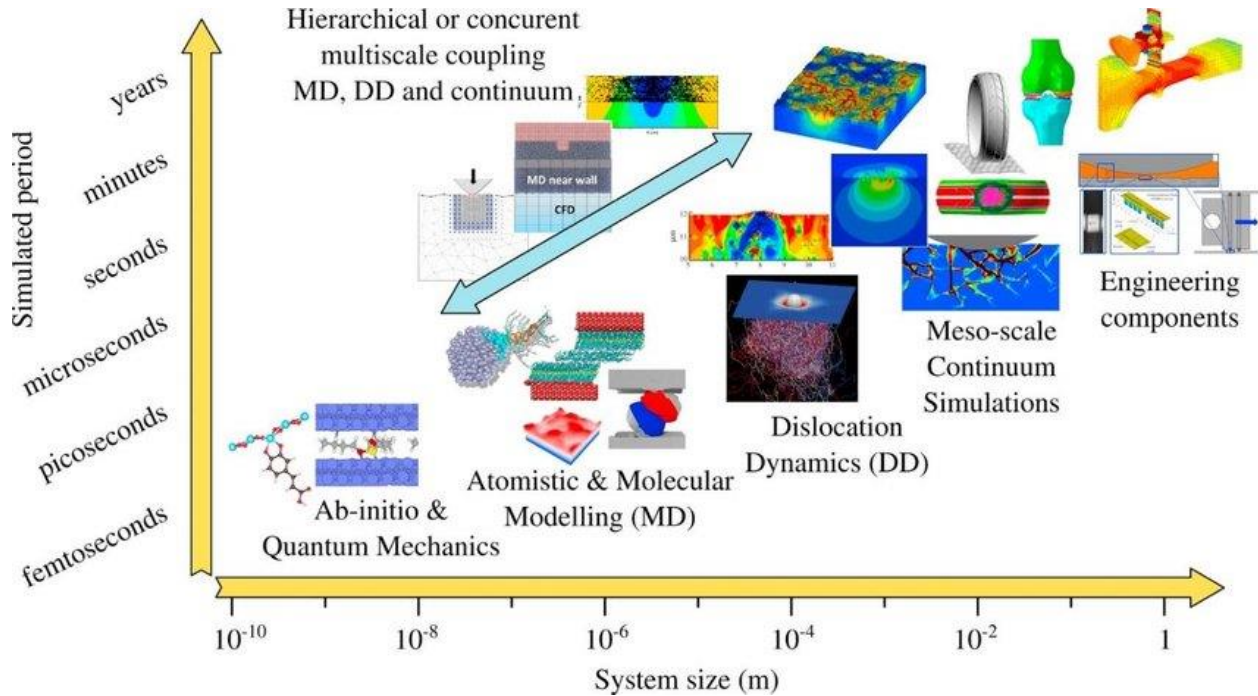


Figure 2-10 System size and simulation periods of various computer simulation types. Taken from (64).

There are plenty of other computer simulation methods besides classical molecular dynamics modeling, which span across multiple timescales and length-scales, as seen in Figure 2-7. Each of these simulation types can have their own domain in which they can be considered the best choice for efficiently producing the desired results. While using ab-initio or molecular dynamics simulations to calculate entire engineering component evolution over years would provide the most accurate data, it would also be prohibitively expensive or time consuming to perform those simulations. Conversely, a higher level modeling cannot be applied to inform behavior on a lower level, such as trying to use Finite Element Analysis to try to determine how dislocations occur, because the higher level models do not contain that information within them.

### 2.8.1 Ab Initio and Quantum Mechanics

One of the other simulations that is particularly relevant to molecular dynamics is the most accurate method currently available for calculating the behaviors of atoms. At the quantum

mechanical level, the interactions between electrons and electronic states control nearly everything about the interactions between atoms. Therefore, by understanding exactly how those electronic states will behave, the deepest understanding of material properties can arise.

The origin of quantum mechanical calculations began with the Schrödinger equation in 1926 (65):

$$\hat{H}|\Psi\rangle = E|\Psi\rangle \quad (19)$$

$$\hat{H} = \sum_i^N \left( -\frac{\hbar^2}{2m_i} \nabla^2_i \right) + \frac{1}{2} \sum_{i=1}^N \sum_{j \neq i}^N \frac{Z_i Z_j}{4\pi\epsilon_0 |\mathbf{r}_i - \mathbf{r}_j|} \quad (20)$$

This is an eigenvalue equation where the Hamiltonian  $\hat{H}$  of the N-body wave function  $\Psi$  is equal to the energy eigenvalues  $E$  of wave function.  $\mathbf{r}$  denotes the spatial positions and  $Z$  indicates the charges of the particles. For an electron in a hydrogen atom, the Schrödinger equation is

$$E\psi = -\frac{\hbar^2}{2\mu} \nabla^2 \psi - \frac{q^2}{4\pi\epsilon_0 r} \psi. \quad (21)$$

When the number of particles,  $N$ , starts to increase, an exact solution usually cannot be found (66). The general time-independent Schrödinger equation has  $3N$  degrees of freedom, where  $N$  is the number of electrons, and this quickly makes systems larger than just a few atoms unsolvable. This is where approximations need to be made so that larger systems can be calculated. Several types of approximation can be used to simplify the equations such as the Born-Oppenheimer approximation (67), the Hartree-Fock method (68), configuration interaction (69), coupled-cluster (70), and more. However, in the realm of computational simulations, the Kohn-Sham Density Functional Theory method has found the most success. This theory reduces the complexity of the system from a  $3N$ -Body problem to  $N$ -number of single body problems. The simplification follows from two theorems (71, 72):

- Theorem 1 - The external potential is a unique functional of the electron density only. Thus the Hamiltonian, and hence all ground state properties, are determined solely by the electron density.
- Theorem 2 - The groundstate energy may be obtained variationally: the density that minimizes the total energy is the exact groundstate density.

The first theorem allows for one representation of electron density to work for all atoms in the system. From the second theorem, the groundstate electron density corresponds to the full solution of the Schrödinger equation, and from it all properties may be calculated. Figure 2-8 illustrates the simplification of the many electron interactions into one electron density cloud.

Using these theorems, the Kohn-Sham equation represents a single electron Schrödinger equation for a fictitious system.

$$-\frac{1}{2}\nabla^2\phi_i(\vec{r}) + \left[ V_{ext}(\vec{r}) + \int d\vec{r}' \frac{n(\vec{r}')}{|\vec{r} - \vec{r}'|} + \epsilon_{xc}[n] + n(\vec{r}) \frac{\delta\epsilon_{xc}[n]}{\delta n(\vec{r})} \right] \phi_i(\vec{r}) = \epsilon_i\phi_i(\vec{r}) \quad (22)$$

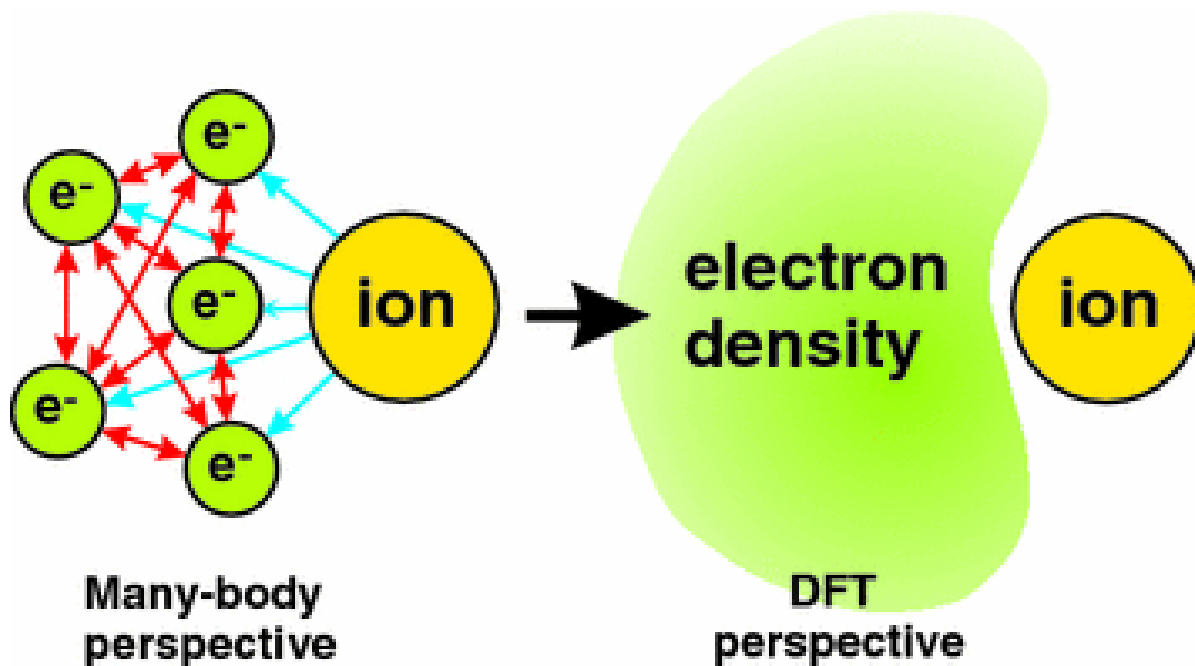


Figure 2-11 The assumption made to simplify the solution of electronic structure calculation for Density Functional Theory. Taken from (73).

The first potential  $V_{ext}$  describes the interaction between an electron and the collection of atomic nuclei in the system. The second part of the equation is  $V_H$ , the Hartree potential, describes Coulomb repulsion between the electron being considered and the total electron density defined by all the electrons in the system. The final term containing  $\epsilon_{xc}$  is the exchange correlation potential, which is simply the rest of the effects not considered, and its true form is unknown. Models such as local density approximation and generalized gradient approximation go towards approximating this  $\epsilon_{xc}$  term.

Thus, the Kohn-Sham Equation can become a set of equations to describe each electron in the system. The system can then be iteratively solved to find the true ground state electron density, which allows for finding the properties of the system (74).

Density functional theory is valuable because it is a practical method of performing *ab initio* accuracy calculations on numbers of atoms that can now reach into the hundreds and thousands, allowing larger structures and crystals to be composed. The values of material properties from these calculations can be used to fit the properties of higher level empirical interatomic potentials, or even used to create training datasets for the latest machine learning potentials.

### **2.8.2 Machine Learning Potentials**

Ab initio quantum mechanical calculations still provide the highest level of accuracy for calculating the properties and evolution of systems. However, their usage is still limited to small systems or shorter timescales. Even with current computational power they can simulate only up to thousands of atoms and picoseconds on the time scale. Practical approximations based on those quantum data can be used to speed up calculation and expand the range of possible calculations. Some early models attempted to fit DFT data to high dimensional six degrees of freedom models of hydrogen adsorption (75, 76). While these early interpolation methods worked, they were

inflexible in their application outside of the defined systems and their complexity grew rapidly with increasing degrees of freedom. A new type of computer-based interpolation method has come about recently called machine learning. One type of machine learning method is the neural network. The neural network is a highly flexible nonlinear model that can theoretically approximate any continuous function to arbitrary accuracy. It is composed of nodes arranged in layers, interconnected via a set of links. Each node in a layer is connected to all the nodes in the layers before and after it, but not to the nodes within its layer. Each link is multiplied by a weight before it is supplied to a new node. These weights are the parameters adjusted to fit the neural network to a set of inputs and outputs.

The neural network error is minimized via the cost function, whose square root is the root mean square error, and this process is called learning. In each epoch, or set of inputs and outputs during the training process, the cost function is minimized by adjusting the weights of the links. The way in which this minimization is performed is an evolving field with many different algorithms and methods to choose from. The process of machine learning has advanced beyond simple neural networks with many more complex algorithms and additions to the types and interconnectivity of the layers involved.

A machine learning potential created and improved to describe amorphous carbon utilized a Gaussian Approximation Potential (GAP) to interpolate interatomic potential energy surfaces using a Gaussian process regression (77). Two and three body terms were added into the machine learning process, improving the accuracy and extending the range at which the potential performed. The potential was then used to recreate many amorphous carbon structures and compared with DFT and empirical potential values.

Another machine learning potential based on the spectral neighbor analysis potential developed by Thompson et al. (78) has been fitted to quantum molecular dynamics data for extreme pressures of up to 5 TPa and tens of thousands of degrees Kelvin (Fig 2-9) (79). The ability to perform quantum molecular calculations at such a wide range of pressures and temperatures and then fit much faster performing machine learning potentials to them will improve the speed and accuracy of future simulations that reach extreme regimes of pressure and temperature such as shock loading. However, these machine learning potentials tend not to be generally transferable and can only predict within the ranges they were trained on, and only on the data they were given. For example, if there was no data on dislocations or vacancies present in the training set for the potential, it is unlikely that it will be able to reproduce those physical characteristics naturally.

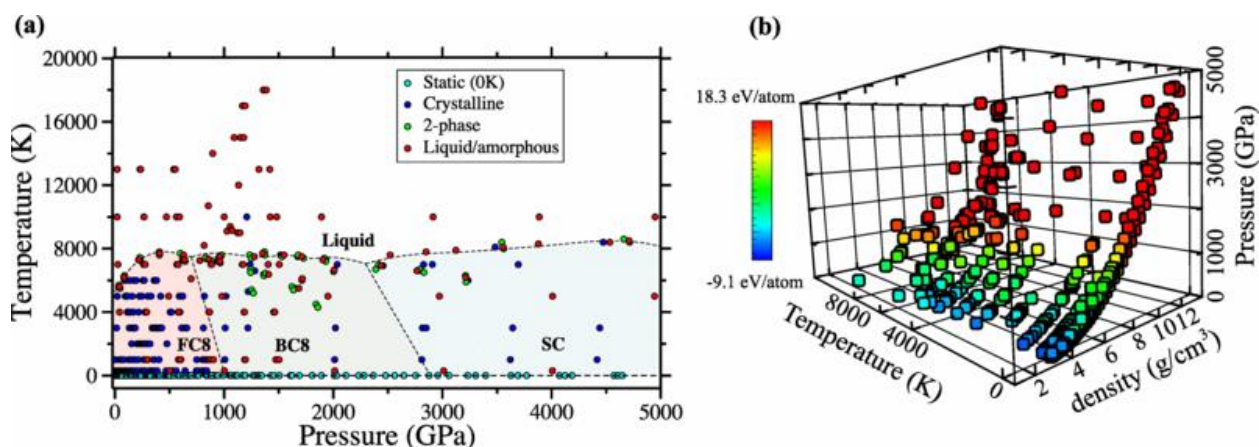


Figure 2-12 Training database for the carbon SNAP machine learning potential. (a) Pressure-temperature map of QMD and static DFT simulations included in the database, each represented by a  $P$ - $T$  point on carbon phase diagram sampling diamond (FC8), body-centered cubic (BC8), and simple cubic (SC) solid and liquid phases (total number of structures - 636). (b) Pressure-temperature-density-energy/atom distribution. Taken from (79).

## 2.9 Simulation Codes

There are a variety of molecular dynamics codes that have been developed with various types of simulations in mind. Each code is unique in its implementation of the basic simulation



process and with different computational efficiencies as well, depending on the system being simulated. Some codes may specialize in handling large amounts of atoms at a time, others may be focused on protein folding or other biomolecular mechanics, and others prioritizing accurate chemical reactions. The generally open-source nature and accessibility of these simulation codes such as Amber (80) and GROMACS (81) has helped MD simulations grow as a widely applied tool, with many users also contributing their own advancements to the capabilities of the programs. The primary code utilized for the work in this dissertation is the Large-scale Atomic/Molecular Parallel Simulator (LAMMPS) code, originally developed by Steve Plimpton at Sandia National Laboratories (82, 83). One of LAMMPS strengths is the algorithms used to enable parallelization of the calculations within the atomistic simulations. Each processor running the simulation can be assigned a fixed amount of atoms, a fixed subset of the interatomic forces, or a fixed spatial region (82). The ability to perform spatial decomposition and to shrink-wrap the boundary conditions to only the atoms present makes for efficient parallel computation and no extra power dedicated to calculating unintended free volumes. This works well for the simulation of shock because the box can expand to match the atoms as they are compressed and moved by the expanding shock wave.

## **2.10 Simulation Process**

Molecular dynamics simulations procedures are performed in the following order of stages:

- 1) Construction and initialization of the simulation domain and relevant parameters such as atom types, crystal structure, interatomic potential, etc. ;
- 2) Ensembles are defined, fixes are implemented, and equilibration is performed;
- 3) The simulation is run following the sequential integration of newton's laws according to the set potential and data is output.

The following sections describe each of these steps in more detail.

### 2.10.1 Initialization

Simulations allow a researcher to decide many properties about the system that they are trying to model. Sometimes called a simulated fabrication, the initialization step involves setting the boundary conditions, simulation size, crystalline structure, and the interatomic potential describing the atomic interactions. Periodic boundaries allow the material to repeat infinitely in specified directions, allowing for pseudo-bulk material modeling instead of being limited to the nanometer dimensions that computational limits may restrict. Fixed boundaries can act as spectral reflectors instead, or the boundaries may be shrink-wrapped so they can adjust themselves to the motion of the atoms which may grow beyond the barrier when expanding or retract from it when compressed. The choice of crystal structure is important for the material as well and allows the atoms to propagate a standard unit cell through the defined simulation space. If desired, the orientation of the crystal can also be changed for testing different loading directions.

It is possible to create more complicated geometries by using the commands within LAMMPS, or third-party software like atomsk (84) can also be used for manipulating atomic systems in even more complex ways, such as creating complex polycrystalline samples, inserting point, line, or planar defects, and other possible transformations. An example of a polycrystalline silicon sample can be seen in Figure 2-13.

The overall domain size and simulated time is limited by the available computational power and time. Typical simulations can contain anywhere from  $10^4$  to  $10^9$  atoms, simulating anywhere between just a few picoseconds to multiple nanosecond events. It is important to take into account what is achievable when setting up the simulation, and what the simulation can then tell us about the underlying physics.

The interatomic potential describing the energies and forces between the atoms present in the simulation is also set at this stage.

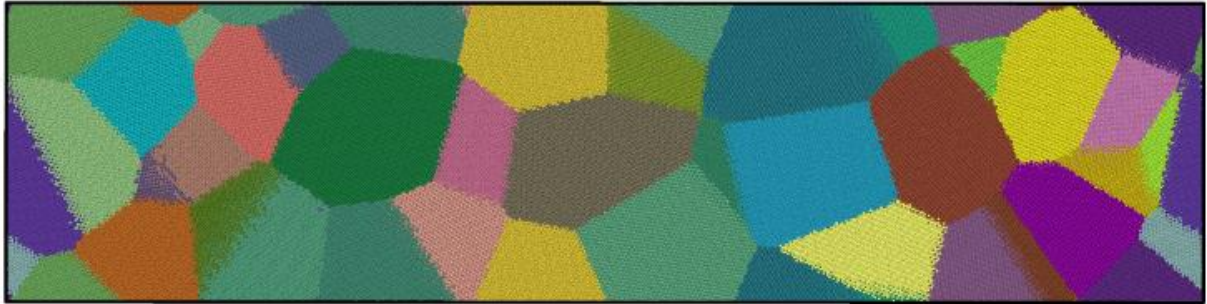


Figure 2-13 Silicon Polycrystal with diamond-cubic grains created with atomsk. Grains are colored by orientation, with periodic boundary conditions.

### 2.10.2 Equilibration and Ensembles

To ensure that the created material is physically representative of reality, equilibration is performed to minimize the entire system's potential energy. This includes any present defects that may already be present in the simulation, such as intentionally included dislocations, voids, inhomogeneous material interfaces, or in polycrystalline materials the presence of grain boundaries which can adjust during annealing. The lattice parameter of a material is also temperature dependent. In the equilibration process, all atoms are given an initial thermalization temperature and then allowed to settle into the stable low energy state. If equilibration or minimization are not performed properly, residual stresses could remain and affect the simulation results.

Additional boundary conditions are considered in the form of the thermodynamic ensemble choice. The microcanonical ensemble (NVE) is commonly used for shock simulations, also known as non-equilibrium molecular dynamics. NVE stands for a constant Number of atoms, a constant Volume, and a constant Energy. Within the ensemble there may be additional conditions that relax or restrict these parameters, such as adjusting the Volume of the simulation in accordance with an applied uniaxial load. The shrink-wrap variable allows for the volume in an NVE ensemble to change as well.

### 2.10.3 Run Integration

Integration involves the sequential application of Newton's equations according to the defined boundary conditions. These conditions can be adjusted during the simulation as the user desires in the input script. Some conditions which may be included are homogeneous tension or compression, nanoindentation, set strain rates in tension or compression, shearing, and shock loading. The system is usually integrated over a discrete time step,  $\delta t$ , by the method of finite differences. A velocity Verlet algorithm is used in LAMMPS and is written as a change of momentum:

$$\mathbf{p}\left(t + \frac{1}{2}\delta t\right) = \mathbf{p}\left(t - \frac{1}{2}\delta t\right) + \mathbf{F}(t)\delta t \quad (23)$$

$$\mathbf{r}(t + \delta t) = \mathbf{r}(t) + \frac{1}{m}\mathbf{p}\left(t + \frac{1}{2}\delta t\right)\delta t \quad (24)$$

Momentum is  $p$  and position is  $r$ , written as functions of half steps forward and backward. In practice, implementation may look like this:

$$\mathbf{p}\left(t + \frac{1}{2}\delta t\right) = \mathbf{p}(t) + \frac{1}{2}\mathbf{F}(t)\delta t \quad (25)$$

$$\mathbf{r}(t + \delta t) = \mathbf{r}(t) + \frac{1}{m}\mathbf{p}\left(t + \frac{1}{2}\delta t\right)\delta t \quad (26)$$

$$\mathbf{p}(t + \delta t) = \mathbf{p}\left(t + \frac{1}{2}\delta t\right) + \frac{1}{2}\mathbf{F}(t + \delta t)\delta t. \quad (27)$$

The updated momentum is first calculated at a half step by using the interatomic potential to find the current forces between atoms. This updated half-step momentum is used to calculate the positions that the particles will be in at the next timestep. These new positions are used with the interatomic potential to recalculate the forces between atoms. These new updated forces are then used to update the half-step momentum to the next full timestep. From these equations, the

velocity-Verlet algorithm can provide the position and momentum/velocity of each atom for each time step in the simulation (85, 86).

### 2.10.4 Producing Shock in Simulations

There are several methods to produce shock loading conditions in molecular dynamics simulations, including simulations of collision between a target and a flyer plate (87), moving a momentum mirror reflective boundary at a set speed through the sample, or using a rigid piston to compress the sample, along with several variations in this piston method including the shrinking periodic boundary condition (88), shock front absorbing boundary condition (89), and moving window method (90, 91). The piston method and the momentum mirror method are illustrated in Figure 2-11.

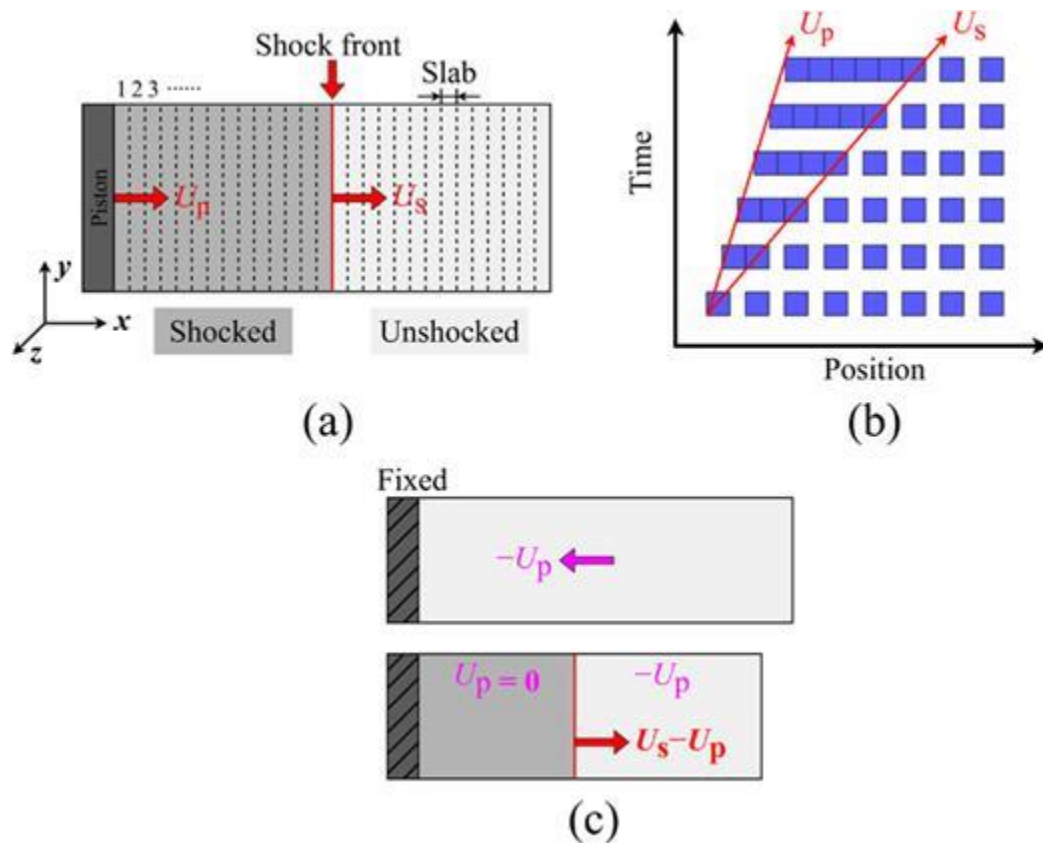


Figure 2-14 Two methods of simulating shock in non-equilibrium molecular dynamics simulations. a) Piston moving at a speed  $U_p$  produces shock of speed  $U_s$ . b) Compression of the

material as a function of time. c) Moving a sample at speed  $-U_p$  into a momentum mirror produces a reflecting shock wave. Taken from (92).

The piston method is used for the simulations in this dissertation. It is suited for modeling general loading conditions such as those from high explosive or laser drives. The piston's velocity can be changed to reproduce stress profiles similar to those experienced in laser shock experiments (93–95). The imposed piston velocity directly translates to the particle velocity  $U_p$  and describes the shock volume and strain rate. In the silicon simulations, piston velocity was varied from 0.9 to 1.5 km/s. For the carbon diamond simulations, piston velocities between 1.9 and 3.5 km/s were tested, depending on orientation and void size. Further discussions of methodology can be found in the relevant sections for silicon and diamond, with full input scripts found in the appendix.

## **2.11 Data Processing**

Pre-processing means using preparatory simulations or other manipulations to do things like sample construction, such as via `atomsk`. Peri-processing includes processing that is done concurrently with the simulation. This includes things like specifying different compute, or thermodynamic readouts from the LAMMPS log file. Post-processing takes place after the simulation has completed, using the files that the simulation has output to perform additional analysis. In LAMMPS a log file is output during the run, and includes global parameters such as total energies, box lengths and volume, temperatures, pressures, or any other user defined computes of global values. Another output command is the “`dump`” command which dictates per-atom data output, and can include values such as the atomic positions and velocities in x, y, and z, or user defined compute quantities such as the virial stresses, mean square displacement, coordination, potential and kinetic energies, or many more possible measurements.

Classical molecular dynamics is concerned with crystalline materials at the atomic scale, and is often used as a method to investigate defects at this scale. Therefore, proper identification or material phenomena is important for understanding their physical behavior. The post-processing of the atomic dump files can be a time consuming process longer than the simulation time itself, involving searching for defects within the simulation and utilizing various visualization methods to better illustrate and help with interpreting the characteristics that are present.

The primary visualization tool used in this dissertation was the Open Visualization Tool OVITO (96). Figure 2-12 illustrates a potential process for aiding in turning simulation data into visually intelligible pictures.

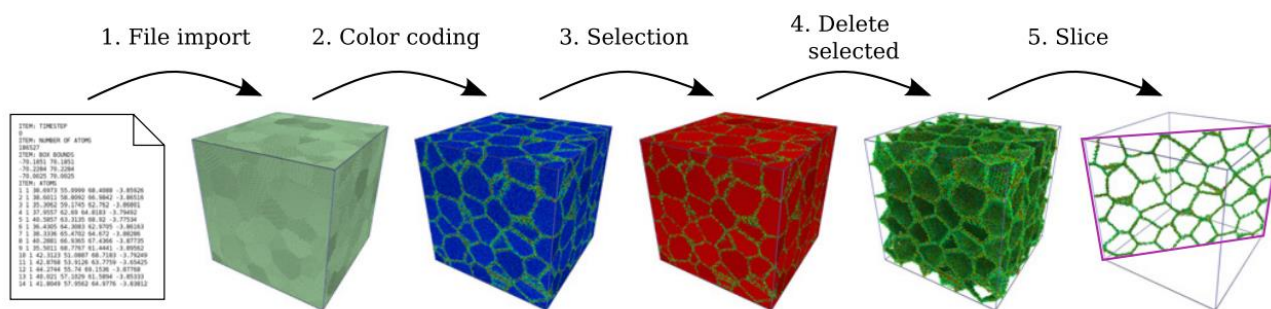


Figure 2-15 Post-processing pipeline in OVITO. Taken from (96).

LAMMPS includes many built-in computes that allow output of calculated measurements to the log or dump files. OVITO also has built in modifications which can help with visualization, as well as allowing custom criteria and calculations. The following sections cover some of the defect identification methods that have been used in these studies, as well as discussions of strain, strain-rate, and stress.

### 2.11.1 Strain-Rate

In a shocked sample, strain rate can be calculated along the direction of shock loading using the first derivative of the density:

$$\dot{\varepsilon} = -\frac{1}{\rho} \frac{\delta \rho}{\delta t} \Big|_z \quad (28)$$

At a single timestep, the strain rate can be evaluated using the derivatives of the velocity  $u$  and density  $\rho$

$$\dot{\varepsilon} = \left( \frac{\delta u}{\delta z} + \frac{u}{p} \frac{\delta p}{\delta z} \right) \Big|_t. \quad (29)$$

### 2.11.2 Stress State

The stress state is measured by the simulation, and is heavily dependent on the interatomic potential as it describes the forces between the atoms. In continuum mechanics, the stress is the first volumetric derivative of potential energy, but in a discretized atomic system this definition does not work. Virial stresses are instead calculated based on atom's interactions with their neighbors, their own velocities, and their atomic volume. The virial stress is defined as (97):

$$\sigma_{\alpha\beta} = -\frac{1}{\Omega_a} \left[ m v_\alpha v_\beta + \frac{1}{2} \sum_{n=1}^N r_{1\alpha} F_{1\beta} + r_{2\alpha} F_{2\beta} \right] \quad (30)$$

Where  $\Omega_a$  is the atomic volume,  $m$  is the mass,  $v$  is the velocity,  $\alpha$  and  $\beta$  mark cartesian components,  $N$  is the number of paired neighbors looped over  $n$ ,  $F$  are the forces on the atoms, and  $r$  are the atomic positions.

For the simulations in this dissertation, shock is directed along the z-axis and given as  $\sigma_{zz}$ . The hydrostatic pressure can be taken from the log files or calculated as

$$P = \frac{\sigma_{xx} + \sigma_{yy} + \sigma_{zz}}{3}. \quad (31)$$

For the diamond cubic materials in this study, the lateral stresses  $\sigma_{xx}$  and  $\sigma_{yy}$  are roughly equivalent, and can be used to calculate the deviatoric stress (87)

$$\tau = \frac{1}{2} \left( \sigma_{zz} - \frac{1}{2} (\sigma_{xx} + \sigma_{yy}) \right). \quad (32)$$



### 2.11.3 Temperature

Temperature is output in the log file in LAMMPS, but due to the additional energy imparted by the piston in the shock simulation, the extra kinetic energy from the translational movement of the atoms along the shock direction may result in inaccurate temperatures from the standard 3-dimensional temperature calculation of:

$$T = \frac{1}{N} \sum_{n=1}^N \frac{m}{3k_b N_A} |\vec{u}_n|^2 \quad (33)$$

Where  $N$  is the number of atoms,  $k_b$  is Boltzmann's constant,  $N_A$  is Avogadro's number,  $m$  is the atomic mass, and  $u_n$  is the velocity vector for each atom. When shocked along the z-axis, it may be best to employ a 2-dimensional temperature measurement ignoring the velocity in the z-direction:

$$T = \frac{1}{N} \sum_{n=1}^N \frac{m}{2k_b N_A} (u_{n,x}^2 + u_{n,y}^2) \quad (34)$$

### 2.11.4 Common Neighbor Analysis, Polyhedral Template Matching, Identify Diamond

Structure analysis algorithms can be used to characterize atomic arrangements. The common neighbor analysis (CNA) computation, available either directly in LAMMPS or through OVITO, is a useful measure of local crystal structure around an atom (98, 99). It uses a fixed cutoff radius to determine whether two atoms are bonded, then each neighbor is taken into account when calculating the orientations of bonds to determine crystal structure. CNA is however unsuited to identifying less symmetric structures like diamond cubic.

The Adaptive Common Neighbor Analysis (a-CNA) works off CNA as its basis but is better suited to identifying multi-phase systems as it can automatically identify optimal cutoff values for each particle (100). It has been extended to the silicon system, where knowledge of

second common neighbors is necessary as the atoms in the diamond cubic system do not necessarily share common neighbors.

The polyhedral template matching function in OVITO promises greater reliability than the CNA, especially in the presence of thermal fluctuations or high strain (101). It can provide a direct calculation of local crystal orientation, elastic deformation, and strain. It identifies local crystalline order by matching the local atomic neighborhood to templates of structural types in the PTM algorithm, using a mix of nearest neighbors and second nearest neighbors.

The identify diamond modification in OVITO can also be used for identifying diamond structure (102). It avoids the problems of CNA by first identifying the nearest neighbors, then identifying the nearest neighbors of those nearest neighbors to obtain the list of second nearest neighbors. The CNA fingerprint is then run on this extended list. If it forms an FCC structure, the central atom is classified as cubic diamond, and if it forms an HCP structure, it is classified as hexagonal diamond.

### **2.11.5 Coordination and Radial Distribution Function**

The coordination calculation is available both as a compute within LAMMPS or through OVITO. It measures the number of neighbors within a spherical shell around a given atom. The pair correlation or radial distribution function (RDF) is calculated based on the probability that an atom will be lying within one of these spherical shells at a given distance away from any atom in the simulation, normalized by the number of atoms and the simulation volume. Strong peaks in the RDF can be correlated to the structure factor through a Fourier transform, and can provide similar results to diffraction patterns for finding characteristic lattice spacing. Coordination number can assist in identifying free surfaces or voids, as there is less coordination where these surface bonds are dangling and can also help in identifying phase changes to disordered regions where liquid or amorphous structures may be. Disordered structures tend to have broader spreads

of the RDF. A comparison of how crystal order can affect the RDF is seen in Figure 2-13. The cumulative radial distribution function can also be measured, summing up each of the bins in the original radial distribution function. This can provide additional information such as atomic density within a certain cutoff radius.

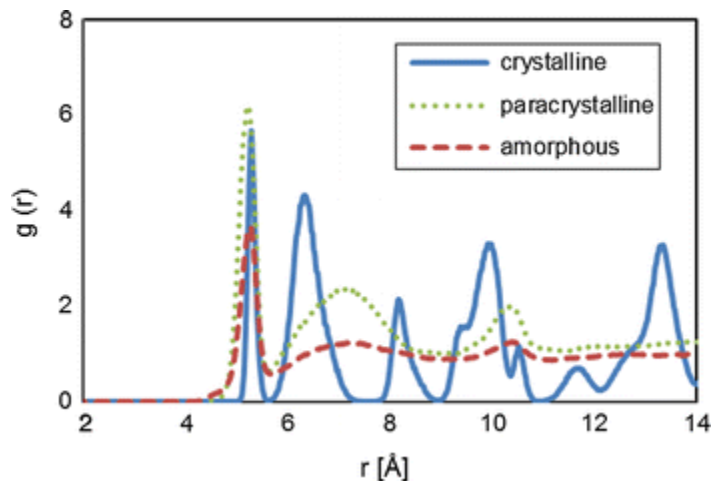


Figure 2-16 Differences between RDF for crystalline, paracrystalline, and amorphous cellulose. Taken from (103).

### 2.11.6 Angular Distribution Function

The angular distribution function (ADF) is available as built in compute for LAMMPS. It calculated one or more ADFs between groups of particles. Each ADF is calculated between a central atom and its bond angle to two neighbor atoms within a specified spherical shell range. A histogram is built up to show the relative prevalence of angles present within the structure. The angular distribution function is commonly used for characterizing electronic orbitals, and may be extended to characterizing molecular bonding.

### 2.11.7 Dislocation Extraction Algorithm

The Dislocation Extraction Algorithm (DXA) in OVITO was developed and refined by Stukowski (104, 105). It is capable of identifying line defects within an atomistic crystal, determine their Burgers vectors, and create a line representation of those dislocations in a dislocation

network. It can recognize partial dislocations and secondary grain boundary dislocations, such as twinning in FCC. It can also create a defect mesh, separating areas where the good crystal region can map atoms to a perfect reference state and the bad region where they cannot. This can help in identifying surfaces, voids, or other unidentified defects. The fundamental concept behind DXA is the Burgers circuit construction (35). It utilizes Delaunay tessellation of the dislocated crystal and compares each atom to atom edge to a perfect reference crystal. Combined with CNA, it can identify which atoms do not fit on the perfect lattice and separate them into good and bad regions. The interface mesh between these regions contains all dislocations in the crystal, and by constructing trial Burgers circuits over it, the Burgers vectors of the dislocations can be identified. The DXA process requires a large amount of memory and computing power to perform. Figure 2-14 shows a completed DXA analysis with dislocations and defect mesh shown.

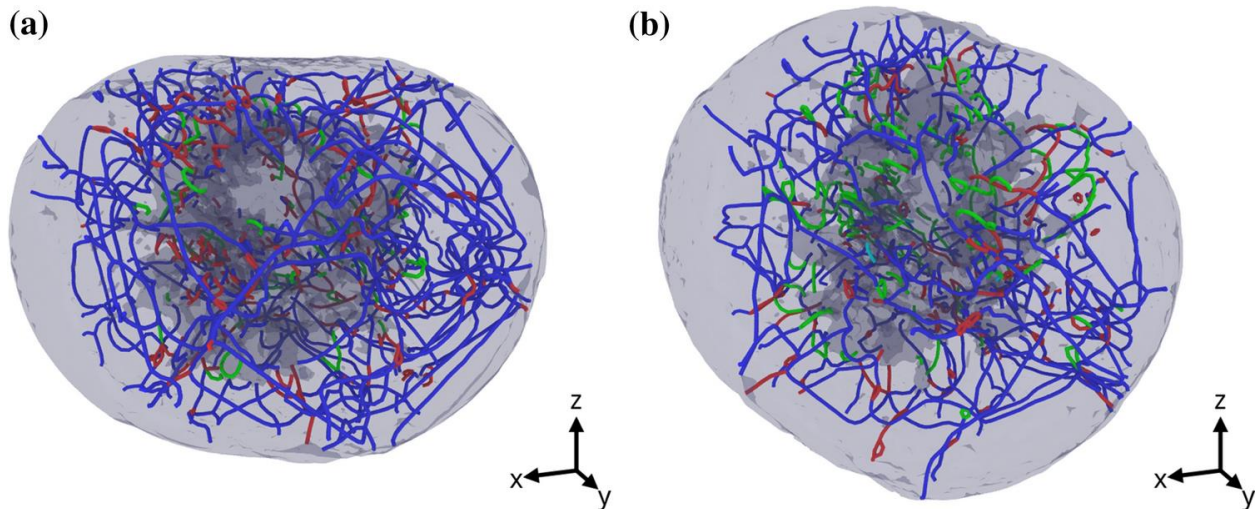


Figure 2-17 DXA analysis of a diamond nanoparticle a) after loading to 0.42 strain and b) After relaxation and annealing at 2000K over 1ns. Taken from (106).

## Chapter 3 Silicon Under Extremes

### 3.1 Introduction

Silicon is one of the most studied elemental materials, primarily because of its ubiquity in semiconductors; a large variety of semi-empirical potentials and parameterizations exist for specific environments and desired properties. Both supporting and contrasting simulations have fueled debate for shock responses ranging from phase changes, fracture, amorphization, twinning, full dislocation activity, and combinations thereof (24, 107–114). However, none of the interatomic potentials developed and explored in the literature were fit with elevated pressure or substantial shear stresses in mind. Individual atomic potentials succeed in reproducing thermal properties and melting temperatures (115–117), dislocation properties (118, 119), phase transformations (60–62, 120, 121), defects and disordered phases (122–124), and brittle behavior (121, 125, 126), but no single potential currently has the capability or transferability to reproduce all properties of interest over a wide variety of environments - a challenge ubiquitous in computational materials science (127). A comparison of a few potentials can be found in previous reports (115, 128). It should be emphasized that none of these potentials have been developed specifically for high stress conditions. Special consideration must be given to accurately simulate the uniaxial strain state achieved during shock loading of silicon.

Plasticity and atomic structural transformations induced by high pressure shock compression in monocrystalline silicon have remained a prevalent research focus for a considerable period of time (24, 94, 129–138). A significant number of shock studies have been performed in silicon, including impact driven (136–140) and laser shock experiments (94, 129, 132–134, 141, 142) as well as molecular dynamics shock simulations (107, 108, 111, 112, 143–145). The intriguing quasi-brittle quasi-ductile response of silicon under shock conditions continues to be challenging to model. Capturing the brittle fracture observed at impact and rear

surfaces (131, 133, 146) as well as the more ductile response of the confined material within remains an outstanding goal. Furthermore, as Smith et al. (133) discuss, as temperature or strain rate are increased, structures with different coordination systems, dislocations, amorphization, and melting may be observed.

Here we discuss several prominent molecular dynamics (MD) studies and their results. Oleynik et al. (111) carried out large-scale shock simulations and showed that shocks could heal defects in bulk single crystal silicon. In another study Oleynik et al. (147) showed that the Stillinger-Weber (SW) potential provides stress-strain curves for the diamond-cubic structure that compares well with ab-initio results when the strain is below 15-20%, translating to shear stresses below 7.5 GPa. Another investigation using an environmentally dependent interatomic potential (EDIP) (112) reproduced two-wave shocks consisting of a plastic wave preceded by an elastic precursor. Work by Mogni et al. (114) used a Tersoff potential (parameterized by Erhart and Albe (EA) (148)) to shock compress Si along the  $\langle 001 \rangle$  axis and identified an Imma phase transition, noting consistency with shear stress relief provided by direct shock-induced phase transition without intermediate plastic deformation. A modified form of the Tersoff bond-order potential (MOD) developed by Kumagai et al. (116), reproduces the experimental melting point in addition to the ambient elastic moduli and has been shown to reasonably well describe both crystalline and disordered phases such as liquid and solid amorphous structures, the kinetics of the crystalline to liquid transition (149), the decrease of melting temperature with pressure between -1 and 3 GPa (150), and has been successfully applied to the shock regime to predict amorphization under shock compression (24).

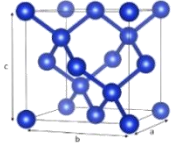
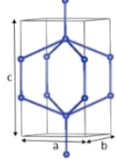
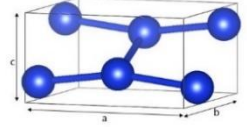
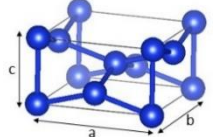
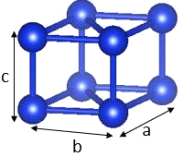
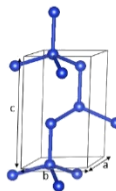
Of foremost importance is the far-from-equilibrium pressure-temperature phase space generated by shock compression of silicon. The need to characterize this space is emphasized by

the variety of phase changes (Table 3-1) and interatomic potentials to draw from. The Stillinger-Weber potential was recently surveyed and a simple cubic allotrope, sc16, was shown to co-exist with the  $\beta$ -Sn structure between pressures of 9.54 and 13.67 GPa (151). Si-III, or bc8, was shown to be energetically unfavorable compared to sc16 for all temperatures and pressures. Romano et al. showed that the negative Clausius-Clapeyron melting temperature with increasing pressure was again demonstrated and a triple point was defined between dc, liquid, and sc16 at 1302 K and 7.28 GPa. In fact, the point represents a quadruple point including the hexagonal diamond (hd) structure of thermodynamically equivalence to dc (151).

Four prominent experimental works identify additional phases. *In-situ* quasi-static investigations indicate that amorphization results from an intermediate hd phase (152) and that dislocations play a critical role (153). State of the art shock experiments by Turneaure et al. (129) completed at the Dynamic Compression Sector (located at the Advanced Photon Source) were able to identify a transition of dc silicon to a simple hexagonal (sh) structure at 19 GPa. Shock recovery efforts have identified bulk amorphization and directional amorphization in concert with dislocation activity, but no phase changes were reported in the recovered samples (24, 94, 131).

Thus, the plethora of available phase changes, deformation modes, and their interplay strongly compel a comparative study of the predominant silicon potentials under shock conditions in order to evaluate our current capability to model silicon in extreme environments.

Table 3-1 Predominant ambient and high pressure ( $P < 25$  GPa) polymorphs of silicon. Data from multiple sources (142, 154–156).

Structure	Space Group	Unit Cell
Diamond cubic (dc) (Si-I)	Fd-3m	$a=b=c=5.43053$ 
Body-centered tetragonal five (bct5)	I4/mmm	$a=b=3.369$ $c=5.470$ 
Imma	Imma	$a=4.373$ $b=4.502$ $c=2.550$ 
$\beta$ -Sn (Si-II)	I41/amd	$a=b=4.686$ $c=2.585$ 
Simple hexagonal (sh) (Si-IV)	P6/mmm	$a=b=2.527$ $c=2.373$ 
Hexagonal diamond (hd)	P63mmc	$a=b=5.392$ $c=5.392$ 



### 3.2 Computational Methods

The purpose of this study is to understand and illustrate how different interatomic potentials are used to simulate the deformation of silicon under shock loading. All simulations are performed using the open-source LAMMPS package (82, 83) with a few different schematics in order to understand the suitability for each potential prior to shock loading. Six interatomic potentials are used to simulate the response of silicon to shock-wave propagation: two Tersoff parameterizations (148), a modified Tersoff form (116), Stillinger-Weber (118), an environmentally dependent interatomic potential (122), and a modified embedded atom method (MEAM) potential (157). Of the Tersoff potentials we employ, both are parameterizations from Erhart and Albe (148) referred to as EA (originally developed for Si-C, Si-Si, and C-C interactions) and EA2 (developed solely for Si-Si interactions). The modified Tersoff form, developed by Kumagai et al. (116), relaxes the original restrictions of the angular dependent term and adds several additional fitting terms. Table 3-2 provides a reference for the interatomic potential forms, parameterizations, and their common abbreviations.

Table 3-2 Table of common semi-empirical silicon potentials, parameterizations, and their abbreviations.

Interatomic Potential [ref]	Parameterization [ref]	Abbreviation
Stillinger-Weber (118)	Stillinger and Weber (118)	SW
Tersoff (60)	Erhart and Albe (148)	EA, EA2
Modified Tersoff (116)	Kumagai et al. (116)	MOD
Modified Embedded Atom Model (157)	Baskes (157)	MEAM
Environmentally Dependent Interatomic Potential (122)	Bazant et al. (122)	EDIP
Reactive Force Field (158)	van Duin et al. (159)	ReaxFF

A preliminary calculation of the elastic moduli (note that the term elastic constant does not appreciate that the elastic response will change as a function of applied pressure, temperature, etc.) for dc Si as a function of pressure was conducted in order to evaluate which potentials may be suited to faithfully reproduce shock wave propagation. Even as the material transitions from an elastic to plastic response, elastic strains remain present and their pressure dependence is paramount to describing the balance between hydrostatic and deviatoric stress components. To calculate the elastic moduli, a cubic cell of Si having  $3 \times 3 \times 3$  units lattice (where the lattice constant is 0.5431 nm) is created with periodic boundaries. Affine displacements are applied to the volume and the resultant pressure is calculated (in this way no relaxation of the material is allowed). Subsequently, small affine deformations are applied along specific directions and the change in forces are registered and translated to their corresponding elastic constituent. While the elastic moduli do not fully describe the behavior of the unit cell under these high stress conditions, they portray a unique ability of MD simulations to isolate properties from one another compare an important component of each potentials. In particular the MEAM potential is significantly “stiffer” than the other potentials, which results in it exhibiting elastic behavior throughout the ranges probed in the present study.

Another crucial factor in the effectiveness of silicon potentials subjected to extreme conditions is the accuracy of the melt temperature (as a function of pressure), of direct relevance to solid-state amorphization or melting, both of which depend on the disruption of the atomic lattice in favor of disorder. We employ a two phase method (150) to calculate the melt conditions with increasing pressure. A single crystal dc Si sample is generated, measuring  $10 \times 10 \times 50$  units lattice with periodic boundaries divided into three sections; the first and last are fixed to remain solid while the inner third is melted. The probed temperature and pressure states are selected and

iterated through via a combination of the velocity verlet algorithm, Nose-Hoover thermostat-barostat (NPT), NVE integration, and energy minimization.

Prior to large-scale shock loading, several locus states on the shock Hugoniot were mapped using the Multi-scale shock technique (MSST) (160). The MSST restrains the system to the macroscopic conservation laws of a shock front by altering the cell volume and temperature to remain along the shock Hugoniot and Rayleigh line. A dc Si cell measuring 10x10x18 units lattice with periodic boundaries is defined and equilibrated via minimization followed by the application of the MSST with variable shock velocities. Here the standard shock formalism is followed with the z-direction as the shock direction, which is aligned with the [001] crystallographic direction. While the MSST allows for a calculation of the Hugoniot curve, the method does not describe the role that the shock front may impart, instead providing an evolving snapshot of the material located a distance behind the shock front and also neglects the full range of multi-wave effects, i.e. for a split-wave elastic-plastic shock the MSST will show only either the elastic or plastic volume, but not both simultaneously.

To observe time-resolved deformation under shock loading, large-scale molecular dynamics (MD) simulations of [001] single crystal dc silicon with dimensions of 25 nm x 25 nm x 300 nm containing  $\sim 10^7$  atoms were used, equilibrated at 300K and zero pressure (using NPT). These shock simulations impose periodic boundary conditions transverse to the shock direction, corresponding to laser-shock experiments that produce uniaxial strain during loading (95). In order to study the heterogeneous nucleation of defects from the target surface, a frozen piston consisting of a few layers of silicon is initially separated from the bulk target and subsequently impacted and evolved using a microcanonical ensemble (NVE). If the piston is perfectly bonded to the specimen it is possible that nucleation of defects is suppressed due to the elimination of natural surface

defects. The piston moves with a specified velocity,  $v$ , as a function of time, imparting a compression wave with a particle velocity,  $U_p$  (where  $v = U_p$ ) (161). In order to mimic modern laser-driven setups, the imposed piston velocity (and thus shock pressure) follows a pseudo-Gaussian form, taken as  $\sim e^{-t^3}$ ; this form arises from the physics of laser ablation using temporal Gaussian laser pulses ablating a polymer (132). The full width half max of the pulse is 16.5 picoseconds (ps) with the maximum occurring at 12 ps, half maxima at 5.5 and 22 ps, and a velocity tail that goes to zero at 50 ps. The material will quickly “shock up”, but it is important to note that the leading edge provides a quasi-ramp loading, providing a limited time for the lattice to adjust to the ultimate stress state. This process has been shown to be important in the production of realistic defect structures (161).

### 3.3 Elastic moduli, Melt temperature vs. pressure, and Hugoniot calculations

The behavior of material under shock loading is complex, requiring thorough analysis of potentials prior to large-scale simulations of Si under shock loading to ensure the accuracy of these simulations. Although shock studies tend to focus on plastic deformation, elastic deformation remains present and accurately capturing the elastic behavior allows for confidence in the structural changes observed during shock. The results of our calculated elastic moduli are shown in Figure 1 and are compared with ab-initio calculations by Karki et al. (162) as well as a reactive force field (reaxF (159), designed to evaluate brittle cracks in silicon.) As seen in Fig. 3-1a,  $C_{11}$  increases with pressure for all potentials except for SW and ReaxFF. MOD provides the best fit to the ab-initio results, followed by EA2. Notably, both SW and EA significantly underestimate  $C_{44}$  (Fig. 3-1c). The effect of pressure on the shear modulus follows the same trend (Fig. 3-1d).

Figure 3-1 also contains the results of the melting temperature as a function of pressure analysis in Fig. 3-1e and are compared to data drawn from Mazhukin et al. (163), limited experimental data, a linear Clausius-Clapeyron equation, and an analytical calculation by Deb et

al. (164). MOD, SW, EDIP, and MEAM most closely match the curves presented by the Clausius-Clapeyron assumption and the curve by Deb et al. More negative  $dT/dP$  slopes results in lower melting temperatures at higher pressures, which may influence the tendency of a potential to favor disordered states at elevated temperature and pressure conditions. The EA and EA2 potentials substantially overestimate the melting temperature at both ambient conditions and under pressure compared to experimental and theoretical results, indicating that melting and amorphization will be suppressed relative to the other potentials.

The culmination of the preliminary analysis is the calculation of Hugoniot states using MSST (160) and NEMD simulations. Note that while the large-scale atomistic shock simulations provide the most informative details about deformation under shock loading, they are significantly more computationally expensive, while each Hugoniot state requires one full simulation but at much reduced computational cost to probe the macroscopic shocked state and evaluate the Hugoniot curve. The locus of Hugoniot states calculated via this method provides important insight as to how we can expect different potentials to behave. The relationship between the shock and particle velocities is fundamental to the nature of the shock wave (and is influenced heavily by the elastic moduli). Figure 3-2a presents the plot of the shock velocity,  $U_s$ , versus the particle velocity,  $U_p$ , for EA, EA2, EDIP, MEAM, MOD, and SW potentials in comparison to available experimental data. Each of the potentials form nearly linear trends which is characteristic of the relation between the particle and shock velocities. While at low particle velocities this relationship breaks down due to the split-wave structure, none of the potentials accurately capture this response fully and are instead clustered above near the longitudinal sound velocity of the material at zero pressure. Because silicon is expected to have a multi-wave structure consisting of elastic and

plastic components, the accuracy of the longitudinal sound velocity (along [001]) is quite relevant to how the elastic wave evolves and the separation of the elastic and wave fronts.

Figure 3-2b shows the relationship between shock stress,  $\sigma_{zz}$ , and normalized specific volume. Figure 3-2c shows data in the elastic and early plastic regimes. The potentials closely match the elastic experimental curve at low compression but lie above the experimental data describing the elastic plastic transition. However this is not expected based on the strain rates applied and idealized defect-free initial conditions. Isolating potentials that show tolerable agreement, MOD and EA2 most closely match the elastic shock response as expected from the  $C_{ij}$  response, due to the well-known relationship between stiffness, density, and wave speeds.

Although the pressures probed subsequently are far below the strong shock regime, when assessing a potential's ability to capture shock phenomena, it is important to bound the area of study. We note again that none of these potentials were designed to be applied to shock conditions and great care must be taken when assessing transferability. Furthermore, MD time scales and strain rates are expected to suppress many transitions (plasticity, phase transitions, etc.) and only at higher pressures may the relevant phenomena be observed, which often nudges researchers to simulate beyond appropriate limits. The higher stresses required for equivalent volume compression in the strong shock regime as compared to experiments suggests that the liquid "stiffness" is much greater than in reality. This is of particular relevance because silicon is notorious for a liquid phase of both high- and low-density variants (similar to the amorphous phases) and possibly indicates that these potentials predict the stiffer variant to dominate.

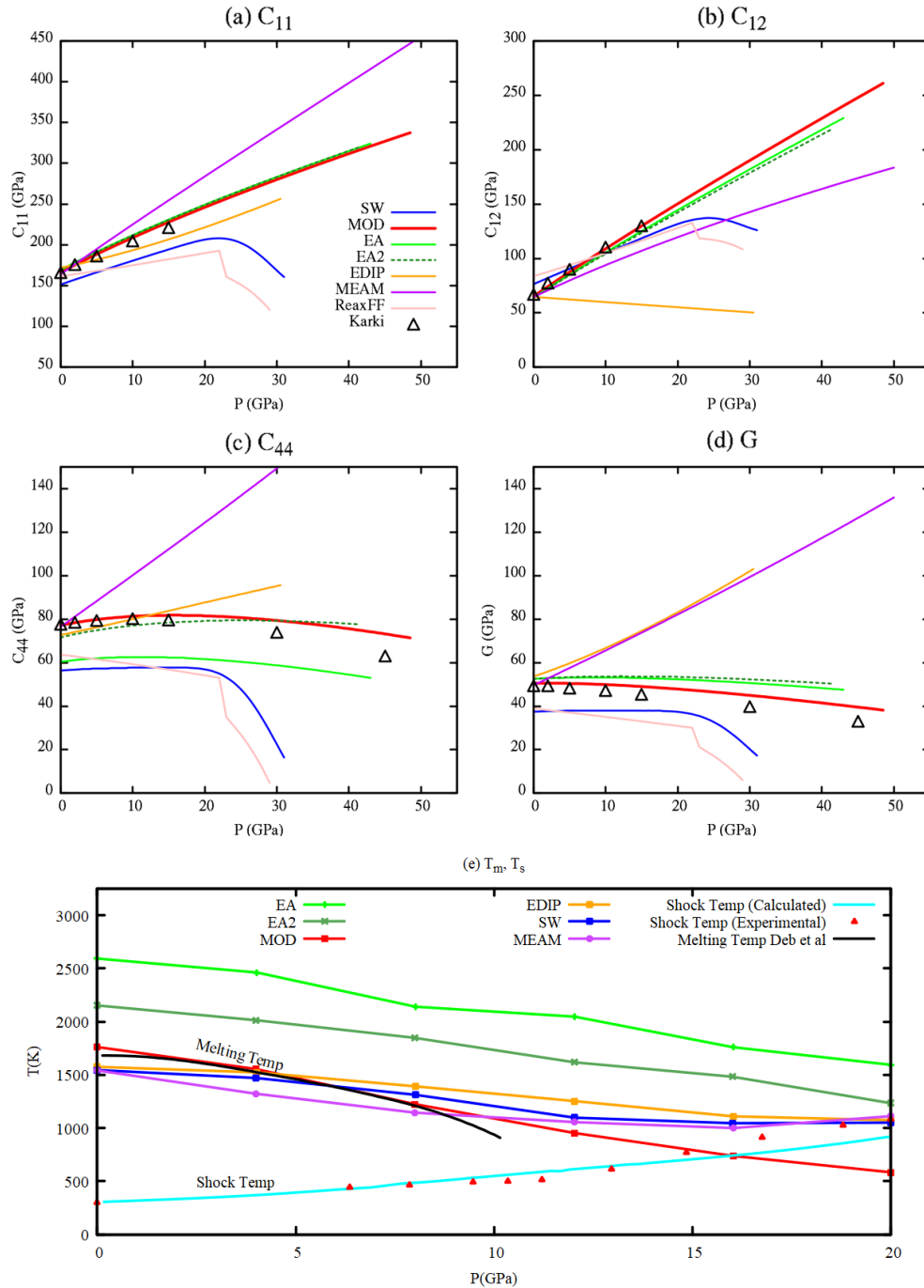


Figure 3-1 - Elastic moduli (a)  $C_{11}$ , (b)  $C_{12}$ , (c)  $C_{44}$  and (d)  $G$  (shear modulus) calculated as a function of increasing hydrostatic pressure; compared against density functional theory results of Karki et al. (162) (e) Pressure dependent melting temperature plotted alongside shock-induced temperature rise. The experimentally derived melting temperature calculated by Deb et. al. (164) according to the Clausius-Clapeyron equation for dc Si is shown in black. Note that if the transition between dc and  $\beta$ -Sn is suppressed that this curve would extrapolate and intersect the melting curve between 12-13 GPa.

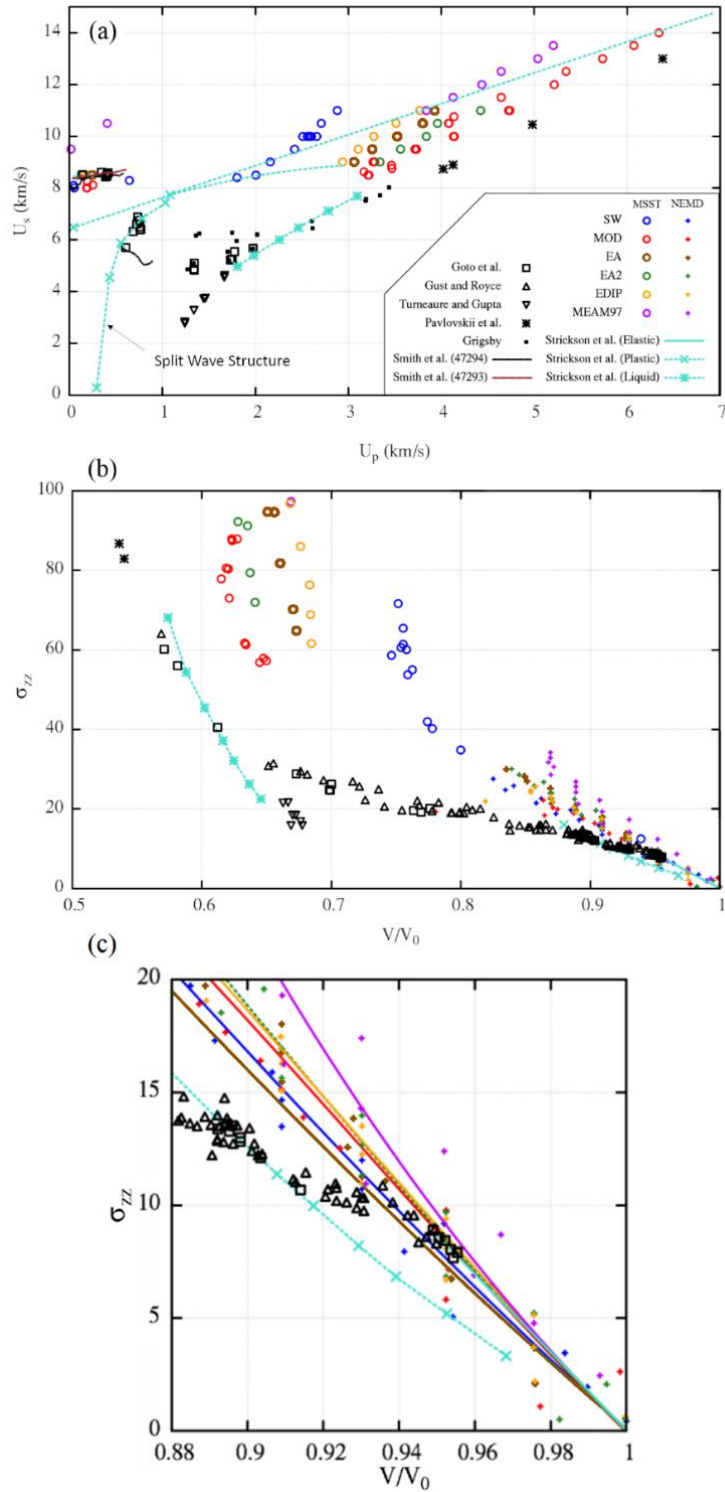


Figure 3-2 - a) Hugoniot (as calculated for each potential) compared to experimental measurements (95, 137, 138, 165–168). b) Pressure-volume diagram for the same potentials and experiments. c) Pressure-volume diagram focused on the elastic and early plastic transition.



### 3.4 Plasticity

As may be expected, each potentials predicts varying shock thresholds to induce plasticity. For direct comparison, simulations shown are conducted at  $U_p = 1.2$  km/s for the EDIP and MOD potentials, and 2.0 km/s for EA, EA2, SW, and MEAM because these potentials do not display plasticity at  $U_p = 1.2$  km/s. All simulations exhibit plastic deformation at  $U_p = 2.0$  km/s except for those conducted with the MEAM potential which requires a higher shock stress to induce deformation, in agreement with simulations by Lane et al. (108). Because we are particularly interested in studying the complexity of the deformation dependence below 25 GPa (where the vast majority of the experimental data resides), the MEAM potential is not explored further.

The Hugoniot elastic limit (HEL) is an important material property describing the elastic to plastic transition. The HEL is often difficult to accurately simulate without introducing pre-existing defects, which are typically absent in single crystalline MD simulations (169). Smith et al. (95) shocked silicon samples of different thicknesses in order to measure the elastic limit for silicon as a function of strain rate for strain rates up to  $4 \times 10^8$  s<sup>-1</sup>. The [001] HEL measured by Smith et al. (95) can be extrapolated to the strain-rates in the present molecular dynamics simulations ( $10^9$ - $10^{10}$  s<sup>-1</sup>) to be  $\sim 16$ -38 GPa. Presently, for SW, we observe homogeneous nucleation of partial dislocations at  $U_p = 1.89$  km/s corresponding to a normal stress of 31.3 GPa and heterogeneous nucleation of partial dislocations at  $U_p = 1.30$  km/s corresponding to a longitudinal shock pressure of 19.1 GPa. For MOD, heterogeneous nucleation of dislocations begins at  $U_p = 0.82$  km/s corresponding to a longitudinal shock pressure of 12.1 GPa. Homogenous thresholds for SW, MOD, and EDIP are consistent with experimental results and projected range detailed by Smith et al. (95).

The initiation of plasticity in shocked silicon is commonly due to emission of partial dislocations bounding stacking faults. Interestingly, in MOD this occurs on both {111} and {110}

crystal planes. Partials of both slip systems can later react and lead to full dislocations. A similar observation has been observed in the deformation of Si nanospheres compressed by a flat indenter, where partial dislocations were emitted from the curved surface of spheres with 10 nm and 5.16 nm radii at normal stresses of 23.5 GPa and 21.3 GPa, respectively; and further compression ultimately led to the formation of a full dislocation (170). Density functional theory has also been applied (171) to evaluate the stacking-fault energy and predict the tendency to slip along {110} planes at uniaxial compressive strains between 0 and 20% strain; a first order approximation places the transition around 12%. Achieving such elastic strains without prior nucleation of dislocations on {111} planes is possible for both shock loading conditions as well in defect-starved nanoscale structures. For direct comparison to the present work in terms of the balance between {111} and {110} slip, the SW potential under shock at  $U_p = 2$  km/s results in a ~9.5% volumetric strain.

At large elastic strains we observe a preferential nucleation of {110} stacking faults over {111} stacking faults with subsequent faults tending to prefer {111} slip as the strain relaxes during plastic relaxation. Here, stacking faults are identified as intrinsic stacking faults consisting of two atomic layers. The typical diamond stacking sequence is  $AA'BB'CC'$  where each letter denotes a set of positions on the {111} plane and prime indicates a plane separated by a covalent bond length in tetragonal arrangement. The diamond cubic structure is referred to in this form by two interpenetrated fcc unit cells with atoms at  $(0,0,0)$  and  $(\frac{a_0}{4}, \frac{a_0}{4}, \frac{a_0}{4})$ . The Burgers vector of a full dislocation for silicon is  $b = \frac{a_0}{2}\langle 1,1,0 \rangle$  and during intermediate slip atoms on the untraditional {110} slip plane may move by  $\frac{b}{2} = \frac{a_0}{4}\langle 1,1,0 \rangle$  (172). Corroborating simulations of plasticity in Si nanospheres that employ the SW potential also showed a {110} slip response in addition to the expected {111} shuffle/glide-set planes.

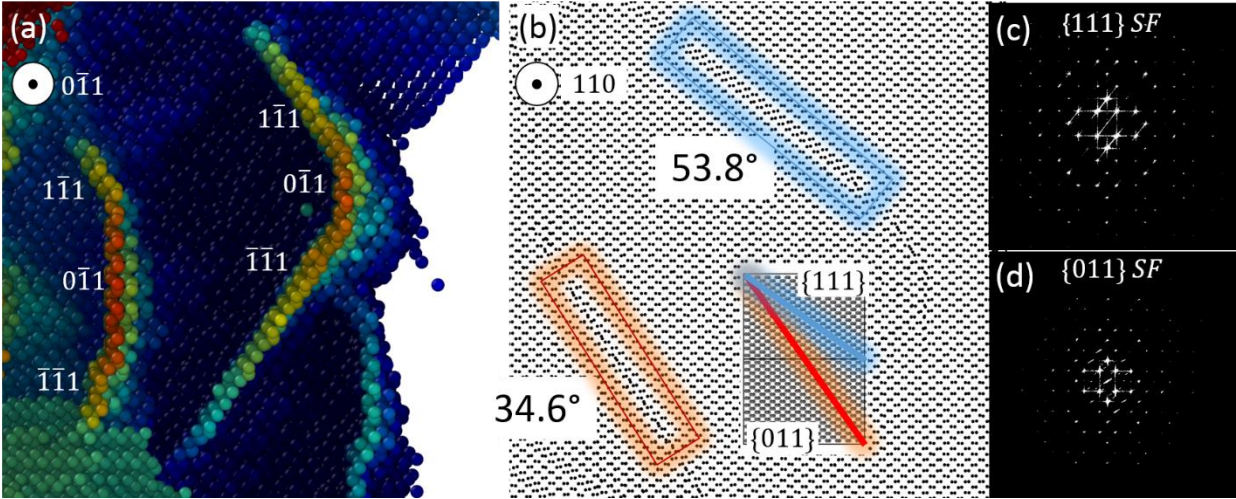


Figure 3-3 Figure 3-4 Snapshots from NEMD shock simulation performed at  $U_p = 2$  km/s (12 GPa) using the MOD potential displaying simultaneous  $\{111\}$  and  $\{110\}$  stacking faults. (a) depth perspective showing interaction between the mutual stacking fault planes. (b) thin section illustrating the resultant angles of the  $\{111\}$  and  $\{110\}$  stacking fault planes with the  $\langle 110 \rangle$  direction. (c) and (d) simulated diffraction patterns of the faulted areas. Taken from (11).

The simulations conducted herein show that only the Stillinger-Weber and MOD potentials predict the quasi-stability of the  $\{110\}$  stacking faults under compression. Figure 3-3 shows the simultaneous activation of both slip systems during shock compression of  $[001]$  silicon at 12 GPa, for the MOD potential. Simulated diffraction patterns are provided for comparison with future experimental results.

### Phase transformations

The predominant equilibrium phase transformation of Si under pressure is the transition from diamond cubic to  $\beta$ -Sn between 11-13 GPa, with a reported volume change of around 30% (133). Table I shows the range of polymorphs that may be expected in shocked Si. In general, shear stress is known to encourage polymorphic transitions and change reaction speeds (173–175); shear stress has been shown to change the dc to  $\beta$ -Sn transition from 11.4 to 3.9 GPa (176–178). In shocked systems, an absence of the dc to  $\beta$ -Sn phase transition at elevated strain rates may be expected due

to kinetic suppression (179–182) as evidenced by experiments by Loveridge et al. up to 20 GPa at  $10^6 \text{ s}^{-1}$  with no observable phase change (134). However, it is possible that detectors were not positioned in such a way to capture phase changes other than dc to  $\beta$ -Sn.

Other phase transitions in silicon under high pressure and temperature indentation have also been reported (129, 142, 154, 183) and a recent review of diamond machining of silicon offers considerable insight into potential phase transformations and anisotropy of deformation (184, 185). Earlier, Boyer et al. (155) demonstrated the (meta)stability of a body-centered tetragonal five (bct5) structure using the SW potential by the application of specific strains. It was emphasized that for such strains to be reached, other deformation modes such as fracture would need to be suppressed and that shock conditions provide an avenue to achieve large lattice strains. Kaxiras and Boyer (186, 187) were the first to thoroughly explore such large lattice strains in silicon. They were able to identify a pathway from the dc structure to the bct5 structure by applying large strains along specific crystallographic directions and evaluating structural energy barriers. In their discussion it is noted that in order for such strains to be reached, any sort of plasticity or polymorphism occurring at moderate strains must be suppressed. This highlights the importance of strain rate and kinetics in the role of deformation in covalently bonded materials such as silicon. The bct5 phase has also recently been identified in nanoindentation simulations conducted by Kim and Oh (113) and Zhang et al. (188), agreeing with in-situ Raman measurements taken during indentation and retraction experiments conducted by Gerbig et al. (189, 190). Note that the bct5 structure is visualized in Table 3-1.

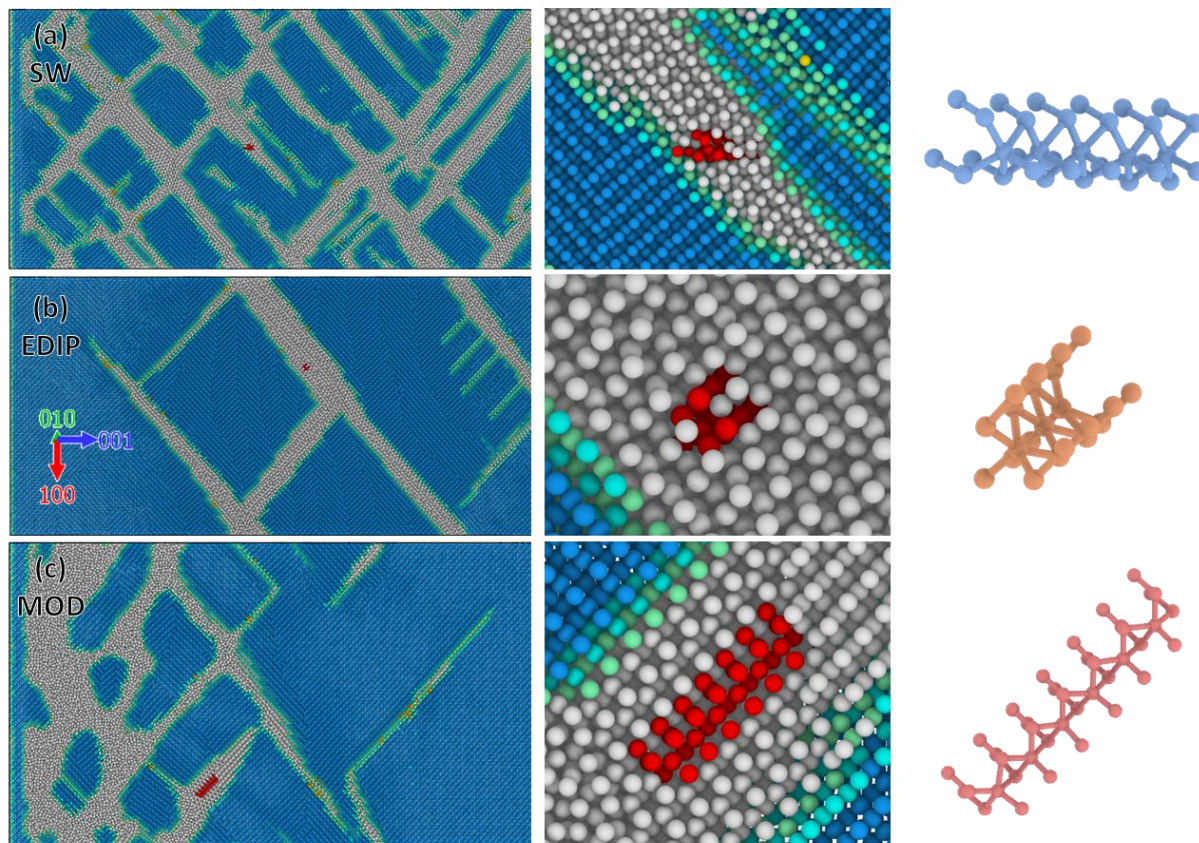


Figure 3-4 - Shocked silicon single crystals ([001]) and the location of bct5-Si structure for (a) SW, (b) EDIP, and (c) MOD at 22 ps

Several of the potentials evaluated here produce directional bands of bct5 under shock compression, yet to be reported in any shock experiments. The bct5 phase was identified in SW, EDIP, and MOD potentials (Figure 3-4) and occurs in concert with the formation of successive stacking fault layers, while the bct5 phase was not observed in the EA or EA2 potentials. Figure 3-5 gives energy-volume (U-V) and enthalpy-pressure (H-P) relationships for several possible phase transitions for the SW potential. These calculations show that the transition from dc to bct5 is comparable to the  $\beta$ -Sn transition pressure, whereas in other potentials, such as EA and EA2, the higher energy barriers can explain the absence of bct5 and the presence of other favorable transitions such as Imma (and Pmma) in the work of Mogni et al. (114).

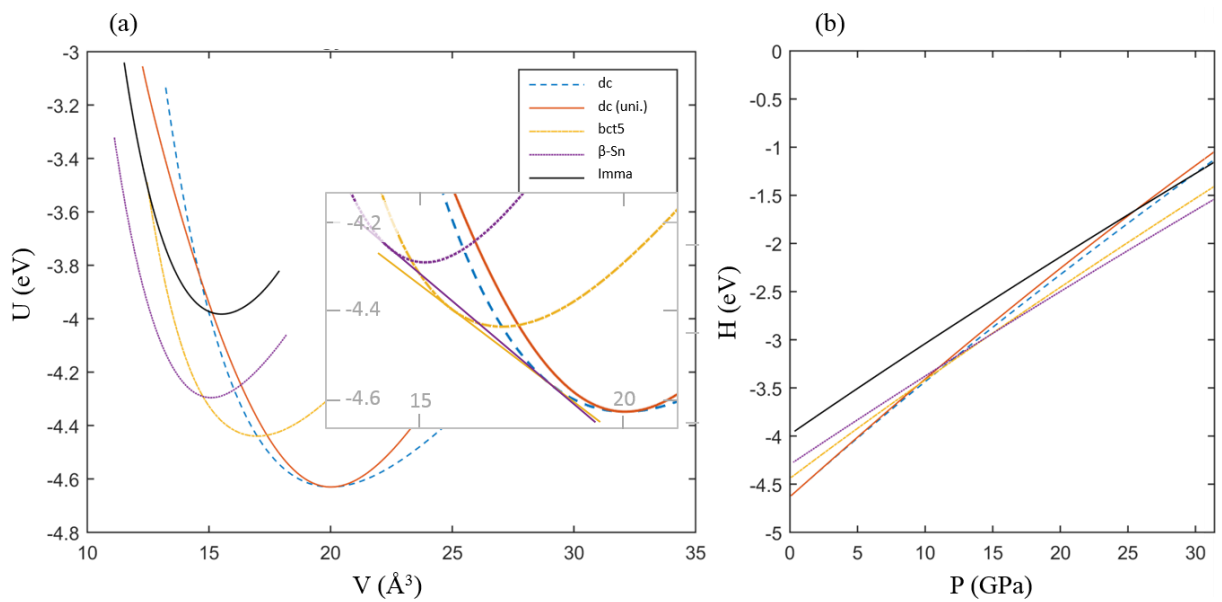


Figure 3-5 - (a) Internal energy as a function of volume and (b) enthalpy as a function of pressure for polymorphs of silicon calculated using the SW potential

### 3.5 Alternative Structure Identification Method

The identification of the BCT5 phase in the previous section was done by manually matching the unidentified phase within the shocked silicon shear bands to templates of BCT5. Here, several methods are explored for identifying the phase of the shocked silicon without requiring manual template matching. The MOD potential by Kumagai et al. (116) was selected for its performance in recreating the conditions for plasticity in silicon accurately.

The first step in this method was to isolate the shocked silicon shear bands from the untransformed bulk silicon. The bulk silicon retained its diamond cubic nature and thus did not need to be characterized. The still diamond-cubic atoms could be removed from the visualization of the simulation, and then one of the diagonal shear bands was cut out. Figure 3-6 shows the different silicon structures.

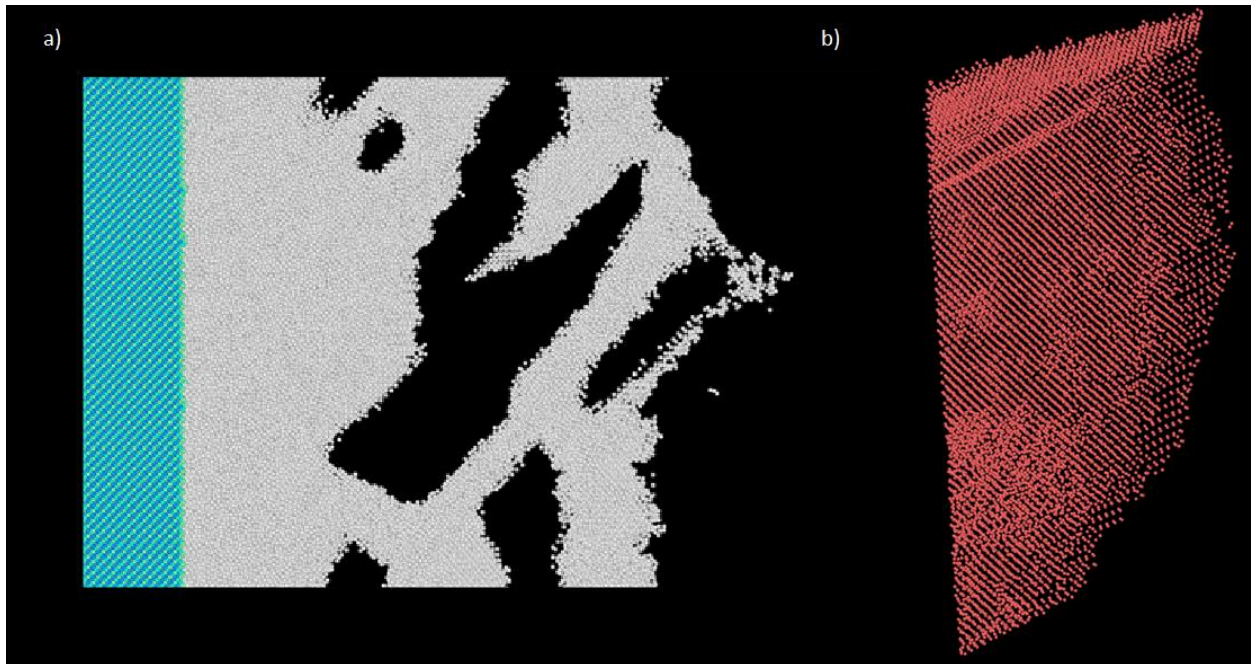


Figure 3-6 a) Shocked Silicon imaged from the [010] face. The diamond-cubic atoms have been removed from the simulation, leaving only the silicon in the shear bands that has undergone phase transformations to either a new phase or to disordered amorphous clusters. b) One of the shear bands is cut out and imaged face-on. There is still plenty of long-range order present, indicating the shear bands are not fully amorphous.

The idea behind the structure identification of the shocked sample would be to compare easily accessible measurements from pristine crystalline structures and compare them to the shocked silicon structures within the shear bands. The first measurement tested was the radial distribution function. As seen in figure 3-7, the peaks of the radial distribution function for Beta-tin did match up favorably against the shocked silicon structure, especially at the elevated temperatures we would expect in a shock heated sample. However, several other polymorphs of silicon also exhibited similar results for the radial distribution of atoms. The bond length across these different structures of silicon simply do not change enough for significant differences in the radial distribution functions to appear and clearly define one structure versus another.

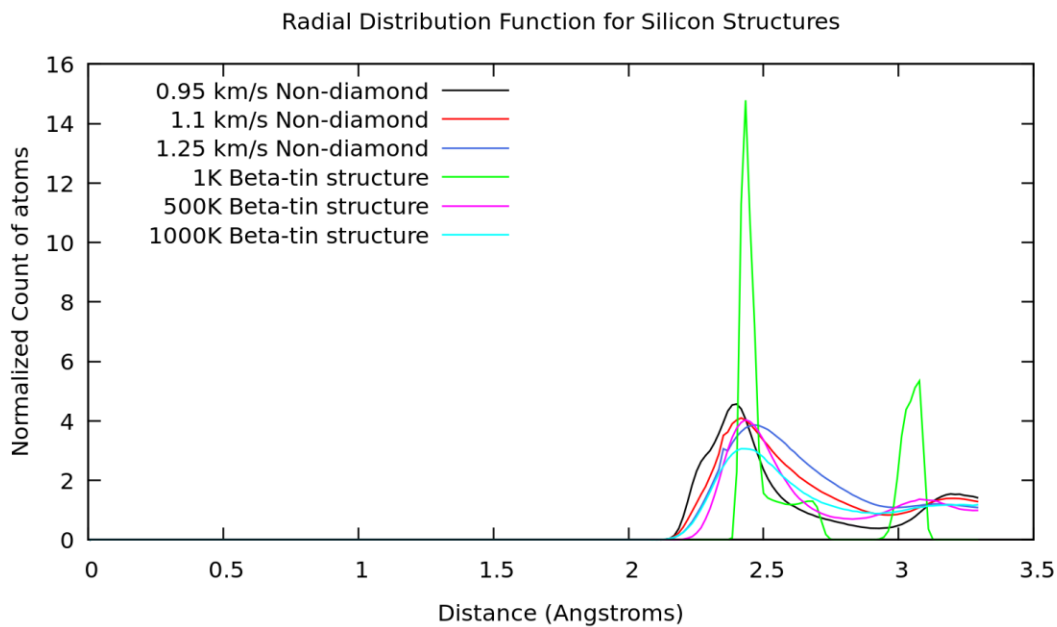


Figure 3-7 Radial Distribution Function for the shocked silicon versus different temperatures of the Beta-tin structure



The cumulative distribution function was also imaged, as seen in figure 3-8. Although there are some clear differences that can be seen here from the shocked sample, the features are still too similar for clear delineation.

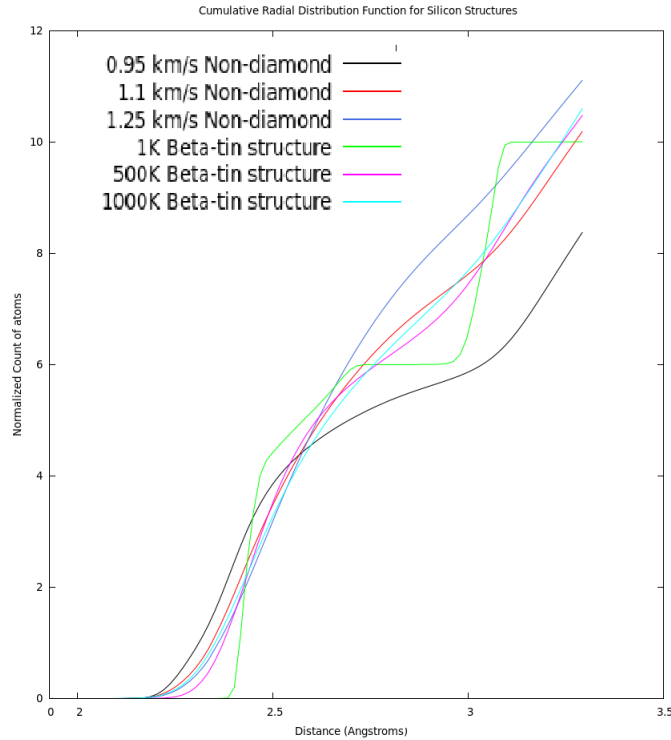


Figure 3-8 Comparison of Cumulative Radial Distribution function for shocked silicon versus beta-tin structure

The next method tested was using the angular distribution function instead of the radial distribution function. For this method, the angles between a center atom and any two neighboring atoms in the simulation are calculated, and shown in a histogram form. This method is sensitive to the angles of the bonds between the silicon atoms instead of just the distance between atoms. The results for several mismatched structures are shown in figure 3-9. The shocked silicon sample clearly has its own peaks for the most common angles within its structure, and none of the other samples match up well against it, with mismatched peaks at multiple locations.

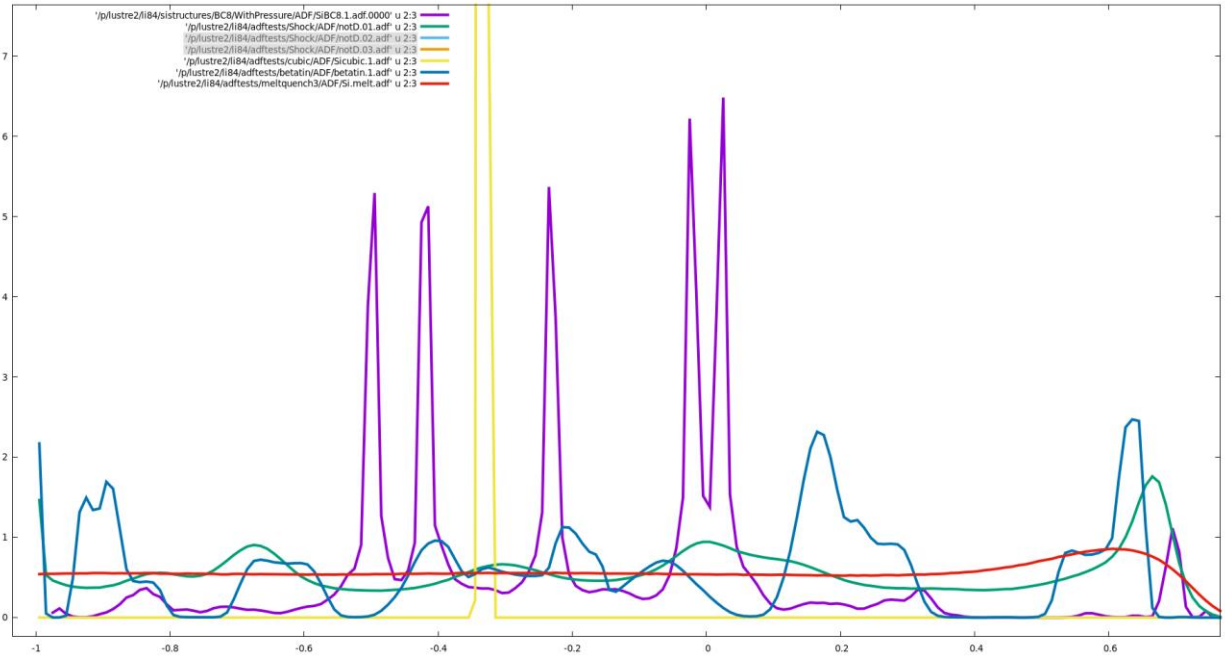


Figure 3-9 Angular Distribution Function for several forms of silicon, including BC8, Simple Cubic, Amorphous Melt, and ST12.

Finally, the match between the BCT5 phase ADF and the shocked silicon ADF can be seen in Figure 3-10. The peaks match up perfectly between the pristine BCT5 sample and the highly thermalized silicon sample, which causes broadening of the peaks. Finally, to fully validate the match between the two, the BCT5 unit crystal was formed into a superlattice and imaged for comparison to the atomistic view of the shocked silicon, as seen in Figure 3-11. The same structure can be seen between the two, although the strain and temperature present in the shocked sample show a less perfect arrangement of atoms.

This method of using the angular distribution function to quickly match known structures of elements to unidentified phases within simulations could serve as another alternative method for structure identification without the need to manually match atoms to templates of structures and should be broadly applicable to any potential for silicon or other elements and the structures they may form.

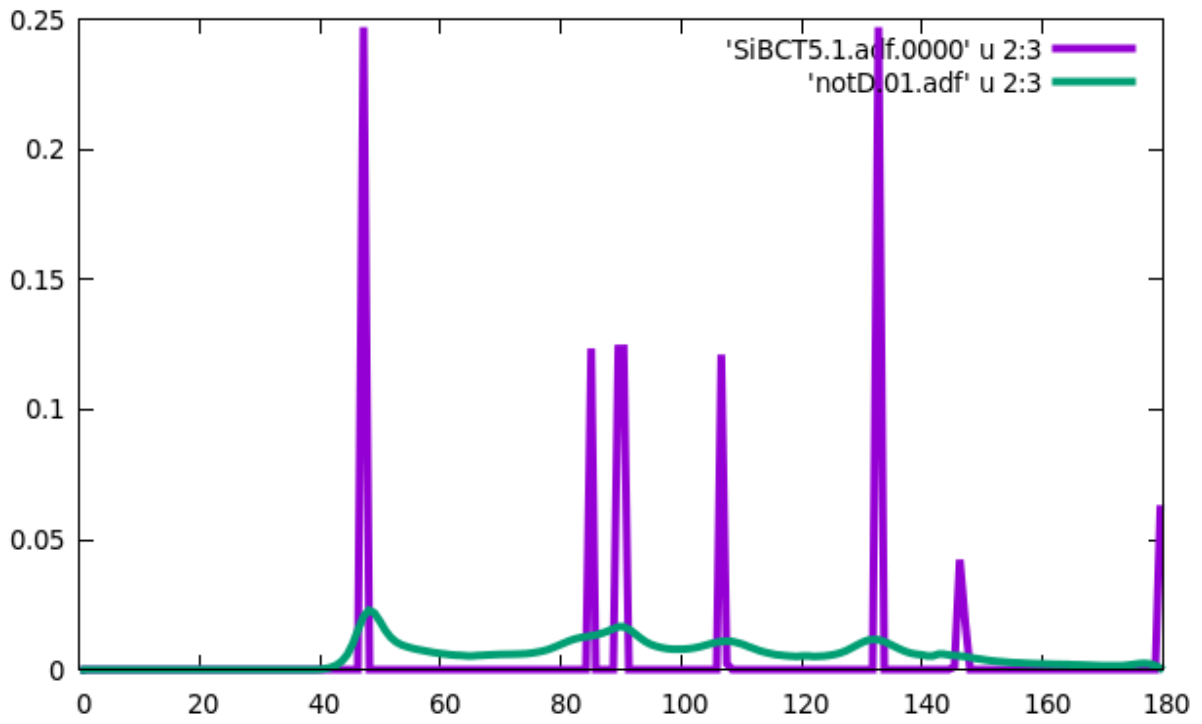


Figure 3-10 ADF match between BCT5 and the shocked silicon shear bands

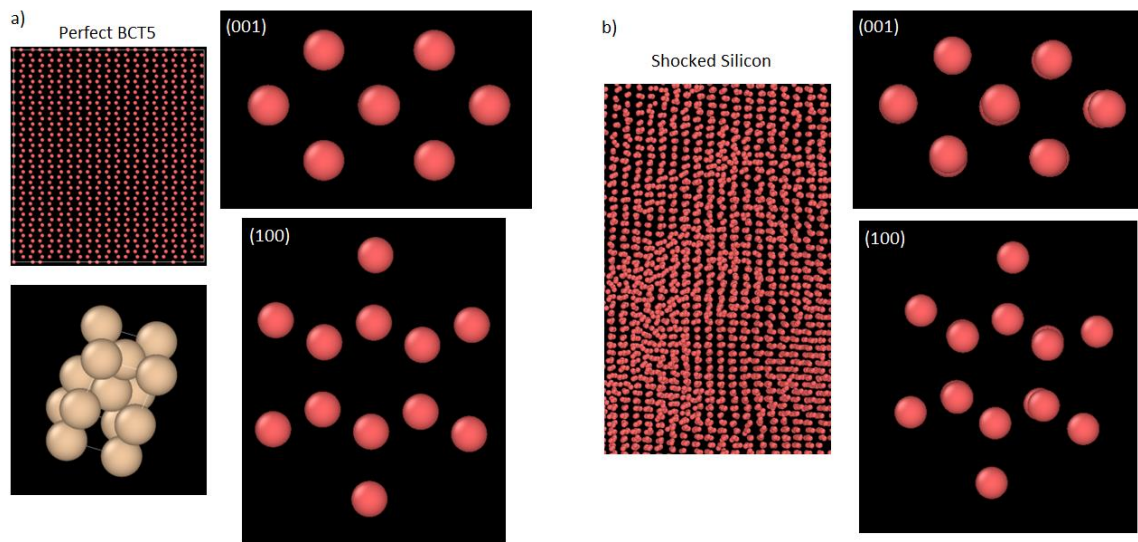


Figure 3-11 Atomistic view of a) the perfect BCT5 structure and b) the shocked silicon structure

### 3.6 Amorphization

Amorphization is another mode of structural transformation, expected to form during shock compression and release as evidenced by recent laser-recovery experiments (24). Silicon is known to have at least two amorphous phases, one high density and one low density (164), in addition to the disordered liquid phases. Notably, the SW potential exhibits a liquid-liquid transition (191). The EA, EA2, and MOD potentials also produced amorphous regions during simulation, while EDIP and MEAM did not. The multiple disordered phases are thought to play a role in solid state amorphization. This is made clear by Zhao et al. (94) in their study that identifies amorphization using postmortem Raman spectroscopy and transmission electron microscopy (TEM). According to Zhao et al. (24), the appearance of amorphization, along with its relative location, temperature, and density, is influenced by concomitant shear and hydrostatic stresses that arise during uniaxial shock compression. The result of this stress state is the formation of profuse stacking faults that travel great distances into the silicon sample (107). The maximum shear stress can be visualized as a cone extending at 45° degrees from the direction of shock wave propagation. Amorphization occurs in the slip planes that align the closest to the direction of maximum shear stress, where the many partial dislocations generated by the shock wave collapse to form the amorphous regions (94). The expected slip systems will intersect at different degrees with this cone based on the loading direction of the sample (3). Several experimental modes of amorphization are shown in Fig. 3-12. Fig. 3-12a depicts bulk amorphization possible due to solidification of liquid melts in the strong shock regime. This is a regime for which the potentials are particularly ill-suited to reveal the exact behavior, so no direct comparison is made at the present. Fig 3-12b displays an amorphous region similar to Fig. 3-12c, while Fig. 3-12c can be compared directly to the simulations shown in Fig. 3-14. Fig. 3-12d demonstrates stacking fault bands similar to those observed in Fig. 3-13, where many bands, some amorphous and some ordered are shown. The

angle in which the amorphous bands occur matches that of the slip planes closest to the direction of maximum shear, and matches the simulation results seen in Figures 3-13 and 3-14. The potentials which best matched the experimental observations of the amorphous regions in recovered shock experiments were the SW, EA, EA2, and MOD potentials which are further examined in Figure 3-13.

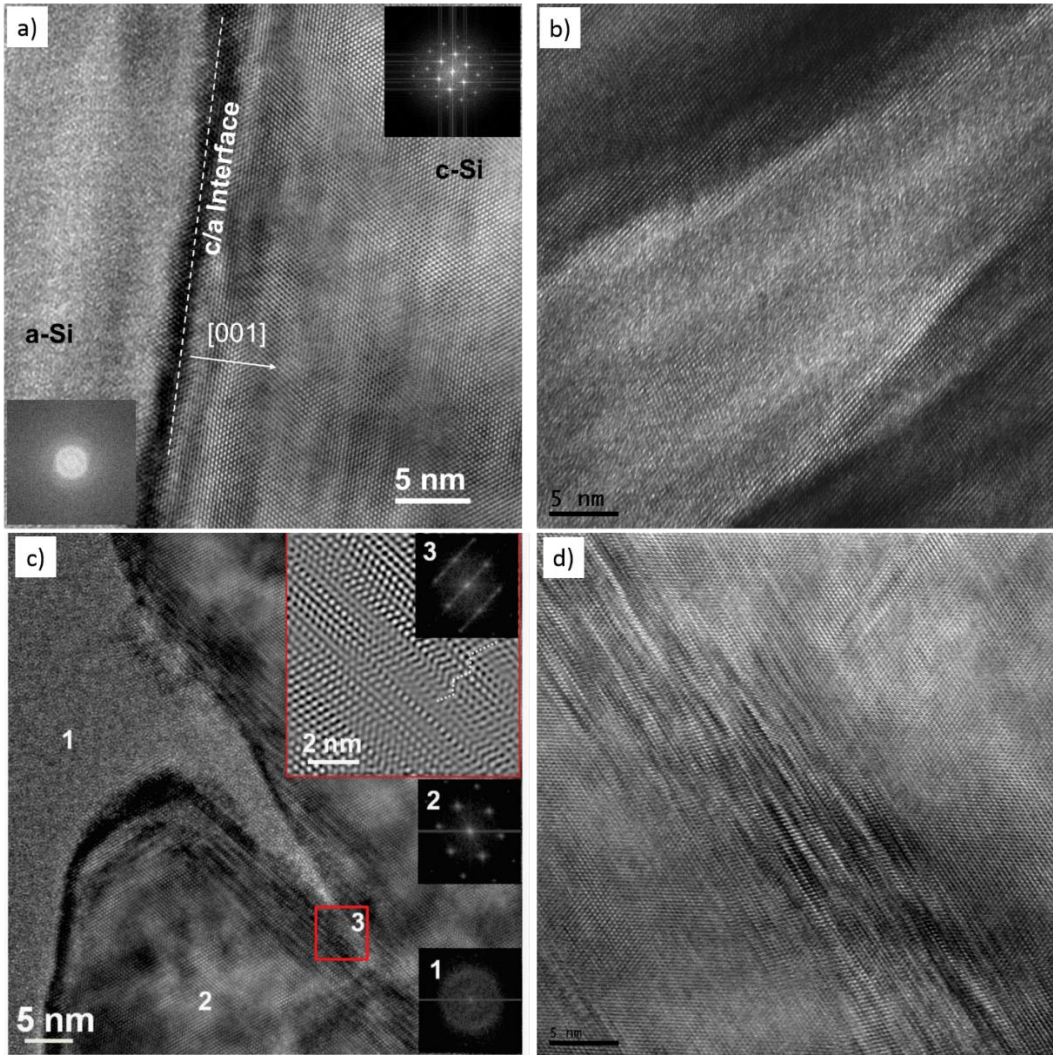


Figure 3-12 Transmission electron microscopy identification of features in shock compressed silicon. (a-c) Configurations of amorphous material, from planar fronts near the shock interface, to bands that do not have adjacent stacking faults, to bands that form at the junction of stacking faults. d) Bands of stacking faults also exist with no amorphous features. Insets in (a, c) show diffraction patterns of stacking faults, the crystalline lattice, and amorphous phases. Figure is reproduced from (24).

In Figure 3-13, select disordered regions are identified during shock compression. For further study of the amorphous phase, computation of  $g(r)$ , the radial distribution function, is conducted here. According to plots of  $g(r)$  versus  $r$ , the probability of existence of an atom in different radii can be observed; the similarities between liquid and amorphous silicon are such that they cannot be simply differentiated; a detailed evaluate of the local coordination of amorphous silicon is left for future study. Analyses of properties along the shock direction provide insight into the conditions for amorphization. The shear stress prior to plastic deformation is significant and can be as much as one half the shock pressure (192). After defect nucleation, the shear stress begins to relax, eventually dropping to zero within the amorphous region. Full relaxation of shear stress does not confirm or deny this as a solid-state process. A liquid would be unable to sustain shear stress, but full 3D plastic relaxation during amorphization is just as plausible.

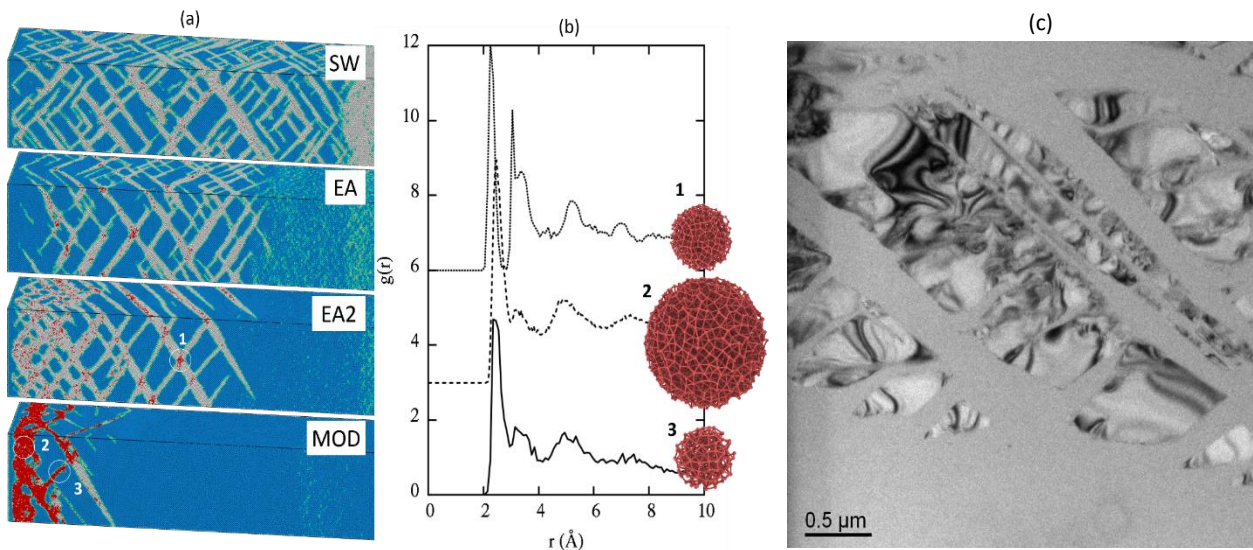


Figure 3-13 (a) Rendition of the shocked systems at 22 ps. The location of the amorphous spheres with maximum volume are identified. From top to bottom: SW, EA, EA2, MOD potentials. Atoms are colored by “Identify Diamond Structure” in OVITO. Blue atoms are diamond cubic; white atoms are unknown, and light blue atoms indicate 2<sup>nd</sup> nearest neighbor dc atoms. Atoms are subsequently identified and colored red which belong to disordered regions. (b) The pair correlation functions from the top down are (1) EA2, (2) bulk MOD, and (3) “directional” MOD. (c) A comparison with shocked silicon, showing amorphous bands of material coming at approximately 45-degree angles from the shocked direction.

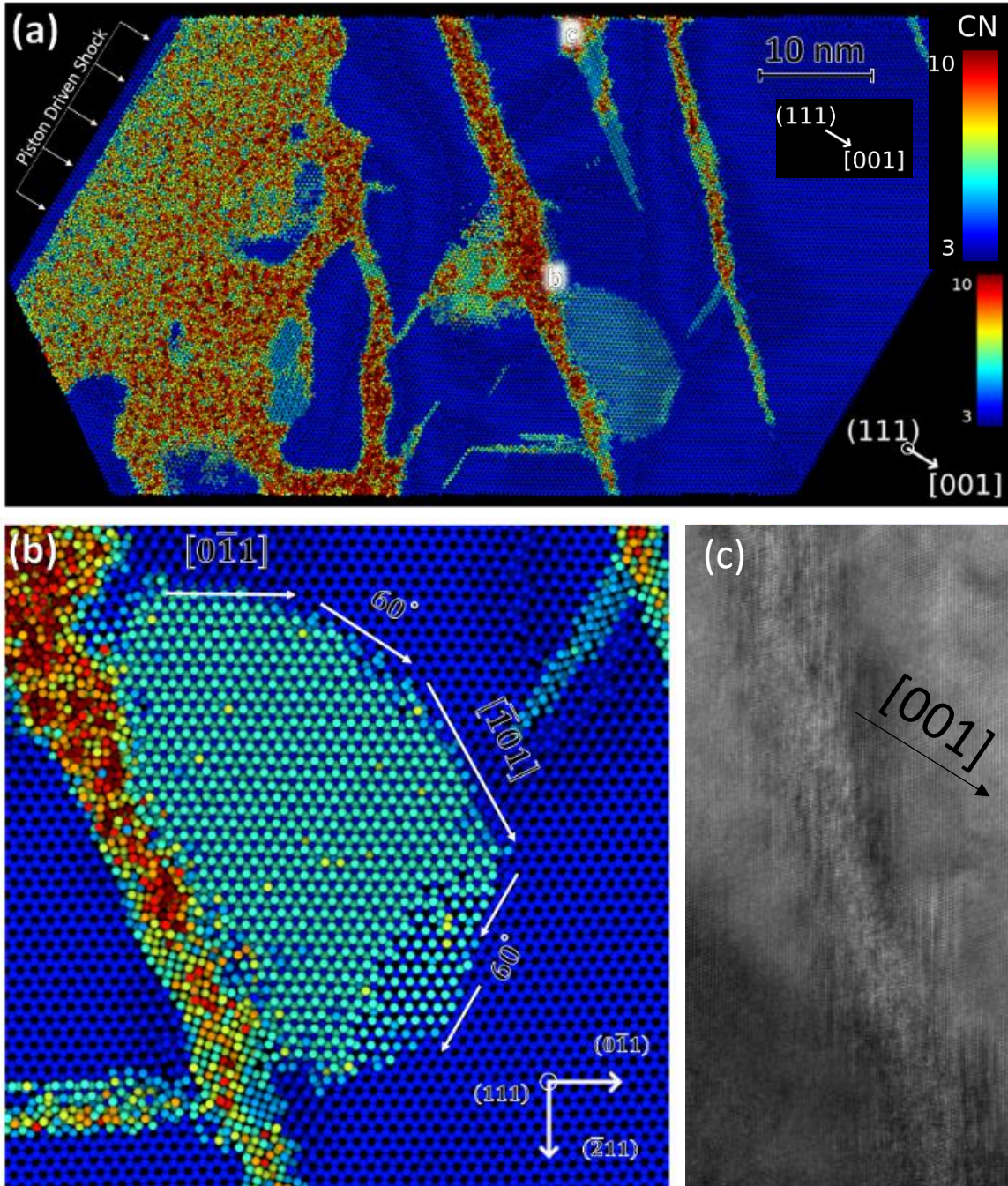


Figure 3-14 - Slice along the [111] direction of a MD simulation of [100] shocked silicon using the MOD potential. (a) Overall image showing bulk amorphization/melting near the shocked surface, directional amorphization/melting, partial dislocation activity, and formation of bct5 bands. Atoms are colored according to local coordination evaluated with a cutoff of 0.3 nm. (b) Region showing stacking fault bounded by partial dislocations. (c) TEM image of amorphous bands in shocked silicon surrounded by stacking faults

### 3.7 Summary

In this section on silicon under extremes, we report on potential-dependent shock response of silicon along the [001] orientation. Analysis of stresses and temperature along the direction of shock compression is critical to the understanding of resultant phase changes and plasticity. A transition to the bct5 phase is observed in 3 potentials: MOD, SW, and EDIP. This structure originates along bands of stacking faults and is related to the atomic structure of the stacking fault and the hexagonal diamond phase. Amorphous pockets at the intersection of defect bands are identified in SW, EA, EA2, and MOD during shock compression. MOD also displays bulk amorphization/melting near the impact interface in addition to the directional amorphous bands, which are magnified by underestimation of melting temperature at elevated pressure.

A separate method of identifying the structure of shocked silicon was tested and verified by use of the angular distribution function to match bond angles within the shocked regions of the silicon against pristine crystalline units of known possible phases. For the MOD potential, the BCT5 phase was successfully matched to the phase change identified within the shear bands formed through the plastic response of silicon to shock compression of over 11GPa.



### **3.8 Acknowledgments**

Chapter 3, in part, is in preparation for publication authored by E. N. Hahn, R.M. Flanagan, A. Li, and M.A. Meyers, Computational Evaluation of Silicon under Shock Compression, (2024).

The dissertation author was the third author of this article.

## Chapter 4 Diamond under Extremes

Carbon is sometimes called the “king of the elements” due to its amazing ability to bond with both itself and other elements. It is one of the most common elements in the universe, and is intimately connected with life on earth. Whether as a part of organic material bonded to many other elements such as oxygen and hydrogen or in its elemental form as graphite or diamond, carbon is a part of so much of the world around us. Even in just its elemental forms, its applications are diverse and dependent upon its morphology, whether from the nanoscale properties of carbon nanotubes and graphene, or to the bulk properties of solid diamond. Its resilience, luster, and clarity has made it popular for jewelry symbolic of unending devotion, while its more practical applications in industry include use in diamond saws or polishing agents, where its high hardness and strength allows it to act as an abrasive for removing other, softer material. Under the immense pressures found in planetary interiors, it adopts the diamond phase, which is the only allotrope that exists up to terapascal (TPa) pressures. Understanding these phase transitions holds the key to unlocking both technological applications and the composition of distant planets.

While theories predict a new carbon phase---BC8 (body-centered with each atom heaving eight nearest neighbors)---emerging at pressures beyond 1 TPa, experimental evidence remains elusive. The mechanisms by which diamond transitions to this new phase are just being investigated by atomistic simulations-based machine learning (*193*), but probing these conditions is very challenging for experiments. Traditional methods like shock compression face limitations, often reaching the melting point before achieving the desired pressure.

However, recent efforts through the ramp compression technique have allowed shockless compression that enable access to TPa pressures with decreased temperature rise, maintaining the sample in the solid phase (*194*). Remarkably, recent experiments compressed diamond to a

staggering 5 Terapascal using this method (195), yet no signs of a phase transition to BC8 were observed later (196). Nevertheless, the question of BC8's existence persists.

The combination of cutting-edge ramp compression with sophisticated characterization tools to bridge the gap between theory and reality should not only confirm the existence of BC8 but also unlock its synthesis pathway, paving the way for exploring high-pressure carbon's implications for planetary understanding and material science advancements.

In this section, we focus on the synthesis and some high energy density uses of carbon diamond under extremes, where some of its unique properties make it an attractive choice for experiments working at the highest temperatures and pressures that humans can achieve. In comparison to other Group IV elements on the periodic table which exhibit similar bonding behavior, diamond has a tensile strength of 95 GPa, almost 5 times that of both silicon and germanium, and a shear strength of almost 15 times (197, 198). This order of magnitude difference comes from the strength of the sp<sup>3</sup> covalent bonds between the carbon atoms. This extreme strength makes it attractive for applications that require high pressures, such as its use as the confining material in diamond anvil cells. A combination of this material strength and other factors such as diamond's thermal conductivity, density, optical transparency and other factors have also made diamond the material of choice as an ablator for high energy density experiments, such as forming the capsules which hold the fusion fuel in current National Ignition Facility experiments for controlled fusion research (20).

## 4.1 Diamond Synthesis

Natural diamonds form deep beneath the earth's surface, involving the reduction of carbonates and oxidation of methane to form diamond crystals within kimberlite (199). This kimberlite is carried up closer to the earth's surface by the exsolution of carbon dioxide from the mineral-rich magma (200).

It was not until the 1950s that diamond was reproducibly synthesized by researchers at General Electric, dissolving graphite in molten transition metals under high pressures and high temperatures. Calculations of diamond's phase diagram gave scientists an idea of the kinds of temperatures and pressures that were needed for the conversion from the more common graphite phase into the metastable diamond phase. Improvements to pressure vessels finally enabled the achievement of up to 10 GPa pressure and over 2300 K temperature, leading to the first synthesized diamonds (201, 202).

Further research into the synthesis of diamonds yielded several other methods to produce them by imposing thermodynamically favorable conditions to convert graphite to diamond, whether through flash-heating at high static pressure (203) or synthesis through shock (204). However, the now dominant method of synthesizing diamond came about with advancements in chemical vapor deposition (CVD) processes using gaseous hydrocarbons in an excess of hydrogen (205–207). This method involved the preferential nucleation and growth of diamond crystals at pressures and temperatures where graphite should be the more stable form. Further enhancements involving the methods for controlling the activation of the gas-phase carbon precursors, such as use of plasma jets or combustion flame synthesis (208–211). While growth rates for these diamond films were measured in hours per micrometer in the early stages of the technology, modern growth rates in CVD diamond synthesis can be measured in hundreds of micrometers per hour (212, 213). The enhanced growth speed and controllability of these CVD processes are what allow the precise

design and implementation of diamond for use in research today. As the technology matures it has become possible to produce single crystalline diamond wafers of increasing size and perfection, as seen in Fig. 4-1.

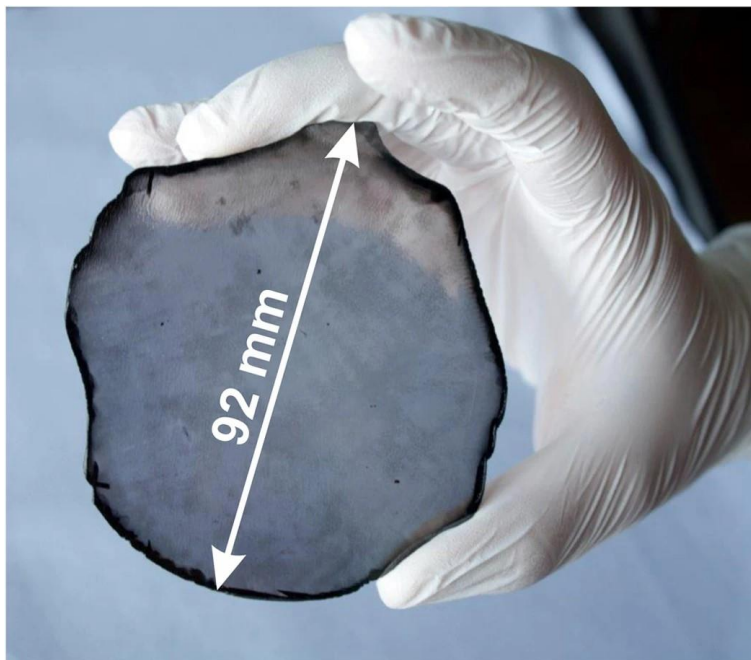


Figure 4-1 A large 155 carat single crystal diamond wafer, heteroepitaxially grown via ion bombardment on a Ir/YSZ/Si 001 substrate. (taken from Ref. (214))

#### 4.1.1 Diamond Synthesis via Shock

The formation of small diamond clusters using shock impacts was one of the earlier methods used to reach the high pressure and temperature conditions necessary for the equilibrium formation of the diamond phase. The first reproducibly created diamonds via shock synthesis were made by DeCarli in 1959 when investigating the similarities between radiation damage and shock wave damage on nuclear-grade graphite, with results published in 1961 after rigorous confirmation via XRD performed by Jamieson (204). Typical experimental setups begin with graphite sheets, which are then subjected to shock pressures of at least 20 GPa (215–217) driven by explosives or gas gun impact (218). Modern use of lasers to produce shock in graphite precursors have also produced diamond and even hexagonal diamond, lonsdaleite, at sufficient shock pressures (219).

The shock pressure and associated temperature rise create the stable conditions for diamond to form, but the time that these conditions are held are so small that usually only small clusters of diamond are formed before the system returns to a graphite stable zone. The fast quenching of the diamond is necessary for it to retain its form and not revert to a graphitic phase, and the method of quenching is also capable of producing different morphologies of diamond (220–222). Because of these fast formation timeframes, shock synthesis is generally unable to create large diamond samples, and the sizes of the clusters themselves are not tightly controlled either. Figure 4-2 shows the different P-T regions for several methods of synthesizing diamond. Shock synthesis uses higher pressures than static methods.

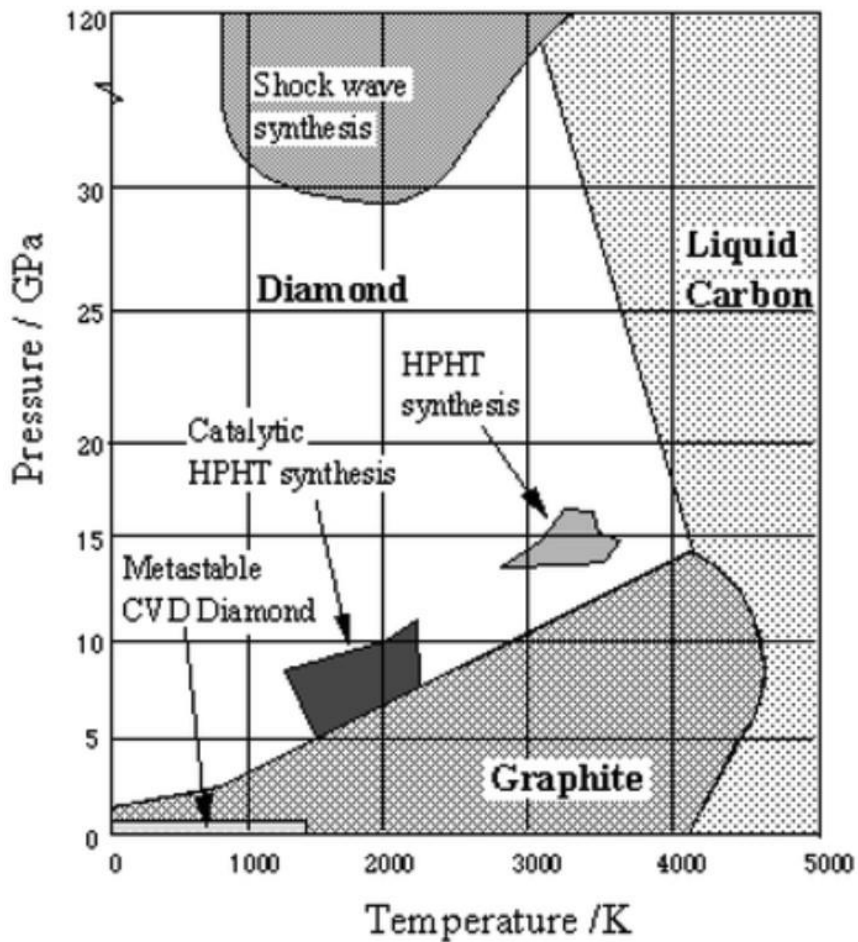


Figure 4-2 Phase diagram of carbon showing the various temperature and pressure conditions that the various methods of creating diamond are located in. (taken from Ref. (223).)

Meteor impacts also can create the conditions necessary for diamonds to form. Many crater impact sites have found evidence of diamond formed via the impact with the earth, such as Canyon Diablo in Arizona (224–227), the Ries crater in South Germany (228), the Popigai Crater in Russia (229), intact meteorites from Antarctica (230), or the possible origin of carbonado (black diamond) in Brazil and Central Africa (231). Figure 4-3 shows a diamond sample embedded within the meteorite sample from the Canyon Diablo site. While not manmade diamonds, the shock produced by the meteor impact produces the conditions necessary for the shock formation of diamond, and several unusual forms of diamond have been found from these impact sites.

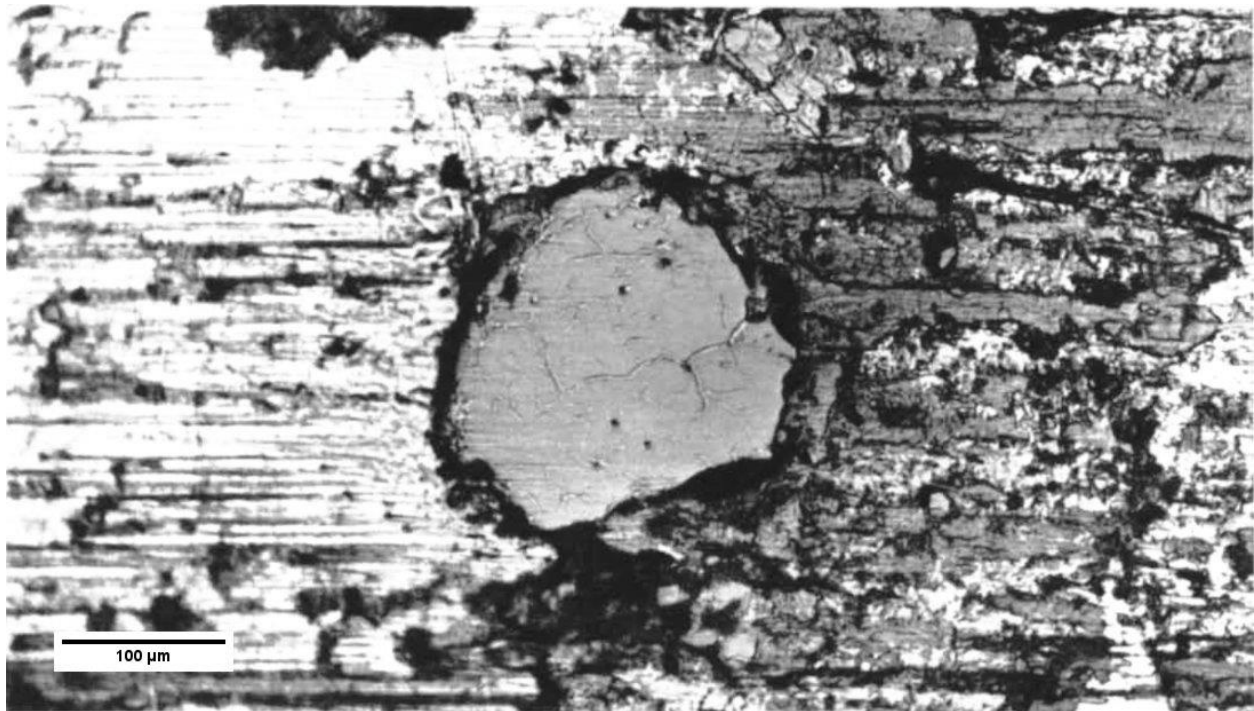


Figure 4-3 375x zoom on a diamond fragment embedded within the Canyon Diablo meteorite. Taken from (225).

#### 4.1.2 Diamonds from Detonation of Explosives (Ultra Dispersed Diamonds)

Diamond can also be the product of the detonation itself. These nanosized diamonds (4-7 nm) were found to be 25\% of the soot resulting from the detonation of TNT/RDX, TNT/TATB, and TNT/IIGU mixtures, as reported by Greiner et al. (232) in 1988. This work was simultaneously reported in the US and USSR. In the USSR, it was pursued with the recovery of the nanosized diamonds for technological applications. One of them was the mixing of the powders with lubrication oil for automotive engineering order to 'break them in' by smoothing the cylinder bores. Newer technology producing smoother bores rendered this product obsolete.

Volkov et al. (233) analyze the formation of diamond and propose that it forms at the Chapman-Jouguet pressure (19-35 GPa) and temperature (3500-4400 K). The carbon is produced by the reaction:  $2CO \leftrightarrow CO_2 + C$ . Carbon is liquid in the Chapman-Jouguet region and therefore liquid droplets are formed, which crystallize upon rapid cooling if conditions are right. Volkov et al. (233) claim that the first experiments forming ultra dispersed diamond date from 1963.

Figure 4-4 shows the Chapman-Jouguet states for a variety of explosives. They are in the liquid region and this explains the formation of nanosized diamond upon solidification.



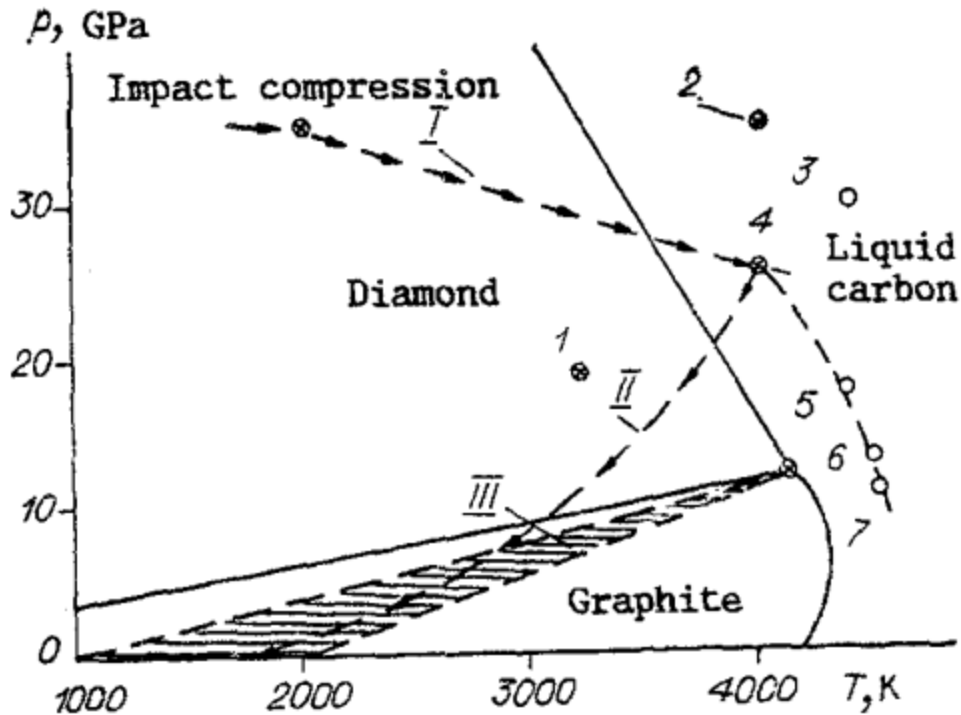


Figure 4-4 Pressure vs. temperature diagram for carbon; points 1 to 7 represent different Chapman-Jouguet states for different explosives. It can be seen that, except for Explosive 1, the points are in the liquid region. Taken from Volkov (233).

#### 4.1.3 Shock Consolidation

Diamond powder with fine particles can be consolidated into a more solid diamond bulk by use of a mechanical means: a shock wave in a process called shock consolidation. This process is more akin to sintering than the formation of diamond from graphite. The important understanding from these experiments are the effects of the diamond particle sizes on how the particles consolidate, as well as the quality of the diamond samples that can be obtained from these methods. Because of diamond's high hardness, pressures of about 100 GPa or above are required for the consolidation process (234), but could be lowered with the presence of graphite powders added to diamond (235). However, because of these high pressure shock waves, cracking is also

likely in the consolidated samples (236). In general, the density of the consolidated samples can go as high as 90% (237). Diamond has a natural hardness in the range of 100-150 GPa, and these consolidated samples range from 25 to 80 GPa in hardness (234, 237, 238).

#### **4.1.3 Presence of Flaws in Diamond**

Field studied strength and fracture properties of manufactured diamonds and has shown that they tend to be full of flaws (239). When compared to natural diamond, manufactured diamonds were on average 3-4 times weaker (198). Testing of tensile strength in CVD diamond samples, with equivalent flaw size calculated from an assumed  $K_{Ic}$  value of  $6 \text{ MN}/\text{m}^{\frac{3}{2}}$ , revealed flaw sizes ranging from 40 to 150 micrometers, obtained from a bursting membrane method. The larger the testing area of the diamond, the more likely that larger flaws are present, resulting in lower values of the strength of diamond for larger samples.

#### **4.1.4 Brown Diamond**

Some of the color in diamonds may be a consequence of the presence of dislocations created by plastic deformation, rather than just the presence of elemental impurities. Both natural and CVD diamonds have been observed with brown coloring. Willems finds evidence of both [101] and [112] type dislocations in brown diamonds (240), and further research showed evidence that small vacancy clusters may affect the coloration as well (241). There is also evidence that high pressure/high temperature treatment of these brown diamonds can remove these discolorations (242).

### **4.2 Static Compression of Diamond**

#### **4.2.1 Diamond Anvil Cell Experiments**

Diamond's unique properties led to it becoming the material of choice in the creation of the Diamond Anvil Cell (DAC) in 1959 (243). By sandwiching other materials between two diamond faces, a very high pressure can be applied to the sample. Due to diamond's remarkable

compressive strength and extreme hardness, it can exert pressures on the sample ranging from tens of gigapascals to even terapascals (244).

Since it is optically transparent, direct microscopic observation of the sample under pressure can be made. However, diamond is transparent to more than just visible light. X-rays were another extremely valuable source of spectroscopic data, and diamond's low atomic number means it has a low absorption. By utilizing the single crystalline nature of the diamonds used in DACs, if the diamond was oriented such that it did not fulfill the Bragg condition, then the x-rays also minimally attenuate due to Rayleigh scattering. Infrared, gamma, UV, and even photons also prove that diamond's transparency make it perfect for the purposes of studying other material under high pressure (245, 246). Figure 4-5 shows the structure and imaging within a DAC.

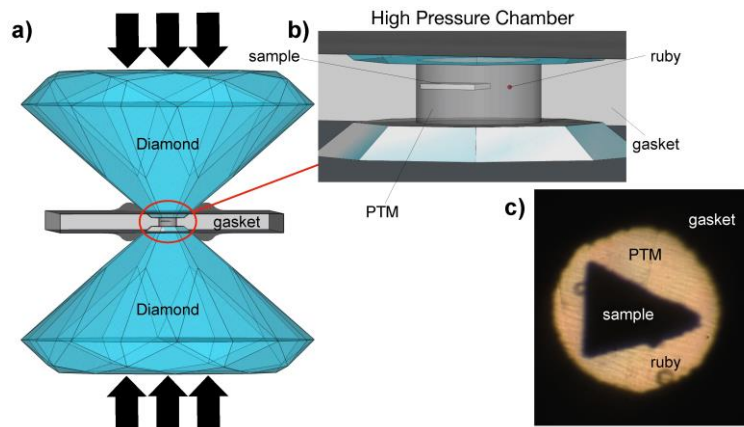


Figure 4-5 Schematic and images of a diamond anvil cell.(a) Diagram of the DAC (b) Zoom in on the high pressure chamber (c) Real image of the sample chamber within the DAC. Taken from (247).

When DACs subject other materials to these high pressures, the diamond itself also experiences those pressures. Physical analysis of anvil cells removed after experiments to pressure of 170 GPa found macroscopic plastic deformation in one of the faces, seemingly dependent on nitrogen platelet concentration (248). Further experiments studying the response of the diamond

itself under these conditions have been performed, observing the deformation of the anvil face up to 400 GPa (249). A theoretical first-principles study of the non-hydrostatic tetragonal compression present in DACs found that the diamond begins to yield when the shear stress present exceeds 200 GPa, or expected experimental pressure in the 300 GPa range (250). These predictions line up with some of the changing properties of the DACs around these conditions, including the fluorescence of the diamond itself interfering with commonly used ruby fluorescence (251). Another study used a moissanite anvil cell capable of pressures up to 500 GPa to study diamond's raman spectra and the effects of hydrostaticity or nonhydrostaticity in loading (252, 253).

First principles calculations and finite element analysis of diamond and its use in DACs has shown good agreement with experimental results, where properly designed setups with [001] oriented diamond can reach pressures of over 500 GPa, and dual stage nano-twinned diamond can reach up to 1TPa (254).

#### **4.2.2 Indentation Testing**

Indentation testing of materials is a common method of relatively non-destructive characterization of physical properties. Hardness values are taken by indenting a material with a tip of a specific shape, depending on the type of indenter test being performed. Diamond's place as the hardest natural material makes it perfect for use as the indenter tip, as it can easily penetrate the surface of other less hard materials, but issues arise when diamond itself needs to be tested. Since diamond is used to indent diamond, deformation or even failure of the indenter tip can occur. The Vickers and Berkovich indenters are unsuitable to the task as they tend to produce irregular indentations on the testing surface (255). Use of the shallower Knoop indenter made of high quality single crystalline or nanopolycrystalline diamond has shown the most consistent results but must still be paired with additional microscopy such as AFM or SEM to accurately measure the size of the indentation (256). One of the earliest measurements of plasticity in diamond used a Knoop test

and interestingly found that shear events formed along the (100) planes rather than the (111) planes as expected (257). A review of diamond indentation hardness by Chaudhri (258) argues that much of the previous data for diamond indentation hardness is incorrect due to these factors, and the true hardness for diamond is likely to lie between 130 and 145 GPa.

Nanoindentation studies on small diamond crystals found a strong orientation dependence in the loading response of diamond. Hardness values of 95 GPa were found for the {100} surface, and 117 for the {111} surface (259). Nanoindentation characterization of thin diamond films grown on a substrate found that hardness tended to increase with pressure, as the deformation increased the sp<sup>3</sup> bonding within the nanocrystalline material (260). Another study looking at obtaining the Young's modulus from nanoindentation tests found it to be 1090 GPa in the [001] orientation, in fair agreement with literature values (261).

#### **4.2.3 Diamond Nanopillar Experiments**

Nanopillar experiments provide a unique set of conditions for observing plasticity in diamond. Recent advances in nanopillar construction techniques and electrostatic deformation have enabled the study of nanoscale diamond pillars under load. These nanoscale experiments may exhibit very different mechanical properties than their bulk counterparts, but are a means to provide insight into its mechanical response.

Researchers at Zhejiang university used in-situ TEM to perform nanopillar compression experiments on diamond. They were able to directly observe dislocation loops forming at the compression zone and were able to identify that these dislocation loops actually lie on the {100} planes (262, 263). A different study observed bending of diamond nanopillars and found that their (111) oriented samples would only deform elastically, returning to their original shapes or failing in a brittle fashion, while their (100) oriented samples underwent plastic deformation, and possibly formed new O8 phase of carbon under these loads (264).

### 4.3 Diamond Phase Diagram

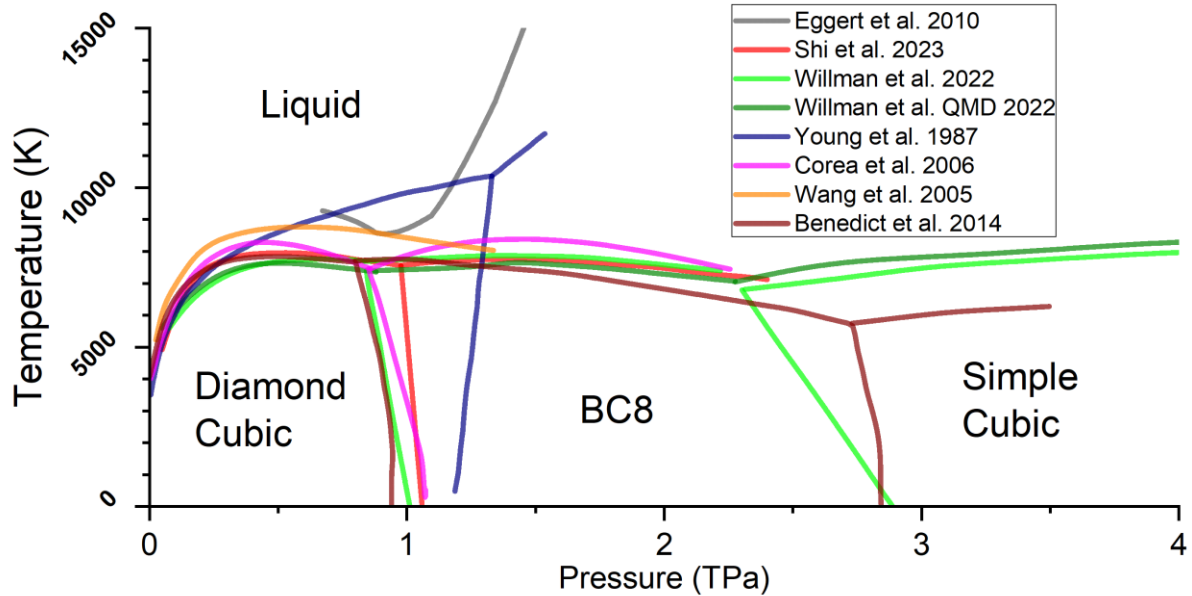


Figure 4-6 A phase diagram for diamond up to 3.5 TPa and 15000K has been consolidated from several sources, including early first principles estimates of the phase boundaries, up to the most recent machine learned calculations for the phase transitions of diamond. Aside from the earliest calculations performed for the transition from cubic diamond to BC8 in 1987, the general features of the different phases tend to line up well. The cubic diamond to BC8 has a negative slope between temperature and pressure, as well as the transition from BC8 to simple cubic at even higher pressures. The BC8 to liquid transition begins with a positive slope which then turns downwards. Eggert's experimental data on the diamond Hugoniot also captures a portion of the melt line.

Figure 4-6 shows a phase diagram that is constructed from an early model by Young and Grover (265) as well as several ab initio calculations of the high pressure and temperature phases in diamond (79, 266–269). Willman's (79) carbon SNAP machine learning potential results are also included. The graphite phase is not shown, but would occupy a sliver of the leftmost portion of the chart, as it is stable only to at most 15 GPa. Experimental data of the shock melting curve can be seen from Eggert's (270) experimental data. The features of most of the phase diagrams are quite similar, apart from the earliest calculations. The transition from diamond cubic to BC8 takes place at around 1 TPa, and diamond's melting point increases with pressure until around 400 GPa,

where it begins a negative Clapeyron slope. This negative slope is also seen for the transition from diamond cubic to BC8. A simple cubic phase exists above  $\sim 2.8$  TPa at 0K, and even further beyond the boundaries of the figure hexagonal phases are predicted.

While the BC8 phase is predicted to occur at 1TPa and above, experimentally it has not been observed (196). Ab initio predictions of the phase changes of diamond agree with the experimental results as well, with the diamond cubic phase remaining as the metastable state until reaching the threshold for the simple cubic phase to occur at  $>2$  TPa (271, 272). The kinetic limits and high energy barriers between the two phases simply do not allow for diamond to directly transition to the BC8 phase. While some calculations did show that relaxation of the simple cubic phase into the equilibrium BC8 region would produce the elusive phase, another pathway for creating it is currently under investigation at the NIF (193, 269). By taking the metastable nanocrystalline diamond into the BC8 phase but above the extended diamond melt line, a metastable supercooled liquid state is formed. If this liquid state is then cooled and held in the thin BC8 region as seen in Figure 4-7, the new crystal phase eventually forms.

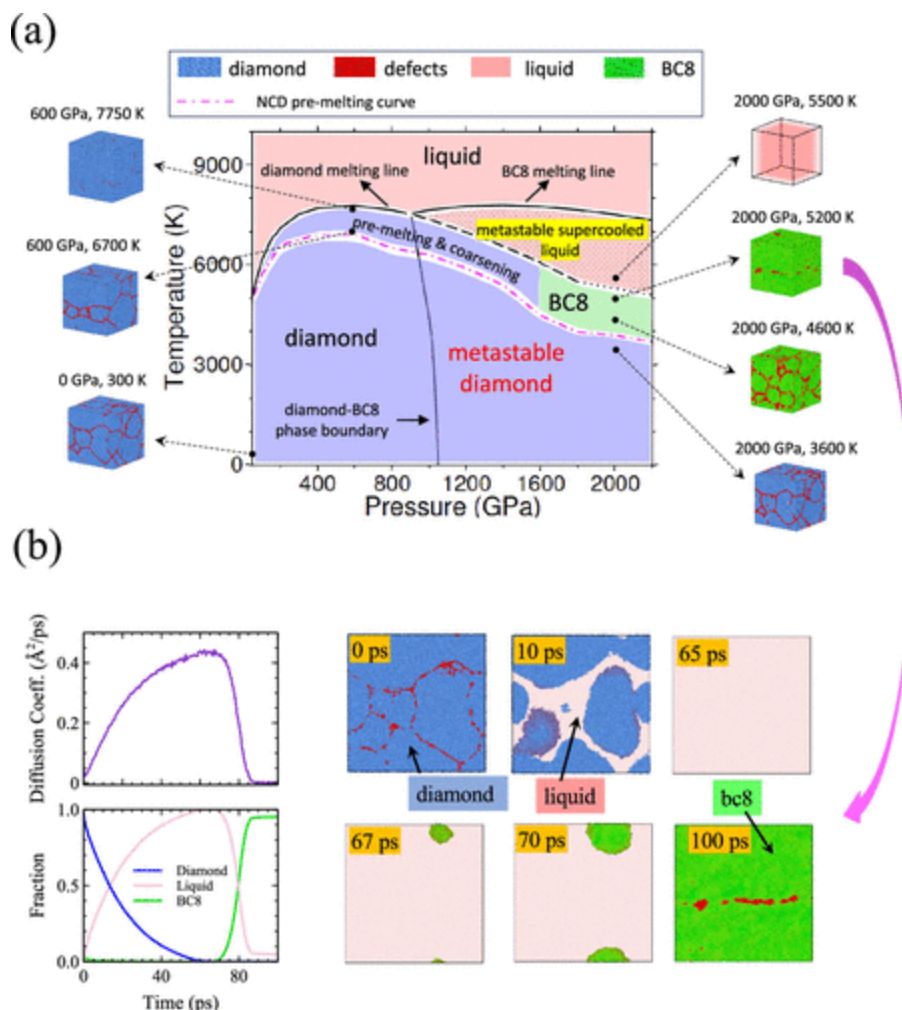


Figure 4-7 A possible metastable pathway towards experimentally forming BC8 diamond. A) Shows the extended diamond melting line, where if the diamond is taken above this line will form a metastable supercooled liquid. If the temperature can then be lowered into the green BC8 zone, the BC8 crystal structure should form. b) A timelapse of the change in diamond simulated when taken from the metastable diamond phase up to the supercooled liquid state, then lowered to the BC8 formation zone.

#### 4.4 Molecular Dynamics for Diamond Under Extremes

Simulating diamond using molecular dynamics or ab initio calculations begins with the ability to model carbon. The first potential developed and widely adopted was the Tersoff potential (61) in 1988. It has a simple description for bonding strength based on the number of nearest neighbors. It is still one of the fastest carbon potentials available and is often used as a benchmark for comparison with other more recent or complex carbon potentials. Further developments in



these types of classical potentials have given rise to other potentials which may all describe a particular part of carbon diamond's behavior well. However, in general these potentials fail to capture every aspect of the behavior across the full range of temperatures and pressures, environments, or bonding behaviors, that diamond and carbon can exhibit. Thus, many studies use molecular dynamics with classical potentials to study diamond behavior. Especially at the lower end of the HEDP regime, below 200 GPa and below the melting curve, the behavior of these potentials can still provide insight into mechanical properties of diamond such as dislocations, stacking fault energies, tensile or yield strengths, and others. Modifications to parameters such as bonding cutoff lengths, bond angle strengths, attractive pair potential, are common in attempts to improve the performance of the Tersoff potential for different ranges of pressure or temperature. Each of these potential endeavor to describe particular system conditions better, such as graphite interlayer interactions, hydrocarbons, and metallic alloy interactions.

#### **4.4.1 Tersoff Potential**

The Tersoff Potential (61) is one of the earliest and still most widely used classical interatomic potentials; it was originally developed for silicon and later adapted to silicon carbide, while also describing the pure carbon-carbon bonds as well. Previous 3-body attempts to describe silicon had proven unsatisfactory for the range of bonding geometries and coordination numbers and increasing the number of bodies considered introduced too many variables to the problem. Tersoff decided to implement the physics of the problem directly into the equation, where the bond order, or bond strength, was influenced by those geometries and coordination. The formulation of the potential and explanation of its parameters can be seen in Section 2.7.

Several different variants of the Tersoff potential exist with just slight tweaks in the parameters used. There are many versions of the Tersoff potential with simply adjusted cutoff distances that improve performance in varieties of pressure environments (273, 274).

The Tersoff potential described physical properties of diamond with good agreement to both experimental data and first principles calculations. Cohesive energies, bond lengths, elastic properties, and point defect properties all were within reasonable error.

#### **4.4.2 Other Potentials**

The Brenner potential's function is based on Tersoff's covalent-bonding formalism with additional terms that correct for an inherent overbinding of radicals and that include nonlocal effects (275). It is one of the most widely implemented and cited versions of the Tersoff potential used. Glosli used the potential in atomistic simulations of diamond melting (276).

The Erhart-Albe potential (148) is a bond order potential fitted for silicon, carbon, and silicon carbide. Compared to previous potentials, it describes elastic properties even better, and demonstrates transferability across regimes by simulating condensation of silicon-carbide in an inert gas environment. It has been used often in conjunction with the Tersoff potential to corroborate results in nanotwinned diamond (277).

The carbon MEAM potential (278) is based on the embedded atom potential. It attempts to describe both the structures of carbon while providing the ability to describe metals and metallic interactions. This allowed it to be extended for use in alloyed metal-carbon systems (279).

Another potential was a formulation based on Tight Binding model (280) to capture the quantum mechanical nature of covalent bonding in carbon. While this potential has been of most interest in the simulations of other carbon materials such as nanotubes (281, 282), there have been some applications for studying diamond as well (283).

The Environment Dependent Interaction Potential (284) is better fitted to liquid and amorphous carbon phases, with superior performance to Tersoff and Brenner in these areas. Buchan used this potential to study radiation damage cascades within diamond (285).

The original reactive force field potential (158) was created with bond order considered specifically for modeling interactions within a chemical system. Modifications of the ReaxFF C-2013 potential (286, 287) were made from a previous potential developed for hydrocarbons. Fitting parameters for the potential were obtained from equations of state for graphite and diamond calculated via DFT. This potential is still best suited for chemical reaction descriptions, as was the original intention of the reactive force field potential.

The Adaptive Intermolecular Reactive Empirical Bond Order (AIREBO) potential was another potential (288) originally created for hydrocarbons, this was an improvement over the previous REBO potential by including torsion, dispersion, and non-bonded repulsion interactions. Repulsive and attractive terms are combined with a proportional bonding term in the Tersoff style, with repulsive terms in the Brenner style.

For the Long-range Carbon Bond Order Potential (LCBOP) potential (289), short-range interactions are described by bond order, while also including long-range interactions for non-nearest neighbors. Short range interactions are based on the Brenner potential. Ghiringelli used this potential to create a very accurate graphite-diamond melt curve and triple point prediction (290).

#### **4.4.3 Monte Carlo Simulations**

Classical molecular dynamics modeling is limited in the timescales it can reproduce, but Monte Carlo simulations instead model events directly and then calculate timescales. Kinetic Monte Carlo has been used to simulate the growth of diamond being produced via chemical vapor deposition (291, 292). Atomistic level definition is given as each step of the vapor deposition growth is simulated with one reaction occurring at each one, with statistically variable time increments between. Different reaction species (293), gaseous environments, and other environmental factors can all affect the growth rates of diamond. As CVD is one of the most

common methods of producing diamond, these studies are important for the optimization of the CVD process. With modern computing power, more complicated geometries and factors can be included in these simulations (294), as well as multiscale combinations of molecular dynamics and Monte Carlo for ultrafine particle growth (295).

#### **4.5 Preliminary Simulations of Diamond Shock to High Pressures**

Preliminary simulations testing out the performance of the Tersoff potential for [001] oriented diamond were performed to observe the effects of extreme pressures on the formation of defects. Although the Tersoff potential is only accurate to around 200 GPa for reproducing the elastic constants of diamond, we simulated pressures far above this just to see how this model of diamond would respond to up to Terapascal pressures. Figure 4-8 shows the compression of diamond using a piston velocity of 6 km/s, producing average pressures of over 250 GPa. While the algorithm for identifying the diamond phase has at this point failed to identify the compressed portion of the image, it is still only being purely elastically compressed along the shock direction. Figure 4-9, shows a similar result for a piston velocity of 8 km/s. There are still no dislocations being formed, but there is much more disorder within the crystalline structure when compared to the results from the 6 km/s piston velocity. At 8 km/s, the average pressure reached within the simulation was over 400 GPa.

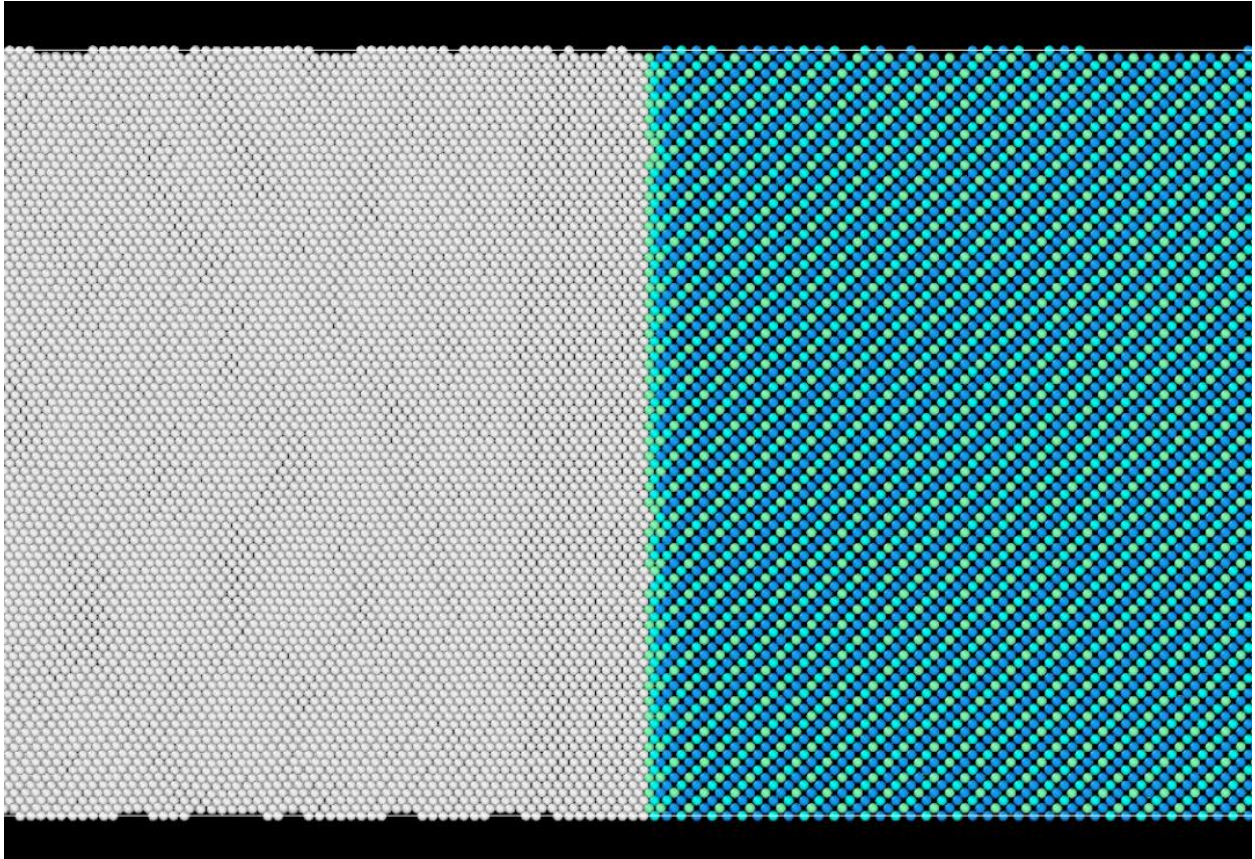


Figure 4-8 6 km/s piston velocity driving shock compression of cubic [001] diamond. Only elastic compression is observed, even as the structure identification algorithm fails to identify the compressed portion.

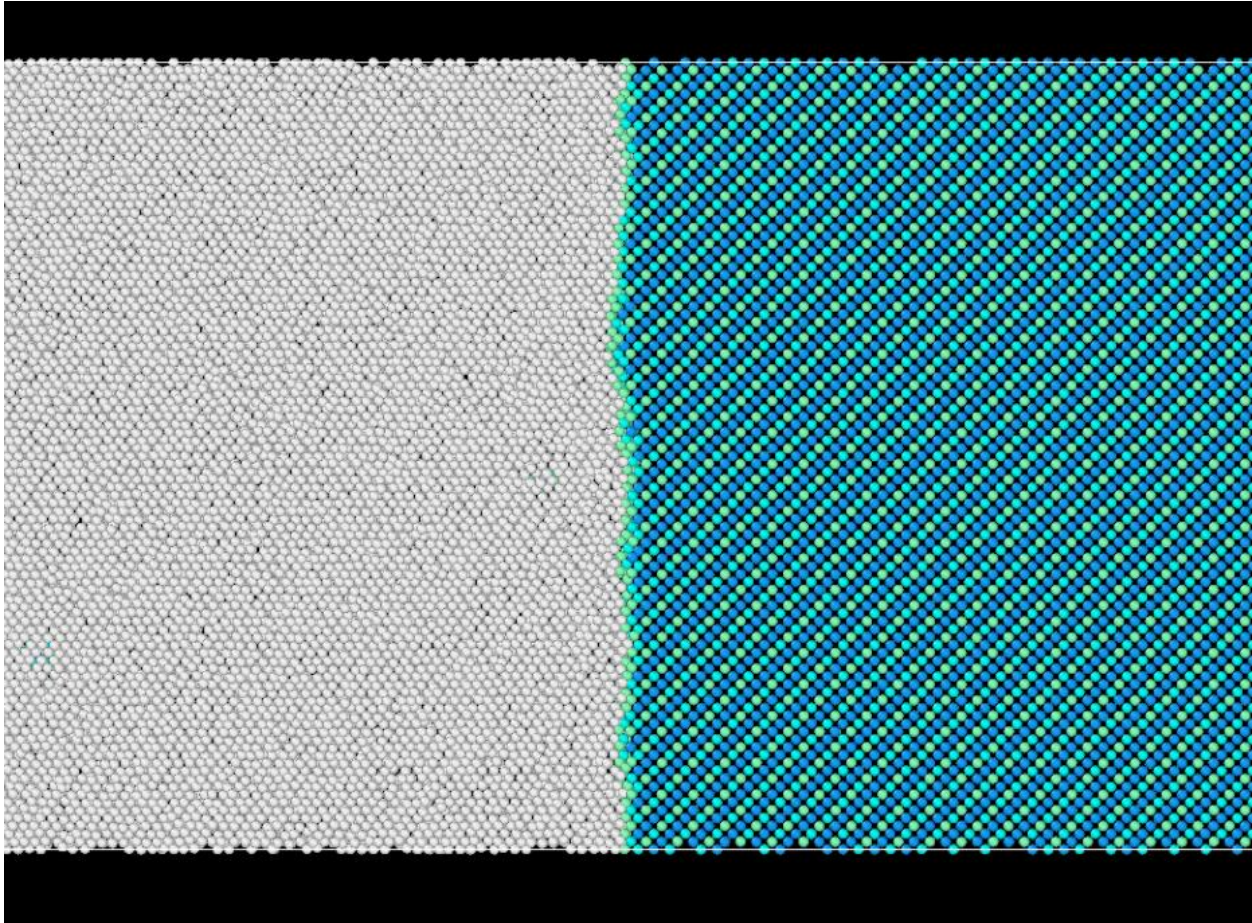


Figure 4-9 8 km/s piston velocity driving shock compression of cubic [001] diamond. Still, only elastic compression is observed. However, much more disorder within the crystalline phase can be seen.

At a piston velocity of 10 km/s, we see the onset of melting or amorphization and the recrystallization of heavily twinned regions. Figure 4-10 shows a comparison between the structure identification and the potential energies of the simulation, indicating that the recrystallized regions are at a lower potential energy state, releasing some of the energy that is present within the amorphous melt. Figure 4-11 shows a closer look at some of those crystals, with the seemingly twinned recrystallized grains.

From these simulations it was gathered that for the [001] orientation of diamond was extremely strong and not prone to the formation of defects, even up to the point where it could undergo melting and recrystallization.

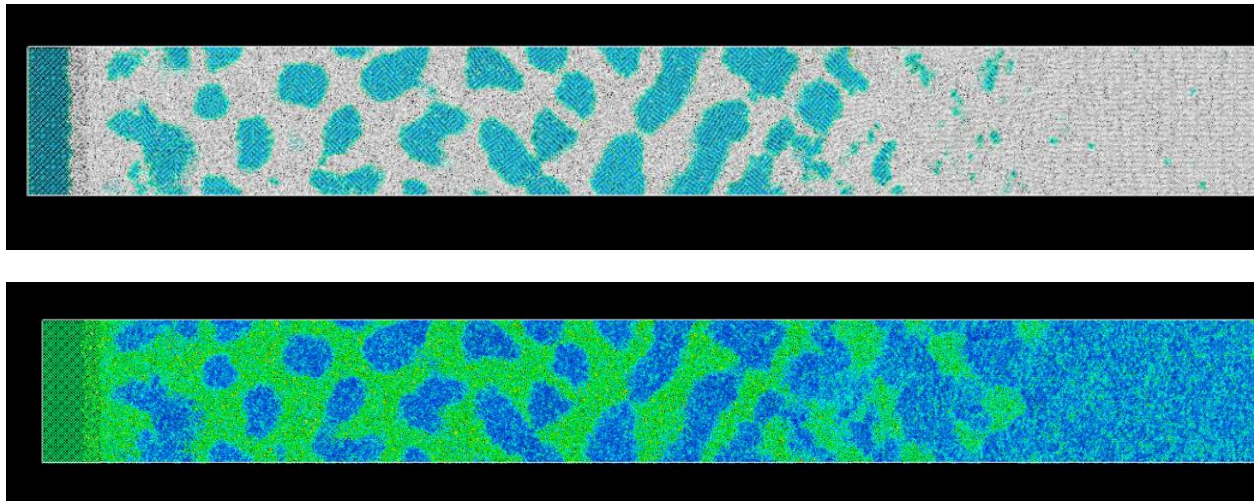


Figure 4-10 Comparison of the (top) diamond cubic recrystallized grains within an amorphous melt and the (bottom) potential energies of atoms within the simulation. The recrystallized grains are of a much lower potential energy, indicating a more stable form.

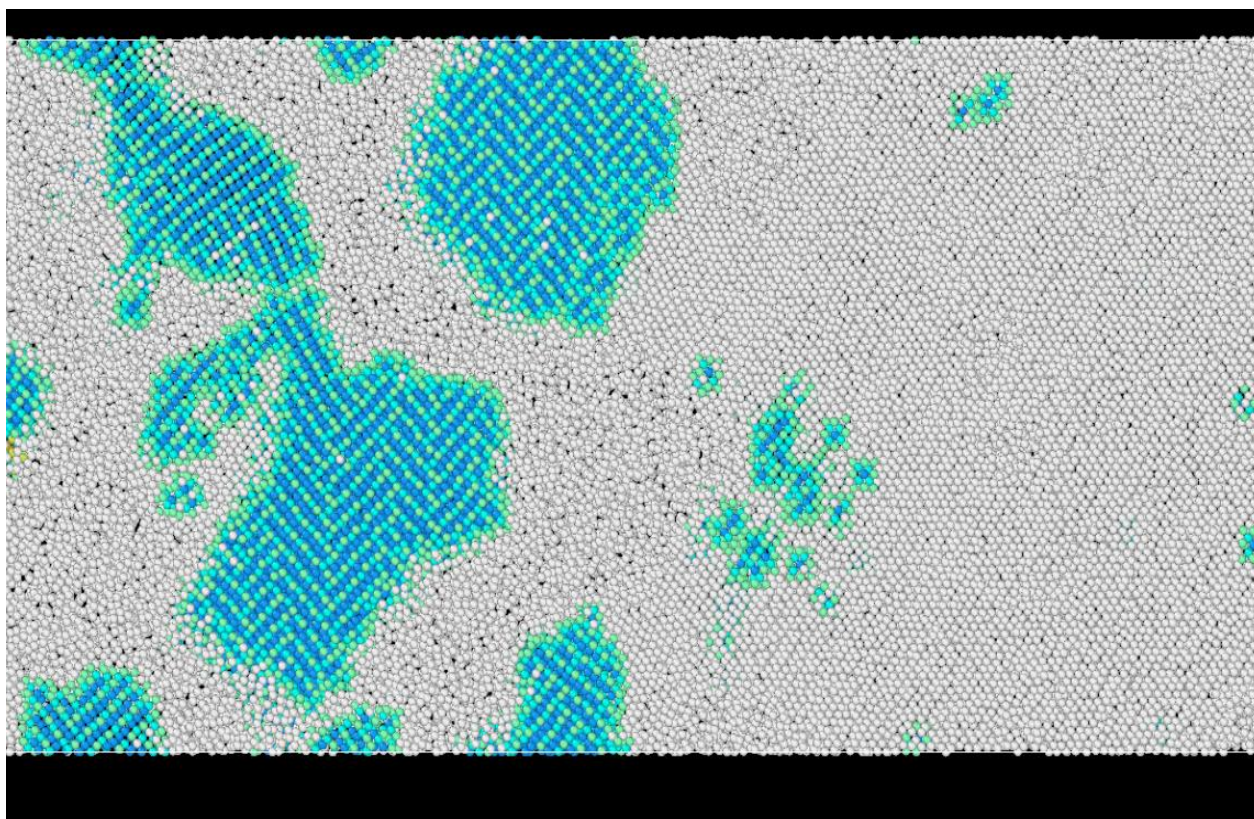


Figure 4-11 A closeup of the transition region between the elastically compressed portion at the right of the image and the amorphous melt and recrystallization that follows in a second plastic wave. The recrystallized grains look to exhibit twinning-like features, due to the patterns of the atomic order present within the simulation.

#### 4.6 Diamond Experimental Laser Shock

To test the strength of diamond along, laser compression experiments were also performed at the Laboratory for Laser Energetics (LLE) at the University of Rochester. We were allowed to place our targets in ride-along shots with Dr. Camelia Stan from Lawrence Livermore National Labs. Three samples were prepared, with the same target dimensions. Figure 4-12 shows the design of our targets, for the purposes of post-shock recovery and characterization. Each sample was shocked at a different laser energy to produce the desired pressures. Three laser energies of 200, 300, and 400 J were used. From the Lindl equation and our laser specifications we reached peak pressures of around 100 GPa. Although the Hugoniot elastic limit (HEL) for diamond is predicted to be lower than this value (296) , from our previous simulation results we could reasonably expect that no dislocations would form for the [001] orientation. Our three shots would probe the pressure ranges above and below the HEL to see if it could be an accurate predictor for the plasticity threshold in diamond along this orientation.

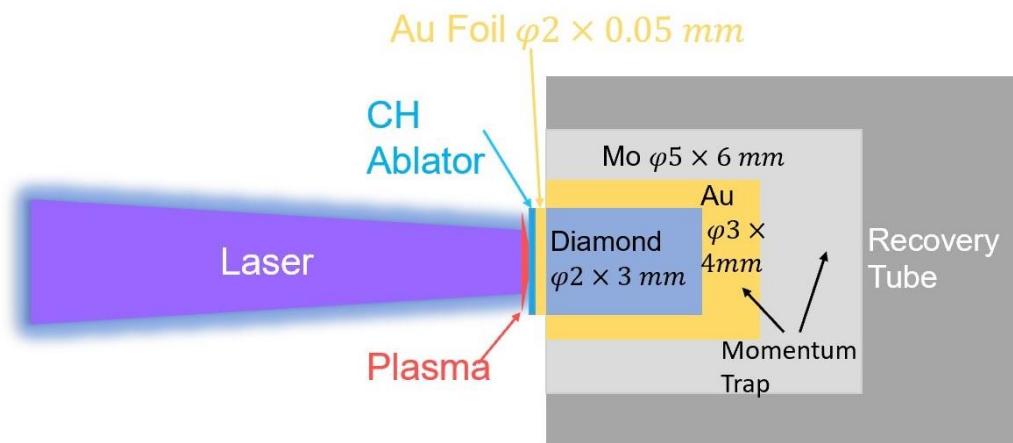


Figure 4-12 Target design for the laser shock of [001] oriented diamond. The diamond was wrapped in a shell of gold and molybdenum, both impedance matched materials to aid in the recovery of the diamond sample for post-shock characterization.



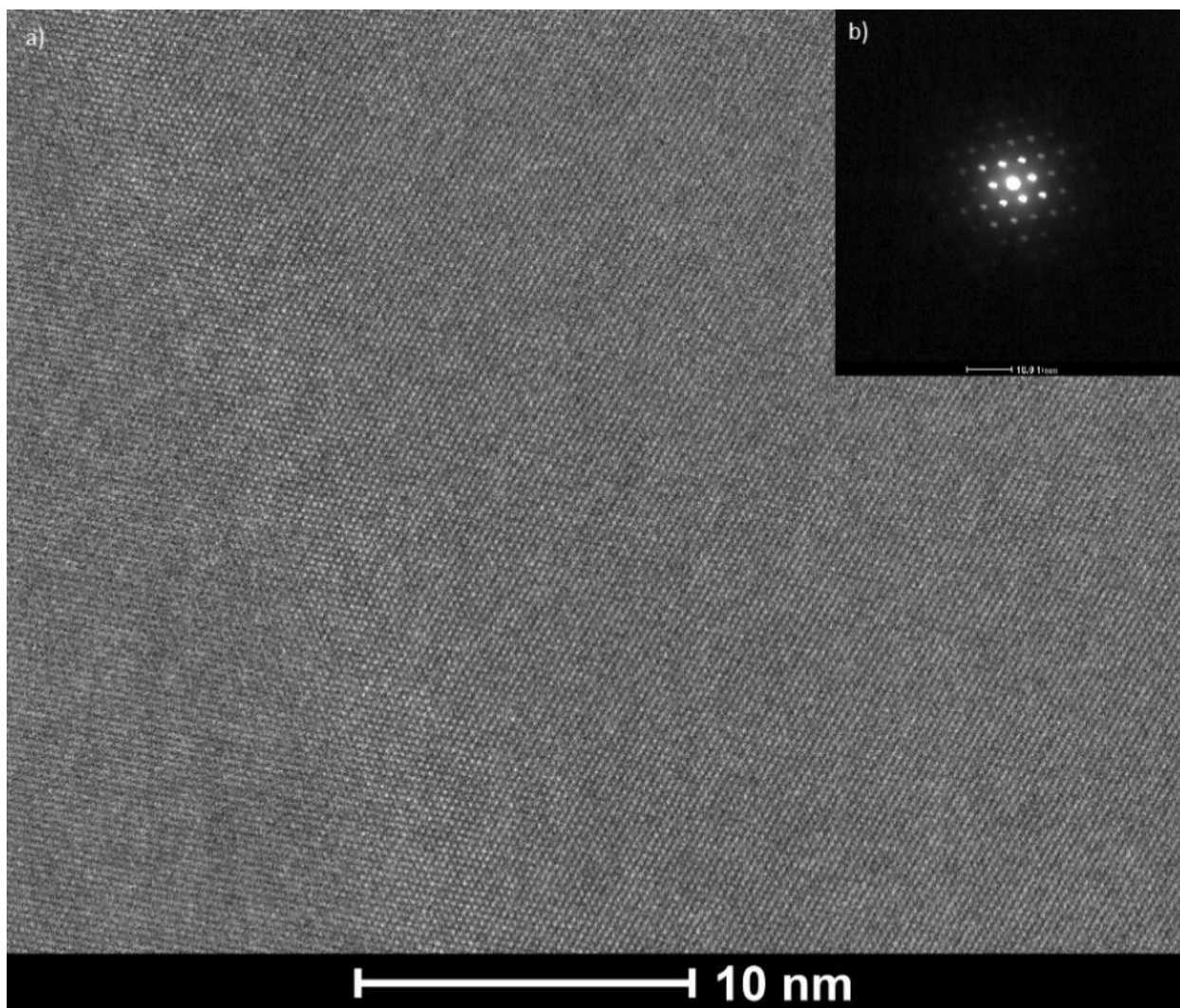


Figure 4-13 Diamond shocked to 60 GPa, below the Hugoniot elastic limit. As expected, the crystalline structure is perfectly preserved.

The samples were recovered post shock and characterized using the resources at the Nano3, MRC facilities at UC San Diego and the Materials Research Institute at UC Irvine. Raman spectroscopy established that no chemical reactions had occurred at the surface of our first two shocked samples. SEM and FIB-SEM tools were used for initial micro-scale characterization of the surface and for preparation of the TEM samples. TEM was then used to gather atomic-scale resolution images of the crystalline lattice within the shocked samples to identify whether any

plasticity had occurred. As seen in Figure 4-13, for the samples below the HEL the perfect crystallinity of the lattice remained with no dislocations in sight.

The 300J shot post recovery had too jagged of a surface for successful creation of a TEM sample through use of the FIB-SEM process.

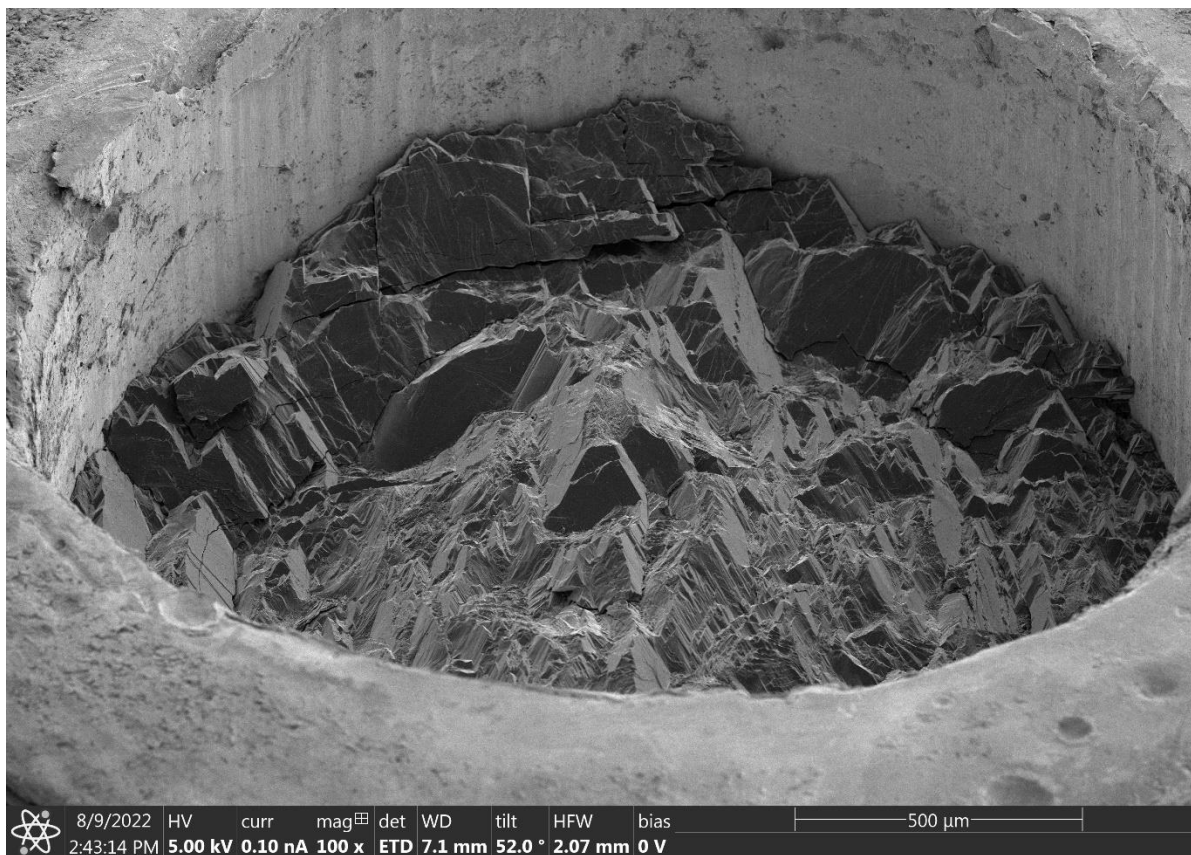


Figure 4-14 The second shot (300J) had too jagged of a surface to allow for TEM characterization

For the highest energy tested, 400J, we were able to recover the sample and perform some SEM and TEM analysis. However, there appears to be some form of amorphous film on the surface of the diamond sample. This could be a contamination issue, or it could have been a reaction on the surface due to possible outgassing of the sample upon laser ablation. There is a crater in the middle, smaller than the one seen in the second sample in Figure 4-14. The SEM image can be seen in Figure 4-15.

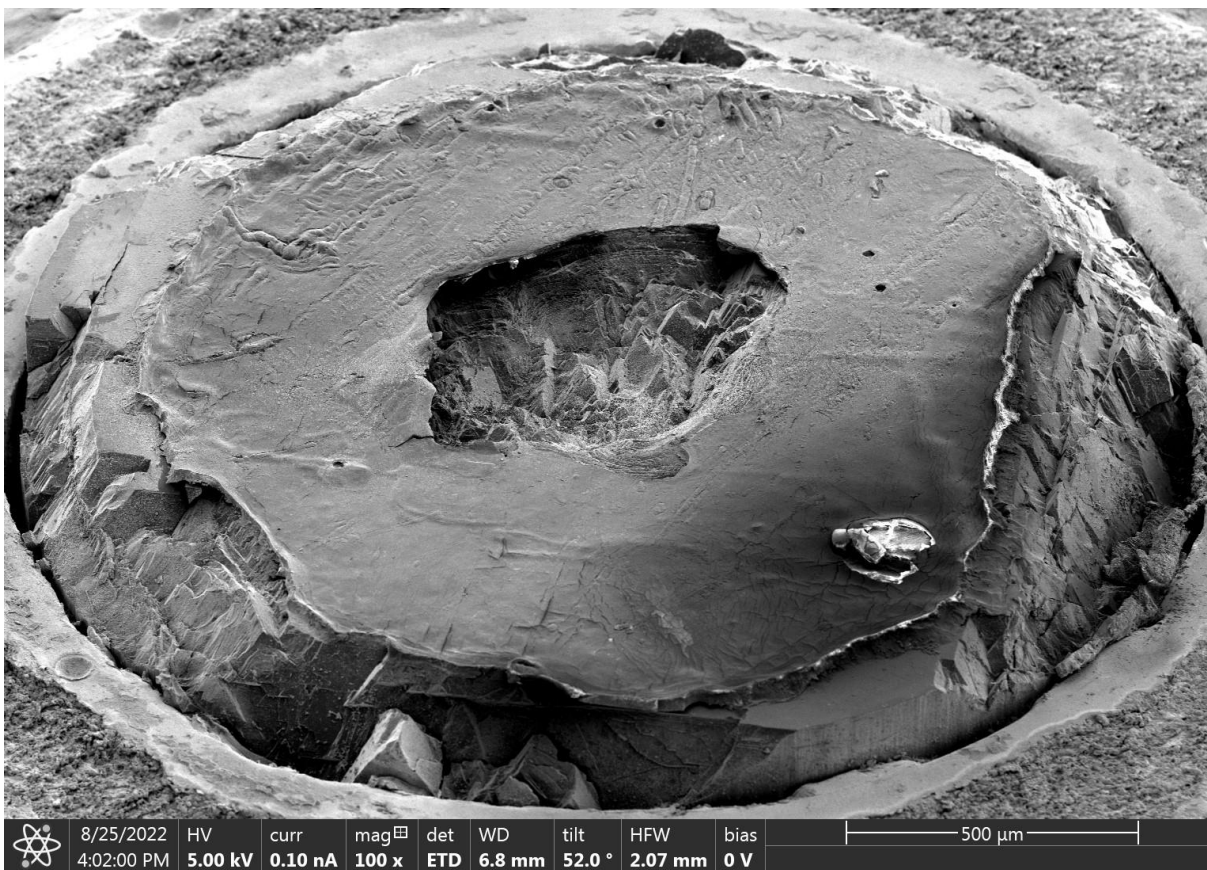


Figure 4-15 400J Diamond 3 sample shot. Crater in the middle, with an amorphous film on the top surface.

FIB-SEM was successful in preparing several samples of the surface of this diamond sample, showing that the material present was indeed amorphous in nature, with diffuse rings shown in the diffraction pattern of the material as seen in Figure 4-16. However, it is still inconclusive whether this is a result of the laser shock pressure driving an amorphization of the sample, or whether this could have been a contamination or reaction from a different source. Further testing is ongoing, involving attempts to create a cross section of the diamond sample to observe how deep the layer goes and whether dislocations could be present underneath the surface of the topmost layer.

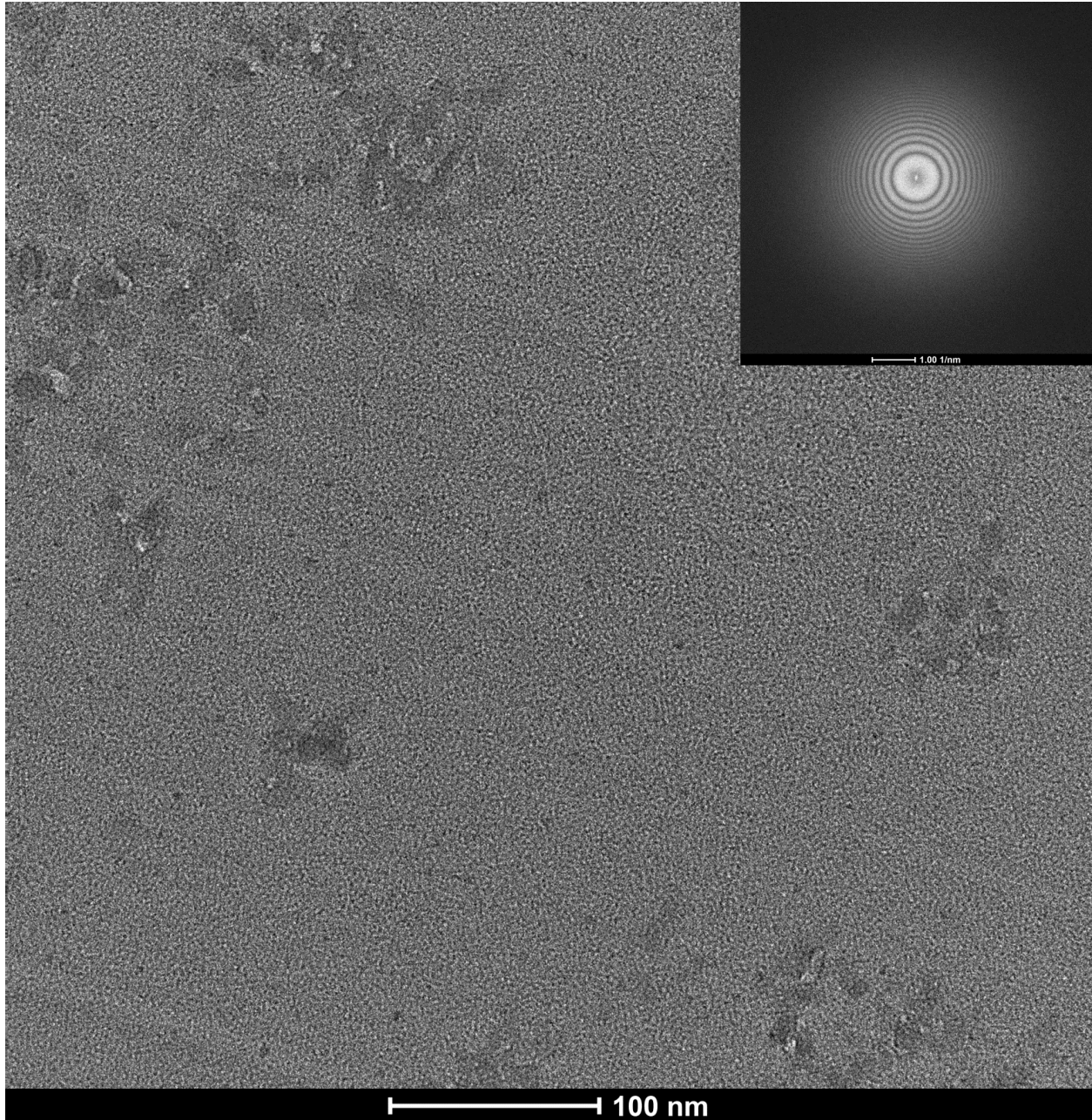


Figure 4-16 Sample of Amorphous surface and diffuse ring pattern from the diffraction.

#### 4.7 Diamond Capsules at the NIF

One of the reasons for the increased interest in diamond in the past decade is its use as the capsule material in the National Ignition Facility fusion shots. The materials and design for the capsule have gone through many iterative improvements before reaching the net gain of energy shot in December 2022. The first capsules were made of plastic with a tent-like wrap to hold the

capsule within its hohlraum shell (20, 297). The switch to diamond ablaters reduced sensitivity to the tent's perturbations due to its higher density as well as improving symmetry by allowing shorter laser pulses to be used. The December 5<sup>th</sup> shot managed to couple 2.05 MJ of energy into the target capsule and produced energy of 3.15 MJ out. This shot has since been exceeded on July 29, 2023, where the use of a higher quality diamond capsule achieved 3.88 MJ of fusion energy (297).

The current capsule design is called the Hybrid-E design. A depleted uranium hohlraum, or cylindrical shell, 11.24mm in length and 6.4mm in diameter, is heated by lasers to >300 eV creating a radiation oven. The diamond capsule, 1050 $\mu\text{m}$  inner radius and 85 $\mu\text{m}$  thick, contains the DT fuel, a 65 $\mu\text{m}$  thick ice layer with a gaseous core. The x-rays from the hohlraum heat and ablate the diamond which expands outwards, while causing the remaining capsule and fuel to accelerate inwards at velocities reaching 400 km/s.

The uniformity of the diamond capsule used in the July 29 shot was the reason it performed so well. The presence of tungsten-carbide chunks along the doped layer of the diamond shell caused some degradation of the initial December 5<sup>th</sup> shot. The July 29<sup>th</sup> shot was actually predicted to have worse symmetry, but still performed better due to the quality of the capsule.

It is important to note that the capsules used at the NIF are made of polycrystalline diamond, while the research in this dissertation is looking only at single crystalline diamond. The grain size of the capsules at the NIF is not expressly measured, but reports place it in the microcrystalline to nanocrystalline regime. Polycrystalline diamond has grain boundaries which may have a large effect on the evolution of the dislocations present, possibly providing an alternate pathway for the shock wave energy to dissipate. Grain boundaries can provide obstacles to the growth of dislocations but may also be the source for dislocations to grow from. The randomized orientation of polycrystalline samples also means that in general, no one orientation is dominant.

This also means that the weakest orientations are likely to be present and may be the limiting grains where defects or dislocations first begin to emerge. As such, it is still valuable to identify the effects of orientation and possible defects in single crystalline samples. Further simulations beyond those presented in Chapters 5 and 6 could look at the effects of grain boundaries on dislocation evolution from a void. Figure 4-17 shows a possible setup for such a simulation, with 3 different grains present oriented in the [001], [011], and [111] directions, with grain boundaries between each.

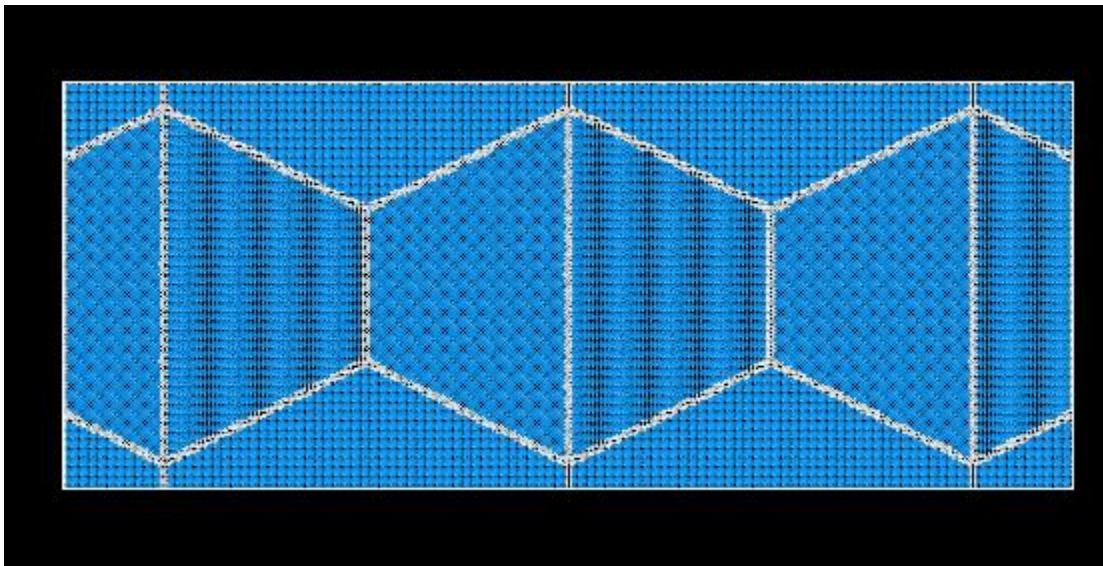


Figure 4-17 A polycrystalline diamond sample. Alternating grains of [001] and [111] oriented diamond are present in the center, bounded by [011] grains at the tops and bottoms. A void placed in the center of the [111] grain would be affected by the presence of the grain boundaries surrounding it.

## 4.8 Acknowledgments

Chapter 4, in part, is in preparation for submission for publication: A.C. Li, B. Li, R.E. Rudd, E.M. Bringa, F. Gonzalez, and M.A. Meyers, Diamond Under Extremes, (2024). The dissertation author was the first and corresponding author of this article.

Chapter 4, in part, is in preparation for submission for publication: B. Li, A.C.Li, M.A.Meyers, Shock Compression of [100] diamond using pulsed lasers. The dissertation author was the second author of this article.

## Chapter 5 Diamond Dislocations and Effects of Voids on Shocked Diamond

Diamond is, by virtue of its high bonding forces and Peierls-Nabarro barrier stresses, among the hardest materials on earth. This extreme hardness is a direct consequence of the difficulty to generate and move dislocations. Thus, dislocations are rarely formed under conventional deformation and extreme regimes of loading are required. Here we demonstrate, using molecular dynamics and analytical calculations, that the generation of defects is highly dependent on the loading orientation. Shock loading single-crystal diamond along [001] and [011] to a shock stress of 137 GPa did not reveal dislocations. On the other hand, loading along [111] generated profuse dislocations at this shock stress, and at even lower stresses down to 72.6 GPa when a nanoscale void was introduced. Two slip systems were identified:  $\langle 011 \rangle \{100\}$  and  $\langle 112 \rangle \{111\}$ . These results demonstrate that the threshold for plastic deformation in diamond is orientation dependent and significantly lower than reported in previous diamond studies as a fraction of the shear modulus: 0.14 G. While no dislocations were formed in [001] loading, in the case with a void its collapse generated localized amorphization, demonstrating that the full elastic-plastic transition requires not only shock stress but superposed shear. These results on the anisotropy of plasticity and effect of voids have relevance for the improvement of symmetry in the collapse of diamond capsules in inertial fusion experiments.

### 5.1 Introduction

Diamond carbon is one of nature's strongest naturally occurring materials. In spite of the low atomic packing factor for diamond cubic systems, the immense strength of the carbon-carbon bonds and the related limitations on dislocations gives diamond extreme hardness and stiffness (298, 299). It is a material of great interest in many applications, including the evolving understanding of carbon-rich exoplanets (300–302), as well as in the material for the fuel-holding



capsules used in recent National Ignition Facility (NIF) inertial confinement fusion experiments (20, 303, 304). It is well known, by virtue of its covalent bonding, that the bonds of diamond are highly directional (197). This results in difficulty in the generation and mobility of dislocations within its crystalline lattice. Moreover, diamond also exhibits strong anisotropic behavior depending on the direction of applied stress (262, 296, 305). In many shock compression experiments, diamond has shown little to no plastic behavior until reaching extreme conditions for both pressure and temperature (254, 305, 306).

Understanding the response of diamond under shock is particularly important for its role in the current inertial confinement fusion effort. The diamond capsules used in these experiments hold the tritium and deuterium fuel, and act as ablative material to produce the extremely high pressures and temperatures needed to initiate fusion. Porosity or other imperfections in the diamond can generate instabilities within the inertial confinement process, leading to imperfect compression and a failure to reach the critical conditions required for fusion (307). By better understanding diamond's behavior under shock, the instabilities and their disastrous effects could be eliminated.

A study of compression of diamond nanopillars with in-situ TEM found a lack of activity when compressed in the [100] direction, but profuse dislocation generation in the [110] and [111] directions (262). An image showing the dislocations and their character can be seen in Figure 5-1. The compression of diamond nanospheres also gives evidence of the effects of nanostructure morphology on defect generation (308). It is well known that voids can act as stress concentrators, lowering the critical stress necessary for the development of dislocations and defects in materials (45, 309, 310), and that small-grained industrial diamond is commonly under-dense.

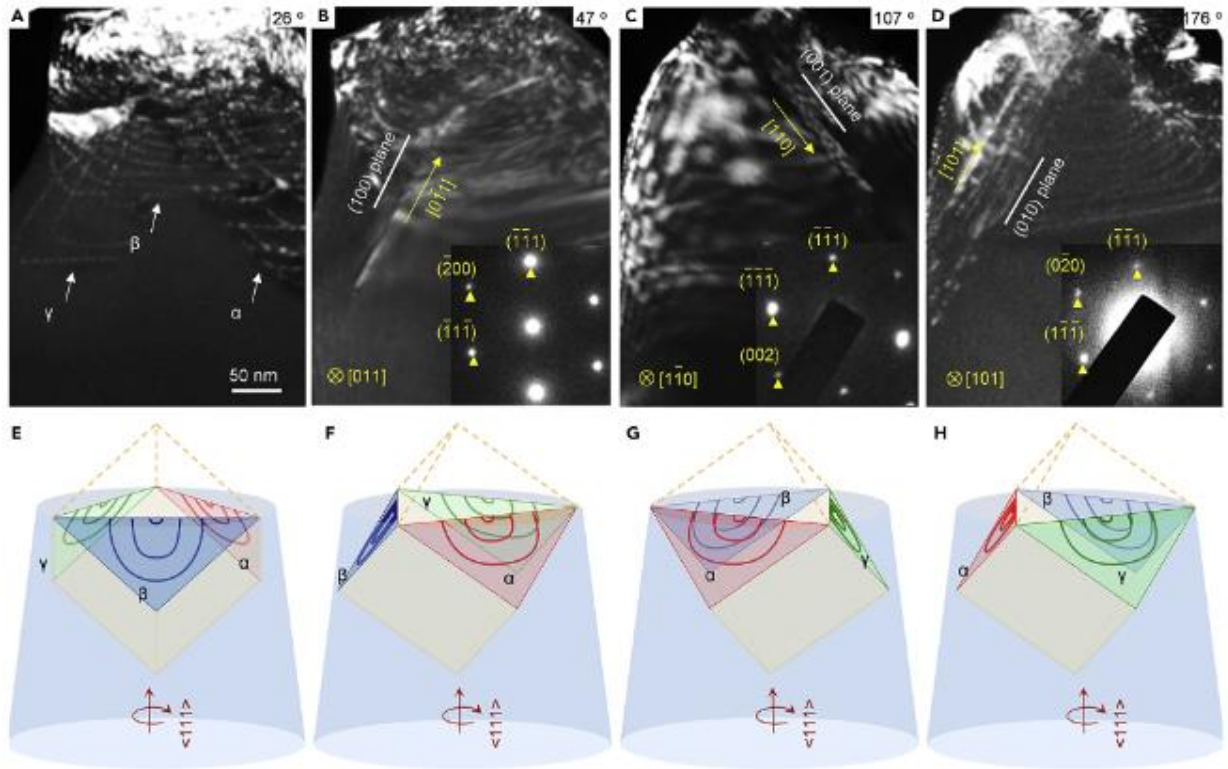


Figure 5-1 Anisotropy of the dislocation response to compression of a diamond nanopillar. Taken from (262)

The molecular dynamics study supplemented by analytical calculations reported here had as primary objective the characterization of defects introduced by high strain rate compressive shock stresses. When shock wave compression produces extremely high strain in uniaxial strain, more conventional modes of deformation or failure can be suppressed. This is the regime experienced by capsules in the National Ignition Facility experiments and by diamond in other ablation experiments. The uniaxial strain state also produces alternate stress states compared to classic uniaxial stress compression, which can alter the types of dislocations generated within the material. In order to generate defects in this study, the applied loading direction was varied; voids were also introduced in order to increase the local shear stresses in an effort to propitiate conditions

for defect generation in diamond-like carbon. Indeed, the voids often occur in experiments and can affect the symmetry of capsule collapse.

## 5.2 Simulation Results

We performed molecular dynamics (MD) simulations on three orientations of diamond under shock compression. Here and below “diamond” refers to carbon in the diamond-cubic structure. It has been shown (262, 296, 311) that diamond has a strong anisotropic behavior, and this stimulated our exploration of the three loading directions [001], [110], and [111]. Shock compression was applied because this is the regime experienced during impact events. Shock compression generates a state of uniaxial strain, in contrast with conventional compression loading, which generates a state of uniaxial stress. The piston velocities, shock pressures, and stresses imposed are provided in Table 1.

Table 5-1 - Loading Orientations, Piston velocities, global pressure, and shock/transverse/shear stresses (GPa) for the simulations presented in this paper.

Loading Orientation	Piston Velocity	Global Pressure	$\sigma_{33}$	$\sigma_{11}$	$\sigma_{22}$	$\tau_{max}$	$\tau_l$
[001]	3.5 km/s	137 GPa	267	72.3	72.3	97.6	196
[011]	3.5 km/s	123 GPa	272	83.1	14.3	129	260
[111]	2.0 km/s	54.2 GPa	145	9.49	8.05	68.6	133
[111]	2.5 km/s	72.6 GPa	188	15.8	13.5	87.5	171
[111]	3.0 km/s	91.4 GPa	226	25.6	23.0	101	198
[111]	3.5 km/s	119 GPa	266	50.3	40.2	113	223

### 5.2.1 Shear Stresses Generated in Shock Compression

The maximum shear stress for uniaxial strain compression along the  $x_3$  direction is (45, 309),

$$\tau_{max} = \frac{|\sigma_3 - \sigma_1|}{2} \quad (1)$$

where  $\sigma_3$  and  $\sigma_1$  are the largest and smallest principal stresses, respectively. For the case of stress localization at the surface of a void, using the equation for a spherical inclusion (312) the maximum local shear stress ( $\tau_l$ ) is

$$\tau_l = \left[ 1 + \frac{13 - 5\nu}{2(7 - 5\nu)} \right] \tau_{max} \quad (2)$$

where the Poisson ratio  $\nu$  for uniaxial strain, defined as the ratio of lateral ( $\varepsilon_{11} = \varepsilon_{22}$ ) and longitudinal strain ( $\varepsilon_{33}$ ) can be written as

$$\nu = \frac{\sigma_{11}}{\sigma_{33} + \sigma_{11}} \quad (3)$$

because under uniaxial strain:

$$\varepsilon_{11} = \varepsilon_{22} = 0 = \frac{1}{E} [\sigma_{11} - \nu(\sigma_{33} + \sigma_{22})] = \frac{1}{E} [\sigma_{22} - \nu(\sigma_{33} + \sigma_{11})] \quad (4)$$

Previous work has shown that the addition of voids can aid in defect generation, including dislocations. This effect is due to the fact the presence of a void increases the shear stresses in selected places in the surface. The normal stress at the void surface is zero (traction free), generating maximal shear stresses at 45° to it. This was quantified by Traiviratana et al. (313), Bringa et al. (314), and Flanagan et al. (309, 310), among others (42, 315–319). Thus, an 8-nm diameter void was introduced in our simulations in order to increase the local stresses within our simulation and stimulate the generation of defects in diamond.

### 5.2.2 Simulations of Shock Compression in [001] Oriented Diamond

For the case of a piston driving the [001] sample at 3.5 km/s, the total pressure (P) within the system reached 137 GPa, with a shock stress ( $\sigma_{33}$ ) of 267.4 GPa in the direction of loading ( $x_3$ ) and 72.26 GPa in the transverse directions ( $\sigma_{11}, \sigma_{22}$ ). Applying Equation 1, a maximum bulk (global) shear stress ( $\tau_{max}$ ) of 97.5 GPa is obtained. The Poisson's ratio  $\nu = 0.2132$  is obtained from Equations 2 and 3; thus,  $\tau_l = 195.5$  GPa, or almost exactly a factor of two higher than the maximum bulk shear stress.

In the [001] direction, little to no dislocation activity is observed (Figure 1a). The diamond structure identification algorithm in OVITO<sup>31</sup> shows that some areas of elastic compression change local coordination by amounts enough to register as only first or second nearest neighbor crystalline diamond, but no defects or dislocations are formed or propagated. For the {001} slip systems observed by Nie et al. (262) for diamond, the resolved shear stress for the [001] loading direction is 0. It will be shown in the analysis section that the resolved shear stress for {100} slip is zero. Highly unusual for a cubic crystal, this characteristic helps explain the lack of defect generation. The introduction of a void did not generate dislocations in this orientation. Only some amorphization of material was observed, an irreversible transformation due to the extreme deformation involved in the collapsing void (Figure 5-2b). This lack of defect generation for shock in the [001] direction of diamond is supported by TEM results taken for diamond shocked up to 40 GPa in pulsed laser shock compression experiments, as seen in section 4.6. A sample of a shock script run on LAMMPS can be found in the Appendix.

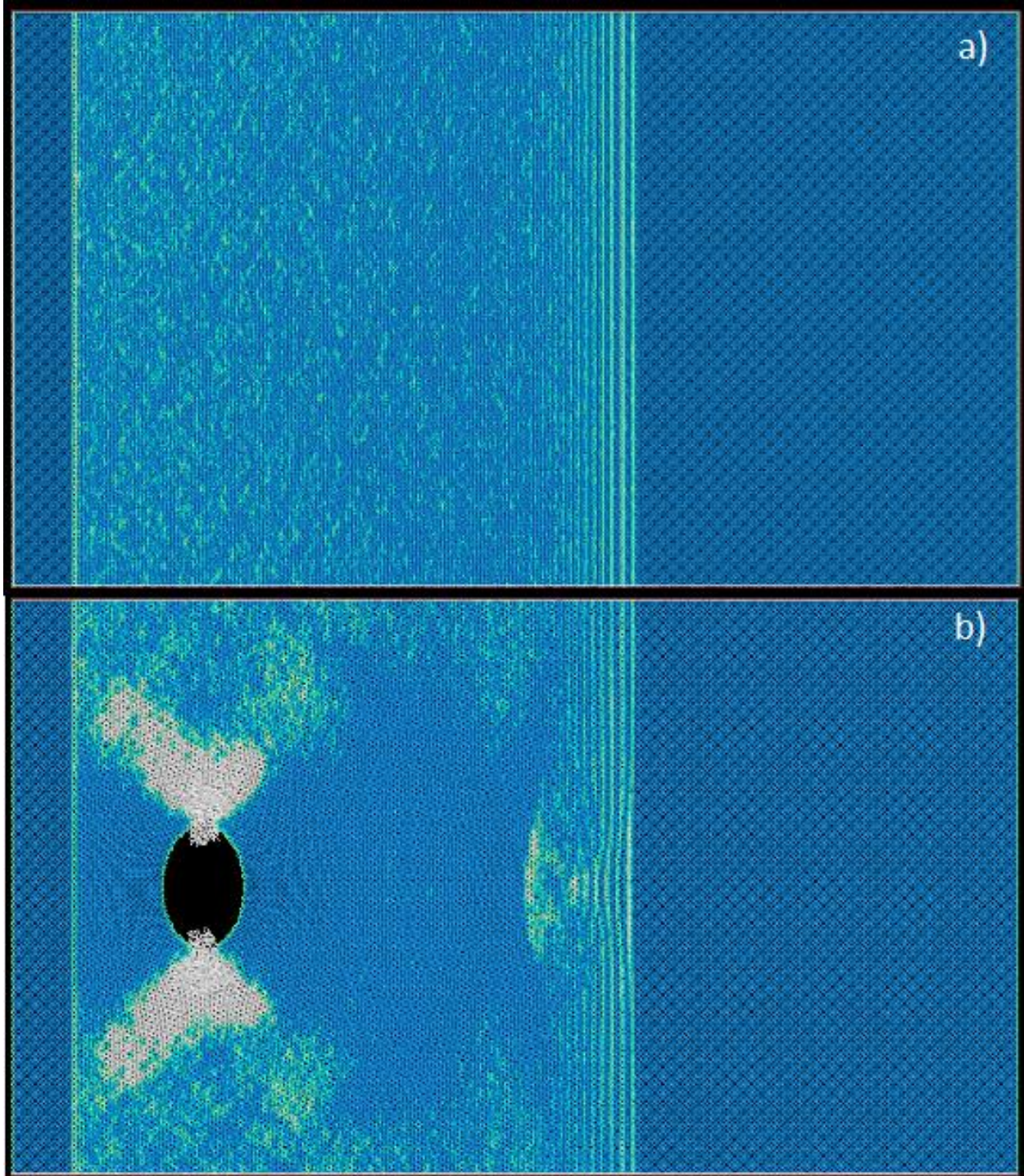


Figure 5-2 137 GPa simulation (3.5 km/s piston velocity) for [001] shock loading direction. Blue color indicates perfectly matched diamond structure, green indicates first or second nearest neighbor diamond cubic, and white indicates a non-diamond structure. a) In the absence of a void, no dislocations or non-diamond regions can be seen under these shock loading conditions. b) With a void there is a region of crystallinity that OVITO does not recognize as diamond cubic, but it is simply compressed beyond the ability for the algorithm to categorize it as such. No lasting dislocations or defects form from the void, though some material jetted into the void.

### 5.2.3 Simulations of Shock Compression in [111] Oriented Diamond

Simulations performed on diamond with the shock propagation direction oriented along its [111] axis yielded defects at pressures where little to no activity was observed for the [001] shock propagation direction. In the absence of a void, planar defects emerged from the piston impact surface creating dislocations in the {100} planes with  $\frac{1}{2} \langle 110 \rangle$  Burgers vectors. As these dislocations advance, they leave planar stacking faults in their wake, with a constant width bounded by a screw-character dislocation with the same Burgers vector (Figure 5-3).

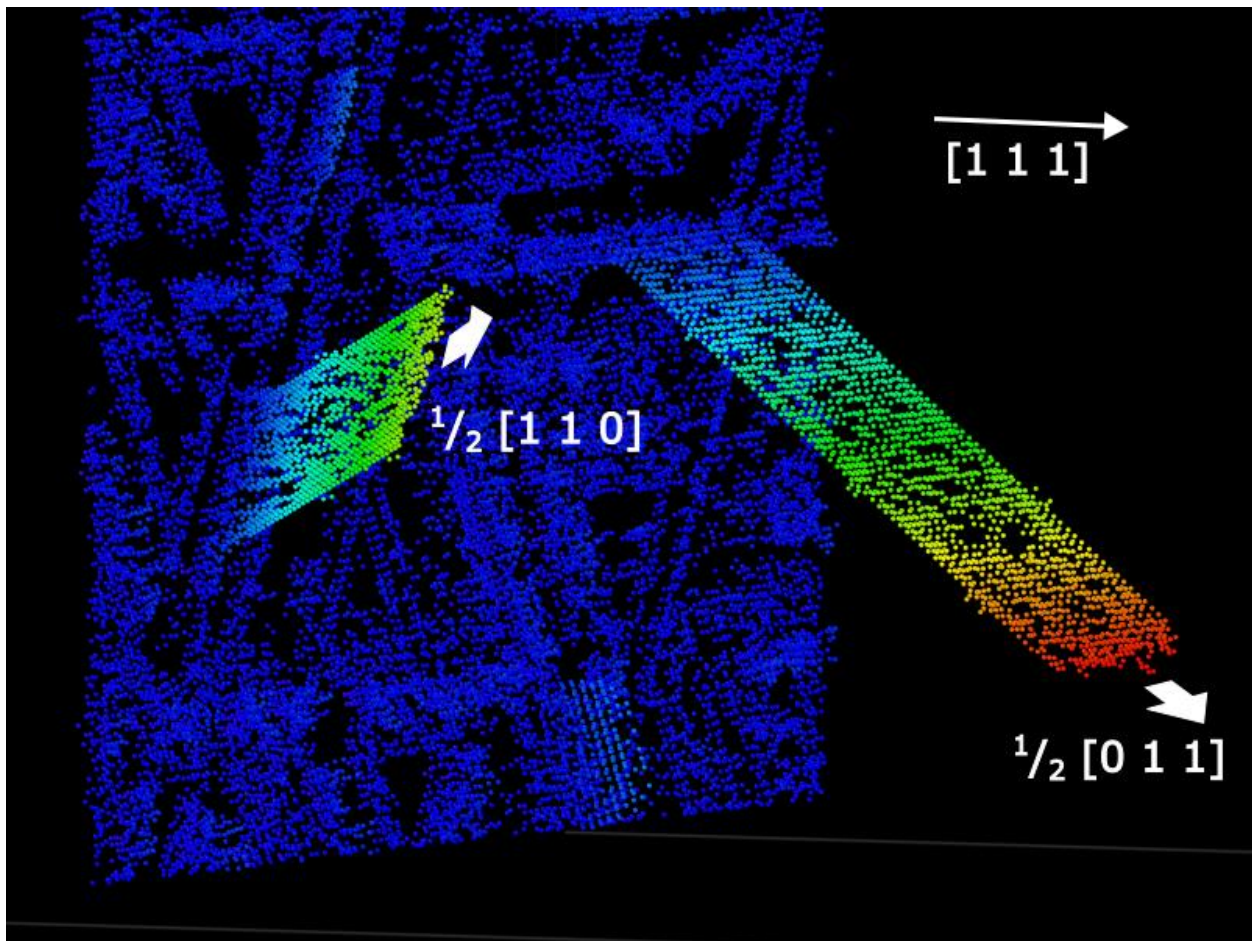


Figure 5-3 Simulation of [111] compressed diamond at 91.4 GPa (2.5 km/s piston velocity) 5 picoseconds into the simulation. Two distinct defects can be seen emanating from the piston surface. The orientations of these faults are in the {100} family of planes in the  $\langle 110 \rangle$  directions.

The maximum pressure within the system for the [111] oriented shock propagation direction at a pressure (piston velocity of 3.5 km/s) is 118 GPa, with corresponding values of  $\sigma_{11} = 50.3$  GPa,  $\sigma_{22} = 40.2$  GPa, and  $\sigma_{33} = 266.0$  GPa. Applying Equations 1 through 3, a maximum shear stress of  $\tau_{sg} = 129.1$  GPa and  $\tau_{sl} = 302.0$  GPa is obtained. Thus, the presence of the void significantly increases the shear stresses.

In the presence of a void, similar  $\frac{1}{2}\langle 011 \rangle \{100\}$  defects are generated at three points symmetrically around the void, corresponding to the  $\{100\}$  planes. The initial formation of these dislocations from the void can be seen in Figure 5-4. Two views are imaged: a) facing the [111] direction and b) from the side  $[01\bar{1}]$  direction. These are perfect dislocations on  $\{100\}$  planes with  $\frac{1}{2}\langle 011 \rangle$  directions. Five of the six systems activate dislocations. The dislocations emanating from the void surface relax the elastic shear stresses in the region, and thus some systems are inhibited from growing. There is a competition among the dislocations and some advance faster than the others. This is seen all the way to their full development. Two of these move towards the front and three away from it. As the shock progresses, these initial defects are joined by half loops with  $\frac{1}{2}\langle 112 \rangle \{111\}$  Burgers vectors (Figure 5-5). These  $\frac{1}{2}\langle 112 \rangle \{111\}$  half loops are consistent with the sum of the two  $\frac{1}{2}\langle 011 \rangle$  Burgers vectors that they connect. Thus,  $\{111\}$  is also a slip plane, with a Burgers vector  $\frac{1}{2}\langle 112 \rangle \{111\}$ .  $\frac{1}{2}\langle 112 \rangle \{111\}$  seems to be a new superdislocation that has formed as a result of the interaction between the void and the  $\frac{1}{2}\langle 011 \rangle \{100\}$  dislocations emanating from it. A visualization of the shear stress magnitudes resolved on these different slip systems is provided in Figure 5-6. The per atom virial stresses were rotated onto the relevant slip planes, and when comparing the averages of the maximum [100] atomic shear stresses at the void surface with the  $\tau_{max}$ , the stresses around the void were found to be between between 1.6 to 3.4 times higher, as seen in Table 5-2. This stress concentrations matches our expected stress



concentration for an ideal spherical void, and the higher stress concentrations could come from the void's collapse which changes its shape from spherical to a prolate ellipsoid, thus increasing the stress concentration.

Table 5-2 - Stress concentration factors for slip systems comparing the stress at the void surface vs the bulk

Slip System	[011](100)	[101](010)	[110](001)	[112](11 $\bar{1}$ )	[121](1 $\bar{1}$ 1)	[211]( $\bar{1}$ 11)
Stress Concentration	1.64	3.37	2.89	3.22	2.03	3.16

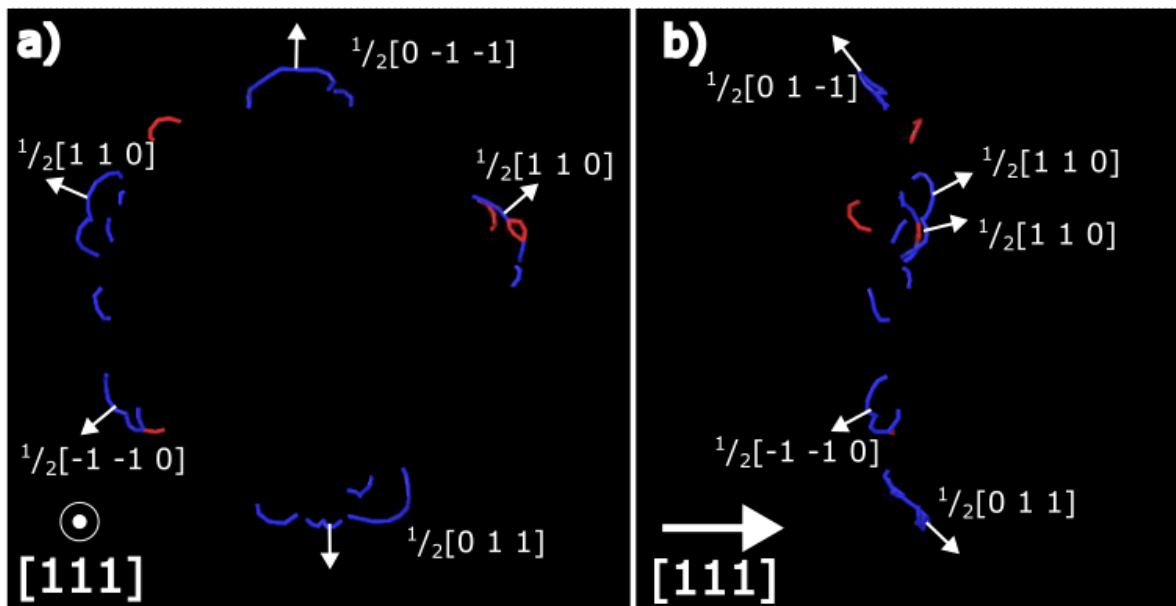


Figure 5-4 Initiation of Defects from the void. Image captured using DXA analysis at 1.5ps in the [111] loading orientation, just as the shock wave has finished passing over the void and the defects have initiated. Several defects can be seen to initiate opposite to the direction of shock. Blue dislocation lines indicate dislocations that lie in the {100} planes. Red dislocation lines are in various other slip systems. a) Viewed facing the [111] direction, shock direction out of the page. b) Viewed from the side [01 $\bar{1}$ ] direction, with shock direction to the right.

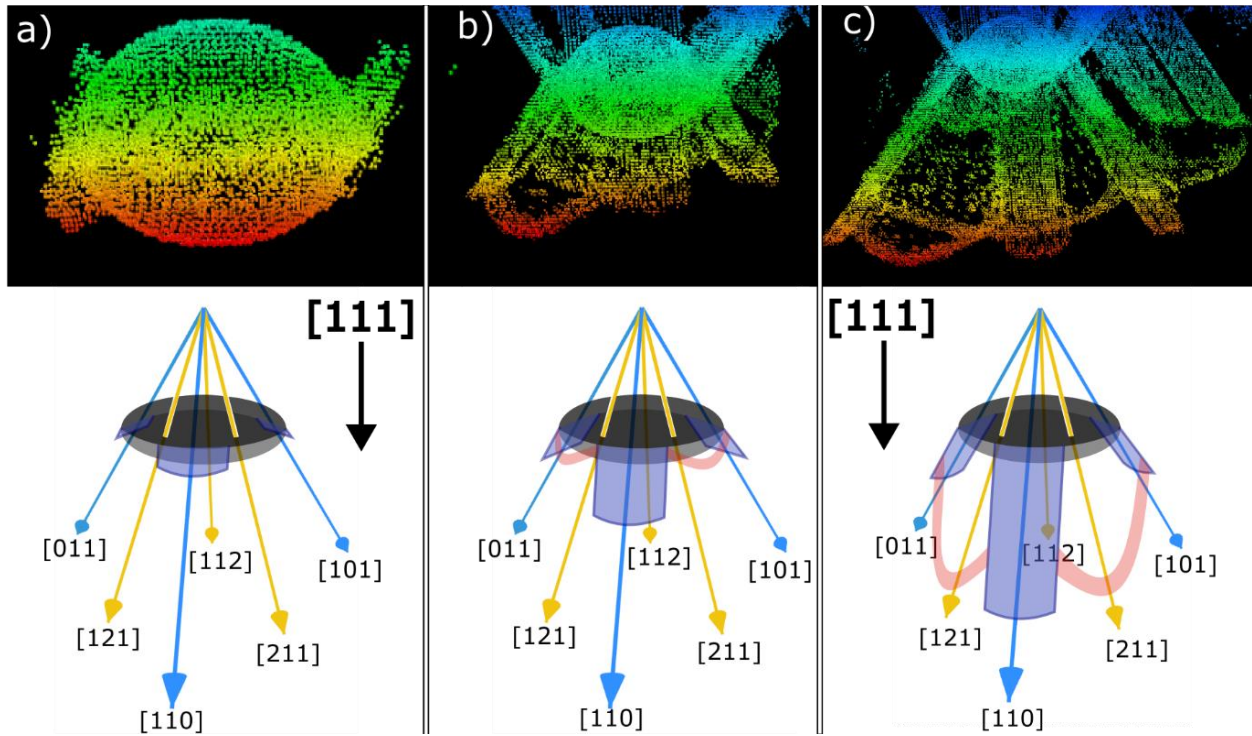


Figure 5-5 Evolution of the defects emanating from the void for  $[111]$  loading orientation. The three-fold symmetric straight bands are the same as the bands seen in the case without a void present,  $\langle 110 \rangle$  direction in the  $\{100\}$  plane. In addition, loops with Burgers vector  $1/2\langle 112 \rangle$  appear on the  $\{111\}$  planes between these 3 straight bands. While the straight  $\langle 110 \rangle$  defects leave behind a stacking fault, the  $\langle 112 \rangle$  dislocations do not. a) 1 ps b) 2.5 ps c) 4 ps.

Interestingly, Pirouz et al. (320), in a systematic transmission electron microscopy study of diamond deformed at  $1,800^\circ\text{C}$ , observed the formation of dislocations on  $\{111\}$  planes. The  $1/2\langle 110 \rangle\{111\}$  dislocations decomposed into partials with a separation of  $\sim 4$  nm, from which the stacking-fault energy could be calculated. The three-fold symmetry of these stacking faults and half loops is reminiscent of the results obtained by Nie et. al. (262) in their nanopillar experiments, with the rectangular stacking faults consistent in plane and direction with the  $\{100\}$  half-loops that they found. However, the presence of the  $1/2\langle 112 \rangle\{111\}$  dislocation is a new feature in this shock compression MD study. The DXA analysis on the defects within the simulation was performed in OVITO (105) was used to determine the location and Burgers vector of these dislocations (Figure 5-7).

Exploring further, [111] simulations were performed at several different piston velocities to obtain information on the threshold of dislocation generation with and without voids. The 2.0 km/s piston velocity generates a maximum total pressure of 54.2 GPa, with maximum bulk shear and local shear stresses of  $\tau_{sg} = 68.6$  GPa and  $\tau_{sl} = 133.4$  GPa respectively. At 2.5 km/s the maximum total pressure is 72.6 GPa, with maximum bulk and local shear stresses of  $\tau_{max} = 87.5$  GPa and  $\tau_l = 170.6$  GPa respectively. At 3.0 km/s the maximum total pressure is 92.4 GPa, with maximum bulk and local shear stresses of  $\tau_{max} = 101.3$  GPa and  $\tau_l = 198.4$  GPa respectively.

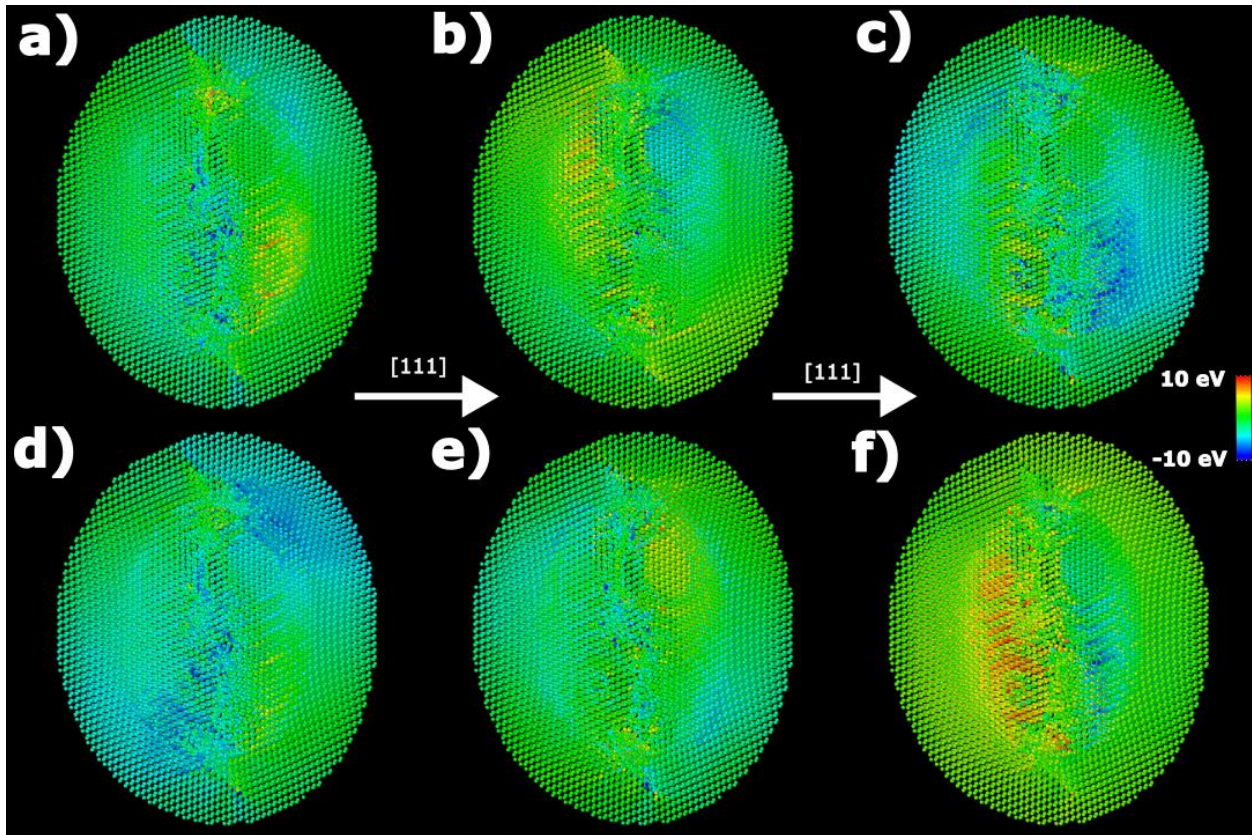


Figure 5-6 Resolved Shear Stresses along different slip systems. A sphere was formed around the void with a 6nm radius, and per atom stress values were taken after the shock wave had passed through the void and dislocations just began to form. The different resolved shear stresses show the directional differences in the stress concentrations for the different slip systems, which may result in the formation of dislocations. The color scale on the right indicates the magnitude of the stress being experienced by the atoms, with red and blue indicating the two extremes. a) [011](100) b) [101](010) c) [110](001) d) [112](11 $\bar{1}$ ) e) [121](1 $\bar{1}$ 1) f) [211]( $\bar{1}$ 11)

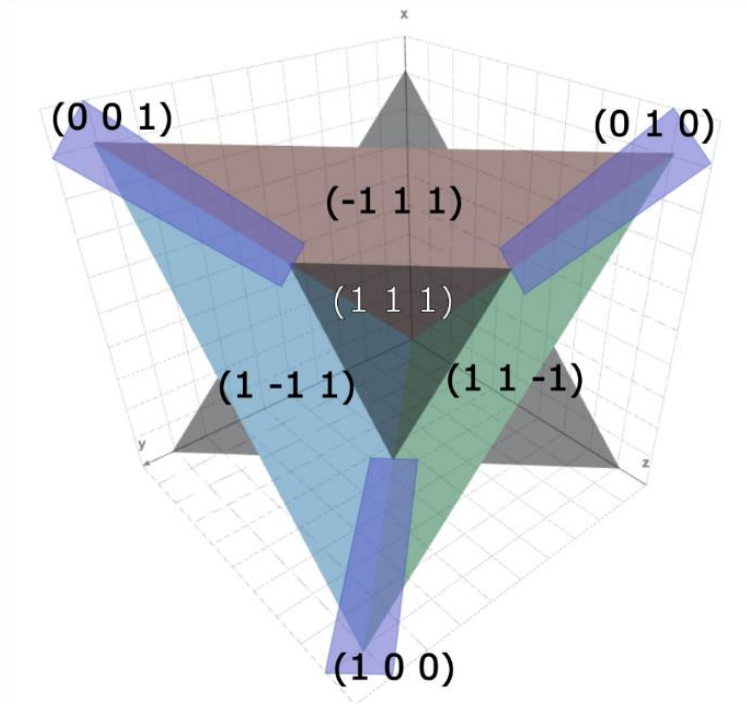
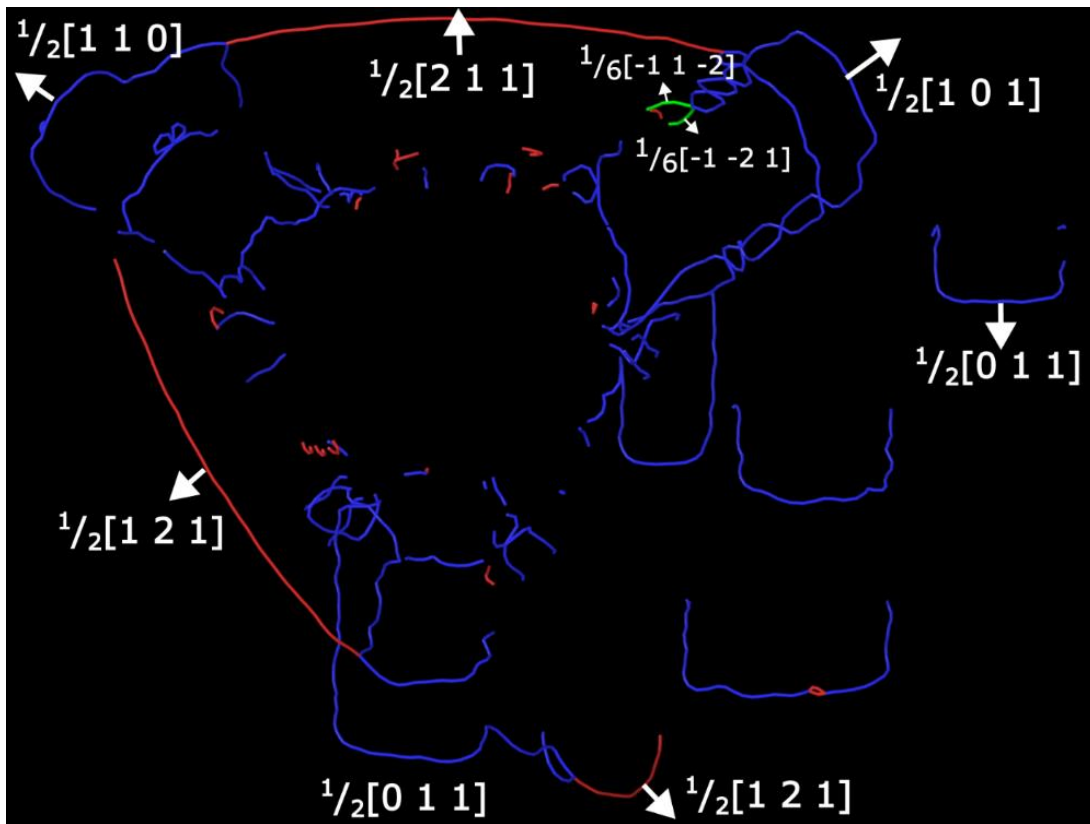


Figure 5-7 Dislocations around a void. a) DXA dislocation and defect analysis of the [111] shocked diamond system at 3.25 ps. b) A graphical representation of the planes and orientations of the system. The rectangular bands propagate within the {100} planes, while the half-loops connecting them are present along the {111} planes.

At 52.4 GPa (2.0 km/s piston velocity), and in the absence of a void, no defects are generated at the planar impact surface (Figure 5-8a). When a void is introduced, the onset of  $\frac{1}{2}\langle 110 \rangle \{100\}$  dislocations can be seen emerging from the compressed void (Figure 5-8b). From this emission it is concluded that the presence of a void or other defect generation site can significantly lower the threshold for dislocation activity and the beginning of plasticity within diamond, depending on its orientation. This effect has been previously analyzed and quantified by Traiviratana et al.(313), Bringa et al. (314), and Flanagan et al. (309, 310) for other materials and is a direct consequence of the increased maximum shear stress generated by the presence of a void. The threshold stress is also dependent on void size, as has been demonstrated (45). This dependence is due to the image forces produced by the free surface of the void, proportional to the curvature (inverse of radius). As the pressure is increased to 72.6 GPa (piston velocity of 2.5 km/s), the defect generation from both the planar impact surface and the compressed void increase rapidly. At 91.4 GPa (3.0 km/s), defect generation was even more pronounced.



Figure 5-8 54 GPa (2 km/s piston velocity) simulation for [111] diamond shock at 10 ps. a) A view of all atoms within the system with coordination number other than 4, the usual value for diamond. No atoms beyond the piston surface are detected, i.e., all are diamond. b) The beginnings of dislocations can be seen to form when a void is present and shocked, but never begin to propagate within the system.

Measurements of the elastic wave and defect propagation velocities indicate that the defects within the simulations approach the shear wave velocity limit of diamond (Figure 5-9), without exceeding it. Shear wave velocities were calculated directly from the Tersoff potential as

$$\sqrt{\frac{G}{\rho}}$$

where  $G$  is the relevant shear modulus for the shear wave direction and polarization, and  $\rho$  is the density in the compressed state. For the three orientations of interest,  $G$  is  $C_{44}$  for  $\langle 001 \rangle$  (both polarizations),  $C'$  and  $C_{44}$  for  $\langle 110 \rangle$  and  $C_{111}$  for  $\langle 111 \rangle$  (both polarizations). Here  $C' = (1/2)(C_{11} - C_{12})$  and  $C_{111} = (2C' + C_{44})/3$ . The wave velocities compare favorably with those taken from literature (321). As the pressure is increased, the dislocation velocity also increases, without reaching the shear-wave velocity. This is in line with the expected relativistic behavior of fast

dislocations, whose energy increases with velocity. Partial dislocations, on the other hand, are known to sporadically exceed the shear wave velocity, but only for picoseconds (322, 323), and transonic dislocations have been observed in special cases in MD simulation but not yet in experiment (107).

### Propagation velocities within shocked <111> Diamond

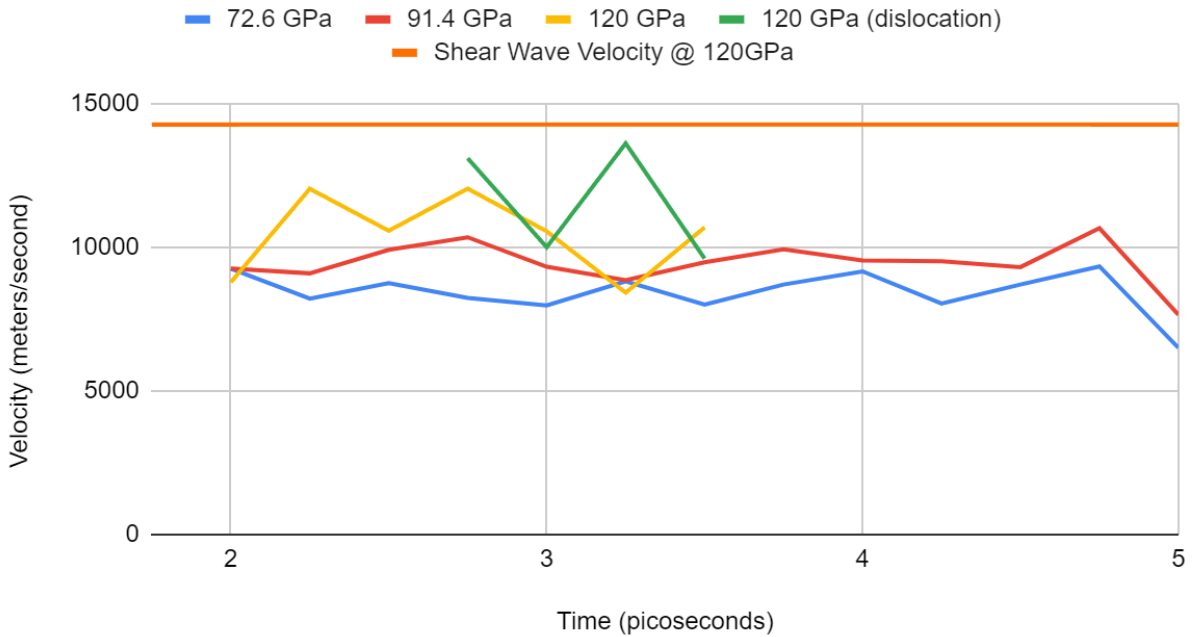


Figure 5-9 Defect propagation velocity at varying simulation pressures and piston velocities (72.6 GPa = 2.5 km/s, 91.4 GPa = 3 km/s, and 123 GPa = 3.5 km/s). An additional measurement was made at 120 GPa (3.5 km/s) corresponding to the green line, measuring the propagation velocity of a dislocation. Shear wave velocity calculated for carbon at 120 GPa using Tersoff potential.

### 5.2.4 Simulations of Shock Compression in [011] Oriented Diamond

When simulating [011] oriented diamond without a void, no plasticity was observed, as in the [001] oriented diamond. No defects formed from the piston surface or within the bulk simulation at a pressure of 123 GPa (piston velocity 3.5km/s), with values of  $\sigma_{11} = 83.1$  GPa,  $\sigma_{22} = 14.3$  GPa, and  $\sigma_{33} = 272$  GPa. However, the presence of a void triggers the formation of a dislocation loop in the  $\frac{1}{2} \langle 112 \rangle \{ 111 \}$  system but lacks the  $\frac{1}{2} \langle 110 \rangle \{ 001 \}$  dislocations that might have been expected to form (Figure 10). There is still significantly more dislocation activity present than in the [001] case, and the presence of large  $\langle 112 \rangle$  oriented defects may be explained by the large resolved shear stress for the  $[211](\bar{1}11)$  slip system. While there was a high population of non-diamond atoms within the [011] oriented system, the DXA algorithm was not as able to conclusively identify the presence of large and sustained dislocation loops as observed in the [111] oriented system.

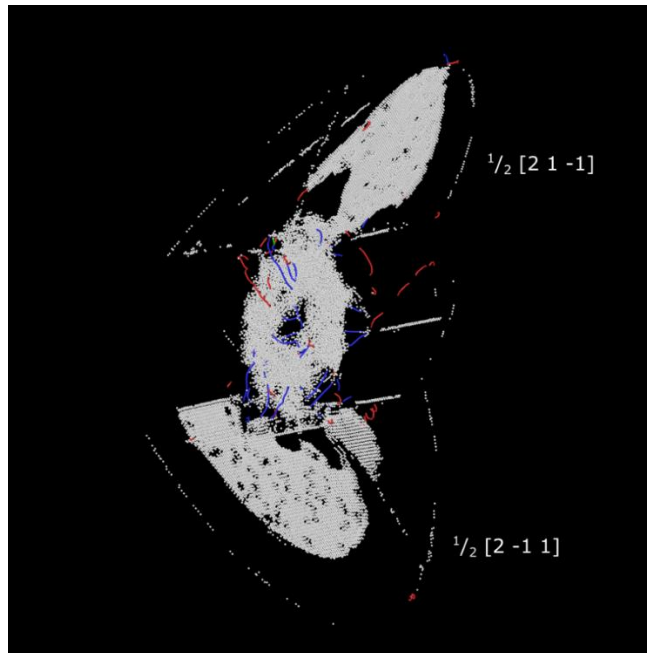


Figure 5-10 Non-diamond atoms and DXA analysis for [011] shocked diamond at 2.5 ps. The defect bands emanating from the void are oriented in the  $\frac{1}{2} \langle 112 \rangle$  directions, and are semicircular in shape as they expand away from the void surface.



## Analysis: Calculation of Resolved Shear Stresses on the Slip Systems

The generation and motion of dislocations is driven by the shear stresses applied to the slip systems. The direction of maximum shear forms a cone  $45^\circ$  away from the direction of shock propagation, and the slip systems most closely aligned with this maximum shear experience the highest resolved shear stress (94). These calculations have traditionally been done using the Schmid factor and, in the simplified case, assuming isotropy in the elastic properties of materials. We conduct here a more rigorous analysis which accounts for the uniaxial strain state produced by shock compression and the anisotropy of the elastic stiffness matrix of diamond. When transforming the stiffness tensor to the [111] orientation and applying a condition of [111] uniaxial strain, values are obtained for all 6 components of the stress within the system. A similar procedure is followed for the [001] orientation. The presence of these shear stresses drives the 3-dimensionality of the defects and dislocations observed in our diamond simulations. This is presented below.

Dislocation generation and motion is driven by shear stresses. The general form of the resolved shear stress on a slip plane is given as

$$\begin{aligned} \sigma_{1'2'} = & \sigma_{11}l_{1'1}l_{2'1} + \sigma_{22}l_{1'2}l_{2'2} + \sigma_{33}l_{1'3}l_{2'3} \\ & + \sigma_{12}(l_{1'1}l_{2'2} + l_{1'2}l_{2'1}) + \sigma_{23}(l_{1'2}l_{2'3} + l_{1'3}l_{2'2}) + \sigma_{13}(l_{1'3}l_{2'1} + l_{1'1}l_{2'3}). \end{aligned} \quad (5)$$

The cosine matrix  $l_{ij}$  is used, where the values are defined as the direction cosines of the loading coordinate system and the coordinate system defined by the slip direction, slip plane normal, and normal to slip direction in the slip plane. The angles between directions are calculated by the scalar product of vectors (324). The rotation matrix is

$$l_{ij} = \cos(\vec{e}_i', \vec{e}_j) = \begin{bmatrix} l_{1'1} & l_{1'2} & l_{1'3} \\ l_{2'1} & l_{2'2} & l_{2'3} \\ l_{3'1} & l_{3'2} & l_{3'3} \end{bmatrix} \quad (6)$$

where  $\bar{e}_i'$  is the new rotated coordinate system and  $\bar{e}_j$  is the old coordinate system.

For a state of uniaxial stress, the resolved shear stress ( $\tau_r$ ) on the slip plane and slip direction is calculated through the well-known Schmid factor ( $m$ ):

$$\tau_r = m\sigma_{33} \quad (7)$$

$$m = \cos(\lambda)\cos(\phi) \quad (8)$$

where  $\lambda$  and  $\phi$  are the angles between the loading direction and the vector along the slip direction and the vector normal to the slip plane respectively. For the Schmid factor,  $\cos(\lambda)$  and  $\cos(\phi)$  correspond to  $l_{1'3}$  and  $l_{2'3}$  respectively. Because in this case there are no lateral stresses present, all stress terms other than  $\sigma_{33}$  are zero. In terms of the generalized indicial notation, the shear stress is expressed as:

$$\sigma_{1'2'} = \sigma_{33}l_{1'3}l_{2'3}. \quad (9)$$

While the Schmid factor describes a state of uniaxial stress, for a uniaxial strain state generated by shock compression, lateral expansion is constrained. Thus, in addition to the shock stress generated by the piston, lateral compressive stresses are generated which have to be computed in the calculation of the resolved shear stresses. Figure 5-11 shows a unit cube subjected to tridimensional compression and the relationship of the slip system (plane and direction) with the cube coordinate axes, which have the  $x_3$  direction aligned with the shock propagation direction. This is done here, following the procedure developed by Lu (93). The first step is to obtain the stiffness matrix for the three orientations by applying a rotation of the stiffness tensor. The elastic stiffness ( $C'_{ijkl}$ ) transformation equation is

$$\mathbf{C}'_{ijkl} = l_{im}l_{jn}l_{ko}l_{lp}\mathbf{C}_{mnop}. \quad (10)$$

A sum over indices repeated on the right-hand side is implied. Each value in the original stiffness tensor is transformed through four cosine matrix values, then summed together to form one element in the rotated stiffness tensor. The values for the tensors in the [001], [011], and [111] directions are provided in Table 5-3.

To calculate the stress in the system from the transformed stiffness tensor, we require the true strain within the deformed material, as

$$\sigma = C\varepsilon. \quad (11)$$

The true strain within the shocked material can be obtained from the Rankine-Hugoniot equations for conservation of mass, momentum, and energy as

$$\varepsilon_{33} = \ln\left(\frac{V}{V_0}\right) = \ln\left(1 - \frac{U_p}{U_s}\right) = \ln\left(1 - \frac{U_p}{C_0 + SU_p}\right). \quad (12)$$

Values for  $C_0$  and  $S$  for diamond are taken from Hicks et al. (324), as 11.9 km/s and 1.01, respectively.

Table 5-3 Transformed Stress Tensors at ~140 GPa with change of basis loading direction. Original values from Orlikowski et al.(325), Güler et al (321), González-Cataldo et al (326)

$C_{[001]} = \begin{bmatrix} 2000 & 500 & 500 & 0 & 0 & 0 \\ 500 & 2000 & 500 & 0 & 0 & 0 \\ 500 & 500 & 2000 & 0 & 0 & 0 \\ 0 & 0 & 0 & 1200 & 0 & 0 \\ 0 & 0 & 0 & 0 & 1200 & 0 \\ 0 & 0 & 0 & 0 & 0 & 1200 \end{bmatrix}$	$\varepsilon = \begin{bmatrix} 0 \\ 0 \\ \varepsilon_3 \\ 0 \\ 0 \\ 0 \end{bmatrix}$	$\sigma_3 = \varepsilon_3 \begin{bmatrix} 500 \\ 500 \\ 2000 \\ 0 \\ 0 \\ 0 \end{bmatrix}$
$C_{[011]} = \begin{bmatrix} 2000 & 500 & 500 & 0 & 0 & 0 \\ 500 & 1550 & 950 & -300 & 0 & 0 \\ 500 & 950 & 1550 & 300 & 0 & 0 \\ 0 & -300 & 300 & 1050 & 0 & 0 \\ 0 & 0 & 0 & 0 & 1200 & 0 \\ 0 & 0 & 0 & 0 & 0 & 1200 \end{bmatrix}$	$\varepsilon = \begin{bmatrix} 0 \\ 0 \\ \varepsilon_3 \\ 0 \\ 0 \\ 0 \end{bmatrix}$	$\sigma_3 = \varepsilon_3 \begin{bmatrix} 500 \\ 950 \\ 1550 \\ 300 \\ 0 \\ 0 \end{bmatrix}$
$C_{[111]} = \begin{bmatrix} 1550 & 650 & 800 & 81.6 & -70.7 & 57.7 \\ 650 & 1550 & 800 & -244 & -212 & -173 \\ 800 & 800 & 1400 & 163 & 282 & 115 \\ 81.6 & -244 & 163 & 700 & -115 & -212 \\ -70.7 & -212 & 282 & -115 & 1100 & -81.6 \\ 57.7 & -173 & 115 & -212 & -81.6 & 1150 \end{bmatrix}$	$\varepsilon = \begin{bmatrix} 0 \\ 0 \\ \varepsilon_3 \\ 0 \\ 0 \\ 0 \end{bmatrix}$	$\sigma_3 = \varepsilon_3 \begin{bmatrix} 800 \\ 800 \\ 1400 \\ 163 \\ 282 \\ 115 \end{bmatrix}$

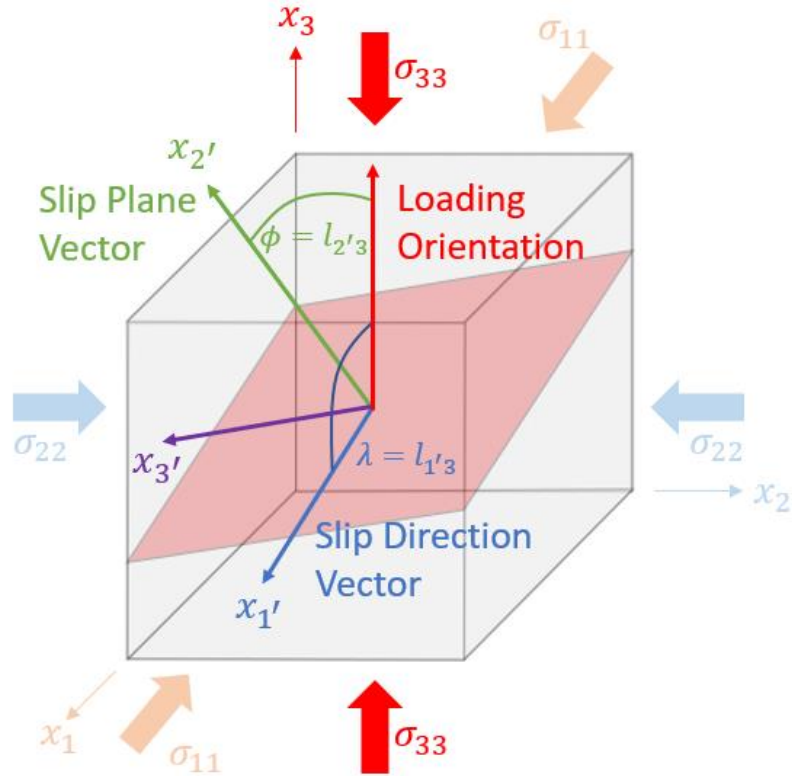


Figure 5-11 Orientation Relationships for Shock Loading and Slip Planes

The resulting shear stress can be normalized to the shock stress to provide the Lu factor:  $m_{Lu} = \sigma_{1'2'}/\sigma_{33}$  in uniaxial strain. In Table 3 the Schmid and Lu factors are presented for the two families of slip systems:  $\langle 211 \rangle \{111\}$  and  $\langle 110 \rangle \{001\}$ . The Lu factor requires knowledge of the strain and shock stress for normalization; the values for the 3.5 km/s simulations were chosen in each orientation.

Table 5-4 Schmid and Lu Factors (resolved shear stress with transformed tensor) for relevant slip systems.

Loading Direction	[Slip Direction] (Slip Plane)	$m$ Schmid Factor (Uniaxial Stress)	$m_{Lu}$ Lu Factor $\frac{\sigma_{1/2'}}{\sigma_{33}}$ (Uniaxial Strain, 3.5 km/s)
[001]	[011](100)	0	0
[001]	[101](010)	0	0
[001]	[110](001)	0	0
[001]	[112](11 $\bar{1}$ )	-0.47	-0.339
[001]	[121](1 $\bar{1}$ 1)	0.23	0.169
[001]	[211]( $\bar{1}$ 11)	0.23	0.169
[011]	[011](100)	0	0
[011]	[101](010)	0.35	0.327
[011]	[110](001)	0.35	0.327
[011]	[112](11 $\bar{1}$ )	0	0.035
[011]	[121](1 $\bar{1}$ 1)	0	0.035
[011]	[211]( $\bar{1}$ 11)	0.47	0.366
[111]	[011](100)	0.47	0.415
[111]	[101](010)	0.47	0.415
[111]	[110](001)	0.47	0.415
[111]	[112](11 $\bar{1}$ )	0.31	0.277
[111]	[121](1 $\bar{1}$ 1)	0.31	0.277
[111]	[211]( $\bar{1}$ 11)	0.31	0.277

Table 5-4 provides the uniaxial stress (Schmid) and uniaxial strain (Lu) factors for the three shock propagation orientations. The Schmid factor is a simple ratio of the stress on the associated slip system with respect to the applied loading direction under the condition of uniaxial stress, a common loading condition in practice and analysis. The Lu factor is similar, giving the same ratio of stress on the slip system to the shock stress but with the uniaxial loading condition appropriate to bulk shocked materials. In the case of uniaxial strain, the system experiences transverse stresses which do not relax since the transverse strain remains zero due to inertial confinement (experiment) or periodic boundary conditions (simulations). These additional stresses lower the shear stress experienced by the slip systems. In the limiting case of hydrostatic loading, where the stress in all directions is equal, there would be no shear stress within the system, whereas the case of uniaxial loading maximizes the shear stress. The condition of uniaxial strain experienced under shock loading lies in between those. For example, in [001] propagation the transverse stress is equal to  $(C_{12}/C_{11})\sigma_{33}$ , so the stress state is a sum of the uniaxial stress  $[1-(C_{12}/C_{11})]\sigma_{33}$  and a hydrostatic pressure. By the same rationale as explained above, multiplying by the Schmid factor gives the resolved shear stress, since the resolved shear stress is independent of hydrostatic pressure. Thus, for [001] uniaxial strain, the Lu factor is  $m_{Lu} = [1-(C_{12}/C_{11})]m$ . In general the Lu factors within Table 5-4 are lower in magnitude compared to the Schmid factors, meaning that the slip systems in shock loading experience less shear stress due to the different loading conditions.

For the  $\frac{1}{2}\langle 110 \rangle \{001\}$  dislocations, the relative values for the Schmid factors and Lu factors are quite close. Notably, the value for the [001] loading case are all 0 for both the Schmid and Lu factors, which explains the lack of dislocation activity in this loading direction. The [011] loading case has similar results for both as well, with two slip systems having non-zero resolved

shear stress. In the [111] direction, all slip systems are active, and this activity is seen in our simulations as well.

For the  $\frac{1}{2}\langle 112 \rangle\{111\}$  dislocations, the [001] loading direction in fact has non-zero values of resolved shear stress for both the Schmid and Lu factors. However, we still see no dislocation activity along these slip systems for the [001] loading case. These dislocations likely have other conditions necessary for them to form, such as a reaction between two different  $\frac{1}{2}\langle 110 \rangle\{100\}$  dislocations present in the other systems but not [001]. In the [011] case two of the Schmid factors are zero, but we still have large activity along one slip system. The corresponding Lu factors are non-zero, but the values in the slip systems corresponding to the zero-stress Schmid factors are still apparently too small to generate dislocations. We observe one slip system in the MD simulations for the [011] loading case, matching what is seen in our simulation. For [111] loading, the Schmid factor predicts equal values for each slip system much like for the  $\frac{1}{2}\langle 110 \rangle\{100\}$  dislocations, and our Lu factors predict the same thing, though with reduced values for the resolved shear stress. However, in our calculation of the resolved shear stress at the void's surface, we found that for the two directions where the half-loop is present, the average stress concentration at the void's surface was over 20 times that of the bulk, whereas for the missing direction it was only 3 times that of the bulk. This difference in the stress concentration along the particular orientation could explain why the final half-loop was missing.

While molecular dynamics simulations are helpful tools for understanding materials behavior and exploring atomistic detail, they are not without limitations. All calculations performed in a simulation are dependent upon the accuracy of the interatomic potential being used. The Tersoff potential used in this paper is an empirical potential and has shown good performance in modelling both mechanical properties as well as dislocations in diamond carbon, but it fails to



produce accurate results when under even higher pressure (>150 GPa) or temperature conditions. While density functional theory simulations provide the highest accuracy available, they are limited to small numbers of atoms due to their computational complexity. Recently, machine learning potentials that are trained on DFT data such as the Gaussian Approximation Potential (GAP) (327) or the Spectral neighbor Analysis Potential (SNAP) (79) have been developed that can simulate higher energy conditions more accurately, but they are still much more costly in terms of computational power required. Another issue with computation power is that because of time constraints on running simulations, larger simulations and longer simulations are both limited. This means that some size effects may be absent as they cannot be captured, and any defects that do not appear within the short time frame of the simulation may be missed. For example, classical molecular dynamics is a bad choice for modelling diffusion activity, which happens on much longer time scales than what is traditionally modelled in these types of simulations. With more computing power available it will be possible to extend both the size and time of our simulations to capture more of the development of how the material reacts to shock. Real diamond could have larger defects or elemental impurities that cannot be captured here, which could further lower thresholds for dislocation activity. Amorphization within diamond is another topic of interest, whose nucleation and growth may not be able to be captured within the time frame used here. However, as computing technology improves and access to faster systems becomes available, these issues may be addressed, leading to longer and larger simulations with more accurate potentials that could fully capture the response of diamond or any other material.

### **5.3 Conclusions**

It is demonstrated that shock compression at pressures in the range of 72.6 GPa can generate dislocations in single-crystal diamond. A significant orientation dependence of defect generation was observed through shock compression MD simulations. While few if any defects

are generated with shock propagation in the [001] direction, significantly more defect activity is observed in the [011] and [111] orientations under the same shock compression conditions. When a void was introduced into the system, even more defects were generated, including novel  $\frac{1}{2}\langle 112\rangle$  superdislocations in the [111] oriented system which formed half loops connecting the three-fold symmetric  $\frac{1}{2}\langle 110\rangle\{001\}$  dislocations formed at the compressed edge of the void. While the  $\frac{1}{2}\langle 110\rangle\{001\}$  dislocations have been experimentally observed before, the influence of voids or similar defect-generation sites may give rise to new dislocation activity such as seen in our simulations and may help us better understand the response of diamond in experiments which may include such voids or defect sites. These results are consistent with transmission electron microscopy observation of quasistatically loaded single crystals with the same orientations by Nie et al. (262).

The results presented here are of relevance in predicting the anisotropy of plastic deformation of polycrystalline diamond under compression and are important in the understanding of the asymmetry of collapse of a capsule under hydrostatic compression. Another important aspect of the findings presented here is a more precise characterization of ablator response. Diamond is among the low Z elements, one of the best choices for ablator in pulsed laser energy deposition (19). Dislocation generation, amorphization, and energy deposition at voids can lead to shear localization. These effects have not been systematically investigated and the simulations point to an approach that can elucidate the occurrence and effect of these phenomena.

## **5.4 Acknowledgments**

Chapter 5, in part, is a reprint of material that has been published: A.C. Li, B. Li, R.E. Rudd, and M.A. Meyers, Dislocation Generation in Diamond Under Extreme Loading, *Matter* 6, 1-17 (2023).

## Chapter 6 Effects of Void Size on Diamond Plasticity Thresholds

### 6.1 Introduction

Diamond plays a critical role in achieving ignition of inertial confinement fusion (ICF) at the National Ignition Facility (10). High-density carbon (HDC), synthetic diamond, is the only successful the capsule material to date, containing the deuterium-tritium fuel and serving as the ablator (19, 20, 328). Figure 6-1 shows the cryogenic target assembly into which up to 192 laser beams are directed into a cylindrical hohlraum (329). The laser beams hit the sides of the hohlraum, generating X-rays which ablate the HDC and drive the compression of the capsule. The 2-mm diameter capsule is suspended in the center of the hohlraum, containing the fuel as a layer of DT ice on the inner surface of the HDC shell. Numerous technical challenges had to be overcome to achieve ignition. A persistent challenge has been the occurrence of defects in the HDC capsule. The symmetric implosion of the capsule is necessary to reach the critical fusion fuel density and temperature required for ignition (303, 304, 330). The presence of voids in the HDC shell can spoil the symmetry, induce meteors and other plasma jets (331), and promote mixing of the carbon and other high-Z elements into the fuel where they radiate and suppress fusion (332). The voids form in the HDC capsules during the manufacturing process which involves chemical vapor deposition, surface polishing, laser-drilling of the filling hole, and pressure cycling to remove the Si mandrel below the diamond shell (21, 333). Their populations have been quantified through non-destructive testing (10, 304, 332). Despite diligent characterization of the defects that form during manufacturing, the shock-wave interaction with the voids during implosion has not been investigated carefully and the process of inelastic deformation of the diamond as the void is compressed is poorly understood. The diamond is still a solid following the first shock (10), and the extraordinary mechanical properties of diamond are certain to influence the void collapse and resulting perturbations to the material flow. Here we use molecular dynamics simulation to

characterize the irreversible deformation around a void in diamond subjected to a strong shock wave, revealing the link between the void characteristics and the requisite shock strength for collapse. We find the ICF first shock is more than strong enough to induce void collapse.

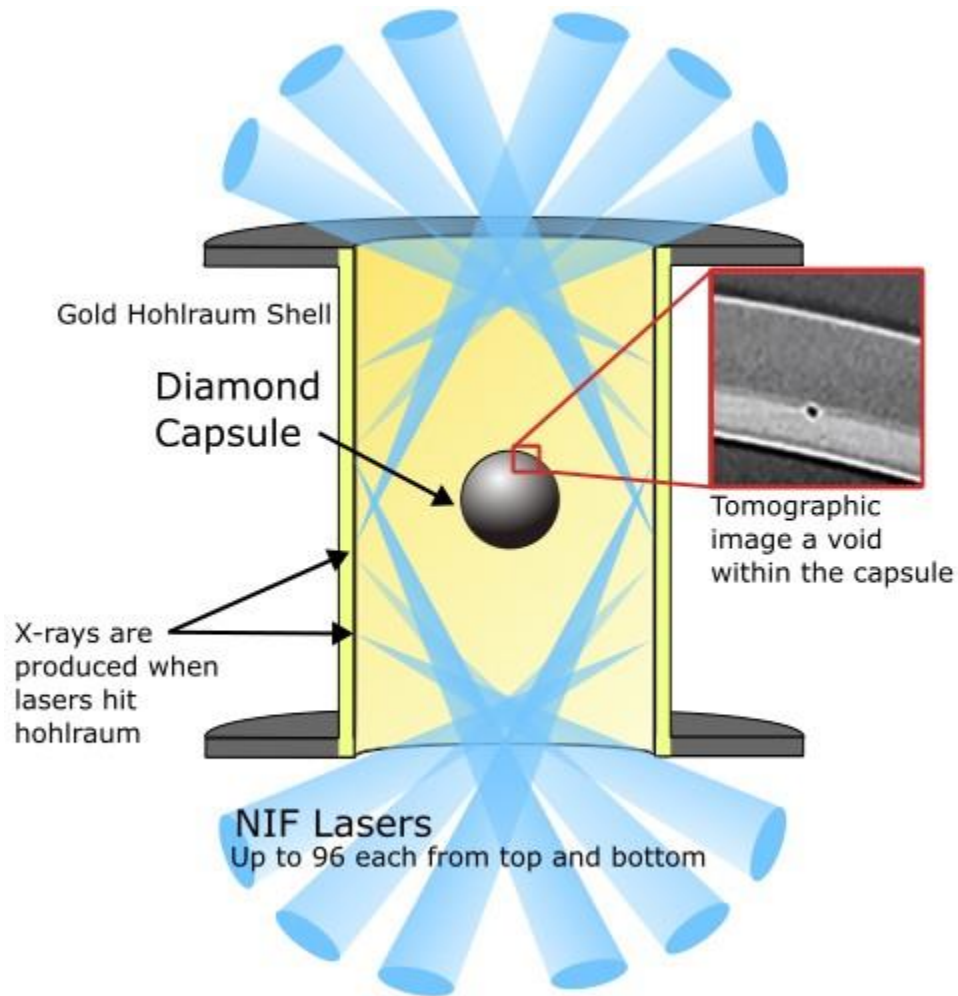


Figure 6-1 – Schematic illustration of the hohlraum and capsule used in NIF experiments. The NIF lasers enter from the top and the bottom, impinging on the gold shell of the hohlraum and heating it up, producing X-rays. These X-rays couple to the surface of the diamond capsule, causing it to ablate away, compressing the remaining capsule and fuel and creating the conditions necessary for fusion to occur. The close-up shows a tomographic image of a void present in a diamond capsule, reproduced from <https://lasers.llnl.gov/news/high-quality-diamond-capsule-enhanced-nifs-record-energy-shot>

## 6.2 Void Size Effects in [111] Oriented Diamond Shock Compression

It was recently established through laser-driven shock loading (306) and flyer-plate impact (296) that there is considerable anisotropy in the mechanical response of monocrystalline diamond. Whereas inelastic deformation during [111] shock loading occurred at a stress as low as 60 GPa, for [100] loading higher stresses were required. The observations were not consistent with conventional bulk dislocation plasticity (296). Molecular dynamics simulations provided a direct visualization of the deformation processes (334). Whereas in the perfect crystal dislocation emission occurred from the (111) piston surface at a shock stress of 226 GPa, the presence of an 8-nm diameter void reduced the threshold to between 145 and 188 GPa. In each case the introduction of voids decreased the threshold to generate dislocations, allowing a detailed investigation of the nature and configuration of dislocations for an 8-nm void within the shocked material (334). These results stimulated the current investigation which seeks to establish whether there is an effect of void size on the formation of dislocations.

In the present work, we determine the effect of void size on the threshold stress for dislocation generation. Different size voids were introduced within [111] oriented diamond samples to study their effect on the dislocation generation stress threshold. Previous work on shock compressed copper and tantalum revealed that the threshold decreased with increasing void size (44, 45). For our work, voids ranging in size from 2 nm to 18 nm were introduced into single crystal diamond bulk; shocks were driven at varying amplitudes until dislocations were observed to emanate from the void. We note that voids in the size range studied here have been observed experimentally in brown diamond (241).

### 6.2.1 Predictions of Threshold stress from molecular dynamics

We find the presence of voids in shocked diamond lowers the threshold stress for dislocation emission. Simulation details are given in Materials and Methods. Dislocation loops are emitted from the voids, as shown in Fig. 6-2. Voids act as both stress concentrators and preferential nucleation sites. The dislocation loops are generated in the regions of highest shear stress on the void surface, establishing the threshold stress required. A shock stress of 232 GPa or greater is required to generate a loop from a 2-nm void (Fig. 6-2a), whereas a much lower stress of 135 GPa generated loops in the larger, 18-nm void (Fig. 6-2d).

The similarity between these events is illustrated in Fig. 6-2. Perfect dislocations form on  $\{100\}$  planes closest to the maximum shear stress plane for all void sizes. The smallest voids limit the sizes of the dislocation loops that are emitted, which increases the stress threshold needed to initiate the dislocations. As the voids become larger, the length of the  $[110]$  dislocation loops seem to approach a limit, and instead multiple dislocations appear along parallel planes. This process is shown in greater detail for the largest and smallest voids modeled, 2 and 18 nm. For the 18-nm void, dislocations on two families of planes are emitted, as indicated in Fig. 2f:  $\{100\}$  and  $\{111\}$ . Their Burgers vectors are identified as (334):

$$b_{100} = \frac{1}{2} [110]\{100\}$$

$$b_{111} = \frac{1}{2} [112]\{111\}.$$

We note that the presence of the unusual  $\{100\}$  slip was observed in experiments of diamond nanopillar compression (262) and indentation testing (257). These dislocations form an expanding front moving behind the shock front and constitute a plastic wave following the initial elastic wave (306). Their velocities can be measured from the absolute positions of atoms at the front of the wave during different snapshots of the simulation.

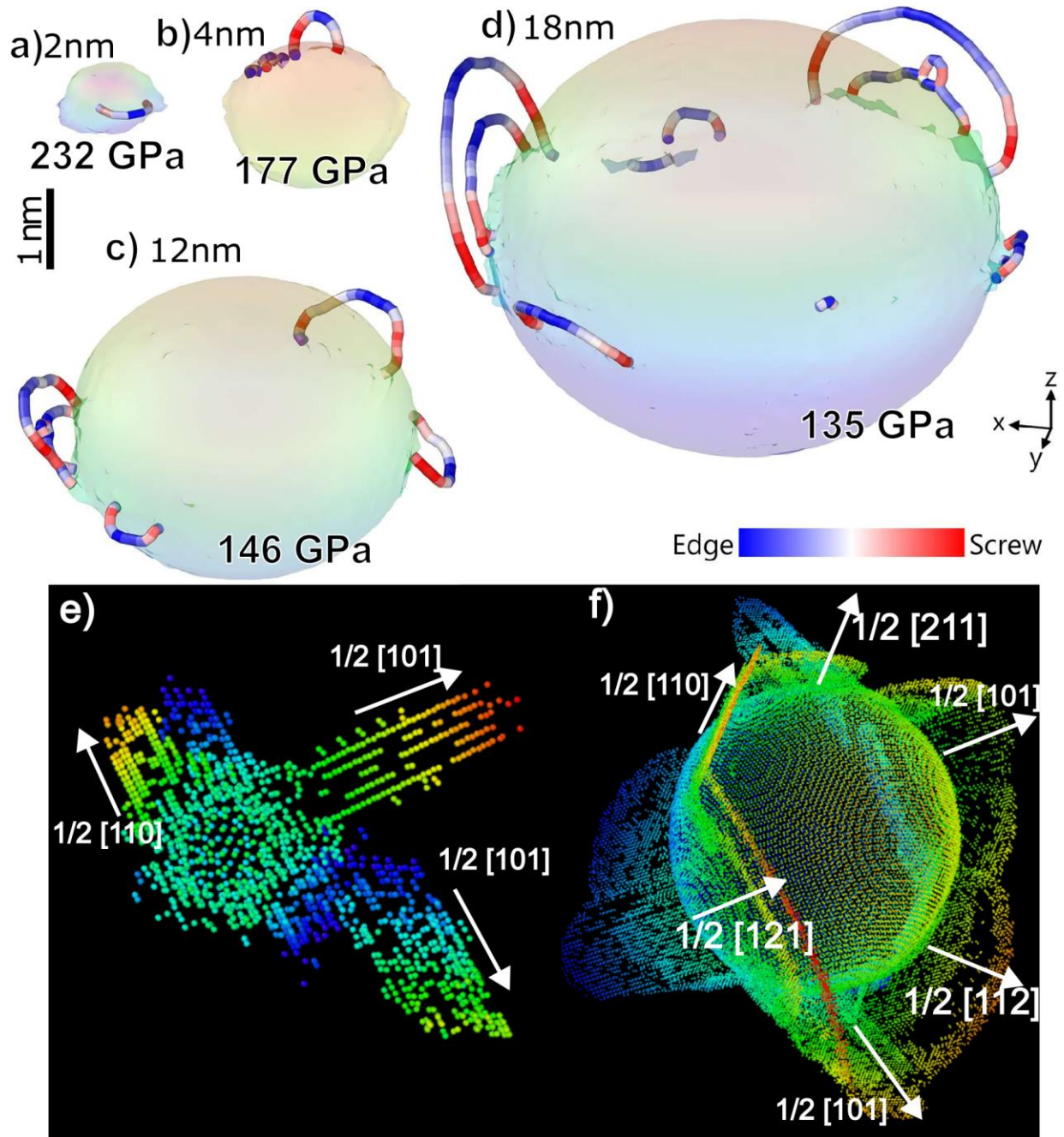


Figure 6-2 - MD simulations showing the threshold for dislocation generation for different void sizes (diameters) and the shock pressure at which they first form dislocations from the void. a) 2 nm, 232 GPa b) 4 nm, 177 GPa c) 12 nm, 146 GPa d) 18 nm, 135 GPa e) and f) Differences in dislocation configurations between e) 2-nm and f) 18-nm voids. Longitudinal position of atoms indicated by color scale, to help visualize three dimensionality. Only dislocations on  $\{100\}$  planes with direction  $[110]$  are formed in the 2-nm void, whereas in the 18-nm void multiple dislocations are created along parallel planes and both  $\{100\}$  and  $\{111\}$  planes are activated. The 2-nm simulation also had dislocations emanating from the planar impact surface, whereas in the 18-nm void case the pressure was too low for surface dislocations to form.



A closer examination of the properties of vicinity of the 12nm radius void shows additional detail in Figure 6-3. The local crystallinity around the void is preserved, except in the areas where the dislocations are being produced, and the compressed zone at the equator of the void. The potential energy of the atoms about the equator of the void are also increased, and there is a split in the orientational rotation of the void on either side of the compression zone.

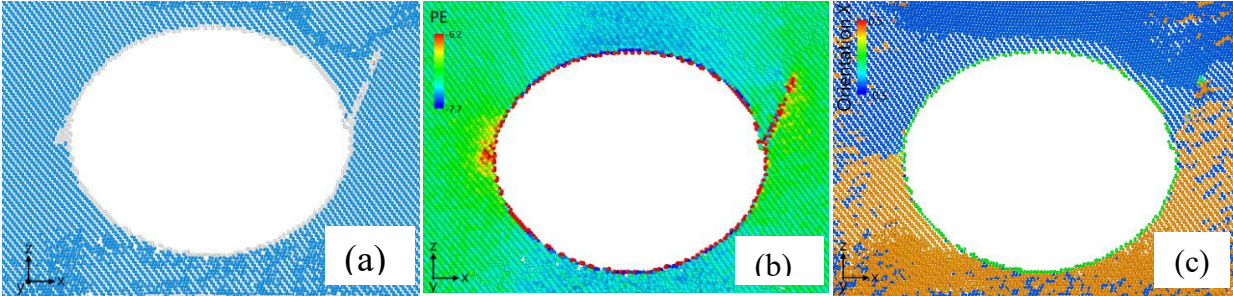


Figure 6-3 12 nm diameter void. Slice, 0.2 nm thick, with different color scales. (a) Structure type: diamond (blue), unknown (white). (b) Atomic potential energy (PE). (c) Atomic rotation, X component of the quaternion from PTM, with rmsd=0.1. The shock moves along z, causing an increase of PE in the equator, where dislocations nucleate. There are local lattice rotations associated with the large shear at the void surface and nearby.

### 6.3 Prediction of threshold stress from dislocation mechanics

Analytical predictions can capture the physics of the emission of dislocations from voids using the fundamental equations of dislocation theory, rooted in elasticity theory (44, 45, 312, 335). Analysis of the effects of void size on dislocation emission stress thresholds show that the shear stress for dislocation emission can be expressed as the sum of three terms:

$$\tau_{max} = \frac{2\gamma}{\pi\rho b} + \frac{Gb(2-\nu)}{4\pi(1-\nu)R_1} \ln \frac{8mR_1}{e^2\rho b} + \tau_{PN} \quad (1)$$

The first term is the shear stress required to create a surface step by emitting a dislocation over the distance  $\rho b$ , where  $\gamma$  is the surface energy and  $\rho$  is an integer multiplier of the length of

the Burgers vector  $b$ , representing the size of the dislocation core. The original derivation is by Rice and Thompson (316).

The second term is comprised of two contributions, the dislocation line energy and the image forces that attract the dislocation to the free surface as it forms. This analysis follows Rice and Anderson (336), Wolfer (337) and Ahn (338).  $m$  describes the geometry of the dislocation; for a mixed character dislocation like the ones seen in our simulations a value of 2.2 is used. For a semi-circular loop, the distance from a surface varies with position. The formation and expansion of a loop also requires additional energy because of the increasing length.  $R_1$  is the loop radius and is taken as a quarter of the void diameter (44, 45).

The third term is the Peierls-Nabarro (PN) stress. We add it to account for the stress required to move a dislocation over the barrier between adjacent crystal lattice sites. Diamond is a covalently bonded material with high Peierls-Nabarro stresses required for dislocation motion to occur. The ratio of the PN stress to shear modulus for tetrahedrally coordinated crystals is around  $PN_{Dia} = 0.1 G$  (339, 340). This is also in line with first-principles calculated values for the PN stress of a screw dislocation in diamond (341), which is the controlling stress under the kink-pair mechanism responsible for plasticity in tetrahedrally coordinated crystals (340, 342). It adds a significant barrier to the creation and movement of new dislocations and is a large contribution to the total stress required for dislocations to form.

Equation 1 does not include any consideration for the strain-rate dependence of the dislocation energy. Dislocation velocities in a compressed diamond nanoparticles were found to be around 1 km/s (106). This is significantly lower than the shear wave velocity of around 14 km/s at the pressures investigated in this paper. From the shock simulations, measurements of the dislocation velocities directly after nucleation were around 0.3 to 0.4 of the shear wave velocity,

$C_s$  for each simulated void size and piston velocity. These were measured for the dislocations along the [111] direction just after formation, rather than the established [112] dislocations measured in previous work (334). This is in the relativistic regime of dislocation motion, and the energy is expressed as (335)

$$E = \frac{E_0}{\sqrt{1 - \left(\frac{v_d}{C_s}\right)^2}} \quad (2)$$

where  $E_0$  is the energy of the dislocation at rest,  $v_d$  is the dislocation velocity, and  $C_s$  is the shear wave velocity, considered to be the limiting velocity of subsonic dislocations.  $C_s$  represents a singularity in the dislocation energy. Exceeding this value creates transonic dislocations. Including this kinetic energy factor into the line energy of the dislocation would leave the whole modified equation for the shear stress as:

$$\tau_{max} = \frac{2\gamma}{\pi\rho b} + \frac{Gb(2-\nu)}{4\pi(1-\nu)R_1} \left( \frac{\ln \frac{8R_1}{e^2\rho b}}{\sqrt{1 - \left(\frac{v_d}{C_s}\right)^2}} + \ln m \right) + \tau_{PN} \quad (3)$$

where the value of the dislocation velocity affects only the dislocation energy itself, and not the image forces contributed by the geometric factor  $m$ .

It is arguable whether the kinetic energy of the dislocation has an effect during the initial formation of the dislocation at the void surface, as discussed in this work. For our measurements of the dislocation velocity in diamond from a void, the contribution would increase the stress threshold by around 2-3% of the total value. For cases where the dislocation velocity is closer to the shear wave velocity, this relativistic effect could be more pronounced.

The threshold formula (1) gives the minimum shear stress required for nucleation of a dislocation within diamond. It is expressed in terms of the shear stress on the dislocation slip plane at the surface of the void, where the stresses are concentrated. For comparison to the average far-

field shock stress, we must divide this value by the Lu factor (93, 334),  $m_{Lu} = 0.415$ , for the stress in plane strain resolved onto the slip plane, and divide by the stress concentration factor for a spherical void (312):

$$\sigma_{zzVoid} = \left[ 1 + 13 - \frac{5\nu}{2(7-5)} \right] \sigma_{zz}. \quad (4)$$

For our diamond sample with a Poisson ratio of  $\nu = 0.2$  calculated at the shock pressure of 232 GPa, this stress concentration factor is equal to 2. Our final conversion is then

$$\sigma_{zz} = \frac{\tau_{max}}{m_{lu} \times \left[ 1 + \frac{13-5\nu}{2(7-5\nu)} \right]} = 1.205 \tau_{max}. \quad (5)$$

#### 6.4 Effect of Void Size on threshold stress

The MD predictions of dislocation nucleation thresholds of voids from 2nm to 18nm are plotted in Fig.3. For a 10-nm void the shock stress was 155 GPa, which is close to the compression stress of 160 GPa to generate dislocations inside a diamond NP with 10-nm diameter (308), which constitutes a dual problem, with similar geometry and material parameters.

This decrease is significant and has been observed before for other materials with voids including Cu and Ta (45). For the larger voids the dislocation loops expand with greater ease, their ends staying attached to the void surface.

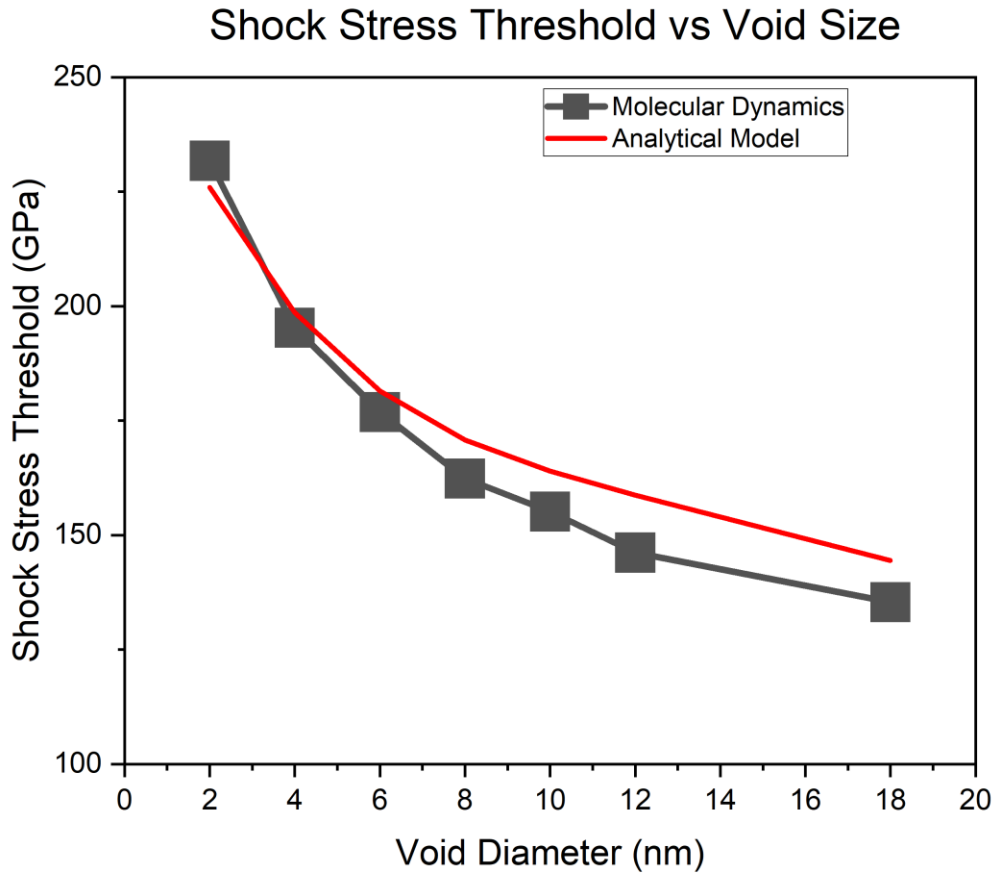


Figure 6-4 - Shock stresses for the emission of dislocations as a function of void diameter; comparison of MD results with analytical predictions (1) and (5).

The analytical formula (1) similarly predicts a decrease in the stress with increasing void size. The dislocation core radius is taken equal to  $b$ , *i.e.*,  $\rho = 1$ . This value reflects the MD dislocation cores being narrow, as shown in Fig. 6-2. We calculated the shear modulus,  $G$ , for each value of the shock pressure from the elastic constants at that pressure. Poisson's ratio is taken to be  $\nu = 0.2$ . The calculations are performed for a  $\{100\}$  dislocation, for which  $b = 0.309$  nm, with a stress concentration of 2 for a spherical void. The surface energy for a dislocation on the (100) plane is given as  $\gamma = 6.910$  J/m<sup>2</sup> (343).

The final prediction combining equations (1) and (3) agree well with our MD results, as shown in Fig. 6-3. This threshold formula should be applicable to voids in other single-crystal materials as well, with the addition of the Peierls-Nabarro stress additionally providing non-negligible stresses for more strongly bonded materials such as diamond, oxides, or ceramic crystals.

## **6.5 Acknowledgements**

Chapter 6, in part, is in preparation for submission for publication: A.C. Li, M.A. Meyers, E.M. Bringa, R.E. Rudd, Diamond Response to Extreme Deformation, (2024). The dissertation author was the first and corresponding author of this article.

## Chapter 7 Conclusions

The shock response of the covalently bonded materials of silicon and diamond were investigated. In the silicon simulations, several interatomic potentials were tested to observe and compare their results for reproducing elastic constants, melting points, phase changes, plasticity thresholds, and amorphization. A separate method of structure identification within shocked silicon was also tested and verified for the modified Tersoff potential, able to identify the phase change within the shear bands produced by the shock wave from the diamond cubic to the BCT5 phase.

The plastic deformation of diamond monocrystal under shock compression was investigated and the effects of the presence of flaws were established. While experimental shots that went beyond the HEL for diamond in the [100] orientation were performed, no dislocations have yet been observed in our TEM work. Using molecular dynamics to investigate, a significant difference in the generation of defects was observed based on the orientation of the diamond, the presence of defects such as voids, and the size of the void included in shock simulations. The following conclusions are drawn from this investigation using molecular dynamics:

1. Spherical voids provided preferential nucleation sites for shock-induced defects.
2. The [001] orientation of diamond is the strongest with respect to the condition of plasticity. No dislocations were identified within this orientation for conditions leading up to the melting or amorphization and recrystallization of the lattice structure.
3. The [011] and [111] orientations produce far more defect activity, with the [111] orientation being the most active.
4. In the [111] orientation, two types of dislocations were observed emerging from 4nm or larger voids, the  $\frac{1}{2} \langle 110 \rangle \{001\}$  dislocations and  $\frac{1}{2} \langle 112 \rangle \{111\}$  dislocations.



5. The Lu Factor was established as a method of quantifying the resolved shear stress along certain slip planes, as a corollary to the Schmid factor but for the case of uniaxial strain, which is the condition present under shock.
6. MD calculations predict that the shock pressure for the initiation of plastic deformation decreases with void size, from a shock stress of 232 GPa for a 2-nm void to 135 GPa for an 18-nm void.
7. An analytical model of the threshold stress for shock-induced plasticity was introduced, extending prior work on metals. Based on an analysis of the stress for dislocation emission from the void surface, it incorporates three terms: formation of a step at the void surface, the work put into the dislocation line energy and elastic field associated with the image force at the void surface, and the Peierls-Nabarro stresses to overcome the lattice friction.
8. The analytical model predicts stresses that agree well with MD calculations.
9. The analytical model is formulated allowing it to be applied to other orientations, void sizes, or materials.
10. The threshold stresses calculated here are exceeded in the solid diamond following the first shock during the ICF implosion process, so the voids are predicted to collapse and generate plastic deformation.

Our extension of the threshold stress formula for plasticity from a void to account for the Peierls-Nabarro stress is important for strongly bonded materials such as diamond, a contribution that could be neglected in the metals studied previously. Diamond capsules in NIF ignition experiments depend on a symmetric implosion with limited mixing to attain fusion. Through the reduced threshold for plasticity and resulting localized shear flow, we have shown that voids clearly affect

the shock compression of diamond. By better understanding the effects of these void defects on the plasticity thresholds in diamond, we may better model how diamond under high pressure deforms.

## REFERENCES

1. C. S. Smith, METALLOGRAPHIC STUDIES OF METALS AFTER EXPLOSIVE SHOCK. *Trans Met Soc AIME* **Vol: 212** (1958).
2. E. Hornbogen, Shock-induced dislocations. *Acta Metall.* **10**, 978–980 (1962).
3. M. A. Meyers, H. Jarmakani, E. M. Bringa, B. A. Remington, “Chapter 89 Dislocations in Shock Compression and Release” in *Dislocations in Solids*, J. P. Hirth, L. Kubin, Eds. (Elsevier, 2009; <https://www.sciencedirect.com/science/article/pii/S1572485909015022>)vol. 15, pp. 91–197.
4. E. J. Workman, “Development of new gun using helium gas for projectile acceleration” (Final Report NMSM/RDD, 1952).
5. W. D. Crozier, W. Hume, High-Velocity, Light-Gas Gun. *J. Appl. Phys.* **28**, 892–894 (1957).
6. H. F. Swift, “Light-Gas Gun Technology: A Historical Perspective” in *High-Pressure Shock Compression of Solids VIII*, L. C. Chhabildas, L. Davison, Y. Horie, Eds. (Springer-Verlag, Berlin/Heidelberg, 2005; [http://link.springer.com/10.1007/3-540-27168-6\\_1](http://link.springer.com/10.1007/3-540-27168-6_1))*High-Pressure Shock Compression of Condensed Matter*, pp. 1–35.
7. R. W. Lemke, M. D. Knudson, J.-P. Davis, Magnetically driven hyper-velocity launch capability at the Sandia Z accelerator. *Int. J. Impact Eng.* **38**, 480–485 (2011).
8. M. K. Matzen, M. G. Mazarakis, J. E. Bailey, M. E. Cuneo, M. P. Desjarlais, S. F. Glover, M. C. Herrmann, B. M. Jones, M. D. Knudson, J. J. Leckbee, B. V. Oliver, J. L. Porter, G. A. Rochau, L. X. Schneider, D. B. Sinars, W. A. Stygar, M. A. Sweeney, R. A. Vesey, J. R. Woodworth, “The science, technology, and applications of Terawatt-class pulsed power drivers at Sandia National Laboratories” in *2010 IEEE International Power Modulator and High Voltage Conference* (2010; <https://ieeexplore.ieee.org/abstract/document/5958282>), pp. 1–16.
9. A. B. Zylstra, A. L. Kritcher, O. A. Hurricane, D. A. Callahan, K. Baker, T. Braun, D. T. Casey, D. Clark, K. Clark, T. Döppner, L. Divol, D. E. Hinkel, M. Hohenberger, C. Kong, O. L. Landen, A. Nikroo, A. Pak, P. Patel, J. E. Ralph, N. Rice, R. Tommasini, M. Schoff, M. Stadermann, D. Strozzi, C. Weber, C. Young, C. Wild, R. P. J. Town, M. J. Edwards, Record Energetics for an Inertial Fusion Implosion at NIF. *Phys. Rev. Lett.* **126**, 025001 (2021).
10. The Indirect Drive ICF Collaboration, H. Abu-Shawareb, R. Acree, P. Adams, J. Adams, B. Addis, R. Aden, P. Adrian, B. B. Afeyan, M. Aggleton, L. Aghaian, A. Aguirre, D. Aikens, J. Akre, F. Albert, M. Albrecht, B. J. Albright, J. Albritton, J. Alcalá, C. Alday, D. A. Alessi, N. Alexander, J. Alfonso, N. Alfonso, E. Alger, S. J. Ali, Z. A. Ali, A. Allen, W. E. Alley, P. Amala, P. A. Amendt, P. Amick, S. Ammala, C. Amorin, D. J. Ampleford, R. W. Anderson, T. Anklam, N. Antipa, B. Appelbe, C. Aracne-Ruddle, E. Araya, T. N. Archuleta, M. Arend, P. Arnold, T. Arnold, A. Arsenlis, J. Asay, L. J. Atherton, D. Atkinson, R. Atkinson, J. M. Auerbach, B. Austin, L. Auyang, A. A. S. Awwal, N. Aybar, J. Ayers, S. Ayers, T. Ayers, S.

Azevedo, B. Bachmann, C. A. Back, J. Bae, D. S. Bailey, J. Bailey, T. Baisden, K. L. Baker, H. Baldis, D. Barber, M. Barberis, D. Barker, A. Barnes, C. W. Barnes, M. A. Barrios, C. Barty, I. Bass, S. H. Batha, S. H. Baxamusa, G. Bazan, J. K. Beagle, R. Beale, B. R. Beck, J. B. Beck, M. Bedzyk, R. G. Beeler, R. G. Beeler, W. Behrendt, L. Belk, P. Bell, M. Belyaev, J. F. Benage, G. Bennett, L. R. Benedetti, L. X. Benedict, R. L. Berger, T. Bernat, L. A. Bernstein, B. Berry, L. Bertolini, G. Besenbruch, J. Betcher, R. Bettenhausen, R. Betti, B. Bezzerides, S. D. Bhandarkar, R. Bickel, J. Biener, T. Biesiada, K. Bigelow, J. Bigelow-Granillo, V. Bigman, R. M. Bionta, N. W. Birge, M. Bitter, A. C. Black, R. Bleile, D. L. Bleuel, E. Bliss, E. Bliss, B. Blue, T. Boehly, K. Boehm, C. D. Boley, R. Bonanno, E. J. Bond, T. Bond, M. J. Bonino, M. Borden, J.-L. Bourgade, J. Bousquet, J. Bowers, M. Bowers, R. Boyd, D. Boyle, A. Bozek, D. K. Bradley, K. S. Bradley, P. A. Bradley, L. Bradley, L. Brannon, P. S. Brantley, D. Braun, T. Braun, K. Brienza-Larsen, R. Briggs, T. M. Briggs, J. Britten, E. D. Brooks, D. Browning, M. W. Bruhn, T. A. Brunner, H. Bruns, G. Brunton, B. Bryant, T. Buczek, J. Bude, L. Buitano, S. Burkhart, J. Burmark, A. Burnham, R. Burr, L. E. Busby, B. Butlin, R. Cabeltis, M. Cable, W. H. Cabot, B. Cagadas, J. Caggiano, R. Cahayag, S. E. Caldwell, S. Calkins, D. A. Callahan, J. Calleja-Aguirre, L. Camara, D. Camp, E. M. Campbell, J. H. Campbell, B. Carey, R. Carey, K. Carlisle, L. Carlson, L. Carman, J. Carmichael, A. Carpenter, C. Carr, J. A. Carrera, D. Casavant, A. Casey, D. T. Casey, A. Castillo, E. Castillo, J. I. Castor, C. Castro, W. Caughey, R. Cavitt, J. Celeste, P. M. Celliers, C. Cerjan, G. Chandler, B. Chang, C. Chang, J. Chang, L. Chang, R. Chapman, T. D. Chapman, L. Chase, H. Chen, H. Chen, K. Chen, L.-Y. Chen, B. Cheng, J. Chittenden, C. Choate, J. Chou, R. E. Chrien, M. Chrisp, K. Christensen, M. Christensen, N. S. Christiansen, A. R. Christopherson, M. Chung, J. A. Church, A. Clark, D. S. Clark, K. Clark, R. Clark, L. Claus, B. Cline, J. A. Cline, J. A. Cobble, K. Cochrane, B. Cohen, S. Cohen, M. R. Collette, G. W. Collins, L. A. Collins, T. J. B. Collins, A. Conder, B. Conrad, M. Conyers, A. W. Cook, D. Cook, R. Cook, J. C. Cooley, G. Cooper, T. Cope, S. R. Copeland, F. Coppari, J. Cortez, J. Cox, D. H. Crandall, J. Crane, R. S. Craxton, M. Cray, A. Crilly, J. W. Crippen, D. Cross, M. Cuneo, G. Cuotts, C. E. Czajka, D. Czechowicz, T. Daly, P. Danforth, C. Danly, R. Darbee, B. Darlington, P. Datte, L. Dauffy, G. Davalos, S. Davidovits, P. Davis, J. Davis, S. Dawson, R. D. Day, T. H. Day, M. Dayton, C. Deck, C. Decker, C. Deeney, K. A. DeFriend, G. Deis, N. D. Delamater, J. A. Delettretz, R. Demaret, S. Demos, S. M. Dempsey, R. Desjardin, T. Desjardins, M. P. Desjarlais, E. L. Dewald, J. DeYoreo, S. Diaz, G. Dimonte, T. R. Dittrich, L. Divol, S. N. Dixit, J. Dixon, A. Do, E. S. Dodd, D. Dolan, A. Donovan, M. Donovan, T. Döppner, C. Dorrer, N. Dorsano, M. R. Douglas, D. Dow, J. Downie, E. Downing, M. Dozieres, V. Draggo, D. Drake, R. P. Drake, T. Drake, G. Dreifuert, O. Drury, D. F. DuBois, P. F. DuBois, G. Dunham, M. Durocher, R. Dylla-Spears, A. K. L. Dymoke-Bradshaw, B. Dzenitis, C. Ebberts, M. Eckart, S. Eddinger, D. Eder, D. Edgell, M. J. Edwards, P. Efthimion, J. H. Eggert, B. Ehrlich, P. Ehrmann, S. Elhadj, C. Ellerbee, N. S. Elliott, C. L. Ellison, F. Elsner, M. Emerich, K. Engelhorn, T. England, E. English, P. Epperson, R. Epstein, G. Erbert, M. A. Erickson, D. J. Erskine, A. Erlandson, R. J. Espinosa, C. Estes, K. G. Estabrook, S. Evans, A. Fabyan, J. Fair, R. Fallejo, N. Farmer, W. A. Farmer, M. Farrell, V. E. Fatherley, M. Fedorov, E. Feigenbaum, T. Fehrenbach, M. Feit, B. Felker, W. Ferguson, J. C. Fernandez, A. Fernandez-Panella, S. Fess, J. E. Field, C. V. Filip, J. R. Fincke, T. Finn, S. M. Finnegan, R. G. Finucane, M. Fischer, A. Fisher, J. Fisher, B. Fishler, D. Fittinghoff, P. Fitzsimmons, M. Flegel, K. A. Flippo, J. Florio, J. Folta, P. Folta, L. R. Foreman, C. Forrest, A. Forsman, J. Fooks, M.

Foord, R. Fortner, K. Fournier, D. E. Fratanduono, N. Frazier, T. Frazier, C. Frederick, M. S. Freeman, J. Frenje, D. Frey, G. Frieders, S. Friedrich, D. H. Froula, J. Fry, T. Fuller, J. Gaffney, S. Gales, B. Le Galloudec, K. K. Le Galloudec, A. Gambhir, L. Gao, W. J. Garbett, A. Garcia, C. Gates, E. Gaut, P. Gauthier, Z. Gavin, J. Gaylord, C. G. R. Geddes, M. Geissel, F. Génin, J. Georgeson, H. Geppert-Kleinrath, V. Geppert-Kleinrath, N. Gharibyan, J. Gibson, C. Gibson, E. Giraldez, V. Glebov, S. G. Glendinning, S. Glenn, S. H. Glenzer, S. Goade, P. L. Gobby, S. R. Goldman, B. Golick, M. Gomez, V. Goncharov, D. Goodin, P. Grabowski, E. Grafil, P. Graham, J. Grandy, E. Grasz, F. R. Graziani, G. Greenman, J. A. Greenough, A. Greenwood, G. Gregori, T. Green, J. R. Griego, G. P. Grim, J. Grondalski, S. Gross, J. Guckian, N. Guler, B. Gunney, G. Guss, S. Haan, J. Hackbarth, L. Hackel, R. Hackel, C. Haefner, C. Hagmann, K. D. Hahn, S. Hahn, B. J. Haid, B. M. Haines, B. M. Hall, C. Hall, G. N. Hall, M. Hamamoto, S. Hamel, C. E. Hamilton, B. A. Hammel, J. H. Hammer, G. Hampton, A. Hamza, A. Handler, S. Hansen, D. Hanson, R. Haque, D. Harding, E. Harding, J. D. Hares, D. B. Harris, J. A. Harte, E. P. Hartouni, R. Hatarik, S. Hatchett, A. A. Hauer, M. Havre, R. Hawley, J. Hayes, J. Hayes, S. Hayes, A. Hayes-Sterbenz, C. A. Haynam, D. A. Haynes, D. Headley, A. Heal, J. E. Heebner, S. Heerey, G. M. Heestand, R. Heeter, N. Hein, C. Heinbockel, C. Hendricks, M. Henesian, J. Heninger, J. Henrikson, E. A. Henry, E. B. Herbold, M. R. Hermann, G. Hermes, J. E. Hernandez, V. J. Hernandez, M. C. Herrmann, H. W. Herrmann, O. D. Herrera, D. Hewett, R. Hibbard, D. G. Hicks, D. P. Higginson, D. Hill, K. Hill, T. Hilsabeck, D. E. Hinkel, D. D. Ho, V. K. Ho, J. K. Hoffer, N. M. Hoffman, M. Hohenberger, M. Hohensee, W. Hoke, D. Holdener, F. Holdener, J. P. Holder, B. Holko, D. Holunga, J. F. Holzrichter, J. Honig, D. Hoover, D. Hopkins, L. F. Berzak Hopkins, M. Hoppe, M. L. Hoppe, J. Horner, R. Hornung, C. J. Horsfield, J. Horvath, D. Hotaling, R. House, L. Howell, W. W. Hsing, S. X. Hu, H. Huang, J. Huckins, H. Hui, K. D. Humbird, J. Hund, J. Hunt, O. A. Hurricane, M. Hutton, K. H.-K. Huynh, L. Inandan, C. Iglesias, I. V. Igumenshchev, I. Ivanovich, N. Izumi, M. Jackson, J. Jackson, S. D. Jacobs, G. James, K. Jancaitis, J. Jarboe, L. C. Jarrott, D. Jasion, J. Jaquez, J. Jeet, A. E. Jenei, J. Jensen, J. Jimenez, R. Jimenez, D. Jobe, Z. Johal, H. M. Johns, D. Johnson, M. A. Johnson, M. Gatu Johnson, R. J. Johnson, S. Johnson, S. A. Johnson, T. Johnson, K. Jones, O. Jones, M. Jones, R. Jorge, H. J. Jorgenson, M. Julian, B. I. Jun, R. Jungquist, J. Kaae, N. Kabadi, D. Kaczala, D. Kalantar, K. Kangas, V. V. Karasiev, M. Karasik, V. Karpenko, A. Kasarky, K. Kasper, R. Kauffman, M. I. Kaufman, C. Keane, L. Keaty, L. Kegelmeyer, P. A. Keiter, P. A. Kellett, J. Kellogg, J. H. Kelly, S. Kemic, A. J. Kemp, G. E. Kemp, G. D. Kerbel, D. Kershaw, S. M. Kerr, T. J. Kessler, M. H. Key, S. F. Khan, H. Khater, C. Kiikka, J. Kilkenny, Y. Kim, Y.-J. Kim, J. Kimko, M. Kimmel, J. M. Kindel, J. King, R. K. Kirkwood, L. Klaus, D. Klem, J. L. Kline, J. Klingmann, G. Kluth, P. Knapp, J. Knauer, J. Knipping, M. Knudson, D. Kobs, J. Koch, T. Kohut, C. Kong, J. M. Koning, P. Koning, S. Konior, H. Kornblum, L. B. Kot, B. Koziowski, M. Kozlowski, P. M. Kozlowski, J. Krammen, N. S. Krashennikova, C. M. Krauland, B. Kraus, W. Krauser, J. D. Kress, A. L. Kritcher, E. Krieger, J. J. Kroll, W. L. Kruer, M. K. G. Kruse, S. Kucheyev, M. Kumbera, S. Kumpan, J. Kunimune, E. Kur, B. Kustowski, T. J. T. Kwan, G. A. Kyrala, S. Laffite, M. Lafon, K. LaFortune, L. Lagin, B. Lahmann, B. Lairson, O. L. Landen, T. Land, M. Lane, D. Laney, A. B. Langdon, J. Langenbrunner, S. H. Langer, A. Langro, N. E. Lanier, T. E. Lanier, D. Larson, B. F. Lasinski, D. Lassle, D. LaTray, G. Lau, N. Lau, C. Laumann, A. Laurence, T. A. Laurence, J. Lawson, H. P. Le, R. R. Leach, L. Leal, A. Leatherland, K. LeChien, B. Lechleiter, A. Lee, M. Lee, T. Lee, R. J. Leeper, E. Lefebvre, J.-P. Leidinger, B. LeMire, R.

W. Lemke, N. C. Lemos, S. Le Pape, R. Lerche, S. Lerner, S. Letts, K. Levedahl, T. Lewis, C. K. Li, H. Li, J. Li, W. Liao, Z. M. Liao, D. Liedahl, J. Liebman, G. Lindford, E. L. Lindman, J. D. Lindl, H. Loey, R. A. London, F. Long, E. N. Loomis, F. E. Lopez, H. Lopez, E. Losbanos, S. Loucks, R. Lowe-Webb, E. Lundgren, A. P. Ludwigsen, R. Luo, J. Lusk, R. Lyons, T. Ma, Y. Macallop, M. J. MacDonald, B. J. MacGowan, J. M. Mack, A. J. Mackinnon, S. A. MacLaren, A. G. MacPhee, G. R. Magelssen, J. Magoon, R. M. Malone, T. Malsbury, R. Managan, R. Mancini, K. Manes, D. Maney, D. Manha, O. M. Mannion, A. M. Manuel, M. J.-E. Manuel, E. Mapoles, G. Mara, T. Marcotte, E. Marin, M. M. Marinak, D. A. Mariscal, E. F. Mariscal, E. V. Marley, J. A. Marozas, R. Marquez, C. D. Marshall, F. J. Marshall, M. Marshall, S. Marshall, J. Marticorena, J. I. Martinez, D. Martinez, I. Maslennikov, D. Mason, R. J. Mason, L. Masse, W. Massey, P.-E. Masson-Laborde, N. D. Masters, D. Mathisen, E. Mathison, J. Matone, M. J. Matthews, C. Mattoon, T. R. Mattsson, K. Matzen, C. W. Mauche, M. Mauldin, T. McAbee, M. McBurney, T. Mccarville, R. L. McCrory, A. M. McEvoy, C. McGuffey, M. Mcinnis, P. McKenty, M. S. McKinley, J. B. McLeod, A. McPherson, B. Mcquillan, M. Meamber, K. D. Meaney, N. B. Meezan, R. Meissner, T. A. Mehlhorn, N. C. Mehta, J. Menapace, F. E. Merrill, B. T. Merritt, E. C. Merritt, D. D. Meyerhofer, S. Mezyk, R. J. Mich, P. A. Michel, D. Milam, C. Miller, D. Miller, D. S. Miller, E. Miller, E. K. Miller, J. Miller, M. Miller, P. E. Miller, T. Miller, W. Miller, V. Miller-Kamm, M. Millot, J. L. Milovich, P. Minner, J.-L. Miquel, S. Mitchell, K. Molvig, R. C. Montesanti, D. S. Montgomery, M. Monticelli, A. Montoya, J. D. Moody, A. S. Moore, E. Moore, M. Moran, J. C. Moreno, K. Moreno, B. E. Morgan, T. Morrow, J. W. Morton, E. Moses, K. Moy, R. Muir, M. S. Murillo, J. E. Murray, J. R. Murray, D. H. Munro, T. J. Murphy, F. M. Munteanu, J. Nafziger, T. Nagayama, S. R. Nagel, R. Nast, R. A. Negres, A. Nelson, D. Nelson, J. Nelson, S. Nelson, S. Nemethy, P. Neumayer, K. Newman, M. Newton, H. Nguyen, J.-M. G. Di Nicola, P. Di Nicola, C. Niemann, A. Nikroo, P. M. Nilson, A. Nobile, V. Noorai, R. C. Nora, M. Norton, M. Nostrand, V. Note, S. Novell, P. F. Nowak, A. Nunez, R. A. Nyholm, M. O'Brien, A. Ocegüera, J. A. Oertel, A. L. Oesterle, J. Okui, B. Olejniczak, J. Oliveira, P. Olsen, B. Olson, K. Olson, R. E. Olson, Y. P. Opachich, N. Orsi, C. D. Orth, M. Owen, S. Padalino, E. Padilla, R. Paguio, S. Paguio, J. Paisner, S. Pajoom, A. Pak, S. Palaniyappan, K. Palma, T. Pannell, F. Papp, D. Paras, T. Parham, H.-S. Park, A. Pasternak, S. Patankar, M. V. Patel, P. K. Patel, R. Patterson, S. Patterson, B. Paul, M. Paul, E. Pauli, O. T. Pearce, J. Percy, A. Pedretti, B. Pedrotti, A. Peer, L. J. Pelz, B. Penetrante, J. Penner, A. Perez, L. J. Perkins, E. Pernice, T. S. Perry, S. Person, D. Petersen, T. Petersen, D. L. Peterson, E. B. Peterson, J. E. Peterson, J. L. Peterson, K. Peterson, R. R. Peterson, R. D. Petrasso, F. Philippe, D. Phillion, T. J. Phipps, E. Piceno, L. Pickworth, Y. Ping, J. Pino, K. Piston, R. Plummer, G. D. Pollack, S. M. Pollaine, B. B. Pollock, D. Ponce, J. Ponce, J. Pontelandolfo, J. L. Porter, J. Post, O. Poujade, C. Powell, H. Powell, G. Power, M. Pozulp, M. Prantil, M. Prasad, S. Pratuch, S. Price, K. Primdahl, S. Prisbrey, R. Procassini, A. Pruyne, B. Pudliner, S. R. Qiu, K. Quan, M. Quinn, J. Quintenz, P. B. Radha, F. Rainer, J. E. Ralph, K. S. Raman, R. Raman, P. W. Rambo, S. Rana, A. Randewich, D. Rardin, M. Ratledge, N. Ravelo, F. Ravizza, M. Rayce, A. Raymond, B. Raymond, B. Reed, C. Reed, S. Regan, B. Reichelt, V. Reis, S. Reisdorf, V. Rekow, B. A. Remington, A. Rendon, W. Requieron, M. Rever, H. Reynolds, J. Reynolds, J. Rhodes, M. Rhodes, M. C. Richardson, B. Rice, N. G. Rice, R. Rieben, A. Rigatti, S. Riggs, H. G. Rinderknecht, K. Ring, B. Riordan, R. Riquier, C. Rivers, D. Roberts, V. Roberts, G. Robertson, H. F. Robey, J. Robles, P. Rocha, G. Rochau, J. Rodriguez, S. Rodriguez, M. D.

Rosen, M. Rosenberg, G. Ross, J. S. Ross, P. Ross, J. Rouse, D. Rovang, A. M. Rubenchik, M. S. Rubery, C. L. Ruiz, M. Rushford, B. Russ, J. R. Rygg, B. S. Ryuji, R. A. Sacks, R. F. Sacks, K. Saito, T. Salmon, J. D. Salmonson, J. Sanchez, S. Samuelson, M. Sanchez, C. Sangster, A. Saroyan, J. Sater, A. Satsangi, S. Sauers, R. Saunders, J. P. Sauppe, R. Sawicki, D. Sayre, M. Scanlan, K. Schaffers, G. T. Schappert, S. Schiaffino, D. J. Schlossberg, D. W. Schmidt, P. F. Schmit, J. M. Smidt, D. H. G. Schneider, M. B. Schneider, R. Schneider, M. Schoff, M. Schollmeier, C. R. Schroeder, S. E. Schrauth, H. A. Scott, I. Scott, J. M. Scott, R. H. H. Scott, C. R. Scullard, T. Sedillo, F. H. Seguin, W. Seka, J. Senecal, S. M. Sepke, L. Seppala, K. Sequoia, J. Severyn, J. M. Sevier, N. Sewell, S. Seznec, R. C. Shah, J. Shamlan, D. Shaughnessy, M. Shaw, R. Shaw, C. Shearer, R. Shelton, N. Shen, M. W. Sherlock, A. I. Shestakov, E. L. Shi, S. J. Shin, N. Shingleton, W. Shmayda, M. Shor, M. Shoup, C. Shulberg, L. Siegel, F. J. Silva, A. N. Simakov, B. T. Sims, D. Sinars, P. Singh, H. Sio, K. Skulina, S. Skupsky, S. Slutz, M. Sluyter, V. A. Smalyuk, D. Smauley, R. M. Smeltser, C. Smith, I. Smith, J. Smith, L. Smith, R. Smith, R. Smith, M. Schölmerich, R. Sohn, S. Sommer, C. Sorce, M. Sorem, J. M. Soures, M. L. Spaeth, B. K. Spears, S. Speas, D. Speck, R. Speck, J. Spears, T. Spinka, P. T. Springer, M. Stadermann, B. Stahl, J. Stahoviak, J. Stanley, L. G. Stanton, R. Steele, W. Steele, D. Steinman, R. Stemke, R. Stephens, S. Sterbenz, P. Sterne, D. Stevens, J. Stevers, C. H. Still, C. Stoeckl, W. Stoeffl, J. S. Stolken, C. Stolz, E. Storm, G. Stone, S. Stoupin, E. Stout, I. Stowers, R. Strauser, H. Streckart, J. Streit, D. J. Strozzi, J. Stutz, L. Summers, T. Suratwala, G. Sutcliffe, L. J. Suter, S. B. Sutton, V. Svidzinski, G. Swadling, W. Sweet, A. Szoke, M. Tabak, M. Takagi, A. Tambazidis, V. Tang, M. Taranowski, L. A. Taylor, S. Telford, W. Theobald, M. Thi, A. Thomas, C. A. Thomas, I. Thomas, R. Thomas, I. J. Thompson, A. Thongstisubskul, C. B. Thorsness, G. Tietbohl, R. E. Tipton, M. Tobin, N. Tomlin, R. Tommasini, A. J. Toreja, J. Torres, R. P. J. Town, S. Townsend, J. Trenholme, A. Trivelpiece, C. Trosseille, H. Truax, D. Trummer, S. Trummer, T. Truong, D. Tubbs, E. R. Tubman, T. Tunnell, D. Turnbull, R. E. Turner, M. Ulitsky, R. Upadhye, J. L. Vaher, P. VanArsdall, D. VanBlarcom, M. Vandenboomgaerde, R. VanQuinlan, B. M. Van Wousterghem, W. S. Varnum, A. L. Velikovich, A. Vella, C. P. Verdon, B. Vermillion, S. Vernon, R. Vesey, J. Vickers, R. M. Vignes, M. Visosky, J. Vocke, P. L. Volegov, S. Vonhof, R. Von Rotz, H. X. Vu, M. Vu, D. Wall, J. Wall, R. Wallace, B. Wallin, D. Walmer, C. A. Walsh, C. F. Walters, C. Waltz, A. Wan, A. Wang, Y. Wang, J. S. Wark, B. E. Warner, J. Watson, R. G. Watt, P. Watts, J. Weaver, R. P. Weaver, S. Weaver, C. R. Weber, P. Weber, S. V. Weber, P. Wegner, B. Welday, L. Welser-Sherrill, K. Weiss, K. B. Wharton, G. F. Wheeler, W. Whistler, R. K. White, H. D. Whitley, P. Whitman, M. E. Wickett, K. Widmann, C. Widmayer, J. Wiedwald, R. Wilcox, S. Wilcox, C. Wild, B. H. Wilde, C. H. Wilde, K. Wilhelmsen, M. D. Wilke, H. Wilkens, P. Wilkins, S. C. Wilks, E. A. Williams, G. J. Williams, W. Williams, W. H. Williams, D. C. Wilson, B. Wilson, E. Wilson, R. Wilson, S. Winters, P. J. Wisoff, M. Wittman, J. Wolfe, A. Wong, K. W. Wong, L. Wong, N. Wong, R. Wood, D. Woodhouse, J. Woodruff, D. T. Woods, S. Woods, B. N. Woodworth, E. Wooten, A. Wootton, K. Work, J. B. Workman, J. Wright, M. Wu, C. Wuest, F. J. Wysocki, H. Xu, M. Yamaguchi, B. Yang, S. T. Yang, J. Yatabe, C. B. Yeaman, B. C. Yee, S. A. Yi, L. Yin, B. Young, C. S. Young, C. V. Young, P. Young, K. Youngblood, J. Yu, R. Zacharias, G. Zagaris, N. Zaitseva, F. Zaka, F. Ze, B. Zeiger, M. Zika, G. B. Zimmerman, T. Zobrist, J. D. Zuegel, A. B. Zylstra, Achievement of Target Gain Larger than Unity in an Inertial Fusion Experiment. *Phys. Rev. Lett.* **132**, 065102 (2024).

11. E. N. Hahn, “Non-Equilibrium Simulations of Defects, Damage, and Phase Transformations in Extreme Regimes,” thesis, UC San Diego (2016).
12. W. J. M. Rankine, XV. On the thermodynamic theory of waves of finite longitudinal disturbance. *Philos. Trans. R. Soc. Lond.* **160**, 277–288 (1997).
13. H. H. Propagation du Mouvement dans les Corps. *J Ec Polyt Paris* **57**, 1–125 (1889).
14. M. A. Meyers, *Dynamic Behavior of Materials* (John Wiley & Sons, 1994).
15. R. Kinslow, *High-Velocity Impact Phenomena* (Elsevier, 2012).
16. R. E. Rudd, T. C. Germann, B. A. Remington, J. S. Wark, Metal deformation and phase transitions at extremely high strain rates. *MRS Bull.* **35**, 999–1006 (2010).
17. B. A. Remington, R. E. Rudd, J. S. Wark, From microjoules to megajoules and kilobars to gigabars: Probing matter at extreme states of deformation. *Phys. Plasmas* **22**, 090501 (2015).
18. A. J. MacKinnon, N. B. Meezan, J. S. Ross, S. Le Pape, L. Berzak Hopkins, L. Divol, D. Ho, J. Milovich, A. Pak, J. Ralph, T. Döppner, P. K. Patel, C. Thomas, R. Tommasini, S. Haan, A. G. MacPhee, J. McNaney, J. Caggiano, R. Hatarik, R. Bionta, T. Ma, B. Spears, J. R. Rygg, L. R. Benedetti, R. P. J. Town, D. K. Bradley, E. L. Dewald, D. Fittinghoff, O. S. Jones, H. R. Robey, J. D. Moody, S. Khan, D. A. Callahan, A. Hamza, J. Biener, P. M. Celliers, D. G. Braun, D. J. Erskine, S. T. Prisbrey, R. J. Wallace, B. Koziowski, R. Dylla-Spears, J. Sater, G. Collins, E. Storm, W. Hsing, O. Landen, J. L. Atherton, J. D. Lindl, M. J. Edwards, J. A. Frenje, M. Gatu-Johnson, C. K. Li, R. Petrasso, H. Rinderknecht, M. Rosenberg, F. H. Séguin, A. Zylstra, J. P. Knauer, G. Grim, N. Guler, F. Merrill, R. Olson, G. A. Kyrala, J. D.ilkenny, A. Nikroo, K. Moreno, D. E. Hoover, C. Wild, E. Werner, High-density carbon ablator experiments on the National Ignition Facility. *Phys. Plasmas* **21**, 056318 (2014).
19. J. Biener, P. B. Mirkarimi, J. W. Tringe, S. L. Baker, Y. Wang, S. O. Kucheyev, N. E. Teslich, K. J. J. Wu, A. V. Hamza, C. Wild, E. Woerner, P. Koidl, K. Bruehne, H.-J. Fecht, Diamond Ablators for Inertial Confinement Fusion. *Fusion Sci. Technol.* **49**, 737–742 (2006).
20. J. Biener, D. D. Ho, C. Wild, E. Woerner, M. M. Biener, B. S. El-dasher, D. G. Hicks, J. H. Eggert, P. M. Celliers, G. W. Collins, N. E. Teslich, B. J. Koziowski, S. W. Haan, A. V. Hamza, Diamond spheres for inertial confinement fusion. *Nucl. Fusion* **49**, 112001 (2009).
21. H. Kato, H. Yamada, S. Ohmagari, A. Chayahara, Y. Mokuno, Y. Fukuyama, N. Fujiwara, K. Miyaniishi, Y. Hironaka, K. Shigemori, Synthesis and characterization of diamond capsules for direct-drive inertial confinement fusion. *Diam. Relat. Mater.* **86**, 15–19 (2018).
22. A. L. Kritcher, D. Clark, S. Haan, S. A. Yi, A. B. Zylstra, D. A. Callahan, D. E. Hinkel, L. F. Berzak Hopkins, O. A. Hurricane, O. L. Landen, S. A. MacLaren, N. B. Meezan, P. K. Patel, J. Ralph, C. A. Thomas, R. Town, M. J. Edwards, Comparison of plastic, high density carbon, and beryllium as indirect drive NIF ablaters. *Phys. Plasmas* **25**, 056309 (2018).



23. J. D. Lindl, P. Amendt, R. L. Berger, S. G. Glendinning, S. H. Glenzer, S. W. Haan, R. L. Kauffman, O. L. Landen, L. J. Suter, The physics basis for ignition using indirect-drive targets on the National Ignition Facility. *Phys. Plasmas* **11**, 339–491 (2004).
24. S. Zhao, B. Kad, E. N. Hahn, B. A. Remington, C. E. Wehrenberg, C. M. Huntington, H.-S. Park, E. M. Bringa, K. L. More, M. A. Meyers, Pressure and shear-induced amorphization of silicon. *Extreme Mech. Lett.* **5**, 74–80 (2015).
25. E. Lescoute, T. De Rességuier, J.-M. Chevalier, M. Boustie, J.-P. Cuq-Lelandais, L. Berthe, Soft recovery technique to investigate dynamic fragmentation of laser shock-loaded metals. *Appl. Phys. Lett.* **95**, 211905 (2009).
26. V. Volterra, “Sur l’équilibre des corps élastiques multiplement connexes” in *Annales Scientifiques de l’École Normale Supérieure* (1907) vol. 24, pp. 401–517.
27. E. Orowan, The crystal plasticity. III: about the mechanism of the sliding. *Z Phys.* **89**, 634–659 (1934).
28. G. I. Taylor, The mechanism of plastic deformation of crystals. Part I.—Theoretical. *Proc. R. Soc. Lond. Ser. Contain. Pap. Math. Phys. Character* **145**, 362–387 (1934).
29. G. I. Taylor, The formation of emulsions in definable fields of flow. *Proc. R. Soc. Lond. Ser. Contain. Pap. Math. Phys. Character* **146**, 501–523 (1934).
30. I. Horiuti, M. Polanyi, Exchange reactions of hydrogen on metallic catalysts. *Trans. Faraday Soc.* **30**, 1164–1172 (1934).
31. J. M. Burgers, Geometrical considerations concerning the structural irregularities to be assumed in a crystal. *Proc. Phys. Soc.* **52**, 23 (1940).
32. J. M. Burgers, “Physics. — Some considerations on the fields of stress connected with dislocations in a regular crystal lattice. I” in *Selected Papers of J. M. Burgers*, F. T. M. Nieuwstadt, J. A. Steketee, Eds. (Springer Netherlands, Dordrecht, 1995; [https://doi.org/10.1007/978-94-011-0195-0\\_11](https://doi.org/10.1007/978-94-011-0195-0_11)), pp. 335–389.
33. A. H. Cottrell, LXXXVI. A note on the Portevin-Le Chatelier effect. *Lond. Edinb. Dublin Philos. Mag. J. Sci.* **44**, 829–832 (1953).
34. F. R. N. Nabarro, Z. S. Basinski, D. B. Holt, The plasticity of pure single crystals. *Adv. Phys.* **13**, 193–323 (1964).
35. J. D. Eshelby, F. C. Frank, F. R. N. Nabarro, XLI. The equilibrium of linear arrays of dislocations. *Lond. Edinb. Dublin Philos. Mag. J. Sci.* **42**, 351–364 (1951).
36. D. Hull, D. J. Bacon, *Introduction to Dislocations* (Elsevier, 2011).
37. V. Bulatov, W. Cai, *Computer Simulations of Dislocations* (OUP Oxford, 2006).

38. M. A. Meyers, C. Taylor Aimone, Dynamic fracture (spalling) of metals. *Prog. Mater. Sci.* **28**, 1–96 (1983).
39. D. B. Reisman, W. G. Wolfer, A. Elsholz, M. D. Furnish, Isentropic compression of irradiated stainless steel on the Z accelerator. *J. Appl. Phys.* **93**, 8952–8957 (2003).
40. R. E. Rudd, J. F. Belak, Void nucleation and associated plasticity in dynamic fracture of polycrystalline copper: an atomistic simulation. *Comput. Mater. Sci.* **24**, 148–153 (2002).
41. P. Erhart, E. M. Bringa, M. Kumar, K. Albe, Atomistic mechanism of shock-induced void collapse in nanoporous metals. *Phys. Rev. B* **72**, 052104 (2005).
42. V. A. Lubarda, M. S. Schneider, D. H. Kalantar, B. A. Remington, M. A. Meyers, Void growth by dislocation emission. *Acta Mater.* **52**, 1397–1408 (2004).
43. T. Hatano, Dislocation Nucleation in Shocked fcc Solids: Effects of Temperature and Preexisting Voids. *Phys. Rev. Lett.* **93**, 085501 (2004).
44. Y. Tang, E. M. Bringa, B. A. Remington, M. A. Meyers, Growth and collapse of nanovoids in tantalum monocrystals. *Acta Mater.* **59**, 1354–1372 (2011).
45. Y. Tang, E. M. Bringa, M. A. Meyers, Ductile tensile failure in metals through initiation and growth of nanosized voids. *Acta Mater.* **60**, 4856–4865 (2012).
46. A. Hospital, J. R. Goñi, M. Orozco, J. L. Gelpí, Molecular dynamics simulations: advances and applications. *Adv. Appl. Bioinforma. Chem.* **8**, 37–47 (2015).
47. N. S. Abramov, S. M. Abramov, November 2022 Top500 List Overview. *Supercomput. Front. Innov.* **10**, 4–17 (2023).
48. V. Rajaraman, Frontier — World’s First ExaFLOPS Supercomputer. *Resonance* **28**, 567–576 (2023).
49. K. Kadau, T. C. Germann, P. S. Lomdahl, B. L. Holian, Atomistic simulations of shock-induced transformations and their orientation dependence in bcc Fe single crystals. *Phys. Rev. B* **72**, 064120 (2005).
50. N. Tchipev, S. Seckler, M. Heinen, J. Vrabc, F. Gratl, M. Horsch, M. Bernreuther, C. W. Glass, C. Niethammer, N. Hammer, B. Krischok, M. Resch, D. Kranzlmüller, H. Hasse, H.-J. Bungartz, P. Neumann, TweTriS: Twenty trillion-atom simulation. *Int. J. High Perform. Comput. Appl.* **33**, 838–854 (2019).
51. K. Nguyen-Cong, J. T. Willman, S. G. Moore, A. B. Belonoshko, R. Gayatri, E. Weinberg, M. A. Wood, A. P. Thompson, I. I. Oleynik, “Billion atom molecular dynamics simulations of carbon at extreme conditions and experimental time and length scales” in *Proceedings of the International Conference for High Performance Computing, Networking, Storage and Analysis* (Association for Computing Machinery, New York, NY, USA, 2021; <https://dl.acm.org/doi/10.1145/3458817.3487400>)SC '21, pp. 1–12.

52. M. W. Finnis, Concepts for simulating and understanding materials at the atomic scale. *MRS Bull.* **37**, 477–484 (2012).
53. J. S. Brown, Interatomic potential parameters of solid neon and argon. *Proc. Phys. Soc.* **89**, 987 (1966).
54. J. E. Lennard-Jones, S. Chapman, On the forces between atoms and ions. *Proc. R. Soc. Lond. Ser. Contain. Pap. Math. Phys. Character* **109**, 584–597 (1997).
55. P. M. Morse, Diatomic Molecules According to the Wave Mechanics. II. Vibrational Levels. *Phys. Rev.* **34**, 57–64 (1929).
56. R. A. Buckingham, J. E. Lennard-Jones, The classical equation of state of gaseous helium, neon and argon. *Proc. R. Soc. Lond. Ser. Math. Phys. Sci.* **168**, 264–283 (1997).
57. A. Lombardi, F. Palazzetti, A comparison of interatomic potentials for rare gas nanoaggregates. *J. Mol. Struct. THEOCHEM* **852**, 22–29 (2008).
58. M. S. Daw, M. I. Baskes, Embedded-atom method: Derivation and application to impurities, surfaces, and other defects in metals. *Phys. Rev. B* **29**, 6443–6453 (1984).
59. J. Tersoff, Chemical order in amorphous silicon carbide. *Phys. Rev. B* **49**, 16349 (1994).
60. J. Tersoff, New empirical model for the structural properties of silicon. *Phys. Rev. Lett.* **56**, 632–635 (1986).
61. J. Tersoff, New empirical approach for the structure and energy of covalent systems. *Phys. Rev. B* **37**, 6991–7000 (1988).
62. J. Tersoff, Modeling solid-state chemistry: Interatomic potentials for multicomponent systems. *Phys. Rev. B* **39**, 5566–5568 (1989).
63. D. W. Brenner, Relationship between the embedded-atom method and Tersoff potentials. *Phys. Rev. Lett.* **63**, 1022–1022 (1989).
64. A. I. Vakis, V. A. Yastrebov, J. Scheibert, L. Nicola, D. Dini, C. Minfray, A. Almqvist, M. Paggi, S. Lee, G. Limbert, J. F. Molinari, G. Anciaux, R. Aghababaei, S. Echeverri Restrepo, A. Papangelo, A. Cammarata, P. Nicolini, C. Putignano, G. Carbone, S. Stupkiewicz, J. Lengiewicz, G. Costagliola, F. Bosia, R. Guarino, N. M. Pugno, M. H. Müser, M. Ciavarella, Modeling and simulation in tribology across scales: An overview. *Tribol. Int.* **125**, 169–199 (2018).
65. E. Schrödinger, An Undulatory Theory of the Mechanics of Atoms and Molecules. *Phys. Rev.* **28**, 1049–1070 (1926).
66. P. R. C. Kent, “Techniques and Applications of Quantum Monte Carlo,” thesis, Cambridge (1999).

67. M. Born, Born-oppeneheimer approximation. *Ann Phys* **84**, 457–484 (1927).
68. D. R. Hartree, The Wave Mechanics of an Atom with a Non-Coulomb Central Field. Part II. Some Results and Discussion. *Math. Proc. Camb. Philos. Soc.* **24**, 111–132 (1928).
69. M. Head-Gordon, R. J. Rico, M. Oumi, T. J. Lee, A doubles correction to electronic excited states from configuration interaction in the space of single substitutions. *Chem. Phys. Lett.* **219**, 21–29 (1994).
70. G. D. Purvis III, R. J. Bartlett, A full coupled-cluster singles and doubles model: The inclusion of disconnected triples. *J. Chem. Phys.* **76**, 1910–1918 (1982).
71. P. Hohenberg, W. Kohn, Inhomogeneous Electron Gas. *Phys. Rev.* **136**, B864–B871 (1964).
72. W. Kohn, L. J. Sham, Self-Consistent Equations Including Exchange and Correlation Effects. *Phys. Rev.* **140**, A1133–A1138 (1965).
73. F. Bechstedt, “Density Functional Theory” in *Many-Body Approach to Electronic Excitations: Concepts and Applications*, F. Bechstedt, Ed. (Springer, Berlin, Heidelberg, 2015; [https://doi.org/10.1007/978-3-662-44593-8\\_5](https://doi.org/10.1007/978-3-662-44593-8_5)), pp. 73–88.
74. D. S. Sholl, J. A. Steckel, *Density Functional Theory: A Practical Introduction* (John Wiley & Sons, 2022).
75. A. Gross, M. Scheffler, *Ab initio* quantum and molecular dynamics of the dissociative adsorption of hydrogen on Pd(100). *Phys. Rev. B* **57**, 2493–2506 (1998).
76. G. Wiesenekker, G. J. Kroes, E. J. Baerends, An analytical six-dimensional potential energy surface for dissociation of molecular hydrogen on Cu(100). *J. Chem. Phys.* **104**, 7344–7358 (1996).
77. V. L. Deringer, G. Csányi, Machine learning based interatomic potential for amorphous carbon. *Phys. Rev. B* **95**, 094203 (2017).
78. A. P. Thompson, L. P. Swiler, C. R. Trott, S. M. Foiles, G. J. Tucker, Spectral neighbor analysis method for automated generation of quantum-accurate interatomic potentials. *J. Comput. Phys.* **285**, 316–330 (2015).
79. J. T. Willman, K. Nguyen-Cong, A. S. Williams, A. B. Belonoshko, S. G. Moore, A. P. Thompson, M. A. Wood, I. I. Oleynik, Machine learning interatomic potential for simulations of carbon at extreme conditions. *Phys. Rev. B* **106**, L180101 (2022).
80. D. A. Case, H. M. Aktulga, K. Belfon, D. S. Cerutti, G. A. Cisneros, V. W. D. Cruzeiro, N. Forouzesheh, T. J. Giese, A. W. Götz, H. Gohlke, S. Izadi, K. Kasavajhala, M. C. Kaymak, E. King, T. Kurtzman, T.-S. Lee, P. Li, J. Liu, T. Luchko, R. Luo, M. Manathunga, M. R. Machado, H. M. Nguyen, K. A. O’Hearn, A. V. Onufriev, F. Pan, S. Pantano, R. Qi, A. Rahnamoun, A. Risheh, S. Schott-Verdugo, A. Shajan, J. Swails, J. Wang, H. Wei, X. Wu, Y. Wu, S. Zhang, S. Zhao, Q. Zhu, T. E. I. Cheatham, D. R. Roe, A. Roitberg, C.

- Simmerling, D. M. York, M. C. Nagan, K. M. Jr. Merz, AmberTools. *J. Chem. Inf. Model.* **63**, 6183–6191 (2023).
81. H. BEKKER, H. BERENDSEN, E. DIJKSTRA, S. ACHTEROP, R. VONDRUMEN, D. VANDERSPOEL, A. SIJBERS, H. Keegstra, M. RENARDUS, GROMACS - A PARALLEL COMPUTER FOR MOLECULAR-DYNAMICS SIMULATIONS: 4th International Conference on Computational Physics (PC 92). *Phys. Comput.* **92**, 252–256 (1993).
82. S. Plimpton, Fast Parallel Algorithms for Short-Range Molecular Dynamics. *J. Comput. Phys.* **117**, 1–19 (1995).
83. A. P. Thompson, H. M. Aktulga, R. Berger, D. S. Bolintineanu, W. M. Brown, P. S. Crozier, P. J. In't Veld, A. Kohlmeyer, S. G. Moore, T. D. Nguyen, LAMMPS-a flexible simulation tool for particle-based materials modeling at the atomic, meso, and continuum scales. *Comput. Phys. Commun.* **271**, 108171 (2022).
84. P. Hirel, AtomsK: A tool for manipulating and converting atomic data files. *Comput. Phys. Commun.* **197**, 212–219 (2015).
85. L. Verlet, Computer “Experiments” on Classical Fluids. I. Thermodynamical Properties of Lennard-Jones Molecules. *Phys. Rev.* **159**, 98–103 (1967).
86. D. Levesque, L. Verlet, Molecular dynamics and time reversibility. *J. Stat. Phys.* **72**, 519–537 (1993).
87. B. L. Holian, P. S. Lomdahl, Plasticity Induced by Shock Waves in Nonequilibrium Molecular-Dynamics Simulations. *Science* **280**, 2085–2088 (1998).
88. B. L. Holian, W. G. Hoover, B. Moran, G. K. Straub, Shock-wave structure via nonequilibrium molecular dynamics and Navier-Stokes continuum mechanics. *Phys. Rev. A* **22**, 2798–2808 (1980).
89. A. V. Bolesta, L. Zheng, D. L. Thompson, T. D. Sewell, Molecular dynamics simulations of shock waves using the absorbing boundary condition: A case study of methane. *Phys. Rev. B* **76**, 224108 (2007).
90. V. V. Zhakhovskii, K. Nishihara, S. I. Anisimov, Shock wave structure in dense gases. *J. Exp. Theor. Phys. Lett.* **66**, 99–105 (1997).
91. V. V. Zhakhovsky, M. M. Budzevich, N. A. Inogamov, I. I. Oleynik, C. T. White, Two-Zone Elastic-Plastic Single Shock Waves in Solids. *Phys. Rev. Lett.* **107**, 135502 (2011).
92. P. Wen, G. Tao, D. E. Spearot, S. R. Phillpot, Molecular dynamics simulation of the shock response of materials: A tutorial. *J. Appl. Phys.* **131**, 051101 (2022).
93. C.-H. Lu, “Laser Compression of Tantalum,” thesis, UC San Diego.

94. S. Zhao, E. N. Hahn, B. Kad, B. A. Remington, C. E. Wehrenberg, E. M. Bringa, M. A. Meyers, Amorphization and nanocrystallization of silicon under shock compression. *Acta Mater.* **103**, 519–533 (2016).
95. R. F. Smith, R. W. Minich, R. E. Rudd, J. H. Eggert, C. A. Bolme, S. L. Brygoo, A. M. Jones, G. W. Collins, Orientation and rate dependence in high strain-rate compression of single-crystal silicon. *Phys. Rev. B* **86**, 245204 (2012).
96. A. Stukowski, Visualization and analysis of atomistic simulation data with OVITO—the Open Visualization Tool. *Model. Simul. Mater. Sci. Eng.* **18**, 015012 (2009).
97. A. P. Thompson, S. J. Plimpton, W. Mattson, General formulation of pressure and stress tensor for arbitrary many-body interaction potentials under periodic boundary conditions. *J. Chem. Phys.* **131**, 154107 (2009).
98. D. Faken, H. Jónsson, Systematic analysis of local atomic structure combined with 3D computer graphics. *Comput. Mater. Sci.* **2**, 279–286 (1994).
99. H. Tsuzuki, P. S. Branicio, J. P. Rino, Structural characterization of deformed crystals by analysis of common atomic neighborhood. *Comput. Phys. Commun.* **177**, 518–523 (2007).
100. A. Stukowski, Structure identification methods for atomistic simulations of crystalline materials. *Model. Simul. Mater. Sci. Eng.* **20**, 045021 (2012).
101. P. M. Larsen, S. Schmidt, J. Schiøtz, Robust structural identification via polyhedral template matching. *Model. Simul. Mater. Sci. Eng.* **24**, 055007 (2016).
102. E. Maras, O. Trushin, A. Stukowski, T. Ala-Nissila, H. Jónsson, Global transition path search for dislocation formation in Ge on Si(001). *Comput. Phys. Commun.* **205**, 13–21 (2016).
103. K. Kulasinski, S. Keten, S. V. Churakov, D. Derome, J. Carmeliet, A comparative molecular dynamics study of crystalline, paracrystalline and amorphous states of cellulose. *Cellulose* **21**, 1103–1116 (2014).
104. A. Stukowski, V. V. Bulatov, A. Arsenlis, Automated identification and indexing of dislocations in crystal interfaces. *Model. Simul. Mater. Sci. Eng.* **20**, 085007 (2012).
105. A. Stukowski, K. Albe, Extracting dislocations and non-dislocation crystal defects from atomistic simulation data. *Model. Simul. Mater. Sci. Eng.* **18**, 085001 (2010).
106. F. Aquistapace, D. Castillo-Castro, R. I. González, N. Amigo, G. García Vidable, D. R. Tramontina, F. J. Valencia, E. M. Bringa, Plasticity in diamond nanoparticles: dislocations and amorphization during loading and dislocation multiplication during unloading. *J. Mater. Sci.* **59**, 4788–4809 (2024).
107. E. N. Hahn, S. Zhao, E. M. Bringa, M. A. Meyers, Supersonic Dislocation Bursts in Silicon. *Sci. Rep.* **6**, 26977 (2016).

108. J. M. D. Lane, A. P. Thompson, T. J. Vogler, Enhanced densification under shock compression in porous silicon. *Phys. Rev. B* **90**, 134311 (2014).
109. K. Mylvaganam, L. C. Zhang, Nanotwinning in monocrystalline silicon upon nanoscratching. *Scr. Mater.* **65**, 214–216 (2011).
110. L. M. Hale, X. Zhou, J. A. Zimmerman, N. R. Moody, R. Ballarini, W. W. Gerberich, Phase transformations, dislocations and hardening behavior in uniaxially compressed silicon nanospheres. *Comput. Mater. Sci.* **50**, 1651–1660 (2011).
111. I. I. Oleynik, S. V. Zybin, M. L. Elert, C. T. White, Nanoscale Molecular Dynamics Simulaton of Shock Compression of Silicon. *AIP Conf. Proc.* **845**, 413–416 (2006).
112. X. Gu, Y. Lin, I. I. Oleynik, C. T. White, MOLECULAR DYNAMICS SIMULATIONS OF SHOCK-INDUCED DEFECT HEALING IN SILICON. *AIP Conf. Proc.* **1195**, 793–796 (2009).
113. D. E. Kim, S. I. Oh, Atomistic simulation of structural phase transformations in monocrystalline silicon induced by nanoindentation. *Nanotechnology* **17**, 2259 (2006).
114. G. Mogni, A. Higginbotham, K. Gaál-Nagy, N. Park, J. S. Wark, Molecular dynamics simulations of shock-compressed single-crystal silicon. *Phys. Rev. B* **89**, 064104 (2014).
115. W. Cai, V. V. Bulatov, J. F. Justo, A. S. Argon, S. Yip, Intrinsic Mobility of a Dissociated Dislocation in Silicon. *Phys. Rev. Lett.* **84**, 3346–3349 (2000).
116. T. Kumagai, S. Izumi, S. Hara, S. Sakai, Development of bond-order potentials that can reproduce the elastic constants and melting point of silicon for classical molecular dynamics simulation. *Comput. Mater. Sci.* **39**, 457–464 (2007).
117. P. M. Agrawal, L. M. Raff, R. Komanduri, Monte Carlo simulations of void-nucleated melting of silicon via modification in the Tersoff potential parameters. *Phys. Rev. B* **72**, 125206 (2005).
118. F. H. Stillinger, T. A. Weber, Computer simulation of local order in condensed phases of silicon. *Phys. Rev. B* **31**, 5262–5271 (1985).
119. K. Nordlund, M. Ghaly, R. S. Averback, M. Caturla, T. Diaz de la Rubia, J. Tarus, Defect production in collision cascades in elemental semiconductors and fcc metals. *Phys. Rev. B* **57**, 7556–7570 (1998).
120. M. Timonova, B. J. Thijsse, Thermodynamic properties and phase transitions of silicon using a new MEAM potential. *Comput. Mater. Sci.* **48**, 609–620 (2010).
121. S. Ryu, C. R. Weinberger, M. I. Baskes, W. Cai, Improved modified embedded-atom method potentials for gold and silicon. *Model. Simul. Mater. Sci. Eng.* **17**, 075008 (2009).

122. M. Z. Bazant, E. Kaxiras, J. F. Justo, Environment-dependent interatomic potential for bulk silicon. *Phys. Rev. B* **56**, 8542–8552 (1997).
123. J. F. Justo, M. Z. Bazant, E. Kaxiras, V. V. Bulatov, S. Yip, Interatomic potential for silicon defects and disordered phases. *Phys. Rev. B* **58**, 2539–2550 (1998).
124. M. Z. Bazant, E. Kaxiras, Modeling of Covalent Bonding in Solids by Inversion of Cohesive Energy Curves. *Phys. Rev. Lett.* **77**, 4370–4373 (1996).
125. D. Sen, A. Cohen, A. P. Thompson, A. V. Duin, W. A. G. III, M. J. Buehler, Direct atomistic simulation of brittle-to-ductile transition in silicon single crystals. *MRS Online Proc. Libr. OPL* **1272**, 1272 (2010).
126. L. Pastewka, A. Klemenz, P. Gumbsch, M. Moseler, Screened empirical bond-order potentials for Si-C. *Phys. Rev. B* **87**, 205410 (2013).
127. C. A. Becker, F. Tavazza, Z. T. Trautt, R. A. Buarque de Macedo, Considerations for choosing and using force fields and interatomic potentials in materials science and engineering. *Curr. Opin. Solid State Mater. Sci.* **17**, 277–283 (2013).
128. J. Godet, L. Pizzagalli, S. Brochard, P. Beauchamp, Comparison between classical potentials and ab initio methods for silicon under large shear. *J. Phys. Condens. Matter* **15**, 6943 (2003).
129. S. J. Turneaure, N. Sinclair, Y. M. Gupta, Real-Time Examination of Atomistic Mechanisms during Shock-Induced Structural Transformation in Silicon. *Phys. Rev. Lett.* **117**, 045502 (2016).
130. D. C. Swift, G. J. Ackland, A. Hauer, G. A. Kyrala, First-principles equations of state for simulations of shock waves in silicon. *Phys. Rev. B* **64**, 214107 (2001).
131. S. Zhao, E. N. Hahn, B. Kad, B. A. Remington, E. M. Bringa, M. A. Meyers, Shock compression of [001] single crystal silicon. *Eur. Phys. J. Spec. Top.* **225**, 335–341 (2016).
132. A. Higginbotham, P. G. Stubbley, A. J. Comley, J. H. Eggert, J. M. Foster, D. H. Kalantar, D. McGonegle, S. Patel, L. J. Peacock, S. D. Rothman, R. F. Smith, M. J. Suggit, J. S. Wark, Inelastic response of silicon to shock compression. *Sci. Rep.* **6**, 24211 (2016).
133. R. F. Smith, C. A. Bolme, D. J. Erskine, P. M. Celliers, S. Ali, J. H. Eggert, S. L. Brygoo, B. D. Hammel, J. Wang, G. W. Collins, Heterogeneous flow and brittle failure in shock-compressed silicon. *J. Appl. Phys.* **114**, 133504 (2013).
134. A. Loveridge-Smith, A. Allen, J. Belak, T. Boehly, A. Hauer, B. Holian, D. Kalantar, G. Kyrala, R. W. Lee, P. Lomdahl, M. A. Meyers, D. Paisley, S. Pollaine, B. Remington, D. C. Swift, S. Weber, J. S. Wark, Anomalous Elastic Response of Silicon to Uniaxial Shock Compression on Nanosecond Time Scales. *Phys. Rev. Lett.* **86**, 2349–2352 (2001).



135. G. J. Cheng, M. A. Shehadeh, Dislocation behavior in silicon crystal induced by laser shock peening: A multiscale simulation approach. *Scr. Mater.* **53**, 1013–1018 (2005).
136. N. L. Coleburn, J. W. Forbes, H. D. Jones, Electrical measurements in silicon under shock-wave compression. *J. Appl. Phys.* **43**, 5007–5012 (1972).
137. W. H. Gust, E. B. Royce, Axial Yield Strengths and Two Successive Phase Transition Stresses for Crystalline Silicon. *J. Appl. Phys.* **42**, 1897–1905 (1971).
138. S. J. Turneaure, Y. M. Gupta, Inelastic deformation and phase transformation of shock compressed silicon single crystals. *Appl. Phys. Lett.* **91**, 201913 (2007).
139. S. J. Turneaure, Y. M. Gupta, Real-time x-ray diffraction at the impact surface of shocked crystals. *J. Appl. Phys.* **111**, 026101 (2012).
140. M. Gamero-Castaño, A. Torrents, L. Valdevit, J.-G. Zheng, Pressure-Induced Amorphization in Silicon Caused by the Impact of Electrosprayed Nanodroplets. *Phys. Rev. Lett.* **105**, 145701 (2010).
141. J. S. Wark, R. R. Whitlock, A. Hauer, J. E. Swain, P. J. Solone, Shock launching in silicon studied with use of pulsed x-ray diffraction. *Phys. Rev. B* **35**, 9391–9394 (1987).
142. L. Rapp, B. Haberl, C. J. Pickard, J. E. Bradby, E. G. Gamaly, J. S. Williams, A. V. Rode, Experimental evidence of new tetragonal polymorphs of silicon formed through ultrafast laser-induced confined microexplosion. *Nat. Commun.* **6**, 7555 (2015).
143. R. Chen, J. Luo, D. Guo, H. Lei, Dynamic phase transformation of crystalline silicon under the dry and wet impact studied by molecular dynamics simulation. *J. Appl. Phys.* **108**, 073521 (2010).
144. F. Saiz, M. Gamero-Castaño, Amorphization of silicon induced by nanodroplet impact: A molecular dynamics study. *J. Appl. Phys.* **112**, 054302 (2012).
145. F. Saiz, M. Gamero-Castaño, Atomistic modeling of the sputtering of silicon by electrosprayed nanodroplets. *J. Appl. Phys.* **116**, 054303 (2014).
146. O. T. Kingstedt, J. Lambros, Ultra-high Speed Imaging of Laser-Induced Spallation. *Exp. Mech.* **55**, 587–598 (2015).
147. I. I. Oleynik, S. V. Zybin, M. L. Elert, C. T. White, Shear Stresses in Shock-Compressed Covalent Solids. *AIP Conf. Proc.* **845**, 417–420 (2006).
148. P. Erhart, K. Albe, Analytical potential for atomistic simulations of silicon, carbon, and silicon carbide. *Phys. Rev. B* **71**, 035211 (2005).
149. P. K. Schelling, Phase behavior and kinetics of a new bond-order potential for silicon. *Comput. Mater. Sci.* **44**, 274–279 (2008).

150. V. S. Dozhdikov, A. Yu. Basharin, P. R. Levashov, Two-phase simulation of the crystalline silicon melting line at pressures from  $-1$  to 3 GPa. *J. Chem. Phys.* **137**, 054502 (2012).
151. F. Romano, J. Russo, H. Tanaka, Novel stable crystalline phase for the Stillinger-Weber potential. *Phys. Rev. B* **90**, 014204 (2014).
152. Y. He, L. Zhong, F. Fan, C. Wang, T. Zhu, S. X. Mao, In situ observation of shear-driven amorphization in silicon crystals. *Nat. Nanotechnol.* **11**, 866–871 (2016).
153. Y.-C. Wang, W. Zhang, L.-Y. Wang, Z. Zhuang, E. Ma, J. Li, Z.-W. Shan, In situ TEM study of deformation-induced crystalline-to-amorphous transition in silicon. *NPG Asia Mater.* **8**, e291–e291 (2016).
154. S. Wippermann, Y. He, M. Vörös, G. Galli, Novel silicon phases and nanostructures for solar energy conversion. *Appl. Phys. Rev.* **3**, 040807 (2016).
155. L. L. Boyer, E. Kaxiras, J. L. Feldman, J. Q. Broughton, M. J. Mehl, New low-energy crystal structure for silicon. *Phys. Rev. Lett.* **67**, 715–718 (1991).
156. D. M. Többens, N. Stüßer, K. Knorr, H. M. Mayer, G. Lampert, E9: The New High-Resolution Neutron Powder Diffractometer at the Berlin Neutron Scattering Center. *Mater. Sci. Forum* **378–381**, 288–293 (2001).
157. M. I. Baskes, Modified embedded-atom potentials for cubic materials and impurities. *Phys. Rev. B* **46**, 2727–2742 (1992).
158. A. C. T. van Duin, S. Dasgupta, F. Lorant, W. A. Goddard, ReaxFF: A Reactive Force Field for Hydrocarbons. *J. Phys. Chem. A* **105**, 9396–9409 (2001).
159. A. C. T. van Duin, A. Strachan, S. Stewman, Q. Zhang, X. Xu, W. A. Goddard, ReaxFFSiO Reactive Force Field for Silicon and Silicon Oxide Systems. *J. Phys. Chem. A* **107**, 3803–3811 (2003).
160. E. J. Reed, L. E. Fried, J. D. Joannopoulos, A Method for Tractable Dynamical Studies of Single and Double Shock Compression. *Phys. Rev. Lett.* **90**, 235503 (2003).
161. E. M. Bringa, A. Caro, Y. Wang, M. Victoria, J. M. McNaney, B. A. Remington, R. F. Smith, B. R. Torralva, H. Van Swygenhoven, Ultrahigh Strength in Nanocrystalline Materials Under Shock Loading. *Science* **309**, 1838–1841 (2005).
162. B. B. Karki, G. J. Ackland, J. Crain, Elastic instabilities in crystals from ab initio stress - strain relations. *J. Phys. Condens. Matter* **9**, 8579 (1997).
163. V. Mazhukin, A. Shapranov, O. Koroleva, A. Rudenko, MOLECULAR DYNAMICS SIMULATION OF CRITICAL POINT PARAMETERS FOR SILICON. *Math. MONTISNIGRI XXXI*, 64–77 (2014).

164. S. K. Deb, M. Wilding, M. Somayazulu, P. F. McMillan, Pressure-induced amorphization and an amorphous–amorphous transition in densified porous silicon. *Nature* **414**, 528–530 (2001).
165. T. Goto, T. Sato, Y. Syono, Reduction of Shear Strength and Phase-Transition in Shock-Loaded Silicon. *Jpn. J. Appl. Phys.* **21**, L369 (1982).
166. W. R. Grigsby, “Experimental studies of high energy density silicon using ultra-fast lasers,” thesis, The University of Texas at Austin, United States -- Texas.
167. M. N. Pavlovskii, Formation of metallic modifications of germanium and silicon under shock loading. *SOV PHYS SOLID STATE FEB 1968 9--11-- 2514- 2518* (1968).
168. O. Strickson, E. Artacho,  $\text{Ab initio}$  calculation of the shock Hugoniot of bulk silicon. *Phys. Rev. B* **93**, 094107 (2016).
169. E. N. Hahn, S. J. Fensin, Influence of defects on the shock Hugoniot of tantalum. *J. Appl. Phys.* **125**, 215902 (2019).
170. D. Chrobak, N. Tymiak, A. Beaber, O. Ugurlu, W. W. Gerberich, R. Nowak, Deconfinement leads to changes in the nanoscale plasticity of silicon. *Nat. Nanotechnol.* **6**, 480–484 (2011).
171. J. Guérolé, S. Brochard, J. Godet, Unexpected slip mechanism induced by the reduced dimensions in silicon nanostructures: Atomistic study. *Acta Mater.* **59**, 7464–7472 (2011).
172. L. M. Hale, D.-B. Zhang, X. Zhou, J. A. Zimmerman, N. R. Moody, T. Dumitrica, R. Ballarini, W. W. Gerberich, Dislocation morphology and nucleation within compressed Si nanospheres: A molecular dynamics study. *Comput. Mater. Sci.* **54**, 280–286 (2012).
173. P. W. Bridgman, Effects of High Shearing Stress Combined with High Hydrostatic Pressure. *Phys. Rev.* **48**, 825–847 (1935).
174. E. Teller, On the Speed of Reactions at High Pressures. *J. Chem. Phys.* **36**, 901–903 (1962).
175. H. C. Chen, J. C. LaSalvia, V. F. Nesterenko, M. A. Meyers, Shear localization and chemical reaction in high-strain, high-strain-rate deformation of Ti–Si powder mixtures. *Acta Mater.* **46**, 3033–3046 (1998).
176. C. Cheng, W. H. Huang, H. J. Li, Thermodynamics of uniaxial phase transition:  $\text{Ab initio}$  study of the diamond-to- $\beta$ -tin transition in Si and Ge. *Phys. Rev. B* **63**, 153202 (2001).
177. K. Gaál-Nagy, D. Strauch, Transition pressures and enthalpy barriers for the cubic diamond  $\rightarrow \beta$ -tin transition in Si and Ge under nonhydrostatic conditions. *Phys. Rev. B* **73**, 134101 (2006).

178. R. G. Hennig, A. Wadehra, K. P. Driver, W. D. Parker, C. J. Umrigar, J. W. Wilkins, Phase transformation in Si from semiconducting diamond to metallic  $\beta$ -Sn phase in QMC and DFT under hydrostatic and anisotropic stress. *Phys. Rev. B* **82**, 014101 (2010).
179. M. Durandurdu, Diamond to  $\beta$ -Sn phase transition of silicon under hydrostatic and nonhydrostatic compressions. *J. Phys. Condens. Matter* **20**, 325232 (2008).
180. I.-H. Lee, J.-W. Jeong, K. J. Chang, Invariant-molecular-dynamics study of the diamond-to- $\beta$ -Sn transition in Si under hydrostatic and uniaxial compressions. *Phys. Rev. B* **55**, 5689–5693 (1997).
181. K. Mizushima, S. Yip, E. Kaxiras, Ideal crystal stability and pressure-induced phase transition in silicon. *Phys. Rev. B* **50**, 14952–14959 (1994).
182. P. Focher, G. L. Chiarotti, M. Bernasconi, E. Tosatti, M. Parrinello, Structural Phase Transformations via First-Principles Simulation. *Europhys. Lett.* **26**, 345 (1994).
183. V. Domnich, Y. Aratyn, W. M. Kriven, Y. Gogotsi, Temperature dependence of silicon hardness: experimental evidence of phase transformations. *Rev Adv Mater Sci* **17**, 33–41 (2008).
184. S. Goel, X. Luo, A. Agrawal, R. L. Reuben, Diamond machining of silicon: A review of advances in molecular dynamics simulation. *Int. J. Mach. Tools Manuf.* **88**, 131–164 (2015).
185. M. C. Gupta, A. L. Ruoff, Static compression of silicon in the [100] and in the [111] directions. *J. Appl. Phys.* **51**, 1072–1075 (1980).
186. E. Kaxiras, L. L. Boyer, Exploring the structure of solids through magic strains: prediction of a new metallic phase of Si. *Model. Simul. Mater. Sci. Eng.* **1**, 91 (1992).
187. E. Kaxiras, L. L. Boyer, Energetics of large lattice strains: Application to silicon. *Phys. Rev. B* **50**, 1535–1540 (1994).
188. Z. Zhang, A. Stukowski, H. M. Urbassek, Interplay of dislocation-based plasticity and phase transformation during Si nanoindentation. *Comput. Mater. Sci.* **119**, 82–89 (2016).
189. Y. B. Gerbig, S. J. Stranick, R. F. Cook, Direct observation of phase transformation anisotropy in indented silicon studied by confocal Raman spectroscopy. *Phys. Rev. B* **83**, 205209 (2011).
190. Y. B. Gerbig, C. A. Michaels, R. F. Cook, In situ observation of the spatial distribution of crystalline phases during pressure-induced transformations of indented silicon thin films. *J. Mater. Res.* **30**, 390–406 (2015).
191. P. Beaucage, N. Mousseau, Liquid–liquid phase transition in Stillinger–Weber silicon. *J. Phys. Condens. Matter* **17**, 2269 (2005).

192. S. Zhao, B. Kad, E. N. Hahn, B. A. Remington, C. E. Wehrenberg, C. M. Huntington, H.-S. Park, E. M. Bringa, K. L. More, M. A. Meyers, Pressure and shear-induced amorphization of silicon. *Extreme Mech. Lett.* **5**, 74–80 (2015).
193. K. Nguyen-Cong, J. T. Willman, J. M. Gonzalez, A. S. Williams, A. B. Belonoshko, S. G. Moore, A. P. Thompson, M. A. Wood, J. H. Eggert, M. Millot, L. A. Zepeda-Ruiz, I. I. Oleynik, Extreme Metastability of Diamond and its Transformation to the BC8 Post-Diamond Phase of Carbon. *J. Phys. Chem. Lett.* **15**, 1152–1160 (2024).
194. D. C. Swift, R. G. Kraus, E. N. Loomis, D. G. Hicks, J. M. McNaney, R. P. Johnson, Shock formation and the ideal shape of ramp compression waves. *Phys. Rev. E* **78**, 066115 (2008).
195. R. Smith, J. Eggert, R. Jeanloz, T. Duffy, D. Braun, J. Patterson, R. Rudd, J. Biener, A. Lazicki, A. Hamza, others, Ramp compression of diamond to five terapascals. *Nature* **511**, 330–333 (2014).
196. A. Lazicki, D. McGonegle, J. R. Rygg, D. G. Braun, D. C. Swift, M. G. Gorman, R. F. Smith, P. G. Heighway, A. Higginbotham, M. J. Suggit, D. E. Fratanduono, F. Coppari, C. E. Wehrenberg, R. G. Kraus, D. Erskine, J. V. Bernier, J. M. McNaney, R. E. Rudd, G. W. Collins, J. H. Eggert, J. S. Wark, Metastability of diamond ramp-compressed to 2 terapascals. *Nature* **589**, 532–535 (2021).
197. D. Roundy, M. L. Cohen, Ideal strength of diamond, Si, and Ge. *Phys. Rev. B* **64**, 212103 (2001).
198. J. Field, The mechanical and strength properties of diamond. *Rep. Prog. Phys.* **75**, 126505 (2012).
199. T. Stachel, J. W. Harris, Formation of diamond in the Earth's mantle. *J. Phys. Condens. Matter* **21**, 364206 (2009).
200. J. K. Russell, L. A. Porritt, Y. Lavallée, D. B. Dingwell, Kimberlite ascent by assimilation-fuelled buoyancy. *Nature* **481**, 352–356 (2012).
201. F. Bundy, H. T. Hall, H. Strong, R. Wentorfjun, Man-made diamonds. *nature* **176**, 51–55 (1955).
202. F. P. Bundy, H. P. Bovenkerk, H. M. Strong, R. H. Wentorf Jr, Diamond-graphite equilibrium line from growth and graphitization of diamond. *J. Chem. Phys.* **35**, 383–391 (1961).
203. F. Bundy, Direct conversion of graphite to diamond in static pressure apparatus. *J. Chem. Phys.* **38**, 631–643 (1963).
204. P. S. DeCarli, J. C. Jamieson, Formation of diamond by explosive shock. *Science* **133**, 1821–1822 (1961).

205. B. Derjaguin, D. Fedoseev, V. Lukyanovich, B. Spitzin, V. Ryabov, A. Lavrentyev, Filamentary diamond crystals. *J. Cryst. Growth* **2**, 380–384 (1968).
206. I. V. Spitsyn, L. Bouilov, B. Derjaguin, Vapor growth of diamond on diamond and other surfaces. *J. Cryst. Growth* **52**, 219–226 (1981).
207. S. Matsumoto, Y. Sato, M. Kamo, N. Setaka, Vapor deposition of diamond particles from methane. *Jpn. J. Appl. Phys.* **21**, L183 (1982).
208. Y. Hirose, S. Amanuma, K. Komaki, The synthesis of high-quality diamond in combustion flames. *J. Appl. Phys.* **68**, 6401–6405 (1990).
209. K. Kurihara, K. Sasaki, M. Kawarada, N. Koshino, High rate synthesis of diamond by dc plasma jet chemical vapor deposition. *Appl. Phys. Lett.* **52**, 437–438 (1988).
210. N. Ohtake, M. Yoshikawa, Diamond film preparation by arc discharge plasma jet chemical vapor deposition in the methane atmosphere. *J. Electrochem. Soc.* **137**, 717 (1990).
211. S. Ferro, Synthesis of diamond. *J. Mater. Chem.* **12**, 2843–2855 (2002).
212. C. Yan, Y. K. Vohra, H. Mao, R. J. Hemley, Very high growth rate chemical vapor deposition of single-crystal diamond. *Proc. Natl. Acad. Sci.* **99**, 12523–12525 (2002).
213. Q. Liang, C. Yan, Y. Meng, J. Lai, S. Krasnicki, H. Mao, R. J. Hemley, Recent advances in high-growth rate single-crystal CVD diamond. *Diam. Relat. Mater.* **18**, 698–703 (2009).
214. M. Schreck, S. Gsell, R. Brescia, M. Fischer, Ion bombardment induced buried lateral growth: the key mechanism for the synthesis of single crystal diamond wafers. *Sci. Rep.* **7**, 44462 (2017).
215. W. Gust, Phase transition and shock-compression parameters to 120 GPa for three types of graphite and for amorphous carbon. *Phys. Rev. B* **22**, 4744 (1980).
216. L. F. Trueb, An electron-microscope study of shock-synthesized diamond. *J. Appl. Phys.* **39**, 4707–4716 (1968).
217. P. S. Decarli, Shock wave synthesis of diamond and other phases. *MRS Online Proc. Libr. OPL* **383**, 21 (1995).
218. D. Erskine, W. Nellis, Shock-induced martensitic phase transformation of oriented graphite to diamond. *Nature* **349**, 317–319 (1991).
219. D. Kraus, A. Ravasio, M. Gauthier, D. Gericke, J. Vorberger, S. Frydrych, J. Helfrich, L. Fletcher, G. Schaumann, B. Nagler, others, Nanosecond formation of diamond and lonsdaleite by shock compression of graphite. *Nat. Commun.* **7**, 10970 (2016).
220. V. Sobolev, Y. Taran, S. Gubenko, Shock wave use for diamond synthesis. *J. Phys. IV* **7**, C3-73 (1997).

221. H. Hirai, K. Kondo, Modified phases of diamond formed under shock compression and rapid quenching. *Science* **253**, 772–774 (1991).
222. E. Wheeler, D. Lewis, The structure of a shock-quenched diamond. *Mater. Res. Bull.* **10**, 687–693 (1975).
223. F. P. Bundy, The P, T phase and reaction diagram for elemental carbon, 1979. *J. Geophys. Res. Solid Earth* **85**, 6930–6936 (1980).
224. M. E. Lipschutz, E. Anders, The record in the meteorites—IV: origin of diamonds in iron meteorites. *Geochim. Cosmochim. Acta* **24**, 83–105 (1961).
225. E. Anders, Diamonds in meteorites. *Sci. Am.* **213**, 26–37 (1965).
226. R. Hanneman, H. Strong, F. Bundy, Hexagonal diamonds in meteorites: Implications. *Science* **155**, 995–997 (1967).
227. P. Németh, H. J. Lancaster, C. G. Salzmann, K. McColl, Z. Fogarassy, L. A. Garvie, L. Illés, B. Pécz, M. Murri, F. Corà, others, Shock-formed carbon materials with intergrown sp<sup>3</sup>-and sp<sup>2</sup>-bonded nanostructured units. *Proc. Natl. Acad. Sci.* **119**, e2203672119 (2022).
228. R. Hough, I. Gilmour, C. Pillinger, J. Arden, K. Gilkess, J. Yuan, H. Milledge, Diamond and silicon carbide in impact melt rock from the Ries impact crater. *Nature* **378**, 41–44 (1995).
229. C. Koeberl, V. L. Masaitis, G. I. Shafranovsky, I. Gilmour, F. Langenhorst, M. Schrauder, Diamonds from the Popigai impact structure, Russia. *Geology* **25**, 967–970 (1997).
230. R. S. Clarke Jr, D. E. Appleman, D. R. Ross, An Antarctic iron meteorite contains preterrestrial impact-produced diamond and lonsdaleite. *Nature* **291**, 396–398 (1981).
231. J. Smith, J. Dawson, Carbonado: Diamond aggregates from early impacts of crystal rocks? *Geology* **13**, 342–343 (1985).
232. N. R. Greiner, D. Phillips, J. Johnson, F. Volk, Diamonds in detonation soot. *Nature* **333**, 440–442 (1988).
233. K. V. Volkov, V. V. Danilenko, V. Elin, Synthesis of diamond from the carbon in the detonation products of explosives. *Combust. Explos. Shock Waves* **26**, 366–368 (1990).
234. S.-S. Shang, K. Hokamoto, M. A. Meyers, Hot dynamic consolidation of hard ceramics. *J. Mater. Sci.* **27**, 5470–5476 (1992).
235. D. K. Potter, T. J. Ahrens, Shock consolidation of diamond and graphite mixtures to fused polycrystalline diamond. *J. Appl. Phys.* **63**, 910–914 (1988).

236. K. Hokamoto, M. Fujita, S. Tanaka, T. Kodama, Y. Ujimoto, High-temperature shock consolidation of diamond powders using converging underwater shock wave. *Scr. Mater.* **39**, 1383–1388 (1998).
237. T. Akashi, A. B. Sawaoka, Shock consolidation of diamond powders. *J. Mater. Sci.* **22**, 3276–3286 (1987).
238. K.-I. Kondo, S. Kukino, H. Hirai, Shock-Compaction of Nano-Sized Diamond Powder, as Examined by Microstructural Analysis. *J. Am. Ceram. Soc.* **79**, 97–101 (1996).
239. J. Field, C. Pickles, Strength, fracture and friction properties of diamond. *Diam. Relat. Mater.* **5**, 625–634 (1996).
240. B. Willems, P. Martineau, D. Fisher, J. Van Royen, G. Van Tendeloo, Dislocation distributions in brown diamond. *Phys. Status Solidi A* **203**, 3076–3080 (2006).
241. U. Bangert, R. Barnes, M. H. Gass, A. L. Bleloch, I. S. Godfrey, Vacancy clusters, dislocations and brown colouration in diamond. *J. Phys. Condens. Matter* **21**, 364208 (2009).
242. D. Fisher, Brown diamonds and high pressure high temperature treatment. *Lithos* **112**, 619–624 (2009).
243. J. C. Jamieson, A. Lawson, N. Nachtrieb, New device for obtaining x-ray diffraction patterns from substances exposed to high pressure. *Rev. Sci. Instrum.* **30**, 1016–1019 (1959).
244. N. Dubrovinskaia, L. Dubrovinsky, N. A. Solopova, A. Abakumov, S. Turner, M. Hanfland, E. Bykova, M. Bykov, C. Prescher, V. B. Prakapenka, others, Terapascal static pressure generation with ultrahigh yield strength nanodiamond. *Sci. Adv.* **2**, e1600341 (2016).
245. W. A. Bassett, Diamond anvil cell, 50th birthday. *High Press. Res.* **29**, 163–186 (2009).
246. A. Jayaraman, Diamond anvil cell and high-pressure physical investigations. *Rev. Mod. Phys.* **55**, 65 (1983).
247. S. Anzellini, S. Boccato, A practical review of the laser-heated diamond anvil cell for university laboratories and synchrotron applications. *Crystals* **10**, 459 (2020).
248. H. Mao, P. Bell, K. Dunn, R. Chrenko, R. DeVries, Absolute pressure measurements and analysis of diamonds subjected to maximum static pressures of 1.3–1.7 Mbar. *Rev. Sci. Instrum.* **50**, 1002–1009 (1979).
249. B. Li, C. Ji, W. Yang, J. Wang, K. Yang, R. Xu, W. Liu, Z. Cai, J. Chen, H. Mao, Diamond anvil cell behavior up to 4 Mbar. *Proc. Natl. Acad. Sci.* **115**, 1713–1717 (2018).
250. J.-J. Zhao, S. Scandolo, J. Kohanoff, G. Chiarotti, E. Tosatti, Elasticity and mechanical instabilities of diamond at megabar stresses: Implications for diamond-anvil-cell research. *Appl. Phys. Lett.* **75**, 487–488 (1999).



251. J. Liu, Y. K. Vohra, Fluorescence emission from high purity synthetic diamond anvil to 370 GPa. *Appl. Phys. Lett.* **68**, 2049–2051 (1996).
252. J. Xu, H. Mao, Moissanite: A window for high-pressure experiments. *Science* **290**, 783–785 (2000).
253. J. Xu, H. Mao, R. J. Hemley, The gem anvil cell: high-pressure behaviour of diamond and related materials. *J. Phys. Condens. Matter* **14**, 11549 (2002).
254. H. Wu, X. Luo, L. Wen, H. Sun, C. Chen, Extreme static compression of carbon to terapascal pressures. *Carbon* **144**, 161–170 (2019).
255. F. Knoop, C. G. Peters, W. B. Emerson, A sensitive pyramidal-diamond tool for indentation measurements. *J. Res. Natl. Bur. Stand.* **23**, 39 (1939).
256. H. Sumiya, Y. Ishida, Real hardness of high-purity ultra-fine nano-polycrystalline diamond synthesized by direct conversion sintering under HPHT. *Diam. Relat. Mater.* **100**, 107560 (2019).
257. P. Humble, R. H. J. Hannink, Plastic deformation of diamond at room temperature. *Nature* **273**, 37–39 (1978).
258. M. M. Chaudhri, Indentation hardness of diamond single crystals, nanopolycrystal, and nanotwinned diamonds: A critical review. *Diam. Relat. Mater.* **109**, 108076 (2020).
259. A. Richter, R. Ries, R. Smith, M. Henkel, B. Wolf, Nanoindentation of diamond, graphite and fullerene films. *Diam. Relat. Mater.* **9**, 170–184 (2000).
260. J. Xiong, L. Liu, H. Song, M. Wang, T. Hu, Z. Zhai, B. Yang, X. Jiang, N. Huang, Mechanical properties evaluation of diamond films via nanoindentation. *Diam. Relat. Mater.* **130**, 109403 (2022).
261. T. Sawa, K. Tanaka, Nanoindentation of natural diamond. *Philos. Mag. A* **82**, 1851–1856 (2002).
262. A. Nie, Y. Bu, J. Huang, Y. Shao, Y. Zhang, W. Hu, J. Liu, Y. Wang, B. Xu, Z. Liu, Direct observation of room-temperature dislocation plasticity in diamond. *Matter* **2**, 1222–1232 (2020).
263. Y. Bu, P. Wang, A. Nie, H. Wang, Room-temperature plasticity in diamond. *Sci. China Technol. Sci.* **64**, 32–36 (2021).
264. B. Regan, A. Aghajamali, J. Froech, T. T. Tran, J. Scott, J. Bishop, I. Suarez-Martinez, Y. Liu, J. M. Cairney, N. A. Marks, M. Toth, I. Aharonovich, Plastic Deformation of Single-Crystal Diamond Nanopillars. *Adv. Mater.* **32**, 1906458 (2020).

265. D. A. Young, R. Grover, “Theory of the carbon phase diagram at high pressures and temperatures” (UCRL-96435; CONF-870753-20, Lawrence Livermore National Lab., CA (USA), 1987); <https://www.osti.gov/biblio/6183943>.
266. X. Wang, S. Scandolo, R. Car, Carbon Phase Diagram from Ab Initio Molecular Dynamics. *Phys. Rev. Lett.* **95**, 185701 (2005).
267. A. A. Correa, S. A. Bonev, G. Galli, Carbon under extreme conditions: Phase boundaries and electronic properties from first-principles theory. *Proc. Natl. Acad. Sci.* **103**, 1204–1208 (2006).
268. L. X. Benedict, K. P. Driver, S. Hamel, B. Militzer, T. Qi, A. A. Correa, A. Saul, E. Schwegler, Multiphase equation of state for carbon addressing high pressures and temperatures. *Phys. Rev. B* **89**, 224109 (2014).
269. J. Shi, Z. Liang, J. Wang, S. Pan, C. Ding, Y. Wang, H.-T. Wang, D. Xing, J. Sun, Double-Shock Compression Pathways from Diamond to BC8 Carbon. *Phys. Rev. Lett.* **131**, 146101 (2023).
270. J. H. Eggert, D. G. Hicks, P. M. Celliers, D. K. Bradley, R. S. McWilliams, R. Jeanloz, J. E. Miller, T. R. Boehly, G. W. Collins, Melting temperature of diamond at ultrahigh pressure. *Nat. Phys.* **6**, 40–43 (2010).
271. S. Scandolo, G. L. Chiarotti, E. Tosatti, SC4: A metallic phase of carbon at terapascal pressures. *Phys. Rev. B* **53**, 5051–5054 (1996).
272. J. Sun, D. D. Klug, R. Martoňák, Structural transformations in carbon under extreme pressure: Beyond diamond. *J. Chem. Phys.* **130**, 194512 (2009).
273. Z. Sha, P. Branicio, Q. Pei, V. Sorkin, Y. Zhang, A modified Tersoff potential for pure and hydrogenated diamond-like carbon. *Comput. Mater. Sci.* **67**, 146–150 (2013).
274. L. Shi, X. Ma, M. Li, Y. Zhong, L. Yang, W. Yin, X. He, Molecular dynamics simulation of phonon thermal transport in nanotwinned diamond with a new optimized Tersoff potential. *Phys. Chem. Chem. Phys.* **23**, 8336–8343 (2021).
275. D. W. Brenner, Empirical potential for hydrocarbons for use in simulating the chemical vapor deposition of diamond films. *Phys. Rev. B* **42**, 9458 (1990).
276. J. N. Glosli, F. H. Ree, The melting line of diamond determined via atomistic computer simulations. *J. Chem. Phys.* **110**, 441–446 (1999).
277. B. Wen, B. Xu, Y. Wang, G. Gao, X.-F. Zhou, Z. Zhao, Y. Tian, Continuous strengthening in nanotwinned diamond. *Npj Comput. Mater.* **5**, 117 (2019).
278. B.-J. Lee, J. W. Lee, A modified embedded atom method interatomic potential for carbon. *Calphad* **29**, 7–16 (2005).

279. L. S. Liyanage, S.-G. Kim, J. Houze, S. Kim, M. A. Tschopp, M. I. Baskes, M. F. Horstemeyer, Structural, elastic, and thermal properties of cementite (Fe<sub>3</sub>C) calculated using a modified embedded atom method. *Phys. Rev. B* **89**, 094102 (2014).
280. C. Xu, C. Wang, C. T. Chan, K. Ho, A transferable tight-binding potential for carbon. *J. Phys. Condens. Matter* **4**, 6047 (1992).
281. A. Thess, R. Lee, P. Nikolaev, H. Dai, P. Petit, J. Robert, C. Xu, Y. H. Lee, S. G. Kim, A. G. Rinzler, others, Crystalline ropes of metallic carbon nanotubes. *science* **273**, 483–487 (1996).
282. D. Qian, G. J. Wagner and, W. K. Liu, M.-F. Yu, R. S. Ruoff, Mechanics of carbon nanotubes. *Appl Mech Rev* **55**, 495–533 (2002).
283. J. Morris, C. Fu, K. Ho, Tight-binding study of tilt grain boundaries in diamond. *Phys. Rev. B* **54**, 132 (1996).
284. N. Marks, Modelling diamond-like carbon with the environment-dependent interaction potential. *J. Phys. Condens. Matter* **14**, 2901 (2002).
285. J. Buchan, M. Robinson, H. Christie, D. Roach, D. Ross, N. A. Marks, Molecular dynamics simulation of radiation damage cascades in diamond. *J. Appl. Phys.* **117** (2015).
286. K. Chenoweth, A. C. Van Duin, W. A. Goddard, ReaxFF reactive force field for molecular dynamics simulations of hydrocarbon oxidation. *J. Phys. Chem. A* **112**, 1040–1053 (2008).
287. S. G. Srinivasan, A. C. Van Duin, P. Ganesh, Development of a ReaxFF potential for carbon condensed phases and its application to the thermal fragmentation of a large fullerene. *J. Phys. Chem. A* **119**, 571–580 (2015).
288. S. J. Stuart, A. B. Tutein, J. A. Harrison, A reactive potential for hydrocarbons with intermolecular interactions. *J. Chem. Phys.* **112**, 6472–6486 (2000).
289. J. Los, A. Fasolino, Intrinsic long-range bond-order potential for carbon: Performance in Monte Carlo simulations of graphitization. *Phys. Rev. B* **68**, 024107 (2003).
290. L. M. Ghiringhelli, J. H. Los, E. J. Meijer, A. Fasolino, D. Frenkel, Modeling the phase diagram of carbon. *Phys. Rev. Lett.* **94**, 145701 (2005).
291. C. C. Battaile, D. J. Srolovitz, J. Butler, A kinetic Monte Carlo method for the atomic-scale simulation of chemical vapor deposition: Application to diamond. *J. Appl. Phys.* **82**, 6293–6300 (1997).
292. P. W. May, N. L. Allan, M. N. Ashfold, J. C. Richley, Y. A. Mankelevich, Simplified Monte Carlo simulations of chemical vapour deposition diamond growth. *J. Phys. Condens. Matter* **21**, 364203 (2009).

293. M. Frenklach, Monte Carlo simulation of diamond growth by methyl and acetylene reactions. *J. Chem. Phys.* **97**, 5794–5802 (1992).
294. W. Rodgers, P. May, N. Allan, J. Harvey, Three-dimensional kinetic Monte Carlo simulations of diamond chemical vapor deposition. *J. Chem. Phys.* **142** (2015).
295. M. Eckert, E. Neyts, A. Bogaerts, Insights into the growth of (ultra) nanocrystalline diamond by combined molecular dynamics and Monte Carlo simulations. *Cryst. Growth Des.* **10**, 3005–3021 (2010).
296. J. M. Lang, J. M. Winey, Y. M. Gupta, Strength and deformation of shocked diamond single crystals: Orientation dependence. *Phys. Rev. B* **97**, 104106 (2018).
297. A. L. Kritcher, D. J. Schlossberg, C. R. Weber, C. V. Young, O. A. Hurricane, E. Dewald, A. B. Zylstra, A. Allen, B. Bachmann, K. L. Baker, S. Baxamusa, T. Braun, G. Brunton, D. A. Callahan, D. T. Casey, T. Chapman, C. Choate, D. S. Clark, J.-M. G. D. Nicola, L. Divol, M. J. Edwards, S. Haan, T. Fehrenbach, S. Hayes, D. E. Hinkel, M. Hohenberger, K. Humbird, N. Izumi, O. Jones, E. Kur, B. Kustowski, C. Kong, O. L. Landen, D. Larson, X. Lepro-Chavez, J. D. Lindl, B. J. MacGowan, S. Maclaren, M. Marinak, P. Michel, M. Millot, A. Nikroo, R. Nora, A. Pak, P. K. Patel, J. E. Ralph, M. Ratledge, M. S. Rubery, N. W. Ruof, S. M. Sepke, M. Stadermann, D. J. Strozzi, T. I. Suratwala, R. Tommasini, R. Town, B. Woodworth, B. Van Wonterghem, C. Wild, Design of first experiment to achieve fusion target gain > 1. *Phys. Plasmas* **31**, 070502 (2024).
298. J. Robertson, Properties of diamond-like carbon. *Surf. Coat. Technol.* **50**, 185–203 (1992).
299. M. I. Eremets, I. A. Trojan, P. Gwaze, J. Huth, R. Boehler, V. D. Blank, The strength of diamond. *Appl. Phys. Lett.* **87**, 1–3 (2005).
300. H. F. Wilson, B. Militzer, INTERIOR PHASE TRANSFORMATIONS AND MASS–RADIUS RELATIONSHIPS OF SILICON–CARBON PLANETS. *Astrophys. J.* **793**, 34 (2014).
301. N. Madhusudhan, K. K. M. Lee, O. Mousis, A POSSIBLE CARBON-RICH INTERIOR IN SUPER-EARTH 55 Cancri e. *Astrophys. J. Lett.* **759**, L40 (2012).
302. N. Mashian, A. Loeb, CEMP stars: possible hosts to carbon planets in the early Universe. *Mon. Not. R. Astron. Soc.* **460**, 2482–2491 (2016).
303. L. B. Hopkins, S. LePape, L. Divol, A. Pak, E. Dewald, D. D. Ho, N. Meezan, S. Bhandarkar, L. R. Benedetti, T. Bunn, J. Biener, J. Crippen, D. Casey, D. Clark, D. Edgell, D. Fittinghoff, M. Gatu-Johnson, C. Goyon, S. Haan, R. Hatarik, M. Havre, D. Hinkel, H. Huang, N. Izumi, J. Jaquez, O. Jones, S. Khan, A. Kritcher, C. Kong, G. Kyrala, O. Landen, T. Ma, A. MacPhee, B. MacGowan, A. J. Mackinnon, M. Marinak, J. Milovich, M. Millot, P. Michel, A. Moore, S. R. Nagel, A. Nikroo, P. Patel, J. Ralph, H. Robey, J. S. Ross, N. G. Rice, S. Sepke, V. A. Smalyuk, P. Sterne, D. Strozzi, M. Stadermann, P. Volegov, C. Weber, C. Wild, C. Yeamans, D. Callahan, O. Hurricane, R. P. J. Town, M. J. Edwards, Toward a

- burning plasma state using diamond ablator inertially confined fusion (ICF) implosions on the National Ignition Facility (NIF). *Plasma Phys. Control. Fusion* **61**, 014023 (2018).
304. A. B. Zylstra, D. T. Casey, A. Kritcher, L. Pickworth, B. Bachmann, K. Baker, J. Biener, T. Braun, D. Clark, V. Geppert-Kleinrath, M. Hohenberger, C. Kong, S. Le Pape, A. Nikroo, N. Rice, M. Rubery, M. Stadermann, D. Strozzi, C. Thomas, P. Volegov, C. Weber, C. Wild, C. Wilde, D. A. Callahan, O. A. Hurricane, Hot-spot mix in large-scale HDC implosions at NIF. *Phys. Plasmas* **27**, 092709 (2020).
305. J. M. Winey, M. D. Knudson, Y. M. Gupta, Shock compression response of diamond single crystals at multimegabar stresses. *Phys. Rev. B* **101** (2020).
306. R. S. McWilliams, J. H. Eggert, D. G. Hicks, D. K. Bradley, P. M. Celliers, D. K. Spaulding, T. R. Boehly, G. W. Collins, R. Jeanloz, Strength effects in diamond under shock compression from 0.1 to 1 TPa. *Phys. Rev. B* **81**, 014111 (2010).
307. K. L. Baker, C. A. Thomas, O. L. Landen, S. Haan, J. D. Lindl, D. T. Casey, C. Young, R. Nora, O. A. Hurricane, D. A. Callahan, Reaching a burning plasma and ignition using smaller capsules/Hohlraums, higher radiation temperatures, and thicker ablator/ice on the national ignition facility. *Phys. Plasmas* **30** (2023).
308. G. Garcia Vidable, R. I. Gonzalez, F. J. Valencia, N. Amigo, D. Tramontina, E. M. Bringa, Simulations of plasticity in diamond nanoparticles showing ultrahigh strength. *Diam. Relat. Mater.* **126**, 109109 (2022).
309. R. M. Flanagan, M. A. Meyers, S. M. Valone, S. J. Fensin, Collapse of helium-filled voids in extreme deformation: Dislocation mechanisms. *Mater. Sci. Eng. A* **839**, 142712 (2022).
310. R. M. Flanagan, S. J. Fensin, M. A. Meyers, The role of pre-existing heterogeneities in materials under shock and spall. *Appl. Phys. Rev.* **9**, 011305 (2022).
311. C. Huang, X. Peng, B. Yang, H. Xiang, S. Sun, X. Chen, Q. Li, D. Yin, T. Fu, Anisotropy effects in diamond under nanoindentation. *Carbon* **132**, 606–615 (2018).
312. S. Timoshenko, J. Goodier, Theory of Elasticity” McGraw-Hill Book Company. *Inc N. Y.* (1951).
313. S. Traiviratana, E. M. Bringa, D. J. Benson, M. A. Meyers, Void growth in metals: Atomistic calculations. *Acta Mater.* **56**, 3874–3886 (2008).
314. E. M. Bringa, S. Traiviratana, M. A. Meyers, Void initiation in fcc metals: Effect of loading orientation and nanocrystalline effects. *Acta Mater.* **58**, 4458–4477 (2010).
315. M. F. Ashby, The deformation of plastically non-homogeneous materials. *Philos. Mag. J. Theor. Exp. Appl. Phys.* **21**, 399–424 (1970).

316. J. R. Rice, R. Thomson, Ductile versus brittle behaviour of crystals. *Philos. Mag. J. Theor. Exp. Appl. Phys.* **29**, 73–97 (1974).
317. J. R. Rice, D. M. Tracey, On the ductile enlargement of voids in triaxial stress fields\*. *J. Mech. Phys. Solids* **17**, 201–217 (1969).
318. A. Needleman, V. Tvergaard, J. W. Hutchinson, “Void Growth in Plastic Solids” in *Topics in Fracture and Fatigue*, A. S. Argon, Ed. (Springer, New York, NY, 1992; [https://doi.org/10.1007/978-1-4612-2934-6\\_4](https://doi.org/10.1007/978-1-4612-2934-6_4)), pp. 145–178.
319. M. A. Meyers, S. Traiviratana, V. A. Lubarda, D. J. Benson, E. M. Bringa, The role of dislocations in the growth of nanosized voids in ductile failure of metals. *JOM* **61**, 35–41 (2009).
320. P. Pirouz, D. J. H. Cockayne, N. Sumida, P. B. Hirsch, A. R. Lang, Dissociation of dislocations in diamond. *Proc. R. Soc. Lond. Math. Phys. Sci.* **386**, 241–249 (1997).
321. E. Güler, M. Güler, Elastic and mechanical properties of cubic diamond under pressure. *Chin. J. Phys.* **53**, 195–205 (2015).
322. V. R. Parameswaran, J. Weertman, Dislocation mobility in lead and Pb-In alloy single crystals. *Metall. Trans.* **2**, 1233–1243 (1971).
323. C. J. Ruestes, E. M. Bringa, R. E. Rudd, B. A. Remington, T. P. Remington, M. A. Meyers, Probing the character of ultra-fast dislocations. *Sci. Rep.* **5**, 16892 (2015).
324. D. G. Hicks, T. R. Boehly, P. M. Celliers, D. K. Bradley, J. H. Eggert, R. S. McWilliams, R. Jeanloz, G. W. Collins, High-precision measurements of the diamond Hugoniot in and above the melt region. *Phys. Rev. B - Condens. Matter Mater. Phys.* **78** (2008).
325. D. Orlikowski, A. A. Correa, E. Schwegler, J. E. Klepeis, “A steinberg-guinan model for high-pressure carbon: Diamond phase” in *AIP Conference Proceedings* (2007)vol. 955, pp. 247–250.
326. F. González-Cataldo, B. K. Godwal, K. P. Driver, R. Jeanloz, B. Militzer, Model of ramp compression of diamond from ab initio simulations. *Phys. Rev. B* **104**, 134104 (2021).
327. P. Rowe, V. L. Deringer, P. Gasparotto, G. Csányi, A. Michaelides, An accurate and transferable machine learning potential for carbon. *J. Chem. Phys.* **153**, 034702 (2020).
328. T. Braun, S. O. Kucheyev, S. J. Shin, Y. M. Wang, J. Ye, N. E. T. Jr, C. K. Saw, D. B. Bober, E. M. Sedillo, N. G. Rice, K. Sequoia, H. Huang, W. Requieron, A. Nikroo, D. D. Ho, S. W. Haan, A. V. Hamza, C. Wild, J. Biener, Tungsten doped diamond shells for record neutron yield inertial confinement fusion experiments at the National Ignition Facility. *Nucl. Fusion* **63**, 016022 (2022).
329. M. L. Spaeth, K. R. Manes, D. H. Kalantar, P. E. Miller, J. E. Heebner, E. S. Bliss, D. R. Spec, T. G. Parham, P. K. Whitman, P. J. Wegner, P. A. Baisden, J. A. Menapace, M. W.

- Bowers, S. J. Cohen, T. I. Suratwala, J. M. Di Nicola, M. A. Newton, J. J. Adams, J. B. Trenholme, R. G. Finucane, R. E. Bonanno, D. C. Rardin, P. A. Arnold, S. N. Dixit, G. V. Erbert, A. C. Erlandson, J. E. Fair, E. Feigenbaum, W. H. Gourdin, R. A. Hawley, J. Honig, R. K. House, K. S. Jancaitis, K. N. LaFortune, D. W. Larson, B. J. Le Galloudec, J. D. Lindl, B. J. MacGowan, C. D. Marshall, K. P. McCandless, R. W. McCracken, R. C. Montesanti, E. I. Moses, M. C. Nostrand, J. A. Pryatel, V. S. Roberts, S. B. Rodriguez, A. W. Rowe, R. A. Sacks, J. T. Salmon, M. J. Shaw, S. Sommer, C. J. Stolz, G. L. Tietbohl, C. C. Widmayer, R. Zacharias, Description of the NIF Laser. *Fusion Sci. Technol.* **69**, 25–145 (2016).
330. A. L. Kritcher, D. T. Casey, C. A. Thomas, A. B. Zylstra, M. Hohenberger, K. Baker, S. Le Pape, B. Bachmann, S. Bhandarkar, J. Biener, T. Braun, D. Clark, L. Divol, T. Döppner, D. Hinkel, C. Kong, D. Mariscal, M. Millot, J. Milovich, A. Nikroo, A. Pak, N. Rice, H. Robey, M. Stadermann, J. Sevier, D. Strozzi, C. Weber, C. Wild, B. Woodworth, J. Edwards, D. A. Callahan, O. A. Hurricane, Symmetric fielding of the largest diamond capsule implosions on the NIF. *Phys. Plasmas* **27**, 052710 (2020).
331. K. L. Baker, C. A. Thomas, T. R. Dittrich, O. Landen, G. Kyrala, D. T. Casey, C. R. Weber, J. Milovich, D. T. Woods, M. Schneider, S. F. Khan, B. K. Spears, A. Zylstra, C. Kong, J. Crippen, N. Alfonso, C. B. Yeaman, J. D. Moody, A. S. Moore, N. B. Meezan, A. Pak, D. N. Fittinghoff, P. L. Volegov, O. Hurricane, D. Callahan, P. Patel, P. Amendt, Fill tube dynamics in inertial confinement fusion implosions with high density carbon ablaters. *Phys. Plasmas* **27**, 112706 (2020).
332. J. Ralph, J. Ross, A. Zylstra, A. Kritcher, H. Robey, C. Young, O. Hurricane, D. Callahan, A. Pak, D. Casey, T. Doppner, L. Divol, M. Hohenberger, S. L. Pape, K. Baker, P. Patel, R. Tommasini, S. Ali, P. Amendt, J. Atherton, B. Bachmann, D. Bailey, L. R. Benedetti, L. B. Hopkins, R. Betti, S. Bhandarkar, R. Bionta, N. Birge, E. Bond, D. Bradley, T. Braun, T. Briggs, M. Bruhn, P. Celliers, B. Chang, T. Chapman, H. Chen, C. Choate, A. Christopherson, D. Clark, J. Crippen, E. Dewald, T. Dittrich, M. J. Edwards, W. Farmer, J. Field, D. Fittinghoff, J. Frenje, J. Gaffney, M. G. Johnson, S. Glenzer, G. Grim, S. Haan, K. Hahn, G. Hall, B. Hammel, J. Harte, E. Hartouni, J. Heebner, V. Hernandez, H. Herrmann, M. Herrmann, D. Hinkel, D. Ho, J. Holder, W. Hsing, H. Huang, K. Humbird, N. Izumi, C. Jarrott, J. Jeet, O. Jones, G. Kerbel, S. Kerr, S. Khan, J. Kilkenny, Y. H. Kim, H. G. Kleinrath, V. Geppert-Kleinrath, C. Kong, J. Koning, J. Kroll, O. Landen, S. Langer, D. Larson, N. Lemos, J. Lindl, T. Ma, M. MacDonald, B. MacGowan, A. Mackinnon, S. MacLaren, A. MacPhee, M. Marinak, D. Mariscal, E. Marley, L. Masse, K. Meaney, N. Meezan, P. Michel, M. Millot, J. Milovich, J. Moody, A. Moore, J. Morton, T. Murphy, K. Newman, J. D. Nicola, A. Nikroo, R. Nora, M. Patel, L. Pelz, J. Peterson, Y. Ping, B. Pollock, M. Ratledge, N. Rice, H. Rinderknecht, M. Rosen, M. Rubery, J. Salmonson, J. Sater, S. Schiaffino, D. Schlossberg, M. Schneider, C. Schroeder, H. Scott, S. Sepke, K. Sequoia, M. Sherlock, S. Shin, V. Smalyuk, B. Spears, P. Springer, M. Stadermann, S. Stoupin, D. Strozzi, L. Suter, C. Thomas, R. Town, E. Tubman, P. Volegov, C. Weber, K. Widmann, C. Wild, C. Wilde, B. V. Wonterghem, D. Woods, B. Woodworth, M. Yamaguchi, S. Yang, G. Zimmerman, J. Biener, C. Trosseille, M. Kruse, B. Kustowski, The impact of low-mode symmetry on inertial fusion energy output in the burning plasma state. [Preprint] (2024). <https://doi.org/10.21203/rs.3.rs-3868740/v1>.

333. K. Kawasaki, H. Yamada, H. Nagatomo, Y. Hironaka, K. Yamanoi, D. Tanaka, T. Idesaka, Y. Mokuno, A. Chayahara, T. Shimaoka, K. Mima, T. Somekawa, M. Tsukamoto, Y. Sato, A. Iwamoto, K. Shigemori, Fabrication of nanocrystalline diamond capsules by hot-filament chemical vapor deposition for direct-drive inertial confinement fusion experiments. *Diam. Relat. Mater.* **135**, 109896 (2023).
334. A. C. Li, B. Li, R. E. Rudd, M. A. Meyers, Dislocation generation in diamond under extreme loading. *Matter* **6**, 3040–3056 (2023).
335. J. Weertman, *Dislocation Based Fracture Mechanics* (World Scientific, 1996).
336. P. M. Anderson, J. R. Rice, The stress field and energy of a three-dimensional dislocation loop at a crack tip. *J. Mech. Phys. Solids* **35**, 743–769 (1987).
337. W. G. Wolfer, W. J. Drugan, Elastic interaction energy between a prismatic dislocation loop and a spherical cavity. *Philos. Mag. A* **57**, 923–937 (1988).
338. D. C. Ahn, P. Sofronis, M. Kumar, J. Belak, R. Minich, Void growth by dislocation-loop emission. *J. Appl. Phys.* **101** (2007).
339. S. Zhao, B. Li, B. A. Remington, C. E. Wehrenberg, H. S. Park, E. N. Hahn, M. A. Meyers, Directional amorphization of covalently-bonded solids: A generalized deformation mechanism in extreme loading. *Mater. Today* **49**, 59–67 (2021).
340. Y. Kamimura, K. Edagawa, S. Takeuchi, Experimental evaluation of the Peierls stresses in a variety of crystals and their relation to the crystal structure. *Acta Mater.* **61**, 294–309 (2013).
341. R. F. Zhang, S. H. Zhang, Y. Q. Guo, Z. H. Fu, D. Legut, T. C. Germann, S. Veprek, First-principles design of strong solids: Approaches and applications. *Phys. Rep.* **826**, 1–49 (2019).
342. V. V. Bulatov, J. F. Justo, W. Cai, S. Yip, A. S. Argon, T. Lenosky, M. de Koning, T. D. de la Rubia, Parameter-free modelling of dislocation motion: the case of silicon. *Philos. Mag. A* **81**, 1257–1281 (2001).
343. J.-M. Zhang, F. Ma, K.-W. Xu, X.-T. Xin, Anisotropy analysis of the surface energy of diamond cubic crystals. *Surf. Interface Anal. Int. J. Devoted Dev. Appl. Tech. Anal. Surf. Interfaces Thin Films* **35**, 805–809 (2003).
344. W. M. Brown, P. Wang, S. J. Plimpton, A. N. Tharrington, Implementing molecular dynamics on hybrid high performance computers—short range forces. *Comput. Phys. Commun.* **182**, 898–911 (2011).



## APPENDICES

### Appendix A – LAMMPS Input Files

The large-scale, open-source MD code LAMMPS was employed to perform classical atomistic molecular dynamics simulations (82, 83). The Tersoff potential (60–62) was used as the interatomic potential for carbon, having shown good performance in modeling the mechanical properties of diamond up to the pressures used in this paper. Simulations were performed with parallel optimizations on GPUs (344) on the supercomputers at Lawrence Livermore national Labs. All simulations were performed with the shock along the z-direction oriented along the [111] diamond cubic lattice direction. The initial simulation box size for the simulations of the 2,4,6,8,10, and 12nm diameter voids were 100 x 100 x 200 lattice parameters in the x, y, and z axes, or approximately 35.6 x 35.6 x 71.3 nm. For the 18nm void diameter, a larger box simulation size of 150 x 150 x 200 lattice parameters was used, or 53.5 x 53.5 x 71.3 nm, to reduce self-interaction of the void across the periodic boundaries. Periodic boundaries were applied in the x and y dimensions, with a shrink-wrapped boundary for z. A piston was formed of the atoms in the first 10 lattice parameters in the z-direction, and atoms in the region between 11 and 13 lattice parameters were removed. The void was placed centered in the x and y dimensions and placed 30 lattice parameters plus the void radius into the bulk to prevent it from interacting with the piston surface. The time step was 0.5 fs to prevent carbon atoms from interacting unphysically if particle velocities became too high. Piston velocities for each void size were sequentially raised by increments of 0.05 km/s until observations of dislocations were found. Far-field shock pressure measurements were taken when then shockwave reached the end of the box and the box average pressure peaked. All visualization was performed using OVITO (96). Defect analysis was performed using the DXA analysis package included in OVITO (104).

```

# Carbon Void Shock in the 111 Direction
# Half Time Step (0.0005 picoseconds)
# Additional Analysis added for resolved shear stresses
# Dump files every 500 times steps (0.1 picosecond)
# 2150 m/s piston velocity (2.15 angstroms/picosecond)
# 2 nm void size, centered in X+Y, 30 lattice spacing+Void size into Z
# Alex Li, R. E. Rudd

#Variable Setup
#t sets piston velocities per run
#voidradius sets radius of centered void
variable t index 2.15
variable voidradius equal 40

label loop

variable      a0 equal 3.565

log log.$t.111

#Setup parameters
units          metal
atom_style     atomic
boundary       p p s

neighbor       2.0 bin
neigh_modify   every 1 delay 2 check yes

variable      xlattice equal floor(100/sqrt(2.25))
variable      ylattice equal ceil(100/sqrt(2))
variable      zlattice equal ceil(200/sqrt(3))

lattice       diamond ${a0} orient z 1 1 1 orient y 0 1 -1 orient x 2 -1 -1
region        box block 0 ${xlattice} 0 ${ylattice} 0 ${zlattice}
create_box    1 box
create_atoms  1 box

mass          1 12.0107

# Potentials
pair_style     tersoff
pair_coeff     * * SiC.tersoff C

#Creating a Single Large, centered void
#Void is centered in X and Y, then placed 30 lattice units into the block

```

```

variable xmid equal (xlo+xhi)/2
variable ymid equal (ylo+yhi)/2
variable zloc equal zlo+v_voidradius+30*v_a0
variable zmid equal (zlo+zhi)/2

region void sphere v_xmid v_ymid v_zloc v_voidradius units box
delete_atoms region void
run 0
region void delete

#Create region and group for stress measurements
variable voidsphereradius equal v_voidradius+20
region voidreg sphere v_xmid v_ymid v_zloc v_voidsphereradius units box
group voidgroup region voidreg

compute vs voidgroup stress/atom NULL pair

#Create vectors for resolved shear stress analysis
variable bhat1_1 equal 0.5428/sqrt(2)
variable bhat1_2 equal 1.3017/sqrt(2)
variable bhat1_3 equal -0.1125/sqrt(2)
variable nhat1_1 equal 0.7677/1
variable nhat1_2 equal -0.3838/1
variable nhat1_3 equal -0.3838/1

variable bhat2_1 equal 1.3105/sqrt(2)
variable bhat2_2 equal 0.2108/sqrt(2)
variable bhat2_3 equal 0.2108/sqrt(2)
variable nhat2_1 equal 0
variable nhat2_2 equal 0.7071
variable nhat2_3 equal -0.7071

variable bhat3_1 equal 0.7677/sqrt(2)
variable bhat3_2 equal 0.3232/sqrt(2)
variable bhat3_3 equal -1.0909/sqrt(2)
variable nhat3_1 equal 0.5428
variable nhat3_2 equal 0.5946
variable nhat3_3 equal 0.5946

variable bhat4_1 equal 1.8533/sqrt(6)
variable bhat4_2 equal 1.5125/sqrt(6)
variable bhat4_3 equal 0.0983/sqrt(6)
variable nhat4_1 equal 0.2248/sqrt(3)
variable nhat4_2 equal -0.2713/sqrt(3)
variable nhat4_3 equal -1.6856/sqrt(3)

```

```
variable bhat5_1 equal 1.3105/sqrt(6)
variable bhat5_2 equal 1.6250/sqrt(6)
variable bhat5_3 equal -1.2034/sqrt(6)
variable nhat5_1 equal 1.3105/sqrt(3)
variable nhat5_2 equal -0.4963/sqrt(3)
variable nhat5_3 equal 0.9179/sqrt(3)
```

```
variable bhat6_1 equal 2.0781/sqrt(6)
variable bhat6_2 equal 0.5341/sqrt(6)
variable bhat6_3 equal -0.8801/sqrt(6)
variable nhat6_1 equal -0.2248/sqrt(3)
variable nhat6_2 equal 1.6856/sqrt(3)
variable nhat6_3 equal 0.2713/sqrt(3)
```

```
#Create resolved stress calculations for each set of vectors
```

```
variable rs_011_100 atom
v_bhat1_1*c_vs[1]*v_nhat1_1+v_bhat1_2*c_vs[2]*v_nhat1_2+v_bhat1_3*c_vs[3]*v_nhat1_3
+2*v_bhat1_2*c_vs[4]*v_nhat1_3+2*v_bhat1_1*c_vs[5]*v_nhat1_3+2*v_bhat1_1*c_vs[6]*v_
nhat1_2
```

```
variable rs_101_010 atom
v_bhat2_1*c_vs[1]*v_nhat2_1+v_bhat2_2*c_vs[2]*v_nhat2_2+v_bhat2_3*c_vs[3]*v_nhat2_3
+2*v_bhat2_2*c_vs[4]*v_nhat2_3+2*v_bhat2_1*c_vs[5]*v_nhat2_3+2*v_bhat2_1*c_vs[6]*v_
nhat2_2
```

```
variable rs_110_001 atom
v_bhat3_1*c_vs[1]*v_nhat3_1+v_bhat3_2*c_vs[2]*v_nhat3_2+v_bhat3_3*c_vs[3]*v_nhat3_3
+2*v_bhat3_2*c_vs[4]*v_nhat3_3+2*v_bhat3_1*c_vs[5]*v_nhat3_3+2*v_bhat3_1*c_vs[6]*v_
nhat3_2
```

```
variable rs_112_11n1 atom
v_bhat4_1*c_vs[1]*v_nhat4_1+v_bhat4_2*c_vs[2]*v_nhat4_2+v_bhat4_3*c_vs[3]*v_nhat4_3
+2*v_bhat4_2*c_vs[4]*v_nhat4_3+2*v_bhat4_1*c_vs[5]*v_nhat4_3+2*v_bhat4_1*c_vs[6]*v_
nhat4_2
```

```
variable rs_121_1n11 atom
v_bhat5_1*c_vs[1]*v_nhat5_1+v_bhat5_2*c_vs[2]*v_nhat5_2+v_bhat5_3*c_vs[3]*v_nhat5_3
+2*v_bhat5_2*c_vs[4]*v_nhat5_3+2*v_bhat5_1*c_vs[5]*v_nhat5_3+2*v_bhat5_1*c_vs[6]*v_
nhat5_2
```

```
variable rs_211_n111 atom
v_bhat6_1*c_vs[1]*v_nhat6_1+v_bhat6_2*c_vs[2]*v_nhat6_2+v_bhat6_3*c_vs[3]*v_nhat6_3
+2*v_bhat6_2*c_vs[4]*v_nhat6_3+2*v_bhat6_1*c_vs[5]*v_nhat6_3+2*v_bhat6_1*c_vs[6]*v_
nhat6_2
```

```
#shell commands to navigate to proper directories
```

```
#shell cd RUNS
```

```
#shell cd $t
```

```
#Settings regions for lindemann parameter calculations
```

```
region          box1 block INF INF INF INF 14 39 units lattice
```

```

group      box1 region box1

region    box2 block INF INF INF INF 40 64 units lattice
group     box2 region box1

region    box3 block INF INF INF INF 65 89 units lattice
group     box3 region box1

region    box4 block INF INF INF INF 90 115 units lattice
group     box4 region box1

```

### #Group Based Computes

```

#compute voro1 box1 voronoi/atom
#compute voro2 box2 voronoi/atom
#compute voro3 box3 voronoi/atom
#compute voro4 box4 voronoi/atom
#
#compute v1 box1 reduce sum c_voro1[1]
#compute v2 box2 reduce sum c_voro2[1]
#compute v3 box3 reduce sum c_voro3[1]
#compute v4 box4 reduce sum c_voro4[1]
#
#compute boxtemp1 box1 temp
#compute boxtemp2 box2 temp
#compute boxtemp3 box3 temp
#compute boxtemp4 box4 temp
#
#compute boxperpress1 box1 stress/atom boxtemp1
#compute boxperpress2 box2 stress/atom boxtemp2
#compute boxperpress3 box3 stress/atom boxtemp3
#compute boxperpress4 box4 stress/atom boxtemp4
#
#compute p1 box1 reduce sum c_boxperpress1[1] c_boxperpress1[2] c_boxperpress1[3]
c_boxperpress1[4] c_boxperpress1[5] c_boxperpress1[6]
#compute p2 box2 reduce sum c_boxperpress2[1] c_boxperpress2[2] c_boxperpress2[3]
c_boxperpress1[4] c_boxperpress1[5] c_boxperpress1[6]
#compute p3 box3 reduce sum c_boxperpress3[1] c_boxperpress3[2] c_boxperpress3[3]
c_boxperpress1[4] c_boxperpress1[5] c_boxperpress1[6]
#compute p4 box4 reduce sum c_boxperpress4[1] c_boxperpress4[2] c_boxperpress4[3]
c_boxperpress1[4] c_boxperpress1[5] c_boxperpress1[6]
#
#variable press1avg equal -(c_p1[1]+c_p1[2]+c_p1[3])/(3*c_v1)
#variable press2avg equal -(c_p2[1]+c_p2[2]+c_p2[3])/(3*c_v2)
#variable press3avg equal -(c_p3[1]+c_p3[2]+c_p3[3])/(3*c_v3)
#variable press4avg equal -(c_p4[1]+c_p4[2]+c_p4[3])/(3*c_v4)

```

```
#variable press1VM equal sqrt(0.5*((c_p1[1]-c_p1[2])^2+(c_p1[1]-c_p1[3])^2+(c_p1[2]-
c_p1[3])^2+6*(c_p1[4]^2+c_p1[5]^2+c_p1[6]^2)))/(c_v1)
#variable press2VM equal sqrt(0.5*((c_p2[1]-c_p2[2])^2+(c_p2[1]-c_p2[3])^2+(c_p2[2]-
c_p2[3])^2+6*(c_p2[4]^2+c_p2[5]^2+c_p2[6]^2)))/(c_v2)
#variable press3VM equal sqrt(0.5*((c_p3[1]-c_p3[2])^2+(c_p3[1]-c_p3[3])^2+(c_p3[2]-
c_p3[3])^2+6*(c_p3[4]^2+c_p3[5]^2+c_p3[6]^2)))/(c_v3)
#variable press4VM equal sqrt(0.5*((c_p4[1]-c_p4[2])^2+(c_p4[1]-c_p4[3])^2+(c_p4[2]-
c_p4[3])^2+6*(c_p4[4]^2+c_p4[5]^2+c_p4[6]^2)))/(c_v4)
```

```
#Defining shock driving piston region
```

```
region      pistonR block INF INF INF INF INF 10 units lattice
group      piston region pistonR
```

```
#Defining Gap between piston and bulk
```

```
region      gap block INF INF INF INF 11 13 units lattice
group      gap region gap
```

```
delete_atoms group gap compress yes
```

```
#Defining the bulk
```

```
group      bulk subtract all piston gap
```

```
#preset defined computes
```

```
compute kea bulk ke/atom
#compute 2 bulk centro/atom 14
compute pea bulk pe/atom
compute s bulk stress/atom NULL pair
#compute 5 bulk cna/atom 4.0
compute coord bulk coord/atom cutoff 2.1
```

```
#MSD Lindemann Compute
```

```
#compute      msdall bulk msd
#compute      msdbox1 box1 msd
#compute      msdbox2 box2 msd
#compute      msdbox3 box3 msd
#compute      msdbox4 box4 msd
#variable     lindparmallx equal sqrt(c_msdall[1])/({a0}*0.7071067811865475)
#variable     lindparmbox1x equal sqrt(c_msdbox1[1])/({a0}*0.7071067811865475)
#variable     lindparmbox2x equal sqrt(c_msdbox2[1])/({a0}*0.7071067811865475)
#variable     lindparmbox3x equal sqrt(c_msdbox3[1])/({a0}*0.7071067811865475)
#variable     lindparmbox4x equal sqrt(c_msdbox4[1])/({a0}*0.7071067811865475)
#variable     lindparmally equal sqrt(c_msdall[2])/({a0}*0.7071067811865475)
#variable     lindparmbox1y equal sqrt(c_msdbox1[2])/({a0}*0.7071067811865475)
#variable     lindparmbox2y equal sqrt(c_msdbox2[2])/({a0}*0.7071067811865475)
#variable     lindparmbox3y equal sqrt(c_msdbox3[2])/({a0}*0.7071067811865475)
#variable     lindparmbox4y equal sqrt(c_msdbox4[2])/({a0}*0.7071067811865475)
```

```
#variable lindparmallz equal sqrt(c_msall[3])/({a0}*0.7071067811865475)
#variable lindparmbox1z equal sqrt(c_msbox1[3])/({a0}*0.7071067811865475)
#variable lindparmbox2z equal sqrt(c_msbox2[3])/({a0}*0.7071067811865475)
#variable lindparmbox3z equal sqrt(c_msbox3[3])/({a0}*0.7071067811865475)
#variable lindparmbox4z equal sqrt(c_msbox4[3])/({a0}*0.7071067811865475)
```

```
#RDF Compute
```

```
compute rdfbulk bulk rdf 100 1 1
compute rdfbox1 box1 rdf 100 1 1
compute rdfbox2 box2 rdf 100 1 1
compute rdfbox3 box3 rdf 100 1 1
compute rdfbox4 box4 rdf 100 1 1
```

```
#initialize velocity
```

```
velocity bulk create 300.0 376847 dist gaussian
velocity bulk zero linear
velocity piston set 0.0 0.0 0.0 sum no units box
```

```
#nve fix
```

```
fix 1 all nve
```

```
#piston fix
```

```
fix 2 piston setforce 0.0 0.0 0.0
```

```
#Processor balance fix
```

```
fix bal all balance 500 1.1 shift z 10 1.2 weight time 0.8
```

```
#equilibration thermo
```

```
thermo_style custom step temp ke pe etotal press pxx pyy pzz pxy pxz pyz ly lx lz vol
thermo_modify lost warn norm yes
thermo 500
```

```
#equilibration run
```

```
run 5000
```

```
reset_timestep 0
```

```
#Dump end of equilibration
```

```
dump VOIDALL all custom 1 C-eqall.* id type x y z
```

```
#
```

```
run 0
```

```
#
```

```
#undump EQPISTON
```

```
undump VOIDALL
```

```

#Test Peratom Stress total
compute peratom all stress/atom NULL
compute p all reduce sum c_peratom[1] c_peratom[2] c_peratom[3]
variable peratompresssum equal -(c_p[1]+c_p[2]+c_p[3])/(3*vol)

#Reset Thermo style for shock

#thermo_style custom step temp ke pe etotal press pxx pyy pzz pxy pxz pyz lx ly lz vol
thermo_style custom step temp ke pe etotal press pxx pyy pzz pxy pxz pyz lx ly lz vol
v_peratompresssum
thermo_modify      lost warn norm yes
thermo             100

#rdf fixes
fix rdfbulk bulk ave/time 10 10 10000 c_rdfbulk[*] file RDF/bulk.rdf mode vector
fix rdfbox1 box1 ave/time 10 10 10000 c_rdfbox1[*] file RDF/box1.rdf mode vector
fix rdfbox2 box2 ave/time 10 10 10000 c_rdfbox2[*] file RDF/box2.rdf mode vector
fix rdfbox3 box3 ave/time 10 10 10000 c_rdfbox3[*] file RDF/box3.rdf mode vector
fix rdfbox4 box4 ave/time 10 10 10000 c_rdfbox4[*] file RDF/box4.rdf mode vector

#Average stress per time

variable period equal 500

fix avgstr voidgroup ave/atom 1 ${period} ${period} v_rs_011_100 v_rs_101_010
v_rs_110_001 v_rs_112_11n1 v_rs_121_1n11 v_rs_211_n111

variable ave_rs_011_100 atom f_avgstr[1]
variable ave_rs_101_010 atom f_avgstr[2]
variable ave_rs_110_001 atom f_avgstr[3]
variable ave_rs_112_11n1 atom f_avgstr[4]
variable ave_rs_121_1n11 atom f_avgstr[5]
variable ave_rs_211_n111 atom f_avgstr[6]

#Defining dumps for entire system
#dump OUT1 all custom 100 DUMP/Cshock.$t.* id type x y z c_coord c_pea c_kea vx vy vz
c_s[1] c_s[2] c_s[3] c_s[4] c_s[5] c_s[6]

dump OUT2 bulk custom 500 DUMP/$t.CnotD.* id type x y z c_coord c_pea c_kea vx vy vz
c_s[1] c_s[2] c_s[3] c_s[4] c_s[5] c_s[6]
dump_modify OUT2 thresh c_coord != 4

dump OUT3 voidgroup custom 500 DUMP/Cvoidstress.$t.* id type x y z vx vy vz c_vs[1]
c_vs[2] c_vs[3] c_vs[4] c_vs[5] c_vs[6] &

```



```

v_ave_rs_011_100 v_ave_rs_101_010 v_ave_rs_110_001 v_ave_rs_112_11n1
v_ave_rs_121_1n11 v_ave_rs_211_n111
dump_modify OUT3 sort id

timestep      0.0005
variable      piston_vel equal 10*$t
print        "Vel=$t km/s"
velocity      piston set 0.0 0.0 ${piston_vel} sum no units box

run           4000

dump OUT1 all custom 500 DUMP/Cshock.$t.* id type x y z c_coord c_pea c_kea vx vy vz
c_s[1] c_s[2] c_s[3] c_s[4] c_s[5] c_s[6]

run           4000

undump OUT1

#run          5800

#write_data 111.10000.data
#write_restart 111.10000.restart

clear

next t

#shell cd ..

jump SELF loop

```

## Appendix B – Calculation of the Lu Factor

Derivation by Dr. Rob E. Rudd

### INTRODUCTION

The Schmid factor is the constant of proportionality that relates the resolved shear stress on a glide system to the applied uniaxial stress. For wave propagation, uniaxial strain is relevant instead of uniaxial stress. In C. H. Lu's 2013 doctoral dissertation (93), she and Marc Meyers computed these resolved shear stresses for many glide systems in tantalum. Li et al. pointed out that the generalization of the Schmid factor to the diamond shock application is useful and potentially powerful and termed it the Lu factor (334). Here we have some brief notes on how to calculate it.

The strategy here is to do the calculation in a few steps:

- Calculate the strain
- Multiply by the elastic constant tensor to get the stress
- Dot the stress into the Burgers vector and glide plane normal to get the resolved shear stress
- Dot the stress into the wave propagation direction to get the reference stress
- Divide the resolved shear stress by the reference stress to get the generalized Schmid factor

## CUBIC ELASTICITY

Consider uniaxial elastic strain. We want to calculate the ratio of the resolved shear stress on a glide system to the longitudinal stress. For uniaxial stress, this ratio would be the Schmid factor:

$$m = \frac{\sigma_{1'2'}}{\sigma_{33}} \quad (1)$$

We consider a cubic crystal with elastic constants  $C_{11}$ ,  $C_{12}$ , and  $C_{44}$ . Let the longitudinal axis of the compression be  $\hat{k}$ , let the Burgers vector be  $\vec{b}$  and the glide plane normal be  $\hat{n}$ . Then  $\vec{b} = \frac{\vec{b}}{|\vec{b}|}$ .

Throughout these notes, the vectors with hats like  $\hat{n}$  are unit vectors.

Consider the case of [001] compression. The strain tensor is given by

$$\epsilon = \epsilon_0 \begin{pmatrix} 0 & 0 & 0 \\ 0 & 0 & 0 \\ 0 & 0 & 1 \end{pmatrix} \quad (2)$$

And  $\hat{k} = (0,0,1)$ .

So the strain may be expressed as:

$$\epsilon = \epsilon_0 \hat{k} \otimes \hat{k} \quad (3)$$

This expression is independent of the coordinate system, so it must be correct regardless of the direction of compression.

## SCHMID FACTOR

The Schmid factor is easier to calculate, so let's start with it. Suppose the uniaxial stress is

$$\sigma = \sigma_0 \hat{k} \otimes \hat{k} \quad (4)$$

$$m = \frac{\sigma_{1'2'}}{\sigma_{33}} \quad (5)$$

$$= \frac{\hat{b} \cdot \sigma \cdot \hat{n}}{\hat{k} \cdot \sigma \cdot \hat{k}} \quad (6)$$

$$= \frac{\sigma_0 \hat{b} \cdot \hat{k} \hat{k} \cdot \hat{n}}{\sigma_0 \hat{k} \cdot \hat{k} \hat{k} \cdot \hat{k}} \quad (7)$$

$$= \hat{b} \cdot \hat{k} \hat{k} \cdot \hat{n} \quad (8)$$

So the Schmid factor  $m$  is purely geometrical, the product of two directional cosines, as expected.

### GENERALIZED SCHMID FACTOR FOR UNIAXIAL STRAIN

In general, the uniaxial strain is

$$\epsilon = \epsilon_0 \hat{k} \otimes \hat{k} \quad (9)$$

So for  $\hat{k} = [0 \ 0 \ 1]$ , the strain is

$$\epsilon = \epsilon_0 \begin{pmatrix} 0 & 0 & 0 \\ 0 & 0 & 0 \\ 0 & 0 & 1 \end{pmatrix} \quad (10)$$

For  $\hat{k} = [0 \ 1 \ 1]/\sqrt{2}$ , the strain is

$$\epsilon = \frac{1}{2} \epsilon_0 \begin{pmatrix} 0 & 0 & 0 \\ 0 & 1 & 1 \\ 0 & 1 & 1 \end{pmatrix} \quad (11)$$

For  $\hat{k} = [1 \ 1 \ 1]/\sqrt{3}$ , the strain is

$$\epsilon = \frac{1}{3} \epsilon_0 \begin{pmatrix} 1 & 1 & 1 \\ 1 & 1 & 1 \\ 1 & 1 & 1 \end{pmatrix} \quad (12)$$

For the cubic system, the elastic constant tensor  $C_{ijkl}$  reduces to the three independent moduli noted above:  $C_{11}$ ,  $C_{12}$ , and  $C_{44}$ . So, the Hooke's Law stress

$$\sigma_{ij} = C_{ijkl}\epsilon_{kl} \quad (13)$$

can be calculated by inspection.

For  $\hat{k} = [0 \ 0 \ 1]$ , the stress is

$$\sigma = \epsilon_0 \begin{pmatrix} C_{12} & 0 & 0 \\ 0 & C_{12} & 0 \\ 0 & 0 & C_{11} \end{pmatrix} \quad (14)$$

$$= C_{12}\epsilon_0 I + (C_{11} - C_{12})\epsilon_0 \hat{k} \otimes \hat{k} \quad (15)$$

Where  $I$  is the 3x3 identity matrix (tensor).

For  $\hat{k} = [0 \ 1 \ 1]/\sqrt{2}$ , the stress is

$$\sigma = \frac{1}{2}\epsilon_0 \begin{pmatrix} 2C_{12} & 0 & 0 \\ 0 & C_{11} + C_{12} & 2C_{44} \\ 0 & 2C_{44} & C_{11} + C_{12} \end{pmatrix} \quad (16)$$

$$\sigma = \frac{1}{2}\epsilon_0 \begin{pmatrix} 0 & 0 & 0 \\ 0 & C_{11} - C_{12} - 2C_{44} & 0 \\ 0 & 0 & C_{11} - C_{12} - 2C_{44} \end{pmatrix} + C_{12}\epsilon_0 I + 2C_{44}\epsilon_0 \hat{k} \otimes \hat{k} \quad (17)$$

For  $\hat{k} = [1 \ 1 \ 1]/\sqrt{3}$ , the stress is

$$\sigma = \frac{1}{3}\epsilon_0 \begin{pmatrix} C_{11} + 2C_{12} & 2C_{44} & 2C_{44} \\ 2C_{44} & C_{11} + 2C_{12} & 2C_{44} \\ 2C_{44} & 2C_{44} & C_{11} + 2C_{12} \end{pmatrix} \quad (18)$$

$$\sigma = \frac{1}{3}(C_{11} + 2C_{12} - 2C_{44})\epsilon_0 I + 2C_{44}\epsilon_0 \hat{k} \otimes \hat{k} \quad (19)$$

We now have everything needed to calculate the generalized Schmid factor for uniaxial strain. In fact, since  $m = \hat{b} \cdot \hat{k}\hat{k} \cdot \hat{n}$  by Eq. (8) and  $\hat{b} \cdot I \cdot \hat{n} = 0$  because the Burgers vector and glide plane normal are orthogonal, the expressions for the generalized Schmid factor in the  $[0 \ 0 \ 1]$  and  $[1 \ 1 \ 1]$  directions are particularly simple:

$$m_{Lu} = \frac{\sigma_{1'2'}}{\sigma_{33}} \quad (20)$$

$$[0\ 0\ 1]m_{Lu} = \left(1 - \frac{C_{12}}{C_{11}}\right)m \quad (21)$$

$$[1\ 1\ 1]m_{Lu} = \frac{6C_{44}}{C_{11} + 2C_{12} + 4C_{44}}m \quad (22)$$

$$[0\ 1\ 1]m_{Lu} = \frac{4C_{44}}{C_{11} + C_{12} + 2C_{44}}m - \frac{C_{11} - C_{12} - 2C_{44}}{C_{11} + C_{12} + 2C_{44}}\hat{b}_1\hat{n}_1 \quad (23)$$

The expression in the  $[0\ 1\ 1]$  is not too complicated, but it is not just proportional to the Schmid factor  $m$ , as in the other cases. There is an extra term that is proportional to the elastic anisotropy  $(C_{11} - C_{12} - 2C_{44})$ . Generally, we have

$$\frac{\sigma_{ij}}{\epsilon_0} = 2C_{44}\hat{k}_i\hat{k}_j + C_{12}\delta_{ij} + (C_{11} - C_{12} - 2C_{44})\hat{k}_i^2\delta_{ij} \quad (24)$$

And

$$\frac{\hat{k} \cdot \sigma \cdot \hat{k}}{\epsilon_0} = C_{12} + 2C_{44} + (C_{11} - C_{12} - 2C_{44}) \sum_{i=1}^3 \hat{k}_i^4 \quad (25)$$

$$\frac{\hat{b} \cdot \sigma \cdot \hat{n}}{\epsilon_0} = 2C_{44}m + (C_{11} - C_{12} - 2C_{44}) \sum_{i=1}^3 \hat{k}_i^2 \hat{b}_i \hat{n}_i \quad (26)$$

$$m_{Lu} = \frac{2C_{44}m + (C_{11} - C_{12} - 2C_{44}) \sum_{i=1}^3 \hat{k}_i^2 \hat{b}_i \hat{n}_i}{C_{12} + 2C_{44} + (C_{11} - C_{12} - 2C_{44}) \sum_{i=1}^3 \hat{k}_i^4} \quad (24)$$

## Tables

Here we present numerical results for diamond (diamond cubic carbon) at absolute zero temperature based on Density Functional Theory calculations of the zero-temperature elastic constants up to 200 GPa.

Table A-1 Table of generalized Schmid factors for uniaxial [001] strain. The 3 left-most columns show the longitudinal direction, the direction of the Burgers vector and the direction of the glide plane normal. The other columns contain the data values at the pressures shown at the top. The spacing between the rows help guide the eye to cases with equal generalized Schmid factors.

$\hat{k}$	$\hat{b}$	$\hat{n}$	0	10	20	50	60	70	80	100	120	140	150	200 (GPa)
[001]	$[\bar{2}\bar{1}1]$	$[1\bar{1}1]$	0.214	0.209	0.205	0.194	0.191	0.187	0.185	0.179	0.175	0.170	0.168	0.159
[001]	$[\bar{1}21]$	$[\bar{1}\bar{1}1]$	0.214	0.209	0.205	0.194	0.191	0.187	0.185	0.179	0.175	0.170	0.168	0.159
[001]	$[1\bar{2}1]$	$[111]$	0.214	0.209	0.205	0.194	0.191	0.187	0.185	0.179	0.175	0.170	0.168	0.159
[001]	$[\bar{1}\bar{2}1]$	$[\bar{1}11]$	0.214	0.209	0.205	0.194	0.191	0.187	0.185	0.179	0.175	0.170	0.168	0.159
[001]	$[121]$	$[1\bar{1}1]$	0.214	0.209	0.205	0.194	0.191	0.187	0.185	0.179	0.175	0.170	0.168	0.159
[001]	$[\bar{2}11]$	$[111]$	0.214	0.209	0.205	0.194	0.191	0.187	0.185	0.179	0.175	0.170	0.168	0.159
[001]	$[2\bar{1}1]$	$[\bar{1}\bar{1}1]$	0.214	0.209	0.205	0.194	0.191	0.187	0.185	0.179	0.175	0.170	0.168	0.159
[001]	$[211]$	$[\bar{1}11]$	0.214	0.209	0.205	0.194	0.191	0.187	0.185	0.179	0.175	0.170	0.168	0.159
[001]	$[0\bar{1}1]$	$[100]$	0.000	0.000	0.000	0.000	0.000	0.000	0.000	0.000	0.000	0.000	0.000	0.000
[001]	$[0\bar{1}1]$	$[\bar{1}00]$	0.000	0.000	0.000	0.000	0.000	0.000	0.000	0.000	0.000	0.000	0.000	0.000
[001]	$[110]$	$[001]$	0.000	0.000	0.000	0.000	0.000	0.000	0.000	0.000	0.000	0.000	0.000	0.000
[001]	$[\bar{1}01]$	$[010]$	0.000	0.000	0.000	0.000	0.000	0.000	0.000	0.000	0.000	0.000	0.000	0.000
[001]	$[101]$	$[0\bar{1}0]$	0.000	0.000	0.000	0.000	0.000	0.000	0.000	0.000	0.000	0.000	0.000	0.000
[001]	$[101]$	$[010]$	0.000	0.000	0.000	0.000	0.000	0.000	0.000	0.000	0.000	0.000	0.000	0.000
[001]	$[\bar{1}01]$	$[0\bar{1}0]$	0.000	0.000	0.000	0.000	0.000	0.000	0.000	0.000	0.000	0.000	0.000	0.000
[001]	$[011]$	$[100]$	0.000	0.000	0.000	0.000	0.000	0.000	0.000	0.000	0.000	0.000	0.000	0.000
[001]	$[1\bar{1}0]$	$[001]$	0.000	0.000	0.000	0.000	0.000	0.000	0.000	0.000	0.000	0.000	0.000	0.000
[001]	$[\bar{1}\bar{1}0]$	$[001]$	0.000	0.000	0.000	0.000	0.000	0.000	0.000	0.000	0.000	0.000	0.000	0.000
[001]	$[\bar{1}10]$	$[001]$	0.000	0.000	0.000	0.000	0.000	0.000	0.000	0.000	0.000	0.000	0.000	0.000
[001]	$[011]$	$[\bar{1}00]$	0.000	0.000	0.000	0.000	0.000	0.000	0.000	0.000	0.000	0.000	0.000	0.000
[001]	$[\bar{1}12]$	$[\bar{1}\bar{1}\bar{1}]$	-0.429	-0.419	-0.410	-0.388	-0.381	-0.375	-0.369	-0.359	-0.349	-0.341	-0.336	-0.318
[001]	$[\bar{1}\bar{1}2]$	$[\bar{1}\bar{1}\bar{1}]$	-0.429	-0.419	-0.410	-0.388	-0.381	-0.375	-0.369	-0.359	-0.349	-0.341	-0.336	-0.318
[001]	$[1\bar{1}2]$	$[1\bar{1}\bar{1}]$	-0.429	-0.419	-0.410	-0.388	-0.381	-0.375	-0.369	-0.359	-0.349	-0.341	-0.336	-0.318
[001]	$[112]$	$[11\bar{1}]$	-0.429	-0.419	-0.410	-0.388	-0.381	-0.375	-0.369	-0.359	-0.349	-0.341	-0.336	-0.318

Table A-2 Table of generalized Schmid factors for uniaxial [011] strain. The 3 left-most columns show the longitudinal direction, the direction of the Burgers vector and the direction of the glide plane normal. The other columns contain the data values at the pressures shown at the top. The spacing between the rows help guide the eye to cases with equal generalized Schmid factors.

$\hat{k}$	$\hat{b}$	$\hat{n}$	0	10	20	50	60	70	80	100	120	140	150	200 (GPa)
[011]	$\bar{2}11$	[111]	0.432	0.424	0.416	0.398	0.392	0.387	0.383	0.374	0.367	0.360	0.356	0.342
[011]	[211]	$\bar{1}11$	0.432	0.424	0.416	0.398	0.392	0.387	0.383	0.374	0.367	0.360	0.356	0.342
[011]	$\bar{1}10$	[001]	0.353	0.351	0.348	0.340	0.338	0.336	0.333	0.329	0.325	0.321	0.319	0.311
[011]	[110]	[001]	0.353	0.351	0.348	0.340	0.338	0.336	0.333	0.329	0.325	0.321	0.319	0.311
[011]	$\bar{1}01$	[010]	0.353	0.351	0.348	0.340	0.338	0.336	0.333	0.329	0.325	0.321	0.319	0.311
[011]	[101]	[010]	0.353	0.351	0.348	0.340	0.338	0.336	0.333	0.329	0.325	0.321	0.319	0.311
[011]	$\bar{1}21$	$\bar{1}\bar{1}1$	0.020	0.022	0.024	0.028	0.029	0.030	0.031	0.032	0.033	0.034	0.035	0.036
[011]	[121]	$1\bar{1}1$	0.020	0.022	0.024	0.028	0.029	0.030	0.031	0.032	0.033	0.034	0.035	0.036
[011]	$\bar{1}12$	$\bar{1}\bar{1}\bar{1}$	0.020	0.022	0.024	0.028	0.029	0.030	0.031	0.032	0.033	0.034	0.035	0.036
[011]	[112]	$1\bar{1}\bar{1}$	0.020	0.022	0.024	0.028	0.029	0.030	0.031	0.032	0.033	0.034	0.035	0.036
[011]	$0\bar{1}1$	$\bar{1}00$	0.000	0.000	0.000	0.000	0.000	0.000	0.000	0.000	0.000	0.000	0.000	0.000
[011]	$0\bar{1}1$	[100]	0.000	0.000	0.000	0.000	0.000	0.000	0.000	0.000	0.000	0.000	0.000	0.000
[011]	[011]	[100]	0.000	0.000	0.000	0.000	0.000	0.000	0.000	0.000	0.000	0.000	0.000	0.000
[011]	[011]	$\bar{1}00$	0.000	0.000	0.000	0.000	0.000	0.000	0.000	0.000	0.000	0.000	0.000	0.000
[011]	$\bar{2}\bar{1}1$	$1\bar{1}\bar{1}$	-0.039	-0.044	-0.048	-0.056	-0.058	-0.060	-0.062	-0.065	-0.067	-0.069	-0.070	-0.073
[011]	$2\bar{1}1$	$\bar{1}\bar{1}\bar{1}$	-0.039	-0.044	-0.048	-0.056	-0.058	-0.060	-0.062	-0.065	-0.067	-0.069	-0.070	-0.073
[011]	$1\bar{2}1$	[111]	-0.216	-0.212	-0.208	-0.199	-0.196	-0.194	-0.191	-0.187	-0.183	-0.180	-0.178	-0.171
[011]	$\bar{1}\bar{2}1$	$\bar{1}11$	-0.216	-0.212	-0.208	-0.199	-0.196	-0.194	-0.191	-0.187	-0.183	-0.180	-0.178	-0.171
[011]	$\bar{1}\bar{1}2$	$\bar{1}\bar{1}\bar{1}$	-0.216	-0.212	-0.208	-0.199	-0.196	-0.194	-0.191	-0.187	-0.183	-0.180	-0.178	-0.171
[011]	$1\bar{1}2$	$1\bar{1}\bar{1}$	-0.216	-0.212	-0.208	-0.199	-0.196	-0.194	-0.191	-0.187	-0.183	-0.180	-0.178	-0.171
[011]	[101]	$0\bar{1}0$	-0.353	-0.351	-0.348	-0.340	-0.338	-0.336	-0.333	-0.329	-0.325	-0.321	-0.319	-0.311
[011]	$\bar{1}01$	$0\bar{1}0$	-0.353	-0.351	-0.348	-0.340	-0.338	-0.336	-0.333	-0.329	-0.325	-0.321	-0.319	-0.311
[011]	$1\bar{1}0$	[001]	-0.353	-0.351	-0.348	-0.340	-0.338	-0.336	-0.333	-0.329	-0.325	-0.321	-0.319	-0.311
[011]	$\bar{1}\bar{1}0$	[001]	-0.353	-0.351	-0.348	-0.340	-0.338	-0.336	-0.333	-0.329	-0.325	-0.321	-0.319	-0.311



Table A-3 Table of generalized Schmid factors for uniaxial [111] strain. The 3 left-most columns show the longitudinal direction, the direction of the Burgers vector and the direction of the glide plane normal. The other columns contain the data values at the pressures shown at the top. The spacing between the rows help guide the eye to cases with equal generalized Schmid factors.

$\hat{k}$	$\hat{b}$	$\hat{n}$	0	10	20	50	60	70	80	100	120	140	150	200 (GPa)
[111]	[011]	[100]	0.459	0.453	0.449	0.436	0.433	0.429	0.426	0.420	0.414	0.409	0.406	0.394
[111]	[110]	[001]	0.459	0.453	0.449	0.436	0.433	0.429	0.426	0.420	0.414	0.409	0.406	0.394
[111]	[101]	[010]	0.459	0.453	0.449	0.436	0.433	0.429	0.426	0.420	0.414	0.409	0.406	0.394
[111]	[112]	[11 $\bar{1}$ ]	0.306	0.302	0.299	0.291	0.288	0.286	0.284	0.280	0.276	0.272	0.271	0.263
[111]	[211]	[ $\bar{1}$ 11]	0.306	0.302	0.299	0.291	0.288	0.286	0.284	0.280	0.276	0.272	0.271	0.263
[111]	[121]	[1 $\bar{1}$ 1]	0.306	0.302	0.299	0.291	0.288	0.286	0.284	0.280	0.276	0.272	0.271	0.263
[111]	[ $\bar{1}\bar{1}2$ ]	[ $\bar{1}\bar{1}\bar{1}$ ]	0.000	0.000	0.000	-0.000	-0.000	0.000	0.000	0.000	-0.000	0.000	0.000	0.000
[111]	[0 $\bar{1}$ 1]	[ $\bar{1}$ 00]	0.000	0.000	0.000	0.000	0.000	0.000	0.000	0.000	0.000	0.000	0.000	0.000
[111]	[ $\bar{1}$ 10]	[001]	0.000	0.000	0.000	0.000	0.000	0.000	0.000	0.000	0.000	0.000	0.000	0.000
[111]	[1 $\bar{1}$ 0]	[001]	0.000	0.000	0.000	0.000	0.000	0.000	0.000	0.000	0.000	0.000	0.000	0.000
[111]	[ $\bar{1}$ 01]	[0 $\bar{1}$ 0]	0.000	0.000	0.000	0.000	0.000	0.000	0.000	0.000	0.000	0.000	0.000	0.000
[111]	[0 $\bar{1}$ 1]	[100]	0.000	0.000	0.000	0.000	0.000	0.000	0.000	0.000	0.000	0.000	0.000	0.000
[111]	[ $\bar{1}$ 01]	[010]	0.000	0.000	0.000	0.000	0.000	0.000	0.000	0.000	0.000	0.000	0.000	0.000
[111]	[1 $\bar{2}$ 1]	[111]	-0.000	0.000	-0.000	0.000	0.000	-0.000	0.000	-0.000	-0.000	0.000	0.000	-0.000
[111]	[ $\bar{2}$ 11]	[111]	-0.000	-0.000	-0.000	-0.000	-0.000	0.000	0.000	0.000	0.000	-0.000	0.000	-0.000
[111]	[1 $\bar{1}2$ ]	[1 $\bar{1}\bar{1}$ ]	-0.153	-0.151	-0.150	-0.145	-0.144	-0.143	-0.142	-0.140	-0.138	-0.136	-0.135	-0.131
[111]	[ $\bar{1}$ 12]	[ $\bar{1}$ 1 $\bar{1}$ ]	-0.153	-0.151	-0.150	-0.145	-0.144	-0.143	-0.142	-0.140	-0.138	-0.136	-0.135	-0.131
[111]	[ $\bar{2}$ 11]	[1 $\bar{1}$ 1]	-0.153	-0.151	-0.150	-0.145	-0.144	-0.143	-0.142	-0.140	-0.138	-0.136	-0.135	-0.131
[111]	[ $\bar{1}$ 21]	[ $\bar{1}\bar{1}$ 1]	-0.153	-0.151	-0.150	-0.145	-0.144	-0.143	-0.142	-0.140	-0.138	-0.136	-0.135	-0.131
[111]	[ $\bar{1}\bar{2}$ 1]	[ $\bar{1}$ 11]	-0.153	-0.151	-0.150	-0.145	-0.144	-0.143	-0.142	-0.140	-0.138	-0.136	-0.135	-0.131
[111]	[2 $\bar{1}$ 1]	[ $\bar{1}\bar{1}$ 1]	-0.153	-0.151	-0.150	-0.145	-0.144	-0.143	-0.142	-0.140	-0.138	-0.136	-0.135	-0.131
[111]	[011]	[ $\bar{1}$ 00]	-0.459	-0.453	-0.449	-0.436	-0.433	-0.429	-0.426	-0.420	-0.414	-0.409	-0.406	-0.394
[111]	[ $\bar{1}$ 10]	[001]	-0.459	-0.453	-0.449	-0.436	-0.433	-0.429	-0.426	-0.420	-0.414	-0.409	-0.406	-0.394
[111]	[101]	[0 $\bar{1}$ 0]	-0.459	-0.453	-0.449	-0.436	-0.433	-0.429	-0.426	-0.420	-0.414	-0.409	-0.406	-0.394